به نام خدا

مرکز دانلود رایگان
مهندسی متالورژی و مواد

www.Iran-mavad.com

Ultrasonic Inspection Technology Development and Search Unit Design

IEEE Press
445 Hoes Lane
Piscataway, NJ 08854

Ultrasonic Inspection Technology Development and Search Unit Design

Examples of Practical Applications

Mark V. Brook

IEEE PRESS

A John Wiley & Sons, Inc., Publication

Published simultaneously in Canada

Library of Congress Cataloging-in-Publication Data:
Brook, Mark V.
Ultrasonic inspection technology development and search unit design : examples of practical applications / Mark V. Brook.
p. cm.
ISBN 978-0-470-87434-9 (hardback)
1. Ultrasonic testing. 2. Ultrasonic waves—Industrial applications. I. Title.
TA417.4.B76 2011
681'.2–dc22
2011008871

Printed in the United States of America

oBook ISBN: 978-1-118-10478-1
ePDF ISBN: 978-1-118-10480-4
ePub ISBN: 978-1-118-10479-8

10 9 8 7 6 5 4 3 2 1

Contents

Foreword xiii

Preface xv

List of Figures xxi

List of Tables xxxi

1. Introduction 1

1.1. General Characteristic of Nondestructive Testing (NDT) Methods, 1

1.2. Ultrasonic Wave Type Overview, 6

2. Introduction to Search Unit Design 13

2.1. Principles of Search Unit Design, 13

2.1.1. Basic Types of Ultrasonic Search Units, 13

2.1.2. Essential Facts about Ultrasonic Wave Propagation, 17

2.1.3. Basic Considerations for Delay Line and Wedge Design, 20

Delay Line for Straight Beam Probes (Figure 2.5), 20

Wedge for Angle Beam Probe, 23

2.1.4. Examples of Probe Design for Automated Inspection, 25

2.1.5. Wedge Design for Surface Wave Probe, 27

2.2. Considerations for Transducer Selection, 32
2.2.1. Basics of Transducer Design, 32
Matching Layer, 33
Backing, 34
Tuning Components, 35
2.2.2. Acoustic Properties of Crystal Materials, 35
2.2.3. Velocity Measurement in Metals, 38
Bulk Velocity Measurement in Thick Metal, 38
Bulk Velocity Measurement Using a Thin Metal Strip, 39
2.2.4. Velocity and Attenuation Measurement in Wedge Materials, 42
Velocity Measurement in Wedge Materials, 42
Attenuation Measurement in Wedge Materials, 45
2.2.5. Crystal Size Selection, 52
2.3. Calculation of Straight Beam Transducer Directional Characteristic, 57
2.3.1. Acoustic Field of a Straight Beam Transducer, 57
2.3.2. Angle of Divergence Calculation, 60
2.3.3. Main Lobe Profile Calculation of a Round Crystal in Far Field, 62
2.3.4. Coefficient *K* Calculation at Any Decibel Level, 63

3. Single Angle Beam Probe Design 65
3.1. Basics of Probe Design, 65
3.2. Considerations Related to the Practical Concept of Wedge Design, 67
3.3. Measurement of Refracted Angles, 69
3.4. Deviation of Refracted Angle Related to Thick Wall Test Object Inspection, 73

4. Dual Straight and Angle Beam Probe Design 77
4.1. Principles of Dual Straight Beam Probe Design, 77

4.2. Sequence of Wedge Calculation, 78
4.3. Sensitivity Curves, 81
4.4. Example of Dual Straight Beam Probe Design, 82
4.5. Basics of Dual Angle Beam Probe Design, 86
4.6. Wedge Conceptual Design, 87
4.7. Wedge Design for Inspection of a Test Object with Flat and Parallel Surfaces, 88
4.7.1. The Wedge Calculation for the Inspection of Test Objects with Flat and Parallel Surfaces, 91
4.8. Wedge Design for the Inspection of a Test Object with a Curved Surface, 92
4.8.1. Wedge Calculation for the Inspection of a Test Object with Concentric Surfaces, 92
The Case of Axial Direction of Beam Propagation, 92
The Case of Circumferential Direction of Beam Propagation, 93

5. Multiple Crystal Probe Design 99
5.1. Concept of "Packaging," 99
5.1.1. Triplex Probes, 100
5.1.2. Dual Duplex Angle Beam Probes, 101
5.1.3. Five Crystal Assemblies Probe, 102
5.2. Example of Triplex Probe Design, 103
5.2.1. Requirements for Triplex Probe Design, 103
5.2.2. Wedge Design for 60°S Refracted Angle, 104
5.2.3. Wedge Design for 45°S Refracted Angle, 106
5.2.4. Dual Straight Beam Probe Design as Portion of Triplex Probe, 107

6. Technique Development and Probe Design for TOFD Method Application 111
6.1. Introduction to Techniques Based on Diffraction Phenomena, 111

6.2. TOFD Forward Scattering Technique, 113
6.2.1. Flat Surface Test Object Inspection, 115
6.2.2. Curved Surface Test Object Inspection (Figure 6.5), 117
6.3. Examples of Probe Calculation for Curved Surface Test Object Inspection, 118
6.3.1. Axial Crack Detection and Sizing, 118
6.3.2. Circumferential Crack Detection and Sizing (Figure 6.7), 120
6.3.3. Probe Design, 121
6.3.4. Comments, 122
6.4. Probe Design for TOFD Back Scattering Technique, 123
6.4.1. Basics of TOFD Back Scattering Technique, 123
6.4.2. Examples of Tandem Probe Design, 127
6.4.3. Gliding Diffracted Waves Technique, 133

7. Technique Development and Probe Design for Cylindrical Rod Inspection 135
7.1. Boundary Effect, 135
7.2. Symmetric and Asymmetric Cylindrical Rod-Guided Waves, 136
7.3. Technique Development and Probe Design for Inspection of Stepped Shaft, 140
7.4. Technique Development and Probe Design for Stud Inspection, 144
7.4.1. Stud Inspection from the Top Surface, 144
7.4.2. Stud Inspection from a Center-Drilled Bore, 148
7.5. Notch Dimension Calculation for Stud Calibration Standards, 157

8. Technique Development and Probe Design for Hollow Cylinder Inspection 163
8.1. Lamb Wave Generation, 163
8.1.1. Phase and Group Velocities, 167
8.1.2. Lamb Wave Propagation Parameters, 170
Selection of the Best Modes and Frequencies, 173

Lamb Wave Attenuation, 174
Reflected Signal Shape, 175
8.2. Technique Development and Probe Design for the Inspection of Hollow Cylinders from the Inside Surface, 176
8.2.1. Test Object Description and Inspection Consideration, 176
8.2.2. Lamb-Type Guided Wave Mode Selection for Practical Application, 182
8.3. Technique Development and Probe Design for the Inspection of Hollow Cylinders from the Outside Surface, 184
8.3.1. Technique Development and Probe Design for Inspection of Cylinders with Welded Adapters, 184
Test Object Description and Inspection Consideration, 184
Selection of the Best Modes and Frequencies, 186
Group Velocity Measurement, 189
8.3.2. Technique Development and Probe Design for Heater Sleeve Inspection, 192
Test Object Description and Inspection Consideration, 192
Lamb-Type Guided Wave Mode Selection, 195
Experiments to Measure Wave Propagation Parameters, 196
8.3.3. Technique Development and Probe Design for a Thick Wall Hollow Cylinder Inspection, 204
Test Object Description, 204
Mode Selection for Transducers with Standard Frequencies, 208
Energy Distribution along the Hollow Cylinder, 213
Influence of Water Gap Thickness on Wave Propagation for S_0 Mode, 215
Rayleigh Wave Velocity Measurement, 216

9. Technique Development and Focused Probe Design for Immersion Method Inspection 219
9.1. Basics of Focused Immersion Probe Design, 219
9.1.1. General Observation, 219
9.1.2. Consideration Relative to Straight Beam Immersion Focused Probe Design, 221
Spherical Aberrations Phenomenon, 221
9.1.3. Acoustic Parameters of Focused Probe, 223
9.2. Geometric and Acoustic Parameter Calculation, 224
9.3. Straight Beam Spherical Focused Probe Design, 226
9.3.1. Assessment of Design Feasibility, 226
9.3.2. Consequence of Calculation, 228
9.3.3. Example of Focused Immersion Probe Calculation with a Single-Surface Lens, 231

10. Technique Development and Probe Design for Reactor Pressure Vessel Nozzle Inner Radius Inspection 237
10.1. Inspection Zone Configuration, 237
10.2. Inspection from the Outside Nozzle Surfaces: Contact Method, 238
10.3. Example of Wedge Design for Inner Radius Inspection from the Outer Surface, 240
10.4. Inspection from the Inside Nozzle Surface: Immersion Method, 243

11. Search Unit Functioning Test 247
11.1. Evaluation of Certain Characteristics of a Search Unit, 247
11.1.1. Definition and Examples of Bandwidth, 248
11.2. Measurement of Specific Parameters of Selected Search Units, 250
11.2.1. IIW Reference Blocks, 251
11.2.2. Additional Test Blocks, 253

Appendix A System of Units and Symbols That Are Accepted for This Book 257

Appendix B American Societies Engaged in Activities Related to Nondestructive Testing and Serving the Needs of NDT Professionals 261

Appendix C An Example of Applying the Third Critical Angle 265

Appendix D WesDyne International Computer Program for Lamb Wave Dispersion Curve Calculation 267

Glossary of Terms Specific to This Book 273

Bibliography 279

About the Author 283

Index 285

Foreword

It is a great privilege to prepare the Foreword for Dr. Mark Brook's book on ultrasonic probe designs. Before we get into the technical aspects of this work, it is worthwhile to discuss some background on how he came to work in our laboratory. Dr. Brook was a professor at the Leningrad Transportation Institute and specialized in the design and implementation of ultrasonic testing methods for propulsion system and hulls of transport ships. He emigrated from the Soviet Union after obtaining an exit visa under the Helsinki Accord in 1979 and moved to Boston, Massachusetts, with the support of the Jewish Family Services organization. While at an American Society for Non-Destructive Testing meeting, an anonymous person (to whom we are forever grateful) suggested that he apply for a position in the fledgling NDE Development Laboratory at Combustion Engineering. The interview was a fascinating experience in which we conversed primarily in the universal language of mathematics. It was obvious at the conclusion of this discussion that Dr. Brook had more knowledge of ultrasonic testing theory than the collective assembly of the other engineers. He settled in quickly in his new environs, but there were a few humorous moments, such as when he came to my office and asked for a permission slip to drive across state lines so he could visit his wife, who was still in Boston.

Over the span of three decades, Dr. Brook's contribution to the application of ultrasonic testing has been immeasurable. His transducer designs were instrumental in many diverse and difficult inspection issues involving such diverse applications as nuclear power plant

components and aerospace components (including the design of the inspection system for solid rocket motors for the space shuttle program after the *Challenger* disaster). In every case, he started first with principles and theory to design a precise transducer concept customized for the job at hand. He consistently brought theoretical concepts to a practical conclusion with a variety of novel transducer designs. His work included breakthrough designs for creeping wave, refracted longitudinal, and, most notably, Lamb wave transducers. The majority of all the transducer designs that we successfully deployed in the field were based directly or indirectly on his teachings, from which we benefited greatly. It has truly been an honor to work with and learn from Dr. Brook over all these years. This educational work is an excellent blueprint for future endeavors in ultrasonic testing applications.

J. P. Lareau
Chief Engineer, NDE Technology
Westinghouse Electric Company

Preface

My many years in ultrasonic nondestructive testing (NDT) as an engineer and a teacher have given me the opportunity to understand what NDT practitioners, technicians, and engineers need to know for everyday activity in an ultrasonic inspection technology development, search unit design, and application.

Ultrasonic nondestructive testing is a relatively new branch of science and industry. The development of ultrasonic testing began in the late 1920s [1]. Initially, the fundamentals of this method were borrowed from basic physics, geometric and wave optics [2], and acoustics and seismology [3]. It later became evident that some of these theories and calculations could not always explain the phenomena observed in many instances during an ultrasonic test. Without understanding the nuances of "ultrasonic" wave propagation in the test object, it is impossible to design an effective inspection technique and search units to accomplish the task. "The devil is in the details."

The development of calculation methods, specifically for ultrasonic testing, began in the 1950s. At first, the development of the ultrasonic field for angle beam probes was addressed to satisfy the practical application of ultrasonics to weld joint inspection [4]. Many methods of calculation were developed and specific calculations were performed and compared with experimental results. Most of these methods were complicated and not suitable for routine inspection procedure development and search unit design. But the results achieved enable an understanding of the acoustic field structure in the test object and of ray

tracing methods. This knowledge now permits the use of much less complicated equations for everyday calculations, followed by, if necessary, correction of test results using experimental data. As we all know, the experiment is the criterion of truth.

By writing this book I have tried to combine basic physics of wave propagation, elementary mathematics, and advanced practical application. Almost every case of a specific technique development and probe design is confirmed with experimental data and examples of the appropriate calculations.

Chapter 1 begins with an NDT methods overview. Short descriptions of NDT methods include physical phenomenon that forms the basis of each method, along with the basic facts about the advantages and limitations. It is apparent from this overview that the ultrasonic method is much more versatile than other methods.

This chapter includes ultrasonic wave type overview of the major parameters of waves most commonly used in the inspection of test objects. The parameters include direction of wave propagation and particle oscillation, as well as their propagation velocity.

Chapter 2 discusses the principles of search unit design and focuses on probes for automated inspection. Description of acoustic properties of crystal materials and, especially, wedge materials, are followed by modern methods of velocity and attenuation measurements and calculation. Practical considerations are given for crystal size selection relative to frequency and test object wall thickness. The chapter includes calculations of a transducer's directional characteristics and main lobe profile. Special attention is given to the near field acoustic structure and major discrepancies between theory and reality. This is illustrated by the field structure of a straight beam transducer obtained by C-scan.

Chapter 3 is dedicated to a single angle beam probe design. It is shown that the main lobe profile calculated by using Snell's law differs from empirically obtained results. Practical concepts of wedge design are based on an imaginary crystal size and its location on a wedge. The phenomenon of the probe's exit point and lobe's central ray deviation leads to the necessity of a wedge angle correction.

Dual straight and angle beam probe design is discussed in Chapter 4. Sequence of wedge calculations for a dual longitudinal wave angle beam probe is presented along with examples of probe design. Two

concepts of wedge calculation and design for dual angle beam probes are presented. Special attention is given to probe design for the inspection of test objects with concentric surfaces including wedge calculations for phased array probes. Description of sensitivity curve construction concludes this section of the chapter.

In Chapter 5 the concept of "packaging" for multi-crystal probe design is discussed. Many variations of probe design are presented. Detailed calculations of the triplex probe are followed by the example of the design.

Technique development and probe design for time of flight diffraction (TOFD) techniques application is the topic of Chapter 6. Forward and back scattering techniques are discussed for inspection of test objects with flat and curved surfaces. Examples of probe calculation and design for both cases are presented in detail. Special attention is given to Tandem probes with examples of signals obtained from different reflectors. A short description of gliding diffracted waves and probe design for their generation is included.

Chapter 7 is dedicated to technique development and probe design for the inspection of cylindrical rods of several types. A description of boundary effects serves as a guideline for generation of symmetrical and asymmetrical rod-guided waves. Technique development and probe design for stud inspection from the stud end surface reveals problems associated with beam propagation. Stud inspection from the center-drilled bore is discussed. Probe design in this case is more complicated, but the results prove to be superior. Particular emphasis has been placed on the convex mirror calculation of probes designed for detection of small reflectors on the outside surface of studs and relatively thick wall cylinders. The end of this chapter includes examples of how to calculate the dimensions and types of reflectors to be machined in stud calibration standards.

Chapter 8 is dedicated to technique development and probe design for the inspection of hollow cylinders by Lamb-type guided waves. The chapter begins with a description of the necessary conditions to create Lamb waves. The concept of phase and group velocities is presented in accordance with physical optics. A list of Lamb wave propagation parameters is illustrated by analysis of dispersion curves. The key features of Lamb wave propagation are very helpful in understanding wave propagation in thin wall hollow circular cylinders. Principles for

selecting the best modes and frequencies for detection of reflectors in water-loaded test objects are correct for both thin plates and hollow cylinders. Several examples are given of how the general rules for Lamb-type guided wave propagation can be applied to technique development and probe design for inspection of different types of hollow cylinders. Experimental results are presented to demonstrate the energy distribution along a hollow cylinder.

Attention is given to experiments and explanation of how a water layer thickness in contact with a plate or hollow cylinder influences the wave propagation.

In Chapter 9, technique development and probe design for immersion methods of inspection is presented. Equations are given for geometric and acoustic parameter calculation. Practical assessment of design feasibility is followed by the example of immersion focused probe calculation with a single-surface lens.

Chapter 10 presents technique development and probe design for reactor pressure vessel nozzle inner radius inspection. The nozzle inner radius region is a unique test configuration. It can be inspected from the outside surface of the nozzle or from its inside surface. Both techniques, contact and immersion, are discussed. Principles of technique development and probe design are discussed, and practical probe design for each of the methods is presented.

Chapter 11 explains how to evaluate probes. The acquired parameters will help the probe designer to assess the correctness of the design. It will also be useful for the technician to avoid using inappropriate probes. Two main parameters measured during the probe evaluation, that is, time response and frequency response, allows the possibility to calculate all other necessary parameters. The choice and design of the appropriate reference blocks is discussed.

The book also includes four appendixes.

ACKNOWLEDGMENTS

My first intention was to substitute the traditional personal acknowledgments with humor, as published in *The Journal of Irreproducible Results*. For example, in the first issue published in 1960, from an article named “How to Read Technical Publications,” the following quote, still applies:

If it is written:	It means:
I thank Mr. A and Mr. B for help in conducting experiments and making measurements.	Mr. A made all the experiments and Mr. B processed the data.
I thank Mr. C for useful discussions.	I have shown to Mr. C the results obtained by Mr. A and Mr. B, and he explained to me what it means.
I thank Mr. D for the opportunity to carry out this project.	Mr. D gave me time and money to do what I really like to do.

Humor aside, I would like to express my sincere gratitude to all my colleagues for their valuable professional and human support. My special appreciation is for what I call the "Old Guard"—people with whom I have been working in the NDT Products & Technology department of Westinghouse Electric Company Nuclear Services for more than 30 years: From Jack Lareau I have received the project ideas; Vincent LaDuca and Marc Camerline managed to schedule them and make them pay off; Russell Devlin shared his enormous experience in technique application and troubleshooting; Mike Concordia, Brian Smith, and Glen Gagner were a great help with instrumentation, and Mark Kirby has his wonderful intuition for solving a variety of computer problems. George Rowland made the prototype of each idea work, thanks to his intelligent approach to mechanical challenges. I have learned a lot from all of them, and wish to pass it all on to the next generation of NDT specialists.

And finally, thanks are to my wife, Nora, and grandson, Thomas—my first editors and supporters of my endeavor.

Mark V. Brook

West Hartford, Connecticut
October 2011

List of Figures

Figure 1.1	Basic types of discontinuities	2
Figure 1.2	Vertically polarized shear waves	7
Figure 1.3	Horizontally polarized shear waves	8
Figure 1.4	Schematic representation of symmetric and asymmetric modes	9
Figure 1.5	Structure of the waves propagating in a test object at the first critical angle according to Snell's law	11
Figure 1.6	Real structure of waves propagating at the first critical angle in a test object with flat front surface	11
Figure 2.1	A typical angle beam probe: a transducer attached to a wedge	15
Figure 2.2	Conceptual design of triplex probe wedges	16
Figure 2.3	Wave reflection and refraction at the wedge–steel interface	19
Figure 2.4	Wave propagation at the critical angles	20
Figure 2.5	Diagram related to a delay line calculation	21
Figure 2.6	A delay line height, according to the concept of the imaginary crystal	22
Figure 2.7	Diagram of an entire quadrant coverage	23
Figure 2.8	Internal reflections in a wedge for single angle beam probe	24
Figure 2.9	Examples of probe and wedge for automated inspection	26
Figure 2.10	Combined wedges for 45°S and 60°S refracted angles	26

Figure 2.11 Surface wave probe conceptual design 28
Figure 2.12 Experimental graph: normalized distance of a reflector versus normalized signal amplitude 31
Figure 2.13 Structure of a straight beam transducer and a crystal assembly 33
Figure 2.14 Diagram related to calculation of a bandwidth 34
Figure 2.15 An angle beam probe with all possible matching layers 38
Figure 2.16 The signal pattern including 11 reflections 40
Figure 2.17 Setup for velocities measurement in a thin strip 40
Figure 2.18 The screen capture related to a bulk velocity measurement in a thin metal strip 41
Figure 2.19 Setup for a wedge material velocity measurement by a contact method 43
Figure 2.20 Setup for a wedge material velocity measurement by an immersion method 44
Figure 2.21 The step sample dimensions 49
Figure 2.22 The nominal transducer frequency versus the coefficient of attenuation (Plexiglas step sample) 50
Figure 2.23 The nominal transducer frequency versus the coefficient of attenuation (Polystyrene step sample) 51
Figure 2.24 Transducer frequency versus parameter $d \times f$ for a steel test object 53
Figure 2.25 Signals from 3.0 mm deep notch in a 6.35 mm thick plate 55
Figure 2.26 Possible interpretation of the signals shown in Figure 2.25A, B 56
Figure 2.27 Signals from a 3.0-mm deep notch in a 6.35-mm thick plate 56
Figure 2.28 Example of a ray tracing in case when the crystal size is not exceeding the wall thickness 57
Figure 2.29 Acoustic intensity on the center axis of circular oscillator and a sound field shape of the circular oscillator 57

Figure 2.30 The field structure of the 19 mm diameter 225 MHz transducer 59
Figure 2.31 Graphical representation of the signal amplitudes in the section *N*/2 59
Figure 2.32 The beam spread plots at –6 dB level (I) and the main lobe shapes (II) 61
Figure 2.33 Example of coefficient *K* calculation 64
Figure 3.1 A main lobe's idealistic shape of shear wave in the plane of incidence 66
Figure 3.2 An imaginary crystal position in a wedge 67
Figure 3.3 Coefficient of transmission for the Plexiglas–steel boundary (for illustration only) 69
Figure 3.4 Overall trend of an experimental refracted angle deviation from the calculated angle by Snell's law (line 1) 70
Figure 3.5 The exit point deviation Δ of an angle beam probe 70
Figure 3.6 Deviation of the exit points 71
Figure 3.7 Measured versus nominal refracted angle for the transducer diameter 9.5 mm 72
Figure 3.8 Example of the graph using angle of incidence correction 73
Figure 3.9 Refracted angles of rays as a function of the reflector depth 75
Figure 3.10 Possible position of reflectors in the main lobe 76
Figure 3.11 Refracted angles and quasi-bent central ray 1′, 2′, 3′ 76
Figure 4.1 Conceptual design of a dual straight beam probe 78
Figure 4.2 A dual straight beam probe wedge 79
Figure 4.3 An example of conceptual design of a dual straight beam probe for a test object with a concave surface 81
Figure 4.4 Sensitivity curve for the "focal" distance 10 mm 82
Figure 4.5 Example of a dual straight beam probe design 85

Figure 4.6 Central ray intersection distance vs. signal amplitude (sensitivity curves) 85
Figure 4.7 Wedge arrangement of a dual angle beam probe 86
Figure 4.8 Two conceptual designs of a dual angle beam probe 87
Figure 4.9 Diagram related to the calculation of a dual angle beam probe 89
Figure 4.10 Foot print of a phased array transducer 89
Figure 4.11 Geometrical parameters of the wedge with a flat footprint 90
Figure 4.12 Sketches related to wedge design for test objects with concentric surfaces 93
Figure 4.13 Diagrams related to wedge calculation for test objects with concentric surfaces 94
Figure 4.14 Diagram for calculation of a dual angle beam probe oriented in the circumferential direction of a pipe 95
Figure 4.15 Definition of Δ_1 97
Figure 5.1 A triplex probe conceptual design to generate beams with the refracted angles 100
Figure 5.2 Conceptual design of a triplex probe to generate beams with refracted angles 101
Figure 5.3 Conceptual design of a triplex probe: a and b are single probes oriented in the opposite directions, T and R are crystal assemblies for the dual 0°L portion of the probe 101
Figure 5.4 Conceptual design of a dual duplex probe: two dual angle beam probes oriented in the opposite directions 102
Figure 5.5 Conceptual design of a five crystal assembly probe: four single angle beam probes and one single straight beam probe 102
Figure 5.6 Conceptual design of a triplex probe 103
Figure 5.7 Ray tracing in the 60°S refracted angle wedge and final dimensions of the wedge 104

Figure 5.8 Ray tracing in the 45°S refracted angle wedge and final dimensions of the wedge 105
Figure 5.9 The dual straight beam portion of the probe calculation 110
Figure 6.1 Interaction of an ultrasonic beam with a crack-like flaw 112
Figure 6.2 TOFD technique definitions 113
Figure 6.3 The wave modes generated by an oblique incident beam in a test object with the flat and parallel surfaces 114
Figure 6.4 Diagram of probe calculation for TOFD forward scattering technique for inspection of a test object with a flat front surface 115
Figure 6.5 Diagram for calculation of minimum crack depth, which can be sized 117
Figure 6.6 Diagram for calculation probe parameters for detection and sizing of an axial oriented crack (inspection from inside a cylinder) 118
Figure 6.7 Sketch related to calculation of probe parameters, for circumferential crack detection and sizing 121
Figure 6.8 Conceptual design of the probe 122
Figure 6.9 Comparison of the results obtained during the inspection of the same test object by using longitudinal waves and shear waves 123
Figure 6.10 A tandem probe conceptual design 124
Figure 6.11 An acoustic field in a steel test object when an angle of incidence α is equal or close to the first critical angle 125
Figure 6.12 Interaction of waves with a crack of height h 125
Figure 6.13 Typical signals produced by a tandem probe in the vicinity of a crack, initiated from a test object opposite surface 126
Figure 6.14 Waves in the vicinity of a crack, initiated from a scanning surface 127

Figure 6.15 Typical signals produced by a tandem probe in the vicinity of a crack, initiated from scanning surface 127
Figure 6.16 Sketch related to calculation of optimum wedges for a tandem probe 128
Figure 6.17 Position of a tandem probe to measure refracted angles 129
Figure 6.18 Dependence of refracted rays from depth of reflectors 130
Figure 6.19 The waves which may be involved in detection and sizing cracks initiated from the scanning surface 131
Figure 6.20 Tip diffraction signals produced by L-L_1 and S-S waves 131
Figure 6.21 Tip diffraction signals parameters versus SDH depth 132
Figure 6.22 Generation of gliding waves and conceptual design of gliding wave prob 134
Figure 7.1 Main lobe of a straight beam transducer in a semi-infinite medium 136
Figure 7.2 Illustration of wave guide effect in a cylindrical rod and near a test object wall 137
Figure 7.3 Beam propagation in a cylindrical rod 137
Figure 7.4 Screen pattern of the symmetrical rod wave, screen capture of signals generated by the symmetrical and the asymmetrical rod waves 139
Figure 7.5 Simplified geometry of the stepped shaft and a geometry of a shaft top surface 141
Figure 7.6 Example of ray tracing in a cylindrical rod 142
Figure 7.7 Simplified sketch of the shaft to be inspected 143
Figure 7.8 Inspection zones of the stud and locations of the reflectors 144
Figure 7.9 Screen captures of signals 144
Figure 7.10 The zones of the stud to be inspected 146
Figure 7.11 The stud first inspection zone parameters 147

Figure 7.12 Duplex probe conceptual design 148
Figure 7.13 Severely corroded stud and corroded zone trap 149
Figure 7.14 Example of probe design for a stud inspection from the bore side 150
Figure 7.15 Position of the probe and signals from reflectors 151
Figure 7.16 Directions of ultrasonic beams reflected from mirrors 152
Figure 7.17 A mirror angle calculation for detection of a circumferential crack 152
Figure 7.18 Comparison of reflections from flat and curved mirrors 153
Figure 7.19 Relative positions of a convex mirror and a transducer in a stud bore 154
Figure 7.20 Profile of the mirror at a section of 45° 154
Figure 7.21 Ray tracing reflected from a curved mirror 155
Figure 7.22 Shape of the notches for studs calibration standards 158
Figure 7.23 Diagram related to "Lentil" notch area calculation 161
Figure 7.24 Real shape and calculated dimensions of the notches 162
Figure 8.1 An angle beam probe main lobe position in a semi-infinite medium 164
Figure 8.2 Illustration of beam propagation change when the wall thickness decreases 164
Figure 8.3 Formation of "Lamb waves" in a liquid layer 166
Figure 8.4 Relationship between bulk V, phase $\boldsymbol{V}_{\mathbf{ph}}$, and group $\boldsymbol{V}_{\mathbf{gr}}$ velocities 168
Figure 8.5 Creation of the wave groups 169
Figure 8.6 Phase and group dispersion curves 172
Figure 8.7 Dimensionless coefficient of attenuation 175
Figure 8.8 Typical shape of Lamb wave reflected signal 176
Figure 8.9 Normalized particle displacement 179

Figure 8.10 Phase velocity determination for selected *fd* parameters 181
Figure 8.11 Tube transition zone and the probe position during inspection 183
Figure 8.12 Example of a probe assembly for SGT inspection 183
Figure 8.13 The circular diagrams showing the results of the tube inspection 184
Figure 8.14 Hollow cylinders with the welded on adapters 185
Figure 8.15 Phase velocity dispersion curves for 1.0 MHz and 2.25 MHz transducers 188
Figure 8.16 Group velocity dispersion curves 188
Figure 8.17 Normalized particle displacement 189
Figure 8.18 An arc length measurement 190
Figure 8.19 The signal from two reflectors 50.8 mm apart 191
Figure 8.20 Reflected signals from a notch 192
Figure 8.21 Simplified configuration of the heater sleeve 193
Figure 8.22 Beam propagation in the step region 195
Figure 8.23 Phase velocity dispersion curves 196
Figure 8.24 Group velocity dispersion curves 197
Figure 8.25 Particle displacement graph for S_1 mode 198
Figure 8.26 Particle displacement graph for S_2 mode 198
Figure 8.27 Diagram related to the signal amplitude distribution measurements 199
Figure 8.28 The signals reflected from two notches 200
Figure 8.29 Relative position of the notches and the probe 201
Figure 8.30 Upper end of the test samples, representing location of two notches in heat-affected zone 202
Figure 8.31 Reflections from the notches that represent the location and size of the real cracks (S_2 mode) 203
Figure 8.32 Example of a wedge design for Lamb-type guided wave generation for the inspection of a cylinder 203
Figure 8.33 Simplified geometry of thick wall hollow cylinder 205

Figure 8.34 Normalized particle displacement: S_1 mode, wall thickness 6.35 mm 206
Figure 8.35 Phase velocity dispersion curves for wall thickness 6.35 mm frequency 0.50 and 10 MHz 207
Figure 8.36 Normalized particle displacement: S_1, S_2, and S_0 modes for 6.35 mm wall thickness 209
Figure 8.37 Group velocity dispersion curves for modes at 1.0 MHz 210
Figure 8.38 An experimental setup 210
Figure 8.39 Examples of signals generated in 6.35 mm thick strip 212
Figure 8.40 Position of the reflectors for a signal amplitude distribution measurement 213
Figure 8.41 Normalized circumferential signal amplitude distribution on the outside surface of the hollow cylinder 214
Figure 8.42 Signals reflected from the notches in the hollow cylinder 214
Figure 8.43 Phase velocity dispersion curves for two zero modes compared with Rayleigh wave velocity 217
Figure 8.44 Comparison between tuned and untuned signals 218
Figure 9.1 Focused immersion probe positions for straight beam inspection and angle beam inspection 220
Figure 9.2 Spherical aberration of a concave spherical mirror 221
Figure 9.3 Aberration explanation of a concave spherical mirror 222
Figure 9.4 Single surface lens aberration and restriction to ray propagation 222
Figure 9.5 Focused probe geometrical parameters 224
Figure 9.6 Focused straight beam immersion probe conceptual design 227
Figure 9.7 Near-field length versus crystal diameter for two frequencies 228
Figure 9.8 Beam diameter at near field versus crystal diameter 229

Figure 9.9	The coefficient K_g determination	230
Figure 9.10	Beam diameter versus spherical lens radius	230
Figure 9.11	Focused immersion probe parameters for straight beam inspection	232
Figure 9.12	Screen capture of the acoustic field of a focused transducer	235
Figure 10.1	The inner radius inspection zones	238
Figure 10.2	The coordinate system of a nozzle and a reactor pressure vessel	239
Figure 10.3	The inspection angles and a crack model	240
Figure 10.4	Sketches relevant to probe design for inner radius inspection	241
Figure 10.5	Example of a wedge calculation	242
Figure 10.6	Example of the wedge design	244
Figure 10.7	The wedge with the transducer	244
Figure 10.8	Conceptual design of an inner radius immersion technique inspection from the inside of the nozzle	245
Figure 10.9	Actual transducer delivery system	246
Figure 11.1	Time response and frequency response examples	249
Figure 11.2	Setups for evaluating search units using the IIW Reference Block	251
Figure 11.3	Deviation of the exit point of probes, measured on different reference blocks	253
Figure 11.4	Simple test block for evaluation of straight and angle beam probes	253
Figure 11.5	Test block for the evaluation of a single straight beam transducer with a matching layer for a Plexiglas wedge	254
Figure 11.6	Small tank for the evaluation of immersion transducers	254
Figure C1	Sketch releted to application of the third critical angle	266
Figure D1	Lamb wave dispersion curves	270

List of Tables

Table 1.1	Basic Characteristics of NDT Methods	3
Table 1.2	NDT Method Preferences	6
Table 2.1	Calculated Wedge Angles	30
Table 2.2	Characteristics of Selected Piezoelectric Materials	35
Table 2.3	Average Acoustic Characteristics of Selected Materials	36
Table 2.4	Formulas to Calculate Longitudinal or Shear Wave Velocities for Selected Modes	41
Table 2.5	Influence of Matching Layer Thickness, as Function of Frequency, on Velocity Measurements	42
Table 2.6	Experimental Data of a Signal Amplitude *A*% Measured on the Plexiglas Step Sample	49
Table 2.7	Calculated Coefficients of Relative Attenuation in dB/mm for the Plexiglas Step Sample	50
Table 2.8	Parameter $d \times f$ for selected crystal diameters	54
Table 2.9	Transducer Ø = 25.4 mm, f = 2.25 MHz, S-wave in Steel λ_S = 1.435 mm, $\pi d/\lambda_S$ = 55.579	63
Table 3.1	Experimental Angles of Incidence	74
Table 6.1	Parameters for Probe Design for Axial Crack Sizing	120
Table 6.2	Parameters for Probe Design for Circumferential Crack Sizing	121

Table 6.3	The Results of Experiments to Confirm Tandem Probe Design	129
Table 7.1	Beam Divergent Angle φ and Angle β of Mode Converted S-Wave	138
Table 7.2	Calculated and Measured TOF	143
Table 8.1	Phase Velocities and Wedge Angles for Selected Modes	180
Table 8.2	Wedge Angles for Selected Modes and Chosen Frequencies	184
Table 8.3	Calculated Phase and Group Velocities for S_2 and A_2 modes	189
Table 8.4	Phase and Group Velocities for Selected Modes	197
Table 8.5	Signal Amplitudes in Probe Positions 0, 90, and 180 Degrees	201
Table 8.6	Calculation Results for Two Modes: S_1 and S_2	206
Table 8.7	Modes Which Can Be Generated at 0.5 MHz and 1.0 MHz Frequencies	207
Table 8.8	Group Velocities for Modes at 0.5 MHz and 1.0 MHz Frequencies	210
Table 8.9	Calculated and Generated Modes and Their Parameters	211
Table 8.10	Signal Amplitude, % for S_0 Mode	213
Table 11.1	Damping and Bandwidth Parameters	250

CHAPTER 1

Introduction

1.1. GENERAL CHARACTERISTIC OF NONDESTRUCTIVE TESTING (NDT) METHODS

Nondestructive testing (NDT) is a process of detection, measurement, and evaluation of discontinuities in raw materials or finished parts, without any damage to these.

NDT methods may be classified under the physical principles that form the basis for each method. NDT methods are named according to these physical principles.

The most common methods are

- Penetrant testing (PT);
- Magnetic particle testing (MT);
- Eddy current testing (ET);
- Radiographic testing (RT);
- Ultrasonic testing (UT);
- Acoustic emission testing (AE);

Ultrasonic Inspection Technology Development and Search Unit Design: Examples of Practical Applications, First Edition. Mark V. Brook.

- Visual testing (VT); and
- Thermal infrared testing (TIR).

Discontinuities are classified based on their types and location and material processes in which they may exist. This important information regarding the detection of these anomalies begins with the question of detectability. There are a number of discontinuities that can occur at any stage of manufacturing and during service. The occurrence of discontinuities is governed by and is paraphrased in Murphy's law: "If any discontinuity can occur—it will."

There are approximately 80 names for the discontinuities that uniquely identify them [5, 6]. All these discontinuities can be reduced to five basic types, as shown in Figure 1.1.

Basic characteristics of NDT methods are presented in Table 1.1, which shows a brief summary of the NDT methods.

A synopsis of NDT method preferences based on the types of discontinuities in materials of test objects is shown in Table 1.2. And once again, this is only a brief look at each NDT method.

The information presented in Table 1.2 provides only a general idea of method preferences. Each inspection situation is unique and requires special consideration. It is apparent that the ultrasonic method is more versatile than the other methods, and in most cases, it can be used as a main or a complementary inspection method.

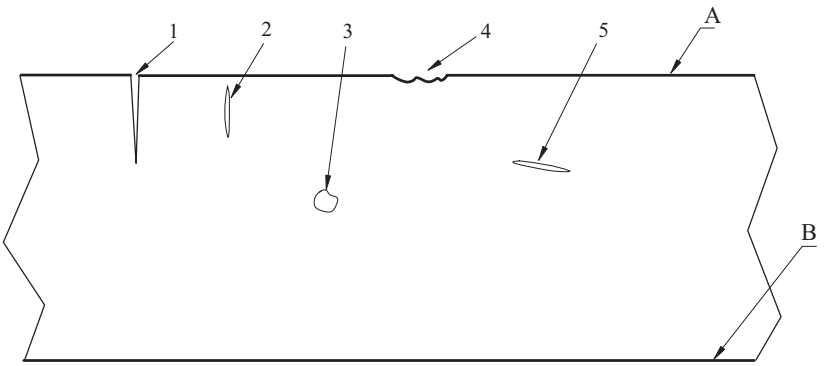

Figure 1.1 Basic types of discontinuities: (1) a planar surface rupture, (2) a subsurface planar rupture, (3) an internal volumetric cavity, (4) a geometric imperfection, (5) an internal planar rupture. (A) Test surface, (B) opposite surface.

Table 1.1
Basic Characteristics of NDT Methods

NDT method	Main characteristic of NDT method
Penetrant testing (PT)	Based on capillary action—a surface tension phenomenon. The method used for the detection of surface discontinuities in nonporous, solid, ferromagnetic, or nonferromagnetic materials. Two types of penetrant are available: visible dye penetrant and fluorescent penetrant.
Advantages	The method is sensitive and inexpensive.
Limitations	Only discontinuities open to the test surface can be detected. Sensitive to temperature variation, surface conditions, and part preparation.
Magnetic particle testing (MT)	Based on the detection of magnetic leakage field, caused by planar discontinuities open to the surface and slightly subsurface. To visualize the leakage field, ferromagnetic particles are applied to the inspection surface of a magnetized test sample. These are attracted to the leakage field, and in doing so render the discontinuity as a visible indication. Ferromagnetic particles follow the contour of the discontinuity.
Advantages	Interpretation of test results is relatively easy; thin, nonferrous metallic or nonmetallic coatings only slightly deteriorate the test results.
Limitations	Only ferromagnetic test objects can be inspected, and only discontinuities open to the surface, or slightly subsurface, can be detected. Demagnetization of the test object is usually required. Sharp changes in the configuration of the test object can make the interpretation of test results difficult.
Eddy current testing (ET)	Based on inductive properties of alternating current. Eddy currents are the circulating electrical fields induced in a conductive test object by an alternating magnetic field. During an eddy current test, a primary circuit (test coil) induces the eddy current into a secondary circuit (test object). Any factor that affects this current flow (e.g., crack open to the scanning surface) will affect the current parameters in the test coil, which can be measured and hence detect a crack.

(*Continued*)

Table 1.1
(Continued)

NDT method	Main characteristic of NDT method
Advantages	Equipment is portable, no powders or other materials needed to be applied to the surface of a test object. Surface preparation is generally not necessary and cleaning is not usually required. For example, the inner surface of the tubing can be inspected with this method.
Limitations	Test object material must be electrically conductive. Ferromagnetic materials present difficulties for inspection. Detectability of subsurface discontinuities is possible but limited.
Radiographic testing (RT)	Based on the sensitivity of X-rays or nuclear radiation to variations in thickness and density of a given test material. This method permits the detection and evaluation of discontinuities in materials. The penetrating radiation produces an image on a film or detector that converts the radiation into a visible image.
Advantages	Provides an accurate and permanent record of test results. Used to detect mostly volumetric discontinuities. Discontinuity characterization is relatively easy to perform.
Limitations	Defect orientation. Radiation safety hazards. With gamma radiography, the discrete energy of the gamma radiation source limits its application.
Ultrasonic testing (UT)	Based on elastic wave propagation in solid materials and subsequent reflection from discontinuities. Ultrasonic energy is generated in most cases by a piezoelectric element. Energy reflected from a discontinuity is received by the same or other elements. Data displayed on an instrument screen in the form of A-, B-, and C-scans. This kind of data presentation provides for accurate sizing and evaluation of detected discontinuities.
Advantages	An inspection can be performed from an accessible surface to detect and size almost all types of discontinuities, volumetric or planar on the same and oppsite surface of a test object. A variety of techniques can be used based on frequencies, part configuration, and modes of propagation.
Limitations	Orientation of planar discontinuities and material grain structure can affect detectability. A complex-shaped scanning surface can reduce the effectiveness of an inspection.

(*Continued*)

Table 1.1
(Continued)

NDT method	Main characteristic of NDT method
Visual testing (VT)	Based on the use of electromagnetic radiation at visible frequencies. Two methods are available: Direct method—using visual aids such as mirrors, telescopes, and cameras. Remote method—using borescopes, fiberscopes, and video technology.
Advantages	Raw materials and finished product can be inspected.
Limitations	Only surface conditions, for example, geometric imperfections, can be detected and evaluated. Access to inspection zone can be restricted.
Acoustic emission testing (AE)	A passive method of nondestructive testing to detect and locate discontinuities in mechanically loaded structures. It is based on the detection of acoustically generated waves from rapidly growing cracks.
Advantages	Sensitive to developing discontinuities. The total structure can be monitored.
Limitations	Noise sensitive. Baseline noise should be measured before testing.
Thermal infrared testing (TIR)	Based on variations in heat propagation and attenuation in a solid material. After a test object is heated, a discontinuity within the material structure presents an obstacle for heat flow, and this leads to a nonuniform thermal spread on the test object surface that can be visualized. Used in the aerospace industry for composite material inspection and in the production of electrical systems to asses their integrity. Anomalies are detected by thermal and infrared sensors.
Advantages	Noncontact, fast method that can create a thermal image. By "real-time" viewing of the image, evaluation can be accomplished almost immediately.
Limitations	Limited application. Generally, only the accessible surface of the test object can be thermally inspected.

Table 1.2
NDT Method Preferences

Type of discontinuities	Type of material	NDT method preferences	
		First order	Second order
Planar surface rupture on test surface	Nonmetallic, nonporous	Penetrant	Ultrasonic
	Ferromagnetic	Magnetic particle	Penetrant, ultrasonic
	Conductive	Eddy current	Penetrant, ultrasonic
Planar surface rupture on opposite surface	Any solid material	Ultrasonic	
Subsurface planar rupture near test surface	Nonmetallic, nonporous	Ultrasonic	
	Ferromagnetic	Ultrasonic	Magnetic particle
	Conductive	Ultrasonic	Eddy current
Subsurface planar rupture near opposite surface	Any solid material	Ultrasonic	
Internal volumetric discontinuity	Any solid material	Radiographic	Ultrasonic
Internal planar rupture	Any solid material	Ultrasonic	Radiographic
Geometric imperfection on test surface	Any material	Visual	
Geometric imperfection on opposite surface	Any solid material	Ultrasonic	Radiographic, if the opposite surface is accessible

1.2. ULTRASONIC WAVE TYPE OVERVIEW

Different types of waves or modes are used in ultrasonic testing. They differ by the direction of propagation and the particle motion as well as by the velocity of propagation ([7, 8]).

Solids, liquids, and gaseous media are characterized by their elasticity of volume, that is, their ability to retain the volume, but the solid,

in addition, has an elasticity of shape, that is, its ability to retain the shape. The shear elasticity of solid materials is a result of this feature. Any attempt of a volume expansion or compression, as well as a shifting of adjacent layers using variable force, will result in an occurrence of an elastic oscillation. Thus, so-called tensile-compression oscillations can be created in all media except within a vacuum. Waves with this type of particle motion are *longitudinal* waves. (Particle motion is parallel to the direction of propagation.)

In addition, *shear* or transverse waves can exist in a solid material. Particle motion in shear waves is perpendicular to the direction of the beam propagation. In most cases, shear waves are propagated at an angle to a test object surface. However, when necessary, S-waves can be generated perpendicular to a test object surface, using a special transducer and couplant. Both longitudinal and shear waves are bulk waves.

There are two types of S-waves: vertically polarized shear waves (SVs) and horizontally polarized shear waves (SHs). In the vertically polarized shear waves, particles oscillate in a plane perpendicular to the test object surface (Figure 1.2). In the horizontally polarized shear waves, particles oscillate in a plane oriented at the refracted angle β to the test object surface (Figure 1.3).

Vertically polarized shear waves are commonly used in ultrasonic testing. Note that in both S-wave cases, the particles oscillate perpendicular to the direction of wave propagation, but in different planes.

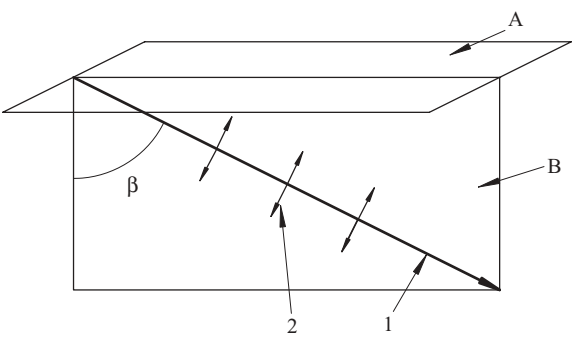

Figure 1.2 Vertically polarized shear waves: (A) a test object surface, (B) the plane vertical to the test object surface. (1) The direction of wave propagation, (2) the direction of particle oscillation.

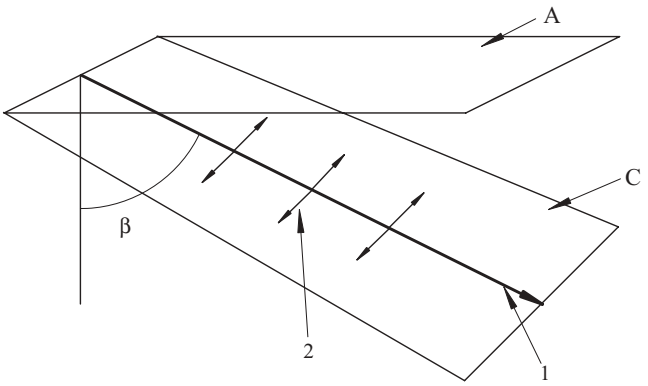

Figure 1.3 Horizontally polarized shear waves: (A) a test object surface, (C) the plane at refracted angle β to the test object surface. (1) The direction of wave propagation, (2) the direction of particle oscillation.

Longitudinal waves are generated by straight beam transducers. Vertically polarized shear waves are generated by a probe comprising a transducer and a wedge. Horizontally polarized shear waves, as a rule, are generated by an electromagnetic acoustic transducer (EMAT).

In addition to bulk waves, a number of other wave types are commonly used in ultrasonic testing: surface or Rayleigh waves, normal or Lamb waves, and several other types of guided waves.

A surface wave is a combination or superimposition of longitudinal and vertically polarized shear waves. A surface wave's maximum energy is concentrated on the surface of the test object where the waves are generated and rapidly decrease with depth. Therefore, surface-breaking discontinuities are detectable with these waves.

If a test object surface is free (e.g., not loaded with liquid), surface waves propagate over a relatively long distance, following the surface curvature, if any, and reflect from surface-breaking planar discontinuities and thus, the discontinuities are detectable. If a test object surface is loaded with a liquid (water or oil), this will result in additional attenuation, reducing the distance of wave propagation. A rough test object surface reduces the sensitivity for discontinuity detection.

In relatively thin plates, when the plate thickness is less than three or four wavelengths, the bulk waves cannot propagate. The thin plate acts as a wave guide. The bulk waves transform, under certain conditions, into normal or Lamb waves. This transformation is caused

by mode conversion and by multiple reflections from the plate boundaries.

The propagation velocity of Lamb waves depend on the frequency, as well as on the acoustic and mechanical properties, of the test object material. The phenomenon of velocity dependence on the frequency is called velocity dispersion.

Two types of probes can be used to generate Lamb waves: a special angle beam and "comb probes." To calculate parameters for these probes, one should use dispersion curves for phase velocities. These curves, along with dispersion curves for group velocities, are precalculated for a given material, such as aluminum, steel, and inconel. Two basic types of modes can be generated: symmetric and asymmetric.

Each dispersion curve on each graph represents one mode, which is traditionally marked by the letters A or S. The letter A is designated for asymmetric modes, and the letter S is designated for symmetric modes.

The symmetric Lamb modes (Figure 1.4S) are named so because the particle displacement is symmetric relative to the neutral axis of a plate, and along this axis, the particle is oscillating only in a longitudinal direction. The asymmetric Lamb modes are the flexural waves; that is, the particles along the neutral axis of a plate are oscillating strictly in a transverse direction (Figure 1.4A).

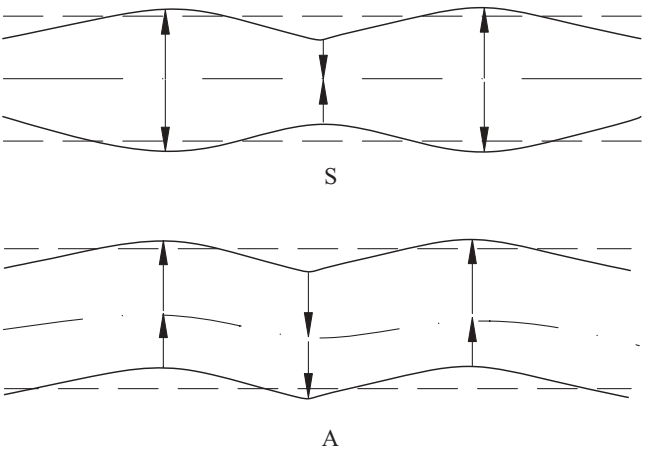

Figure 1.4 Schematic representation of symmetric (S) and asymmetric (A) modes.

Each of these modes can be generated in different orders, depending on the probe frequency and the thickness of the plate. These orders are marked by subscripts 0, 1, 2, and so on, for example, S_0 and A_1.

The group velocity is the velocity of energy propagation along a plate (see Chapter 8). It is used for the distance calculation between the probe and the location of the detected discontinuity. Plate waves are only one example of guided waves. There are other examples when shapes and dimensions of a test object can determine the type of the propagating waves. For example, a thin hollow cylinder or a relatively small diameter rod can serve as a guide for wave propagation.

As compared with a thin plate, in a thin wall hollow cylinder, additional modes are propagating, for example, torsion. To distinguish Lamb waves from waves propagating in hollow cylinders, the latter can be named "Lamb-type"-guided waves.

The waves propagating in a small diameter rod (rod waves) are similar to those in a thin wall hollow cylinder. A relatively long rod with a relatively large diameter can also serve as a guide for wave propagation due to the "boundary effect," but in this case, the waves are not dispersive.

There are other sets of waves that are very often used in ultrasonic testing. These waves are produced at or near the first critical angle. According to Snell's law, at the first critical angle α_{1CR}, the longitudinal wave L should propagate along the front surface of a test object, and only shear wave S should propagate inside the test object at a calculated refracted angle β (Figure 1.5).

In reality, the composition of waves propagating in a test object at the angle of incidence equal to or near the first critical angle is different. We will describe these waves using the conventional terminology accepted at the time of discovery.

Along the near surface propagates *creeping* wave Cr, which has a velocity close to the longitudinal wave (Figure 1.6). The distance of propagation is short, approximately 30 or 40 mm in a steel test object. This wave is not sensitive to the roughness of the test object surface and is therefore used for the detection of surface and subsurface discontinuities. At each point of the creeping wave propagation, an S-wave S_{IND} is emitted. It is termed as *indirect shear wave*, which propagates at an angle β_{IND} equal to approximately 33° in steel.

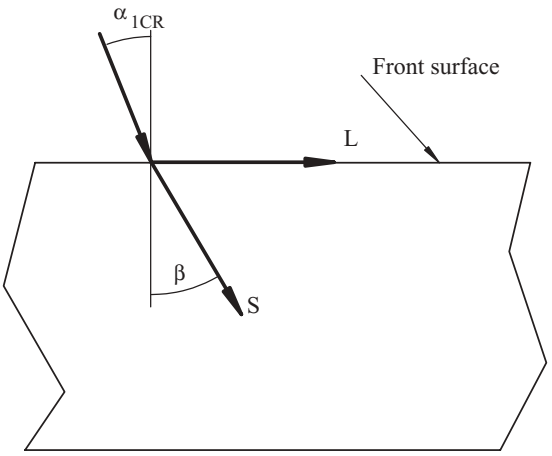

Figure 1.5 Structure of the waves propagating in a test object at the first critical angle according to Snell's law.

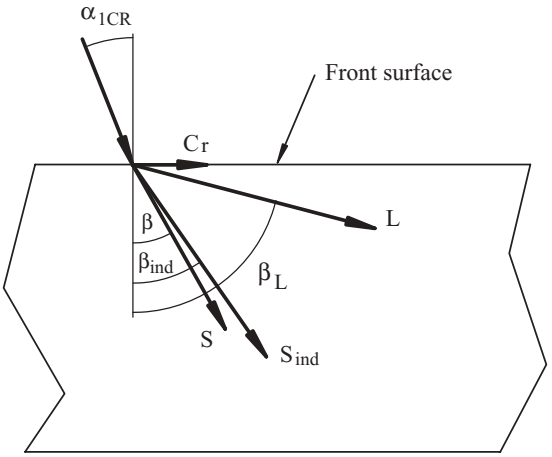

Figure 1.6 Real structure of waves propagating at the first critical angle in a test object with flat front surface.

If the opposite surface of the test object is parallel to the front surface, this wave generates creeping wave on that surface also, but as a mirror image.

The longitudinal wave L propagates at a refracted angle β_L. This angle is equal to approximately 75° for steel, and therefore, this wave

is termed a *high angle L-wave* or *head wave*. This wave is more efficiently used for the detection of deeper-than-subsurface discontinuities and, what is more important, for the generation of tip diffraction waves if the targets are planar, crack-like flaws.

And finally, the shear wave S propagates at angle β, calculated in accordance with Snell's law. This is *a direct shear wave*.

All these terminologies became familiar to the NDT community; however, during the years that followed, research has shown that not all of these waves exist as individual waves.

There are other "exotic" wave types that are sometimes used in ultrasonic testing, for example, *Stoneley waves* and *Love waves*. These waves are not discussed in this book. For more information, see References 9 and 10.

CHAPTER 2

Introduction to Search Unit Design

2.1. PRINCIPLES OF SEARCH UNIT DESIGN

2.1.1. Basic Types of Ultrasonic Search Units

The success of any ultrasonic inspection depends very much on the right selection of the search units or transducers, which generate, transmit, and receive ultrasonic waves and thus provide a considerable amount of information about existing reflectors in the test object.

According to the definition in the American Society for Testing and Materials (ASTM) E 1316-10b, *a transducer is an electro acoustical device for converting electrical energy into acoustical energy and vice versa*. A search unit (or the more popular term *probe*), consists not only of a transducer but also of other components, for example, a wedge, lens, or mirror, to redirect and shape the ultrasonic beam according to the inspection requirements.

A probe design, inspection method, and technique development are interrelated processes. Almost any inspection task requires the development of a specific technique, after which a probe can be selected or designed to satisfy the inspection requirements. The availability of ultrasonic instruments with the required parameters influences the

Ultrasonic Inspection Technology Development and Search Unit Design: Examples of Practical Applications, First Edition. Mark V. Brook.

probe design. Therefore, to describe a probe design separately from the inspection technique development, or at least without understanding its capabilities, is impracticable.

It is interesting to trace the evolution of probe design along with the evolution of ultrasonic methods, instrument development, and inspection requirements.

Initially, ultrasonic instruments were designed for manual scanning and had only one channel. Therefore, only one probe, single or dual, could be connected to the instrument. If the inspection procedure required several scans with different refracted angles, different probes had to be employed.

To speed up inspections, multichannel instruments in the form of multiple pulser–receiver units were designed to meet the capability for automated scanning. This led to the creation of multielement and multibeam probes. The goal was to design miniature probes with many piezoelectric elements, oriented in the desired direction to produce beams with several refracted angles. As a result, the scan pattern was changed—the linear scan appeared. The next step was the creation of the phased array method, transducers, and probes. This led us back to the possibility of using a single instrument with a single acquisition channel to accommodate the transducer array. Currently, these techniques are very popular; however, single-element probes are still very much in use.

In some cases, a conventional probe can be applied for manual inspection, but as a rule for automated inspection, a conventional probe has to be modified or a special probe designed for the specific application.

Manufacturers of ultrasonic transducers, wedges, and probes fabricate mostly common products for manual inspection. The basic types of common transducers and probes for manual examination are well known: straight beam transducers with or without a delay line, dual straight beam and angle beam probes. A typical angle beam probe is shown in Figure 2.1.

Many manufacturers do not fabricate special probes to the customer specifications or designs. Fabrication of the transducer itself requires special skills and equipment and can be accomplished only by specialized companies. However, companies providing nondestructive testing (NDT) services need to design and often fabricate probes for their own needs or for the needs of their customers.

Figure 2.1 A typical angle beam probe: a transducer attached to a wedge.

The main portion of a transducer, or as many practitioners named it, wedge driver, is a piezoelectric ceramic element (crystal) that, in most cases, generates longitudinal waves (L-waves). The main mode of vibration for crystals used in the ultrasonic NDT is the *thickness expansion* mode. The generated L-waves pass through a matching layer and an acoustic delay line into the material of the test object.

In the case of angle beam probes, the acoustic delay lines are in the shape of a wedge. The material of the delay lines or wedges can be either some kind of liquid (usually water) for an immersion test technique or hard plastic for a contact inspection.

In almost any industry, there are many applications that require special probes. An automated inspection can also require specially designed probes such as multielement probes with couplant supply systems and wear protection.

The special probes for automated inspection contain the same basic components as conventional probes, but their combinations and characteristics should be unique to provide the quality and reliability of the inspection results. These custom-designed probes have additional parts. A stainless-steel housing, for example, acts as a wear protector as well as a shield for all internal components. It also contains fixtures to connect the probe to a scanning system, as well as internal passages for couplant delivery to the probe's footprint. Instead of a complete transducer, only the crystal assembly portion is to be used. The crystal assembly usually consists of the crystal itself with an electrical circuit,

a matching layer, and the element backing to reduce the "ring-down" time to improve the resolution.

These types of probes can be called *sealed probes* in contrast to *open*, replaceable transducer probes. An example of a probe where the transducer or the wedge can be replaced is shown in Figure 2.1. Sealed probe designs are more compact than the open type for the same number of transducers or crystal assemblies. Probes that utilize only crystal assemblies are less expensive than open probes with the same number of transducers. One example of the special probe is the triplex probe (see Figure 5.6 for details).

The most common triplex probe consists of two wedges and four crystal assemblies. For example, one pair of wedge and crystal assembly is for generating an ultrasonic beam of 45° shear wave (S-wave) refracted angle and the other is for a 60° S-wave refracted angle. The front portions of the wedges and crystal assemblies are the dual straight beam portion of the probe (Figure 2.2 shows only the wedges).

The basic parameters of the probe have to be selected and calculated to ensure its proper function in a given test situation (see Section 2.1.5 for an example of a calculation).

Crystal assemblies or transducers are very specific components of the probe. As mentioned before, only a specialized manufacturer can fabricate them. However, delay lines and wedges are easy to fabricate in almost any machine shop. This is why, in specific cases of

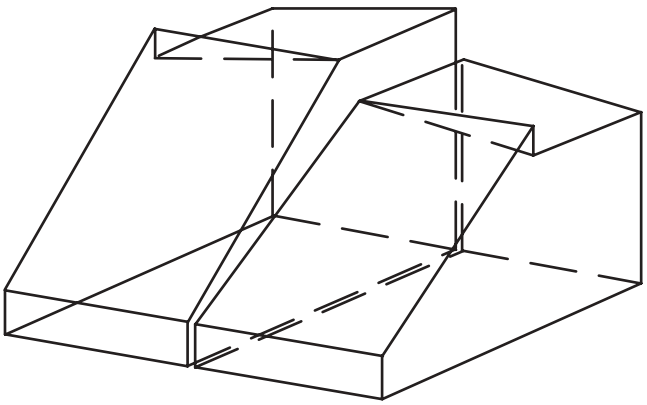

Figure 2.2 Conceptual design of triplex probe wedges.

inspection, the transducers are bought as finished or semifinished components (crystal assemblies), but the wedges are calculated, designed, and machined separately and then assembled with the crystal assemblies.

The parameters of the transducer or crystal assembly to be chosen or calculated are frequency, size and shape of crystal, bandwidth, and, in some cases, type of ceramic (crystal). All these and several more parameters are listed in the manufacturer's specifications. Recommendations for choosing a transducer or writing specifications for the manufacturer will be discussed later.

The main objective of the wedge is to transmit ultrasonic energy from the transducer through the interface with a test object to create in it an acoustic field suitable for a given inspection application. In the case of a single angle beam probe, the most important wedge parameter to calculate is the angle of incidence, or the wedge angle. This angle basically defines the parameters of an acoustic field, such as types of refracted waves and their refracted and divergent angles.

The purpose of an acoustic field calculation is to determine its parameters at every point of the field, specifically the sound pressure and the direction of particle motion which defines the mode. The basic parameters of the directional characteristics are the central ray refracted angle and the shape of the main lobe.

2.1.2. Essential Facts about Ultrasonic Wave Propagation

As is well known, to detect and determine the size of discontinuity in a test object, two basic modes of ultrasonic waves and their superposition are used: L-waves and S-waves. In the case of angle beam probes, the L-wave, generated by the transducer or crystal assembly, changes its direction and, in many cases, experiences mode conversion at the interface of the wedge and an inspection material.

The laws of reflection and refraction of light rays are well known from geometrical optics [11] and can be applied to calculate this directional change, as a first approximation. These are

> The law of reflection—*the reflected ray lies in the plane of incidence, and the angle of reflection equals the angle of incidence*.

The law of refraction—*the refracted ray lies in the plane of incidence, and the sine of the angle of refraction bears a constant ratio to the sine of the angle of incidence*:

$$\frac{\sin\beta}{\sin\alpha} = const \tag{2.1}$$

where α = angle of incidence and
β = refracted angle.

This law is usually called Snell's law. The value of this constant is called the index of refraction n. It later became clear that the angle of refraction depends on the wavelength of light in each medium, which is a function of wave velocities. The law of refraction was then formulated in the way we know it today:

$$\frac{\sin\alpha}{\sin\beta} = \frac{V_1}{V_2} \quad \text{or} \quad \frac{\sin\alpha}{V_1} = \frac{\sin\beta}{V_2} \tag{2.2}$$

where V_1 = sound velocity in the first medium and
V_2 = sound velocity in the second medium.

In addition to the laws of reflection and refraction, a phenomenon of wave transformation or mode conversion has to be considered, according to which one mode of waves can be converted into another. In a specific case when a hard wedge (e.g., Plexiglas) is coupled with a metal test object with parallel surfaces, and the L-wave is obliquely incident on the interface; in a general case, four additional waves occur: two reflected and two refracted. A portion of the energy of the L-wave and the S-wave will reflect back into the wedge, and the other portion will be transmitted (refracted) into the test object material (Figure 2.3).

The angles of reflection and refraction can be calculated preliminarily using the laws mentioned above, knowing the angle of incidence and velocities in both mediums, according to the formula

$$\frac{\sin\alpha_l}{V_{wl}} = \frac{\sin\alpha_{l1}}{V_{wl}} = \frac{\sin\alpha_{s1}}{V_{ws}} = \frac{\sin\beta_{l2}}{V_{sl}} = \frac{\sin\beta_{s2}}{V_{ss}} \tag{2.3}$$

where α_l° = angle of incidence L-wave;
α_{l1}° = angle of reflection L-wave;

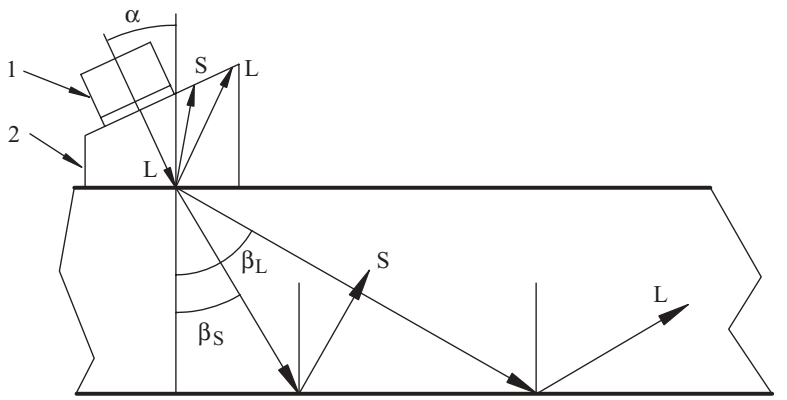

Figure 2.3 Wave reflection and refraction at the wedge–steel interface. (1) Transducer, (2) wedge. α, angle of incidence, β_L, longitudinal wave refracted angle, β_S-shear wave refracted angle.

$\alpha_{s1}°$ = angle of reflection S-wave;
$\beta_{l2}°$ = angle of refraction L-wave;
$\beta_{s2}°$ = angle of refraction S-wave;
V_{wl}, mm/μs = velocity in the wedge material, L-wave;
V_{ws}, mm/μs = velocity in the wedge material, S-wave;
V_{sl}, mm/μs = velocity in the test metal, L-wave; and
V_{ss}, mm/μs = velocity in the test metal, S-wave.

And conversely, if the desired refracted angle and mode are known, the angle of incidence can be calculated, which is the most common scenario in a wedge design.

The angles of incidence at which one or the other wave mode "disappears" during reflection or refraction at the interface are called critical angles (Figure 2.4).

According to Snell's law, there are two critical angles connected with the incident L-wave at the wedge–metal interface. If the angle of incidence is equal to the first critical angle α_{1CR}, the refracted L-wave should propagate along the surface rather than, for example, in the metal of the test object (this is not completely accurate, as it will be shown later).

If the angle of incidence is further increased to the second critical angle α_{2CR}, the S-wave will transform into a surface wave, propagating, for example, along the metal–air interface. Beyond this angle,

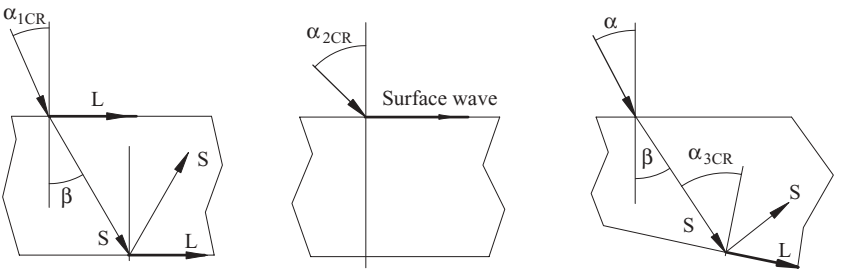

Figure 2.4 Wave propagation at the critical angles. α_{1CR}, first critical angle, α_{2CR}, second critical angle, α_{3CR}, third critical angle.

according to this law, no wave will be transmitted into the material of the test object.

There is one more critical angle connected with the incidence of the S-wave on the opposite inclined surface of the test object or on the inclined lamination inside it. Under a certain lowest angle of incidence (the third critical angle α_{3CR}), the reflected L-wave begins to "slide" along the test object metal–air interface, and only the S-wave is reflected. If the back surface or a lamination within the material is parallel to the front surface, the L-wave begins to "slide" along the metal–air interface at the first critical angle. But if these surfaces are not parallel, the angle of incidence will be different from the first critical angle in order to achieve the third critical angle. These critical angles are essential for wedge design in certain cases. One of the examples of the third critical angle calculation is presented in Appendix C.

2.1.3. Basic Considerations for Delay Line and Wedge Design

Delay Line for Straight Beam Probes (Figure 2.5)

A delay line for an immersion test is a column of water, and for a contact probe it is usually a cylinder (for a round crystal) of acrylic or polystyrene. In both cases, only one parameter should be calculated—the height of the delay line h to satisfy the inspection requirements, for example, to detect the reflector at distance H. The time of flight (TOF) in the delay line (Figure 2.5, τ_d) should be slightly greater than the TOF

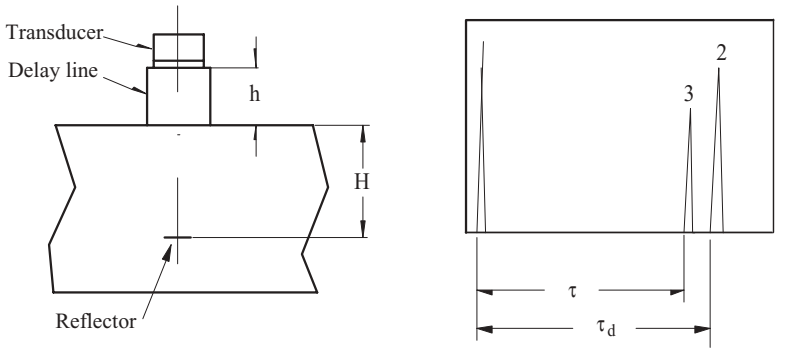

Figure 2.5 Diagram related to a delay line calculation.

τ to the specified reflector in a test object in order to avoid signal coincidence with the second multiple 2 in the delay line and the signal 3 from the reflector or back wall. The difference of $\tau_d - \tau$ should be not less than several microseconds. This depends on the probe bandwidth, wave duration, and depth of reflection.

The idea of the delay line height calculation can be illustrated by using the concept of an imaginary crystal [4]. The real crystal is located in the position *a*, at the distance *H* from the surface of the test object. When an ultrasonic ray strikes the interface of the test object at the angle α, it changes direction (refracted at angle β). If two refracted rays are extended back into the delay line, they will cross at the distance *h*. This is the position of the imaginary crystal b. The unknown position of the imaginary crystal *h* can be expressed in terms of the known position of the real crystal *H* and the velocities in the first (1) and second (2) mediums (Figure 2.6):

$$h = \frac{c}{\tan\beta} \tag{2.4}$$

$$H = \frac{c}{\tan\alpha} \tag{2.5}$$

$$h = H\frac{\tan\alpha}{\tan\beta}. \tag{2.6}$$

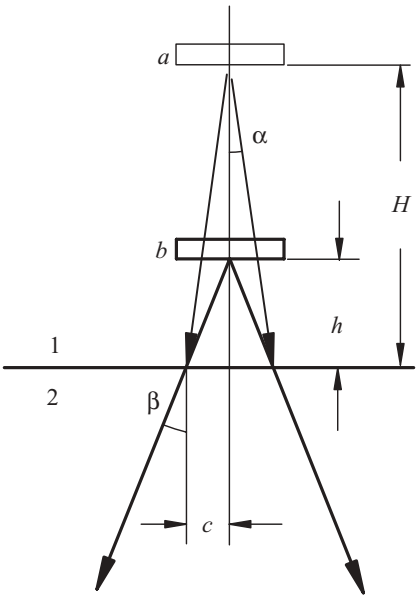

Figure 2.6 A delay line height, according to the concept of the imaginary crystal. (1) A delay line medium, (2) a test object medium.

For small angles tan ≅ sin; thus,

$$\begin{aligned} \tan\alpha &\approx \sin\alpha \\ \tan\beta &\approx \sin\beta \end{aligned} . \tag{2.7}$$

According to the law of refraction,

$$\frac{\sin\alpha}{\sin\beta} = \frac{V_1}{V_2} \tag{2.8}$$

and

$$h \cong H\frac{V_1}{V_2} \tag{2.9}$$

where V_1 = sound velocity in delay line material and
V_2 = sound velocity in test object material.

This means that the delay line medium of height H was exchanged with the test object medium, and the test object surface is moved up on the distance h. Thus, the TOF in the test object material at distance h is equal to the TOF in the delay line material at distance H:

$$\tau_d = H/V_1 \quad \text{and} \quad \tau = h/V_2. \tag{2.10}$$

The concept of the imaginary crystal is also useful for near-field distance calculation in a test object when using a delay line: The distance h should be subtracted from the calculated near-field distance.

Wedge for Angle Beam Probe

A material for a solid wedge should meet several requirements. The wave velocity in the wedge material should be less than the wave velocity in the inspected material in order to cover the entire quadrant Q from 0° to 90° with refracted L- and S-waves (Figure 2.7). More precisely, the L-wave velocity in the wedge material has to be less than the S-wave velocity in the material of the test object.

Attenuation in the wedge material is also significant. It should be as low as practically possible not to attenuate ultrasonic energy on the way from the crystal to the interface with the test object. At the same time, it should be high enough to attenuate reflections from the interface (or within the wedge itself), which can produce noise in

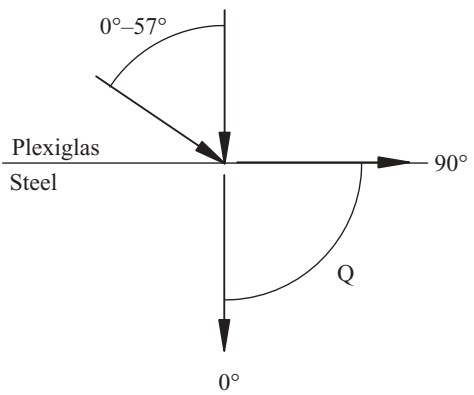

Figure 2.7 Diagram of an entire quadrant coverage.

the wedge. The wedge material also has to be wear resistant to prolong its life.

The plastics, such as acrylics and polystyrene, which are used for wedge fabrication, partly meet the first two requirements but do not meet the wear resistance requirement.

It is very important to standardize wedge material in order to maintain consistency. Each new batch of materials has to be carefully measured for velocity before it is used.

Methods of velocity and attenuation measurements in wedge materials will be discussed later.

Proper wedge design can totally eliminate wedge noise [12]. The first requirement for the design is to prevent the reflection of energy from the interface and wedge corners back to the crystal. Due to the fact that the wedge contains only the near-field portion of a beam, that is, the "cylindrical" portion, the distance n between the exit point and the wedge front edge (the index) can be calculated as: $n \geq n_1$ where $n_1 = d/2\cos\alpha$ (Figure 2.8). This will be achieved if the ray from the upper edge of the crystal will not touch the wedge front surface. It is also desirable that the reflected S-wave's ray from the low edge of the crystal should not touch the crystal's upper edge.

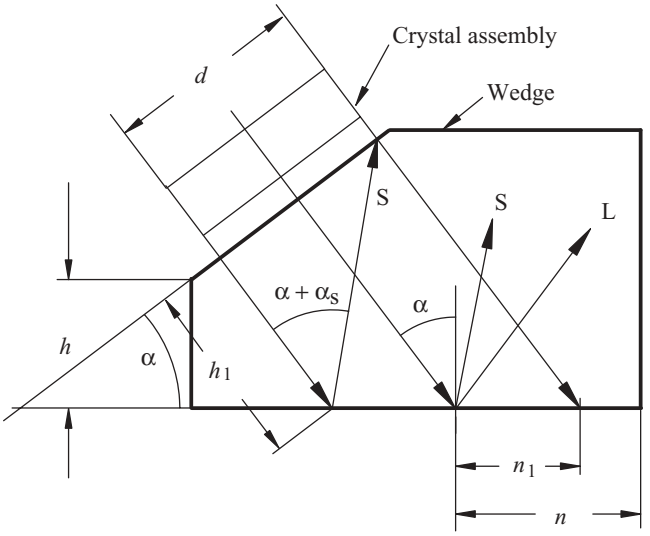

Figure 2.8 Internal reflections in a wedge for single angle beam probe.

Thus, the height $h \geq h_1 \times \cos\alpha$ and should be calculated as

$$h \geq d \frac{\cos\alpha}{\tan(\alpha + \alpha_s)}. \tag{2.11}$$

Reflections from the upper wedge corner, along with reflections from the front and top surfaces, can also produce wedge noise. A geometrical ray tracing of the reflected L-wave inside the wedge will help to find potential sources of noise. S-wave ray tracing is not as important as L-wave ray tracing due to the higher attenuation of the S-wave.

There are ways to reduce or eliminate this kind of noise, such as to redirect the reflected waves, to serrate the front and/or top wedge surfaces, and to cover the front and/or top wedge surface with a high-absorption material. Generally, it is easier to reduce or eliminate noise in the wedge for refracted S-wave than for refracted L-wave. The L-wave wedge has to be taller to achieve the same results of noise reduction as for the S-wave.

2.1.4. Examples of Probe Design for Automated Inspection

The variety of wedge geometries of common probes for manual inspection can be seen in catalogs from any probe manufacturer. Examples of simple probe and wedges, designed for automated inspection, are shown in Figures 2.9 and 2.10.

The single straight beam probe (Figure 2.9A) has a couplant delivery system incorporated into its housing, along with pivot point bearings for connection to a scanner. The wedge (Figure 2.9B) comprises two parts: insert and body.

This insert serves as a wave guide and is made from regular wedge material. There are several ways to fabricate this type of wedge. For example, it can be pressed or glued in the body, or the body can be cast around the wave guide material. The body can be fabricated from hard polyurethane (or similar material), which has good wear resistance and sound absorption properties. This kind of wedge does not need serration or an additional absorber.

If the wedge needs serrations, its angles should be in the region of 45–90°. This is not as critical as its depth, which should be not less than the wavelength λ of the L-wave in the wedge material. As usual,

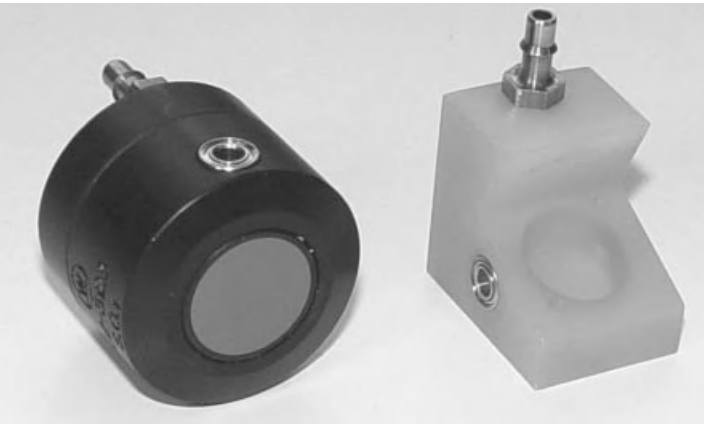

(A) (B)

Figure 2.9 Examples of probe and wedge for automated inspection. (A) Single straight beam probe; (B) wedge with insert. Reprinted by permission of Westinghouse Electric Company LLC.

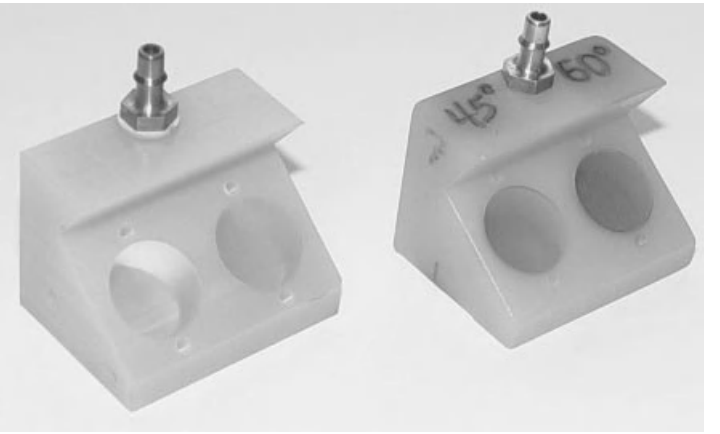

Figure 2.10 Combined wedges for 45°S and 60°S refracted angles. Reprinted by permission of Westinghouse Electric Company LLC.

the serration should be filled in with absorption material to reduce possible wedge noise. The absorber can reduce the wedge noise by approximately 10–12 dB or more, depending on the wedge design.

In many cases, it may be practical to design one combined wedge with two refracted angles. The inserts should be machined from two different wedge materials. As an example, let us calculate the wedge

angle for combined wedge 45°S and 60°S for the inspection of a test object from carbon steel:

V_{ST} = 3.23 mm/μs = S-wave velocity in steel;
V_{PL} = 2.74 mm/μs = L-wave velocity in Plexiglas; and
V_{POL} = 2.24 mm/μs = L-wave velocity in polystyrene.

The wedge angle for the 45°S portion of the wedge can be made from Plexiglas, and the wedge angle for the 60°S portion of the wedge can be made from polystyrene. The angles of incidence are

$$\alpha = \arcsin 45\frac{2.74}{3.23} = 36.86°$$

$$\alpha = \arcsin 60\frac{2.24}{3.23} = 36.91°.$$

The combined wedges with an angle of 37° are shown in Figure 2.10. The wedge on the right also has protection plates of aluminum oxide. These plates can increase the sensitivity. For example, on the 60°S portion of the wedge, an increase of approximately 10 dB can be observed.

2.1.5. Wedge Design for Surface Wave Probe

Wedge design for a surface wave probe requires special attention. In Reference [13], it was mentioned that the best condition to generate Rayleigh waves will be in the case when the upper ray of the crystal will touch the front edge corner of the wedge (point *c* in Figure 2.11A).

The distance between the exit point and the wedge front edge (index) in conventional S-wave or L-wave probes should usually be longer than the allowed minimum in an attempt to prevent wedge noise. Normally, this distance is not critical from an acoustic point of view as the acoustic field of S- or L-waves in the test object will not be influenced by an increased index. The only design consideration for wedge length would be, for example, to make the probe as short as possible to meet specific test conditions.

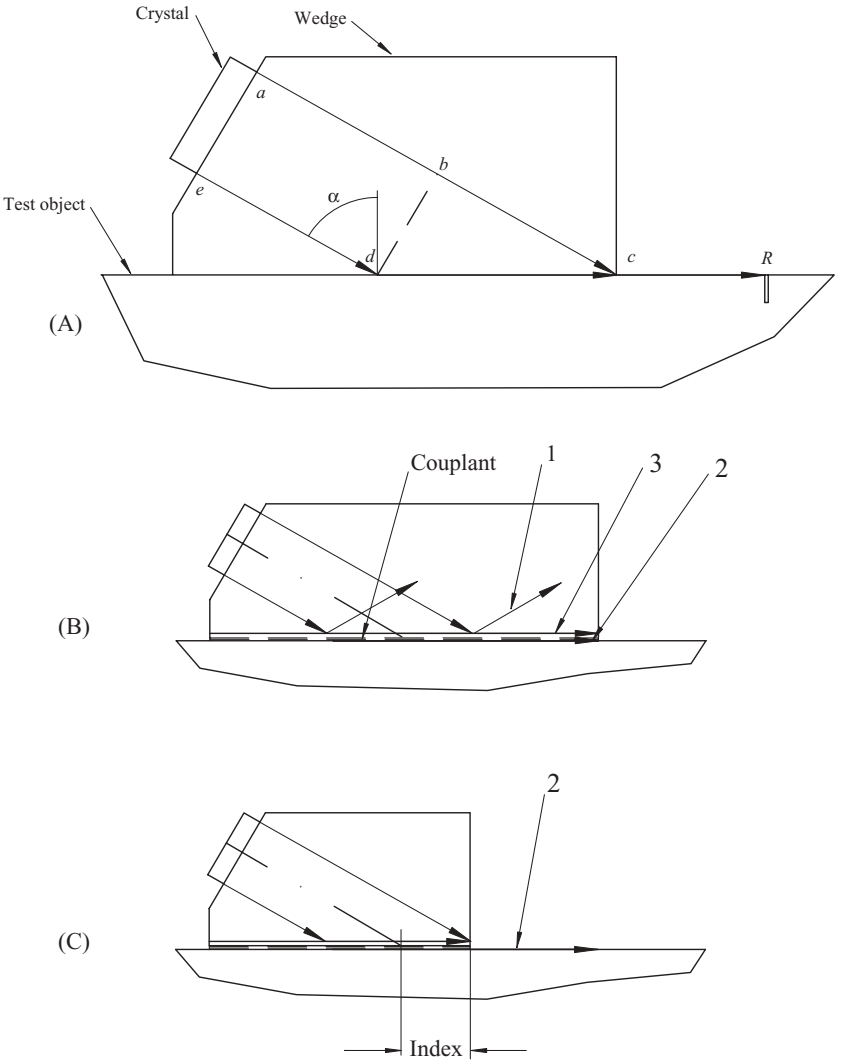

Figure 2.11 Surface wave probe conceptual design. (A) Upper ray of crystal touches the front edge corner of the wedge at point *c*; (B) wave structure in the long wedge; (C) wave structure in the wedge with optimum length.

For a surface wave probe, on the other hand, the length of the index is critical from the acoustic point of view. It was shown in Reference [14] that the extended index causes decay of the signal from a reflector due to the redistribution of ultrasonic energy from surface wave propagating in the test object into surface wave in the wedge.

The best condition for surface wave generation will be the case when the rays from any point of the crystal in the plain of incidence arrive at point "*c*" at the same time and hence to reflector *R* (Figure 2.11A).

Let us consider the situation of two rays from the upper and the lower points of the crystal directed to the front edge of the wedge. It can be shown that these two rays will arrive at point "*c*" simultaneously, as well as any other rays in between. This situation can be formulated as follows: The TOF t_1 between points *ac* and t_2 between points *edc* are

$$t_1 = \frac{ac}{V_L} \tag{2.12}$$

$$t_2 = \frac{ed}{V_L} + \frac{dc}{V_R} \tag{2.13}$$

where V_L is the L-wave velocity in the wedge material and

V_R is the Rayleigh wave velocity in a test object.

If these two TOFs will be equal, the two rays will arrive in point "*c*" at the same time:

$$\frac{ab}{V_L} + \frac{bc}{V_L} = \frac{ed}{V_L} + \frac{dc}{V_R} \tag{2.14}$$

then

$$ab = ed \quad \text{and} \quad bc = dc \times \sin\alpha, \tag{2.15}$$

where α is the incident or wedge angle

$$\frac{ed}{V_L} + \frac{dc}{V_L}\sin\alpha = \frac{ed}{V_L} - \frac{dc}{V_R} \tag{2.16}$$

$$dc\left(\frac{\sin\alpha}{V_L} - \frac{1}{V_R}\right) = 0. \tag{2.17}$$

If

$$\left(\frac{\sin\alpha}{V_L} - \frac{1}{V_R}\right) = 0 \tag{2.18}$$

Table 2.1
Calculated Wedge Angles

Wedge material	L-wave velocity mm/μs	Wedge angle α, degree	
		Optimum	Snell's law
Plexiglas	2.735	65.73	57.86
Polystyrene	2.24	48.3	43.91

L-wave, longitudinal wave.

then the optimum wedge angle is

$$\alpha = \arcsin \frac{V_L}{V_R}. \tag{2.19}$$

Equation 2.19 permits the calculation of the optimum wedge angle for a given wedge material and the surface wave velocity in the test object material. For example, for the steel test object having L-wave velocity V_{LS} = 5.85 mm/μs and S-wave velocity V_{SS} = 3.23 mm/μs and for two common wedge materials (Plexiglas and polystyrene), calculated wedge angles are summarized in Table 2.1 along with the second critical angles calculated according to Snell's law.

One can see that the optimum wedge angles are larger than those calculated according to Snell's law.

It can be shown that the maximum signal amplitude from a reflector will be achieved when the acoustic contact between surfaces of a wedge and a test object is as short as practically possible.

When the wave from the transducer incidents the border wedge–couplant–test object surface, three waves will appear (Figure 2.11B): reflected wave 1, surface wave 2 propagated along the test object surface, and surface wave 3 propagated along the surface of the wedge. Wave 3 appears due to the redistribution of the energy from the surface wave propagating along the test object surface. It is obvious that the energy of surface wave 2 is diminishing. If the acoustic contact between the wedge and the test object is interrupted, the distribution of energy is terminated. Thus, the length of the acoustic contact between the wedge and the test object should be minimized to retain the energy in surface wave 2 (Figure 2.11C). The objective of the

wedge design is to provide conditions for keeping as much energy as possible in the surface wave that propagates along the surface of the test object.

It means that the index *n* should be as short as practically possible. A compromise between tolerable wedge noise and desirable signal amplitude from a specified reflector should be considered. A practical and acceptable index can be determined by the following experiment. The probe with the wedge length far greater than the calculated index should be used to generate a surface wave. The signal amplitude from the reflector should be measured after cutting the wedge length in regular increments up to the point when the maximum signal amplitude will be achieved at the minimum wedge noise.

As an example, the results obtained from such an experiment are shown in Figure 2.12.

The wedge from Plexiglas with the length of seven indexes, counting from point *c* (Figure 2.11A), was used in this experiment. The test sample was machined from a carbon steel with a notch reflector one wavelength deep.

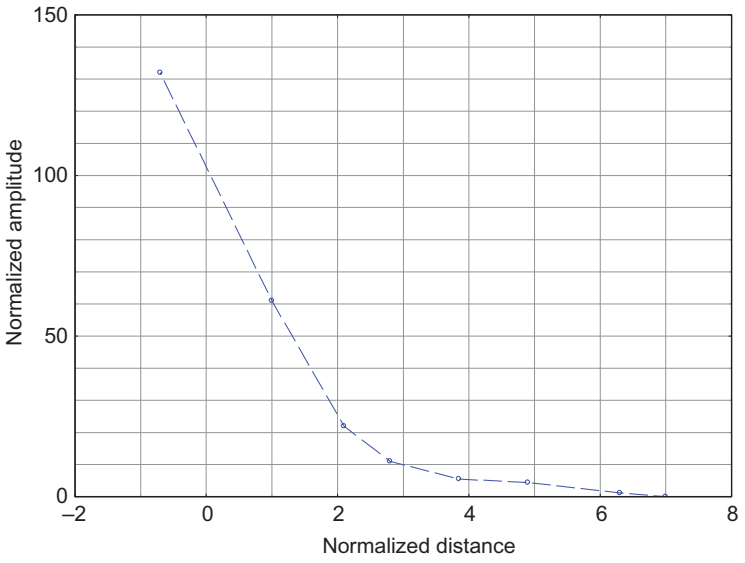

Figure 2.12 Experimental graph: normalized distance of a reflector versus normalized signal amplitude.

On the abscissa, the normalized distances in index increments are plotted. Normalized signal amplitude is laid off along the vertical axis. This amplitude is the ratio of the signal amplitude measured after each cutting to the signal amplitude measured at the maximum wedge length that is at seventh indexes. One can see that at wedge lengths greater than approximately three indexes, the signal amplitude from a given reflector is little affected. For wedge lengths less then three indexes, the signal amplitude increases drastically up to the point slightly beyond the index: in this case up to –0.6 of the index. It is explainable having in mind a deviation of a wedge exit point (see Section 3.3).

Comparison of the performance of two wedges machined from Plexiglas with optimum angles of 65.73° and 57.86° (Table 2.1) indicates that

1. the signal amplitude from the same reflector at the same distance is approximately 10 dB less for the probe with a wedge angle of 57.86° and
2. the surface wave generated by using the probe with a wedge angle of 65.73° propagates at a much longer distance than the probe with a wedge angle of 57.86°.

These are due to the fact that the probe with a wedge angle of 65.73° generates mostly a surface wave, as the probe with a wedge angle of 57.86° also generates an S-wave at a refracted angle of approximately 80°, depending on the probe frequency and the test object material.

2.2. CONSIDERATIONS FOR TRANSDUCER SELECTION

2.2.1. Basics of Transducer Design

The information presented in this section are intended only as guidelines for selecting a transducer or a crystal assembly for a given inspection, or for writing specifications for their fabrication. As an example, for determining transducer or crystal assembly parameters, a typical straight beam transducer, as shown in Figure 2.13, will be discussed.

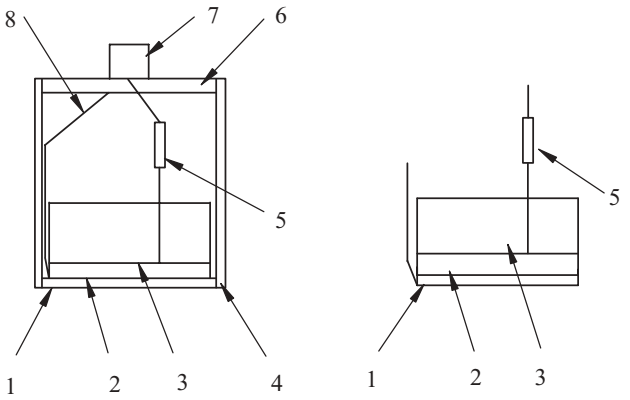

Figure 2.13 Structure of (A) a straight beam transducer and (B) a crystal assembly. (1) Matching layer, (2) crystal, (3) backing, (4) housing, (5) tuning component, (6) cover, (7) connector, (8) ground.

A piezoelectric ceramic element, or a crystal, is the main component of a transducer.

The crystal vibrates more effectively at the resonance frequency, which is determined by its thickness and shape, for a given composition of the ceramic material.

The other transducer components are designed to make the performance of the crystal as efficient as practically possible [15, 16].

Matching Layer

The purpose of the matching layer is to match the acoustic impedance of the crystal with the acoustic impedance of the load (water, wedge, test object, etc.). It provides conditions for the acoustic energy to be transmitted from the crystal to the load with the least possible loss of energy. If the acoustic impedance of the crystal and the load are exactly equal, all ultrasonic energy generated by the crystal will be transmitted at the interface. Three types of matching layers are commonly used depending on the transducer application: matching layer for water (immersion inspection), matching layer for wedge material, and wear plate for straight beam contact probe for the inspection of metals. In the last case, the plate is also a wear protector.

Backing

The word *backing* refers only to its location on the *back* side of the crystal. The purpose of it is to *damp* or reduce the crystal vibration duration to a desirable level, for example, to one or two cycles. It also absorbs a portion of the ultrasonic energy generated by the back side of a crystal. The most common backing material is a mixture of resin epoxy and tungsten powder in different proportions, depending on the crystal material and the desirable level of damping [16,17]. Other material combinations can be used.

While the positive influence of the backing is "resolution" enhancement, the negative side is reduction in sensitivity or output energy. The degree of damping depends mainly on the acoustic impedance match between the backing material and the crystal. The composition of the backing material, along with the type of crystal, and electrical tuning, as a secondary influencing parameter, are the main determining factors used to achieve the desirable bandwidth. The bandwidth (*BW* in %) calculation is based on the frequency response at the level of –6 dB below the central frequency (Figure 2.14) and is expressed as a percentage:

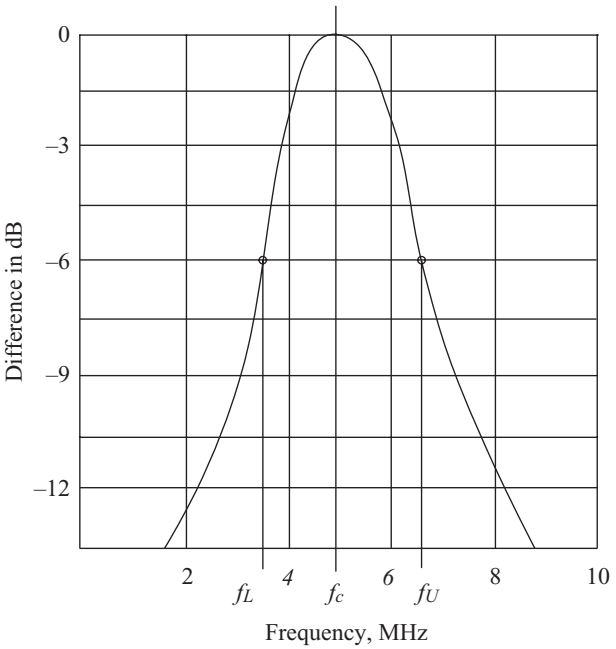

Figure 2.14 Diagram related to calculation of a bandwidth.

$$BW = \frac{f_U - f_L}{f_C} \times 100 \tag{2.20}$$

where f_L = lower frequency at the level of –6 dB, MHz;
f_U = upper frequency at the level of –6 dB, MHz; and
f_C = center frequency, MHz.

Tuning Components

Tuning components and wires, along with the crystal's electrodes, are the transducer's electrical circuit. The tuning components are incorporated for matching *electrical* impedances of the crystal assembly with the ultrasonic inspection system. These components are also used for tuning the crystal's resonant frequency. The wires connect the crystal's electrodes to an external connector and then to the pulser–receiver system of an ultrasonic instrument.

2.2.2. Acoustic Properties of Crystal Materials

Knowledge of the acoustic properties of the crystal material is necessary for correct transducer or crystal assembly selection. The main characteristics of currently used piezoelectric crystals are summarized in Table 2.2 as average data based on different literary sources, for example, Reference [18]. Each of the listed materials is fabricated in several varieties suitable for different applications.

Table 2.2
Characteristics of Selected Piezoelectric Materials

Physical property	Crystal material		
	Lead metaniobate (LM)	Lead zirconate titanate (PZT)	Piezo-composite
Acoustic impedance Z, kg/m^2 s 10^6	20–27	30–39	8–12
Coupling coefficient, k_t	0.30–0.40	0.40–0.53	0.5–0.7
Coupling coefficient for radial vibration mode, k_p	<0.1	0.58	<0.1
Dielectric constant, κ	300	1000–2000	300–600

Table 2.3
Average Acoustic Characteristics of Selected Materials

Material	Acoustical properties			
	L-wave velocity, mm/μs	S-wave velocity, mm/μs	Density, g/cm^3	Acoustic impedance, kg/m^2 s × 10^6
Aluminum	6.42	3.04	2.70	17.5
Aluminum oxide	9–11	5.5–6.5	3.6–3.9	32–43
Epoxy resin	2.6–2.7	1.1–1.2	1.21–1.25	2.7–3.5
Plexiglas	2.7–2.74	1.1–1.3	1.15	3.1–3.3
Polystyrene	2.3–2.4	1.1	1.05	2.4–2.5
Steel	5.7–5.9	3.1–3.3	7.8–7.9	44–46
Tungsten	5.2	2.9	19.4	101
Water	1.49		1.0	1.49

L-wave, longitudinal wave; S-wave, shear wave.

The most common material used is lead metaniobate. The use of PZT material has declined, but it is the most desirable material for the production of *piezo-composite* crystals and phased array transducers. In order to select the correct crystal material or crystal assembly for the specified application, the acoustic impedance of piezoelectric crystals should be compared with the acoustic impedance of the materials to be inspected as well as with that of materials suitable for matching layers and backing (Table 2.3).

When the load is water (immersion inspection) or plastic (angle beam probes), 85–90% of ultrasonic energy will be reflected on the interface with the bare crystal due to the differences in their acoustic impedances.

The electromechanical coupling coefficient shows the quantity of electrical energy coming from the pulser to the crystal that will be converted into the mechanical energy of vibration in the crystal thickness mode. The coupling coefficient for the radial vibration mode shows the amount of mechanical vibration that will be converted to this mode. It is not just a loss of potentially useful energy, but this can also become an additional source of undesirable probe noise.

The parameters of lead metaniobate, such as relatively low acoustic impedance and very low coupling coefficient for radial vibration mode, are suitable for the design of both broadband and efficient transducers.

Piezo-composite crystal materials have approximately half the acoustic impedance of lead metaniobate and almost double the coupling coefficient. Therefore, they are very suitable for transducers intended for immersion inspection, and for coupling with wedges in angle beam probes. The sensitivity of probes with composite crystals, in many cases, is approximately 6–8 dB greater compared with a same-size crystal of lead metaniobate. When sensitivity is a high priority and the test object is thick (150–250 mm), probes with PZT crystals are preferable due to their relatively high electromechanical coupling coefficient. The dielectric constant of piezo-composite and lead metaniobate crystals is less then that of PZT but high enough to withstand a 400 V pulse which is typical for most ultrasonic inspection systems.

To achieve desirable performance and to optimize transducer parameters, certain calculations have to be performed [19]. To *calculate a transducer* means to determine the values of all of its components that will satisfy the given requirements. The computer program based on the KLM (Krimholtz, Leedom, and Mitthaei) theoretical model is the one mostly used by leading transducer manufacturers at this time [20]. The theoretical model relates electrical input parameters to mechanical ones (and vice versa) and can predict waveform, bandwidth, and so on. The problem with modeling is that there are variations in the actual transducer's component values that may not appear in the model, as well as the manufacturer's ability to reproduce the same values when fabricating the actual transducer.

As can be noted in Tables 2.2 and 2.3, the acoustical mismatch between crystal materials, test objects, and wedge materials is an obvious problem. The challenge to a probe designer is to make a probe with as little insertion (mismatch) losses as practically possible. One of the ways to achieve this is to include matching layers between each component of a probe as shown in Figure 2.15.

The acoustic impedance of a backing material composition can be made very close to that of the crystal; therefore, a matching layer between the crystal and the backing in most cases is unnecessary. A matching layer on the wedge–crystal interface is most frequently used. A matching layer between the wedge and the test object is very rare, although this interface is a major source of energy loss. If the test object

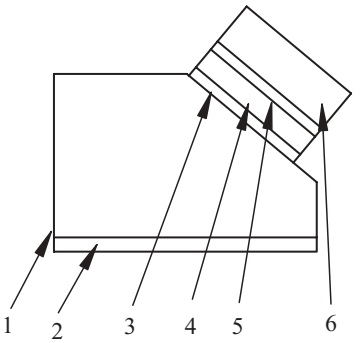

Figure 2.15 An angle beam probe with all possible matching layers. (1) A wedge, (2) a matching layer wedge–test object, (3) a matching layer wedge–crystal, (4) a crystal, (5) a matching layer crystal–backing, (6) a backing.

surface is flat, the energy loss can be minimized by gluing a plate of aluminum oxide to the wedge base (assuming that the test object is steel). This can result in, approximately, a 6- to 8-dB increase in the sensitivity, as well as an extension of the wedge service life due to the added wear protection.

2.2.3. Velocity Measurement in Metals

Bulk Velocity Measurement in Thick Metal

ASTM Standard Practice E 494-05 describes the method of comparative ultrasonic velocity measurement using a reference material (velocity standard) whose ultrasonic velocity is known. This method can be used mostly for metals with thicknesses greater than 5 mm. The velocity of the standard is determined using techniques of higher accuracy. The procedure calls for the measuring of bulk, longitudinal, or shear velocities by comparing the TOF in the velocity standard with the TOF in a sample of an unknown material of the same thickness.

The signal pattern should contain several back reflections that are clearly separated. It is recommended to adjust the last signal amplitude to approximately the same level as the first back signal amplitude. After measurements on both samples, the velocity of the unknown sample can be calculated.

For practical purposes, ultrasonic velocity measurement can be performed by using only one sample with an unknown velocity. Using the same signal pattern, the TOF should be measured, but it is not

necessary to adjust the last signal amplitude to the same level as the first back signal amplitude if a modern ultrasonic system is being used. These systems automatically locate the highest signal amplitude and display the TOF. The last chosen signal amplitude should be set up by the operator. The number of back reflections (signals) should be as many as possible. The system calculates the difference in TOF between first and last chosen signals (Delta TOF).

To calculate ultrasonic velocity V, the cumulated distance should be divided by the measured TOF:

$$V = \frac{(N-1)\times 2T}{\Sigma\tau} \tag{2.21}$$

where N = number of back reflections;
T = thickness of the sample; and
$\Sigma\tau$ = total measured TOF.

For example, by using an L-wave transducer on a steel sample with a thickness of $T = 12.7$ mm and a signal pattern that includes 11 reflections, total transition TOF is 43.8 μs and longitudinal velocity is (see Figure 2.16)

$$V = \frac{(11-1)\times 25.4}{43.8} = 5.799\ \text{mm}/\mu s.$$

Bulk Velocity Measurement Using a Thin Metal Strip

The bulk velocities, longitudinal or shear, can be different in a thin or a thick plate of the same material due to the plate manufacturing technology. The velocities of materials, listed in published tables, are relative, as a rule, to the thick plates. To calculate, for example, the Lamb wave's dispersion curves, it is a good practice to use the bulk velocity values measured in the thin strip, which represents the material and thickness of the real object to be inspected.

This technique is based on the fact that the Lamb wave modes become standing waves at a normal angle of incidence. The measured resonant frequency can then be correlated to the L-wave or S-wave velocities. The diagram of the setup for the bulk velocity measurement in a thin strip is shown in Figure 2.17.

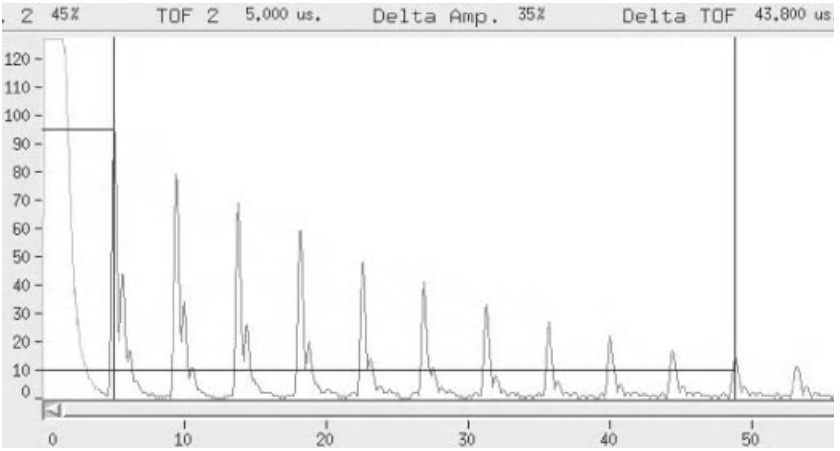

Figure 2.16 The signal pattern including 11 reflections. Delta TOF = 43.800 μs. TOF, time of flight.

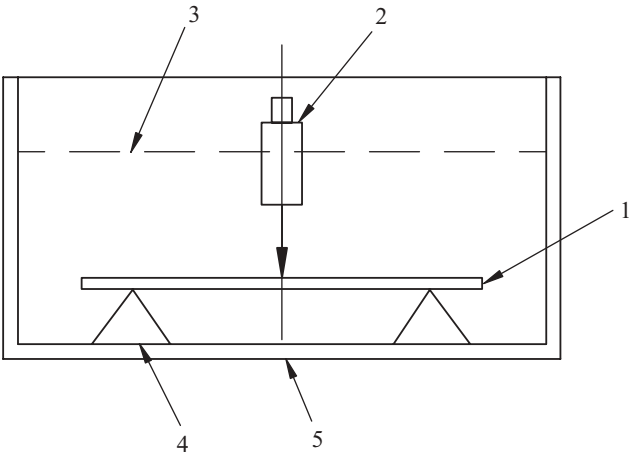

Figure 2.17 Setup for velocities measurement in a thin strip. (1) A metal strip, (2) a transducer, (3) water level, (4) supports, (5) immersion tank.

The strip 1 should be freely placed on two sharp prisms 4 in an immersion tank 5 with water level 3. Transducer 2, with a nominal center frequency to generate selected modes, is positioned normal to the strip and connected to a sweep frequency generator. The driving frequency is varied in the range of ±2 MHz from the transducer center frequency.

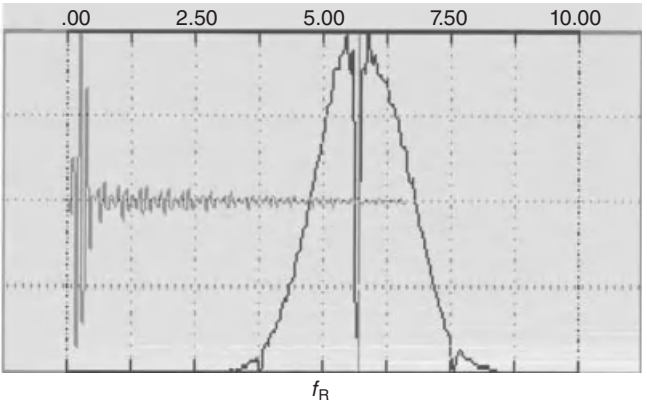

Figure 2.18 The screen capture related to a bulk velocity measurement in a thin metal strip.

Table 2.4
Formulas to Calculate Longitudinal or Shear Wave Velocities for Selected Modes

Mode	S_1	A_1	S_2	A_2
Formula	$V_l = 2d \times f_R$	$V_S = 2d \times f_R$	$V_l = d \times f_R$	$V_S = d \times f_R$

At a certain frequency, a phase cancellation phenomenon can be observed on the screen of the transducer evaluation station or the other ultrasonic instrument. The result resembles a divided frequency spectrum (see Figure 2.18).

The frequency related to the minimum amplitude of the separated line is the resonant frequency f_R. This frequency, along with the known thickness of the strip, is used to determine the corresponding L-wave or S-wave velocities according to the formulas listed in Table 2.4. It is also necessary to know the mode generated in the test strip.

As an example, let us determine the bulk velocity of a steel strip $d = 0.51$ mm thick. The resonant frequency is 5.69 MHz. (Figure 2.18). Transducer nominal frequency is 5.0 MHz. At this frequency and wall thickness, the S_1 mode should be generated. Thus, bulk L-wave velocity can be calculated as

$$V_l = 2d \times f_R = 2 \times 0.51 \times 5.69 = 5.804 \text{ mm}/\mu s.$$

2.2.4. Velocity and Attenuation Measurement in Wedge Materials

Velocity Measurement in Wedge Materials

The recommended ASTM Standard Practice E 494-2005 comparative method is not suitable for velocity measurements in wedge materials such as Plexiglas or polystyrene.

Two other methods for measuring ultrasonic velocity in wedge materials provide better results.

Contact Method. A single straight beam transducer with a matching layer for the wedge material is usually used for these measurements. The thickness of the matching layer effectively *increases* the thickness of the sample, so the value of the measured velocity in the wedge material would not be accurate. If the material of the matching layer has approximately the same velocity as the wedge material itself, but with a different thickness, depending on the transducer frequency, the measured velocity in the wedge material will apparently vary with the transducer frequency. Examples of matching layer thickness, as function of frequency, influence on velocity measurements in Plexiglas sample is shown in Table 2.5.

The data in this table demonstrate that the matching layer thickness influences the velocity measurement results, and the variation of these values also depends on the transducer frequency. To eliminate the influence of the matching layer, the measurements should be performed on two samples of the same material, but with different thicknesses (or a step sample), as shown in the sketch (Figure 2.19).

Table 2.5
Influence of Matching Layer Thickness, as a Function of Frequency, on Velocity Measurements

Transducer frequency, MHz	Velocity value, mm/μs			
	Minimum	Maximum	Average	Difference max.–min., %
1.0	2.52	2.72	2.65	7.35
2.25	2.60	2.745	2.715	6.46
5.0	2.705	2.746	2.732	1.49

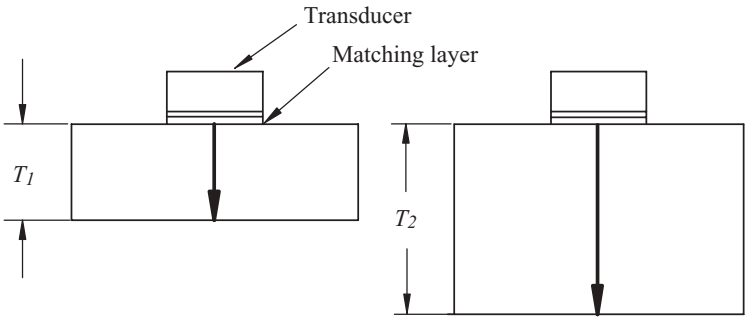

Figure 2.19 Setup for a wedge material velocity measurement by a contact method.

Two measurements should be performed: one on the thinner sample T_1 and another on the thicker sample T_2. The difference in thickness $\Delta T = T_2 - T_1$ has to be divided by the difference in transit time $\Delta\tau = \tau_2 - \tau_1$ to obtain velocity. So, the velocity is

$$V_W = 2\Delta T/\Delta\tau \tag{2.22}$$

where V_W is the velocity in the wedge material.

The measurements should be made with as high a frequency as possible to reduce the differences in the data (see Table 2.5).

Immersion Method. This method provides a more accurate measurement but requires special fixturing, such as a small immersion tank with two transducers, transmitter T and receiver R, mounted in line on two opposite sides of the tank. To measure the velocity, the sample is placed in the tank, approximately in the middle of the two transducers. The rationale of the measurement and the velocity calculation is as follows. The main idea is to replace the known transit time on distance T with the unknown one and to calculate the difference (Figure 2.20).

The distance L_W between the transmitter and the receiver is known and is constant. The transit time τ_w for this distance, along with the velocity in water V_W under a fixed temperature, is known and is constant as well.

Let us assume that the transit time in water without the sample in the tank is $\tau_w = A$ μs. To measure velocity in a wedge material sample, it should be placed somewhere in the middle of the transmitter and

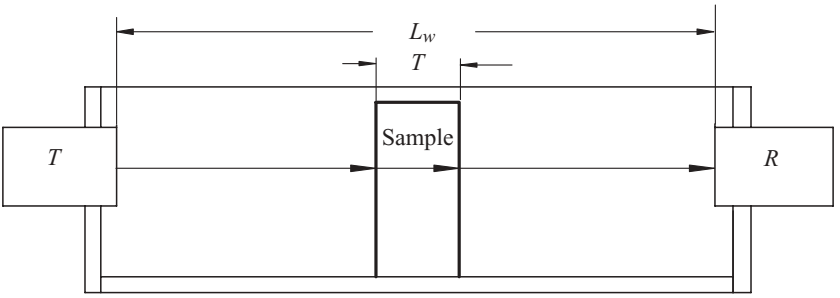

Figure 2.20 Setup for a wedge material velocity measurement by an immersion method.

the receiver, perpendicular to the sound path (line connecting two transducers). The new transit time that was measured with the sample in the tank is B μs.

Time *B* is less then time *A* due to the higher velocity in the wedge material sample.

Therefore, the transit time in the water and in the sample is

$$B = A - T/V_w + \tau_t \tag{2.23}$$

where τ_t is the transit time in the wedge material sample

$$\tau_t = \mathrm{B} - A + T/V_w \tag{2.24}$$

and the velocity in the sample is

$$V_t = T/\tau_t. \tag{2.25}$$

Another way of calculating the velocity after B was measured is

$$A - B = \Delta\tau \tag{2.26}$$

$$\Delta\tau = T/V_w - T/V_t. \tag{2.27}$$

Consequently, the velocity in the wedge material sample is

$$V_t = \frac{T}{\frac{T}{V_w} - \Delta\tau}. \tag{2.28}$$

For example, velocity measurement in a sample of Plexiglass 25 mm thick in an immersion tank with distance L_W = 100 mm:

$$A = \frac{Lw}{V_W} = \frac{100}{1.49} = 67.114\,\mu s.$$

Measured transit time B = 59.477 μs.
Thus,

$$\tau_t = B - A + \frac{T}{V_W} = 59.477 - 67.114 + \frac{25}{1.49} = 9.141\,\mu s$$

$$V_t = \frac{T}{\tau_t} = \frac{25}{9.141} = 2.735\,\text{mm}/\mu s.$$

In both cases of velocity measurement, the following tips are useful in enhancing its accuracy:

1. The test sample surfaces have to be machined as smooth as practically possible.
2. The TOF measurements have to be performed in the same way as shown in Section 2.2.3.
3. It is important to measure the TOF difference between the first and second multiples but not between the initial and first signals.

Attenuation Measurement in Wedge Materials

The discussions of attenuation usually begin with an introduction of the equation

$$P = P_0 e^{-\delta t} \tag{2.29}$$

where P = sound pressure at the end of distance t;
P_0 = sound pressure at the beginning of distance t;
e = Neper number; and
δ = coefficient of attenuation.

This equation demonstrates that the sound pressure decreases exponentially with the distance. Since the sound pressure is proportional to the signal amplitude A, this equation can be rewritten as

$$A = A_0 e^{\delta t} \tag{2.30}$$

where A_0 = signal amplitude (%) at the beginning of distance t and
A = signal amplitude (%) at the end of distance t.

To single out a coefficient of attenuation δ, certain calculations are necessary:

$$e^{-\delta t} = \frac{A}{A_0}$$

$$\frac{1}{e^{\delta t}} = \frac{A}{A_0}$$

$$e^{\delta t} = \frac{A_0}{A}.$$

It is easier to use the natural logarithm for this equation due to fact that $\ln e = 1$. Then:

$$\begin{aligned} \delta t \ln e &= \ln \frac{A_0}{A} \\ \delta t &= \ln \frac{A_0}{A} \\ \delta &= \frac{\ln \frac{A_0}{A}}{t}, \text{ Np/mm.} \end{aligned} \tag{2.31}$$

This equation was in use at a time when signal amplitude could be measured only in %, and the instrument attenuator was not calibrated in decibels. It is also not common to express the coefficient of attenuation in Np/mm. The decibel is a more appropriate unit to use. For this purpose, the last equation should be rewritten by using Briggs's logarithm:

$$\delta = \frac{20 \lg \frac{A_0}{A}}{t}, \text{ dB/mm.} \tag{2.32}$$

When it is necessary to convert the results calculated by using the natural logarithm into decibels, this can be accomplished by using the formula

$$\delta = \frac{\ln \frac{A_0}{A}}{t} 8.686, \text{ dB/mm.} \tag{2.33}$$

The number 8.686 is derived as follows:

$$\lg \frac{A_0}{A} = \frac{\ln \frac{A_0}{A}}{\ln 10}$$

$$\frac{1}{\ln 10} = 0.434$$

$$\lg \frac{A_0}{A} = 0.434 \ln \frac{A_0}{A}$$

$$20 \lg \frac{A_0}{A} = 20 \times 0.434 \ln \frac{A_0}{A} = 8.686 \ln \frac{A_0}{A}.$$

In modern ultrasonic instruments, the gain controls are calibrated in decibels, and therefore, it is much easier to calculate the coefficient of attenuation as

$$\delta = \frac{(A_0 - A)_{dB}}{t}, \text{ dB/mm} \tag{2.34}$$

where the difference $(A_0 - A)$ are measured in decibels.

The arithmetical exercise shown above helps to understand the nature of the coefficient of attenuation and can be used to recalculate the values from Np/mm to dB/mm when its value is taken from a table.

Thus, there are a total of four equations used to calculate the coefficient of attenuation:

$$\delta = \frac{\ln \frac{A_0}{A}}{t}, \text{ Np/mm}$$

$$\delta = \frac{20 \lg \frac{A_0}{A}}{t}, \text{ dB/mm}$$

$$\delta = \frac{\ln \frac{A_0}{A}}{t} 8.686, \text{ dB/mm}$$

$$\delta = \frac{(A_0 - A)_{dB}}{t}, \text{ dB/mm.}$$

Of course, all four equations will produce identical results. As an example, let us calculate the coefficient of attenuation for a sample of polystyrene with a wall thickness $t = 32$ mm, using all these equations. The measured signal amplitudes are $A_0 = 80\%$ and $A = 17\%$, and the difference in decibels between these two signals is 13.5 dB:

$$\delta = \frac{(A_0 - A)_{dB}}{t} = \frac{13.5}{2 \times 32} = 0.2109, \text{ dB/mm.}$$

Note that measurements of signal amplitude, in % or decibels, show the value of the apparent attenuation only. Actual attenuation measurements are difficult to perform because the value of the measured coefficient of attenuation generally includes also loss of the energy due to the beam divergence, losses at the transducer–test sample interface, losses caused by the test sample roughness, and others.

ASTM Standard Practice E 664/E664M-10 describes the procedure for the measurement of the apparent attenuation of longitudinal ultrasonic waves by immersion method. This practice describes a method of obtaining apparent attenuation values based on measuring the decay of multiple back reflection signals of ultrasonic energy introduced into a sample having flat, parallel surfaces by the immersion technique only. The procedure is suitable for materials with a relatively low attenuation.

In the case of measuring the coefficient of attenuation in wedge materials that have a relatively high attenuation, multiple back reflections are difficult to achieve. Therefore, it is more suitable to use a different procedure for measuring the coefficient of attenuation, the rational for which is described below.

In plastics like Plexiglas, Lucite, and polystyrene, as well as in other plastic materials, the coefficient of attenuation depends on the wave mode as well as on the frequency. Several publications offer contradictory statements about the influence of frequency on attenuation in plastics. Some sources claim that if attenuation is a matter of pure absorption, which is correct for homogeneous plastics, this

influence is proportional to the *square* of the frequency. Other sources claim that attenuation occurs proportionally to the frequency. It can be demonstrated that these assumptions are not completely correct.

Let us look at the results of coefficient of attenuation calculation using, for example, suggested procedure. The first stepped is to measure signal amplitudes in Plexiglas and polystyrene stepped samples (Figure 2.21) at selected frequencies, for example, 1.0, 2.25, 5.0, 10.0, and 15 MHz. These data are shown in Table 2.6 for the Plexiglas stepped sample and are obtained using straight beam L-wave transducers. The measurement procedure is as follows: The transducer is placed on the thinner step, with the gain adjusted to obtain the signal amplitude of approximately 100%.

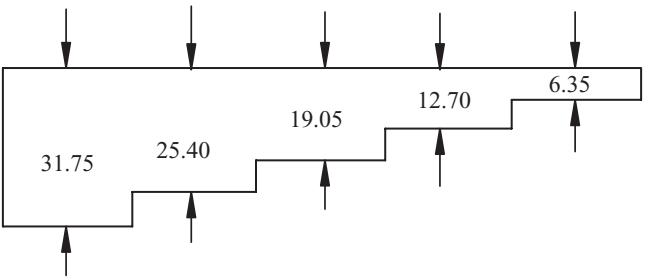

Figure 2.21 The step sample dimensions.

Table 2.6
Experimental Data of a Signal Amplitude *A*% Measured on the Plexiglas Step Sample

Step thickness, mm	Transducer nominal frequency, MHz at gain, dB (MHz/dB)				
	1.0/16	2.25/20	5.0/20	10.0/28	15/38
	Signal amplitude, *A*%				
6.35	120	120	104	106	100
12.70	94	77	56	30	28
19.05	70	48	28	8	7
25.40	48	28	13	2	—
31.75	31	16	5.5	—	—

Table 2.7
Calculated Coefficients of Relative Attenuation in dB/mm for the Plexiglas Step Sample

Step thickness	Transducer nominal frequency, MHz at gain, dB (MHz/dB)				
range, mm	1.0/16	2.25/20	5.0/20	10.0/28	15/38
	Coefficient of attenuation, δ dB/mm				
12.70–6.35	0.167	0.303	0.423	0.863	0.871
19.05–12.70	0.201	0.323	0.474	0.904	0.948
25.40–19.05	0.258	0.368	0.525	0.948	—
31.75–25.40	0.299	0.378	0.588	—	—

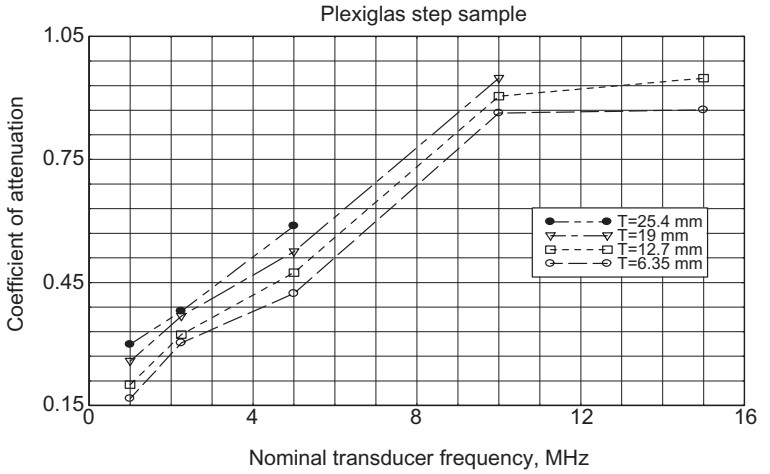

Figure 2.22 The nominal transducer frequency versus the coefficient of attenuation (Plexiglas step sample).

This procedure is repeated on each subsequent step. Then, for each pair of values (for example, 12.70–6.35 and 19.05–12.70.), the coefficients of relative attenuation in dB/mm should be calculated. As an example, the results of the calculations are summarized in Table 2.7.

Figures 2.22 and 2.23 were plotted using the coefficients of relative attenuation obtained on Plexiglas and polystyrene step samples: nominal

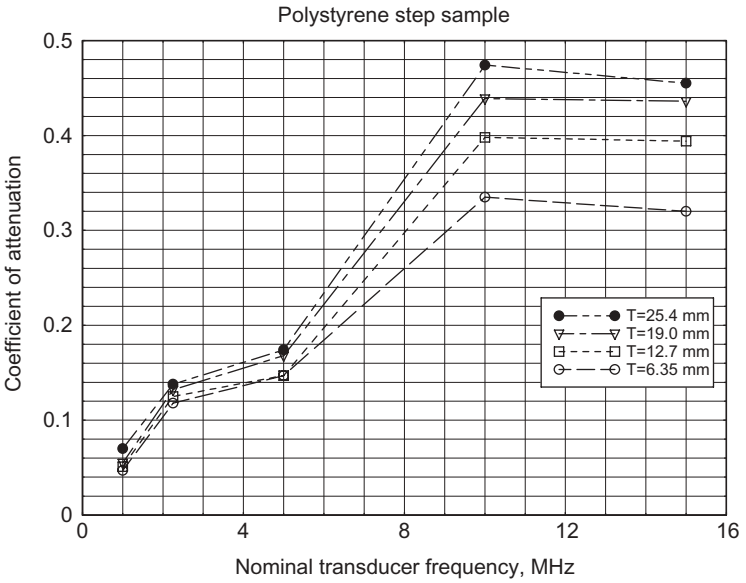

Figure 2.23 The nominal transducer frequency versus the coefficient of attenuation (Polystyrene step sample).

transducer frequency versus coefficients of relative attenuation for the thickness of each step in the samples. Analysis of the data, presented in these tables and figures, offers several useful suggestions.

First of all, it is interesting to note that for both plastics—Plexiglas and polystyrene—coefficients of relative attenuation for any step thickness in the samples leveled out at approximately 10 MHz. These plastics and many other materials are functioning as high-frequency filters. Therefore, the use of polystyrene, and especially Plexiglas, for wedges intended for a 15-MHz transducer is not recommended.

Plexiglas can be used as a material for wedges where the sound path is not more than 25 mm and for transducer frequencies up to 5.0 MHz. In any case, the sound path in the wedge material should be as short as possible. There is no sense in using polystyrene as a wedge material for low-frequency transducers like 1.0 and 2.25 MHz: The attenuation is too low, and therefore, it is difficult to eliminate wedge noise, not to mention the very low wear resistance of the polystyrene.

Attenuation of L-waves in plastics is less than it is for S-waves but not proportional to the wavelength. Thus, to recalculate the coefficient

of attenuation when using L-waves to the coefficient of attenuation for S-waves, using the ratio of the wavelengths is inappropriate. Experiments show, for example, that on a 25-mm thick sample, the ratio of attenuation for L-waves and S-waves is approximately 1:1.5 for both Plexiglas and polystyrene.

2.2.5. Crystal Size Selection

The basic parameters to consider are crystal size and shape, not to mention the crystal thickness, of course. For conventional ultrasonic inspection, three shapes are typically used: round (disk), square, and rectangular.

It is well known that for a given resonant frequency, the divergent characteristics of an acoustic field depend on the crystal size and shape. Theoretically, the divergent characteristic of a square crystal in the near field is slightly different from that of a disk. For a square crystal, the maximum and minimum amplitude fluctuations are less, and the side lobes are smaller than those of a round crystal. Practically, the differences are almost unnoticeable. In the case of rectangular crystals, these differences are more prominent. Furthermore, the length of the near field increases if the ratio of the crystal length to its width is more than 2:1. Beam spread in the plane of incidence and in the perpendicular plane is not equal. For elongated (rectangular) transducers (*paint brush probes*), the sensitivity along the long side is uneven. To equalize the sensitivity, special techniques, such as crystal shaping, have to be applied.

There is no practical solution for calculating the crystal size. Many variables are involved in the decision-making process relating to transducer parameters other than crystal size: for example, the sensitivity of the instrumentation, test object material attenuation, and reflectivity of defect models. Theoretically, there are ways to calculate the expected signal amplitude from models of the reflectors. Equations based on these parameters correlate signal amplitude with the reflector's size and shape, transducer to reflector distance, transducer frequency, and crystal size or area [47]; however, the practical applicability of such equations is very limited. Empirical and experimental data are needed to achieve meaningful results. To derive crystal size from these equations is impractical. The best guidance is practice. Some practical considerations for crystal size selection are given in the ASTM Standard Practices for Ultrasonic Examination:

1. ASTM E 114-10 Standard Practice states that *typical search unit sizes usually range from 1/8 in (3.2 mm) in diameter to 1 1/8 in (28.6 mm) in diameter.*
2. ASTM E 164-2008 Standard Practice recommends: . . . *Transducer sizes recommended for weld examination range from a minimum of 1/4 in. (6.4 mm) diameter or 1/4 in square to 1 in (25.4 mm) square or 1.1/8 in (28.6 mm) diameter.*

These recommendations reflect the practical tendency of applicability of crystal sizes in the NDT industry but do not correlate crystal sizes with crystal frequency. To connect these two parameters, another parameter can be used, that is, the product of the crystal diameter and frequency $d \times f$ [22]. In the case of a steel test object, it is recommended that the crystal size is selected so that this parameter should be in the range of $d \times f \approx 12.5$–125 mm·MHz. For more information, see Reference 23.

For selected crystal diameters and frequencies, these parameters are plotted in Figure 2.24, based on the data shown in Table 2.8.

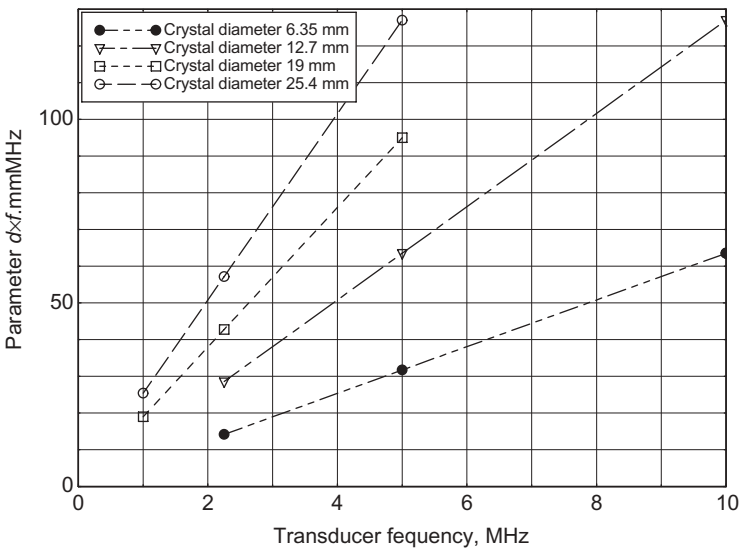

Figure 2.24 Transducer frequency versus parameter $d \times f$ for a steel test object.

Table 2.8
Parameter d × *f* for Selected Crystal Diameters

Crystal diameter, mm	Frequency, MHz			
	1.0	2.25	5.0	10.0
6.35	(6.35)	14.29	31.75	63.5
12.7	12.7	28.57	63.5	127
19.0	19.0	42.75	95.0	(190)
25.4	25.4	57.15	127	(254)

The data in parentheses show the $d \times f$ parameter values, which are not recommended for use. The rationale behind this recommendation is as follows:

1. It is not practical to make a transducer that is 6.35 mm in diameter with a frequency of 1.0 MHz due to the radial vibration mode increase with the crystal thickness, and therefore, energy losses of the thickness mode. Note that the radial vibration is very difficult to suppress.
2. It is also not practical to make a transducer that is 25.4 mm in diameter with a frequency of 10.0 MHz because of brittleness due to the relatively thin crystal and because of energy losses due to the possibility of flexural mode vibrations.

For several specific applications, the recommendations are

1. Probes intended for time of flight diffraction (TOFD) forward scattering techniques should have the smallest possible crystal size in the plane of incidence in order to increase the angle of beam divergence to cover larger portions of the test object thickness. The limitation here is sensitivity.
2. Crystal size in the plane of incidence for angle beam probes should be equal to or less than the thickness of the relatively thin wall test object.
3. Crystal size in the plane of incidence for probes intended to generate Lamb waves should be approximately three to five times larger than the thickness of the test object.

In case of crystal size selection for a relatively thin wall test object inspection, irrelevant signals and wedge noise can occur as a result of multiple signals from the same reflector.

Specification for technique development commonly includes a request to make an angle beam probe with a crystal size as large as possible in order to reduce the time needed for scanning. However, when the crystal size of the angle beam probe in the plane of incidence exceeds the test object wall thickness, confusing signals from a crack can appear. For example, the inspection of a 6.35-mm thick plate, using an angle beam probe with a crystal diameter $d = 12.7$ mm, produces three signals from a 3.0-mm deep notch, located on the opposite surface (Figure 2.25A). The reflections from the same-size notch, located on the scanning surface, are shown in Figure 2.25B. It would appear that the reflections are from three or two reflectors. The results can be interpreted as shown in Figure 2.26.

Usually, it is only one reflector that produces multiple signals due to multiple reflections. To avoid the phenomenon of multiple reflections from one reflector in this case, the crystal size in the plane of incidence should not exceed the wall thickness of a test object. The inspection of a 6.35-mm thick plate by using the angle beam probe with crystal

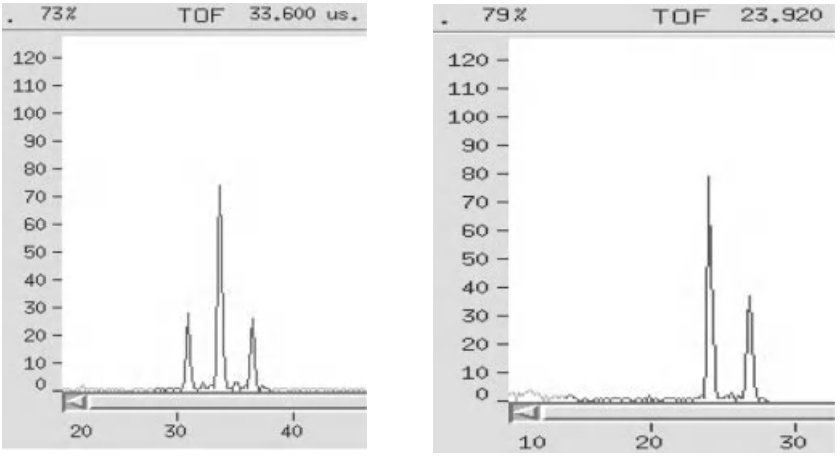

(A) (B)

Figure 2.25 Signals from 3.0 mm deep notch in a 6.35 mm thick plate. The crystal diameter d = 12.7 mm. (A) Signals on opposite surface; (B) signals on the scanning surface.

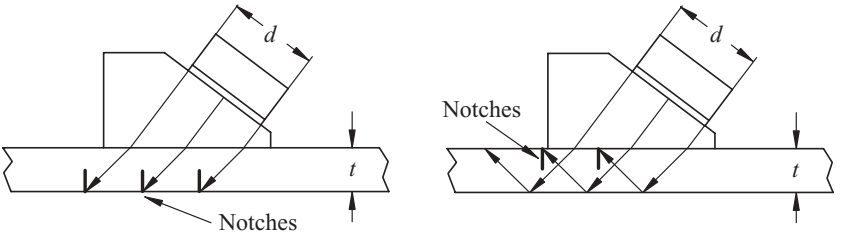

(A) (B)

Figure 2.26 Possible interpretation of the signals shown in Figure 2.25A, B. Notches located (A) on opposite surface; (B) on scanning surface.

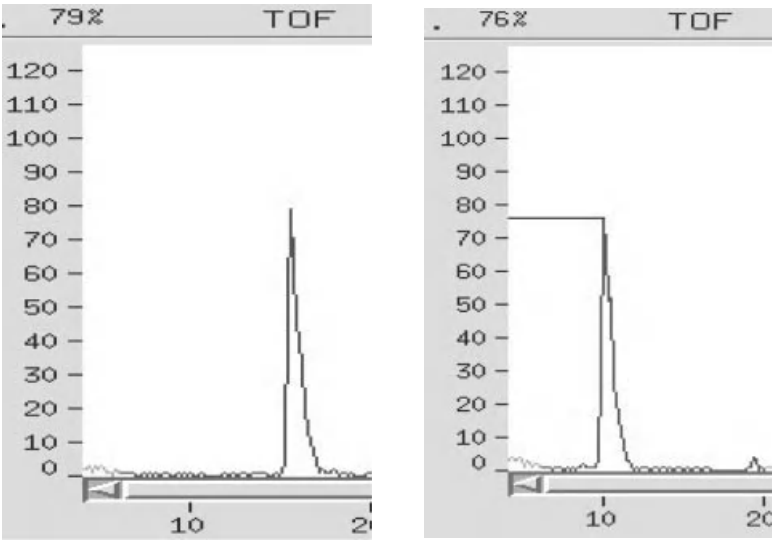

(A) (B)

Figure 2.27 Signals from a 3.0-mm deep notch in a 6.35-mm thick plate. The crystal diameter $d = 6.35$ mm. Notches located (A) on sopposite surface; (B) on scanning surface.

diameter $d = 6.35$ mm produces only one signal from the 3.0-mm deep notch, located on the opposite surface (Figure 2.27A) as well as on the scanning surface, as shown in Figure 2.27B.

Possible interpretation of signals and the ray tracing are shown in Figure 2.28.

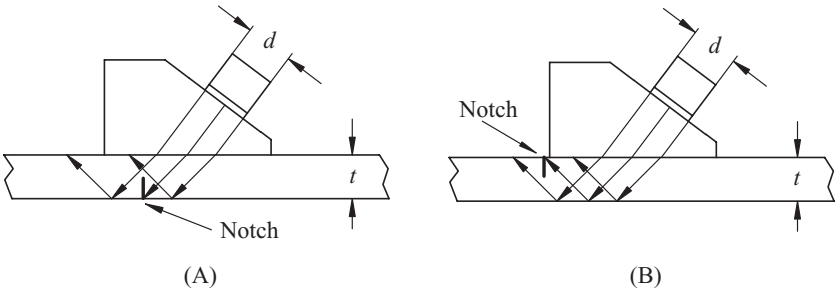

Figure 2.28 Example of a ray tracing in case when the crystal size is not exceeding the wall thickness.

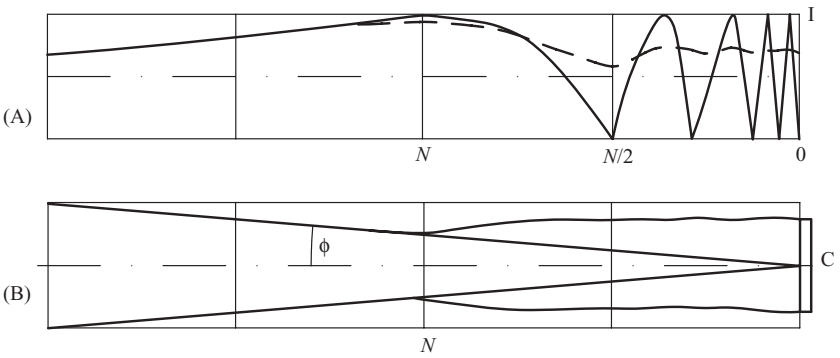

Figure 2.29 Acoustic intensity on the center axis of circular oscillator (A) and a sound field shape of the circular oscillator (B).

2.3. CALCULATION OF STRAIGHT BEAM TRANSDUCER DIRECTIONAL CHARACTERISTIC

2.3.1. Acoustic Field of a Straight Beam Transducer

In most of the literature dedicated to ultrasonic testing, one can find two common diagrams that illustrate the sound field of a circular piston oscillator [7]. These two diagrams that resemble this phenomenon are shown in Figure 2.29, with the exception of the dashed line shown in Figure 2.29A.

The above diagrams illustrate that there is a difference between when the sound field shape is close to the transducer crystal C and when it is far from it. Immediately in front of the transducer the field has a

cylindrical shape, but just barely beyond it, the picture is different: Maximum and minimum amplitudes of sound intensity appear (Figure 2.29A). The last minimum amplitude is located approximately at the distance $N/2$—half of the near-field length N. The last maximum is located at the distance N, which represents the border between the near and the far fields. If the crystal diameter is much greater than the wavelength, the near-field length can be approximately calculated as

$$N = \frac{S}{\pi\lambda} \tag{2.35}$$

where S is the crystal area and λ is the wavelength in a given medium.

In the far field, the ultrasonic energy propagates in the form of a cone with the angle of divergence ϕ.

It is important to note that this description of the sound field is correct only for continuous excitation and that these diagrams are based on and calculated in accordance with theoretical data. The main discrepancy between the theory and reality applies to the description of the near field. The fluctuation of intensity (signal amplitude) in the near field depends on the pulse length and the pulse repetition rate: The shorter the pulse and the higher the pulse rate, the less the fluctuations in intensity. In practice, the amplitude fluctuation from zero to maximum is not observed. The dashed line shown in Figure 2.29A represents experimentally observed fluctuations.

Nevertheless, many references do not recommend inspecting test objects in the near field. The reason for this is that a defect can be missed due to fluctuations of signal amplitude from zero to maximum. In many cases, the requirement to inspect the test object, especially thin objects, only in the far field leads to more complicated and larger scanning systems.

At the same time, there is the other possibility to misinterpret the inspection results in the near field, which is clear from analyzing the image of the sound field.

To visualize the sound field structure of an ultrasonic transducer in water, the field can be scanned using a small ball or a thin wire reflector as a target. The C-scan of the sound field structure of a 19 mm diameter 2.25 MHz transducer is shown in Figure 2.30. The sound intensity at the section $N/2$ (≈60 mm) is shown schematically in Figure 2.31.

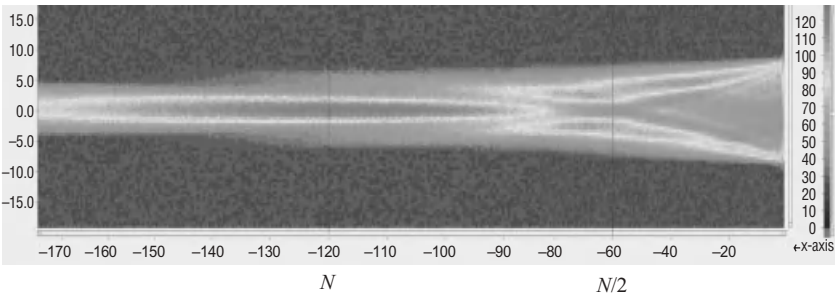

Figure 2.30 The field structure of the 19 mm diameter 2.25 MHz transducer.

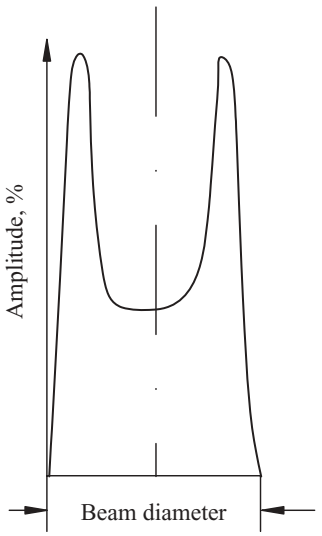

Figure 2.31 Graphical representation of the signal amplitudes in the section *N*/2.

The C-scan in Figure 2.30 shows that the near-field distance is approximately $N = 120$ mm. At the distance $N/2$, half of the near field at the beam axis, there is a zone of low amplitude, approximately 45%. On both sides of this there are zones of higher amplitudes 100–110% (see Figure 2.31).

If a small reflector is detected in the low-intensity zone, an error could occur. Let us assume that a small reflector is detected in the low-amplitude zone at the beam central axis. The transducer is then indexed

left and right (shown as up and down in Figure 2.30), and the same reflector produces a signal with an amplitude of 100–110%. If a defect evaluation is based on signal amplitude, two rejectable indications would be apparent.

2.3.2. Angle of Divergence Calculation

The beam parameters in the far field can be calculated using well-known equations.

For practical purposes, to calculate probe beam spread that is represented by a half angle of divergence, the following formula can be used:

$$\varphi = \arcsin K \frac{\lambda}{d} \tag{2.36}$$

or

$$\varphi = \arcsin K \frac{V}{d \times f} \tag{2.37}$$

where λ = wavelength, mm;

f = frequency, MHz;

d = crystal diameter, mm;

V = sound velocity, mm/μs; and

K = coefficient related to dB level for a free or reflected fields.

Let us calculate angles of divergence for a straight beam transducer in water and steel for a free field. The transducer parameters are

diameter d = 25.4 mm;

frequency f = 2.25 MHz;

velocity in water V_W = 1.49 mm/μs;

velocity of L-wave in steel V_{SL} = 5.85 mm/μs; and

velocity of S-wave in steel V_{SS} = 3.23 mm/μs.

Coefficient K can be found in tables for the most common cases of −3, −6, and −12 dB levels. For the free field on the level of −6 dB coefficient K = 0.7:

$$\varphi = \arcsin 0.7\frac{1.49}{25.4\times 2.25} = 1.046^\circ$$
$$\varphi = \arcsin 0.7\frac{3.23}{25.4\times 2.25} = 2.27^\circ \quad .$$
$$\varphi = \arcsin 0.7\frac{5.85}{25.4\times 2.25} = 4.11^\circ$$

Beam spread plots of calculated half angles of divergence are shown in Figure 2.32, I. The plot of the beam spread gives very limited description of a real acoustic field created by a search unit. It shows only the direction of the central ray at the angle of divergence.

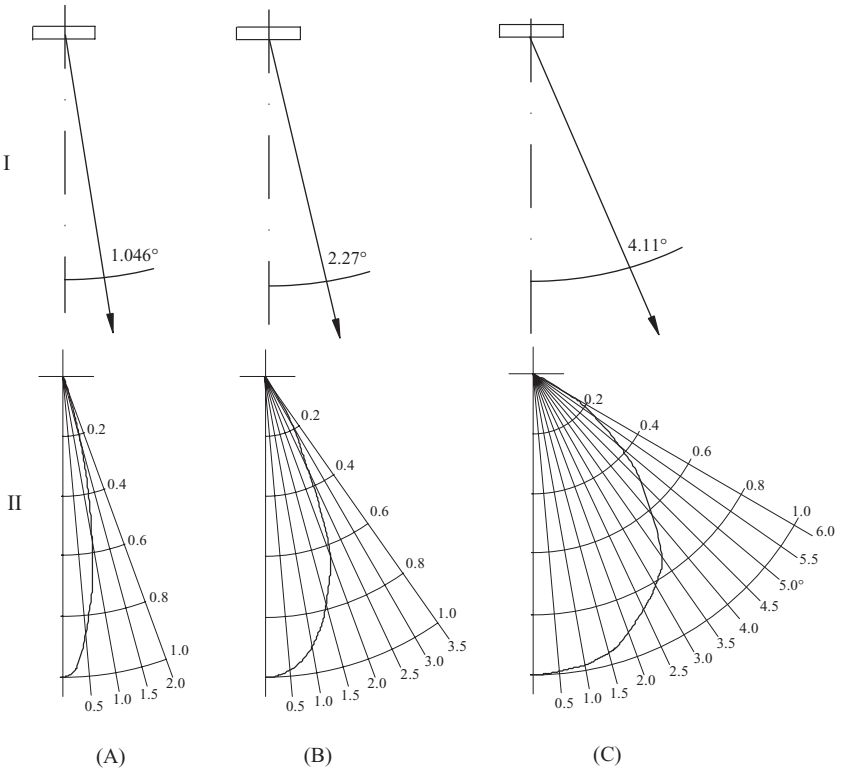

Figure 2.32 The beam spread plots at −6 dB level (I) and the main lobe shapes (II). (A) L-wave in water, (B) S-wave in steel, (C) is L-wave in steel. S-wave, shear wave; L-wave, longitudinal wave.

2.3.3. Main Lobe Profile Calculation of a Round Crystal in Far Field

A more realistic picture of an acoustic field is given by a plot of a search unit's directional characteristic, or at least a plot of its main lobe. In many cases of probe design, the plot of the main lobe gives additional information for the comparison of probes of different frequencies, wave modes, crystal shape, and size.

For a directional characteristic calculation of a round crystal in the far field, the following equation is used:

$$\Phi(\varphi) = \frac{2J_1(x)}{x} \tag{2.38}$$

where

$$x = \frac{\pi d}{\lambda}\sin\varphi$$

$$\lambda = \frac{V}{f}.$$

$J_1(x)$ is the Bessel function of the first kind of zero order taken from mathematical tables, for example, CRC Standard Mathematical Tables.

As an example, the calculation of the main lobe in steel for S-wave straight beam transducer diameter of 25.4 mm and a frequency of 2.25 MHz are shown below. For the sake of convenience and representation, the sequence of the calculation is presented in the form of a table (Table 2.9).

The calculation of the main lobe is chosen only because it contains approximately 85% of a crystal's energy. But if it is necessary to calculate side lobes, this can be done by using the same equation.

For a comparison of the lobe's shapes for S-wave in steel, the calculations were performed for L-wave in steel and in water.

Based on these calculations, three plots are presented in polar coordinates in Figure 2.32, II. Since each plot is symmetrical, only the right side (one-half) of the directional characteristics is shown for each plot. To make the plot more readable, the scale for angle of divergence is shown as 5 to 1.

Table 2.9
Transducer Ø = 25.4 mm, f = 2.25 MHz, S-wave in Steel λ_S = 1.435 mm, $\pi d/\lambda_S$ = 55.579

φ	sin φ	x	$J_1(x)$	$\Phi_{(\varphi)}$
0.25	0.00436	0.2424	0.0995	0.995
0.75	0.01309	0.7725	0.3572	0.9248
1.00	0.01745	1.0299	0.5491	1.00
1.25	0.02181	1.2122	0.5008	0.8263
1.5	0.02618	1.4551	0.510	0.7010
1.75	0.03054	1.6974	0.5778	0.6808
2.00	0.0349	1.9397	0.5799	0.5979
2.20	0.03838	2.1331	0.5390	0.5053
2.25	0.03929	2.1837	0.4587	0.4201
2.50	0.04362	2.4244	0.4158	0.3430
2.75	0.0480	2.6678	0.4507	0.3378
3.00	0.05233	2.9084	0.3719	0.2557
3.50	0.06105	3.3931	0.2876	0.1695
3.83	0.03838	3.7121	0.005	0.0026
4.00	0.06976	3.8772	–0.0193	–0.0099

The plot for S-wave in steel is presented also in Cartesian coordinates (Figure 2.33A). This provides an easier way to calculate the coefficient K for any dB level.

2.3.4. Coefficient *K* Calculation at Any Decibel Level

Let us calculate coefficient K for 0 dB and for –6 dB levels for a free field.

The first zero on the plot, which represents the boundary of the main lobe, has a value of $x_0 = 3.83$. Therefore,

$$\varphi_0 = \arcsin\frac{3.83\lambda}{\pi d} = 1.219\frac{\lambda}{d}.$$

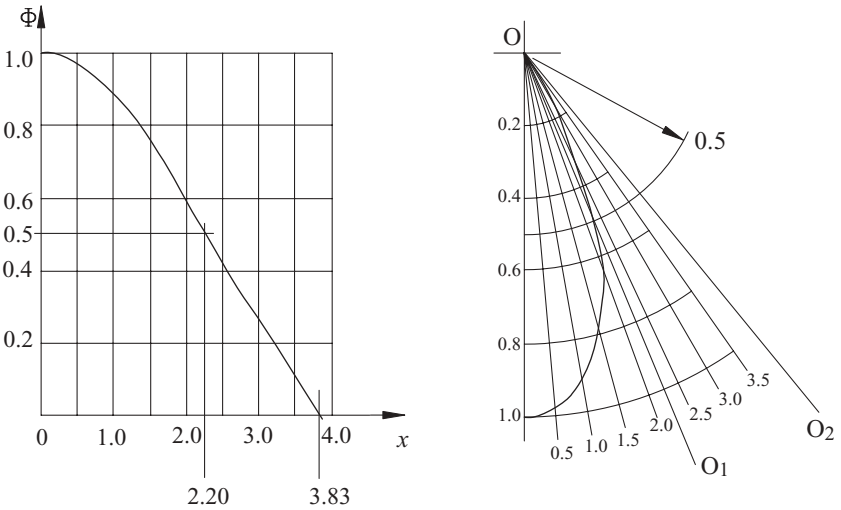

Figure 2.33 Example of coefficient *K* calculation. (A) Cartesian and (B) polar coordinates.

For –6 dB level or 50% of the maximum, the value for $x_0 = 2.20$ and

$$\varphi_{50} = \arcsin\frac{2.20\lambda}{\pi d} = 0.70\frac{\lambda}{d}.$$

On the right side of Figure 2.33B (plot in polar coordinates), the line $O–O_2$ represents the boundary of the main lobe (maximum angle of divergence), and the line $O–O_1$ represents the boundary at the –6 dB level. Coefficient *K* can be calculated the same way for any level of decibel. In actuality, the real shape of a straight beam transducer's directional characteristic, and, especially, angle beam probe, is more complicated.

CHAPTER 3

Single Angle Beam Probe Design

3.1. BASICS OF PROBE DESIGN

The wedge angle for a single crystal angle beam probe can be calculated as a first approximation, by using Snell's law, if the desired refracted angle is known. However, Snell's law is correct only for planar waves and for the frequency of light.

It is worth mentioning the purpose of the calculation. A wedge angle is calculated, assuming that the maximum signal amplitude from a reflector will be located at a predetermined refracted angle, that is, it will be measured at the central ray of the main lobe. However, empirically obtained results often differ from those obtained from the calculations using Snell's law. Generally, the actual refracted shear wave (S-wave) angle β is less than β_{sn} as calculated by Snell's law (Figure 3.1). This phenomenon was theoretically explained by exact solution of the acoustic field of an angle beam probe [4, 24]. As an example, the shape of the calculated main lobe in the plane of incidence, depicted in the polar coordinates, is shown in Figure 3.1.

Ultrasonic Inspection Technology Development and Search Unit Design: Examples of Practical Applications, First Edition. Mark V. Brook.

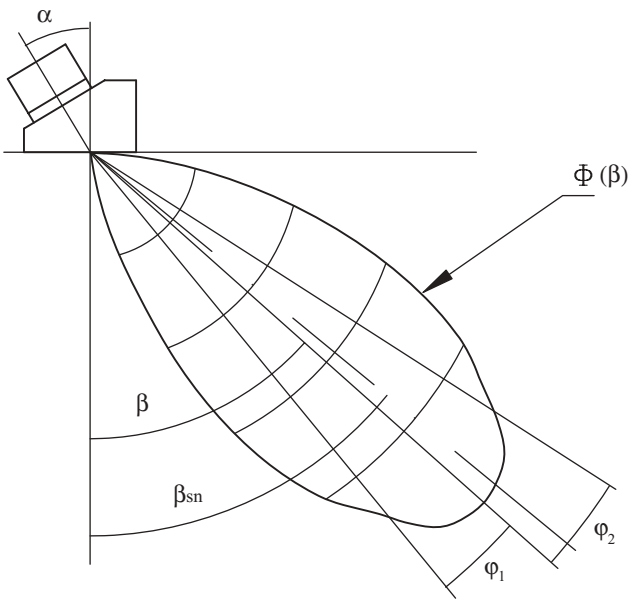

Figure 3.1 A main lobe's idealistic shape of shear wave in the plane of incidence.

The parameters of a main lobe, including the refracted angle, are known as divergent characteristics. These parameters, as examples for S-wave, can be described as

$$\Phi_{(\beta)} = \Phi_{0(\beta)} D_{ls(\beta)} \Phi_{1(\beta)} \tag{3.1}$$

where $\Phi_{(\beta)}$ = the divergent characteristic of S-wave probe in the plain of incidence;

$\Phi_{0(\beta)}$ = the main function;

$\Phi_{1(\beta)}$ = the secondary (correction) function; and

$D_{ls(\beta)}$ = the transmission coefficient on the wedge–metal interface.

Expanding this equation will result in complicated formulas, which are not suitable for practical, "everyday" applications for wedge design. But analysis of the formulas shows that the main lobe directivity deteriorates with the increase of the wedge angle and the decrease in the frequency and the crystal diameter. It leads to a deviation of the lobe's central ray, which confirms the experimental results. It also shows that

the main lobe is not symmetrical. The angle φ_1 is less than φ_2 (Figure 3.1).

3.2. CONSIDERATIONS RELATED TO THE PRACTICAL CONCEPT OF WEDGE DESIGN

One of the considerations is connected to the concept of the imaginary crystal. This idea was developed to simplify the calculation of the divergent characteristics in the test object by substituting a portion of the wedge material with a test object material. The diagram presenting this concept is shown in Figure 3.2. The wedge 2 with the crystal assembly 1 is located on the test object. The real crystal diameter is *d*. The crystal assembly is located at distance 1 from the wedge exit point. The goal is to calculate the diameter of the imaginary crystal 3 and its distance from the exit point l_1.

For the purpose of practical calculation and visual presentation, the real shape of the main lobe can be schematically replaced with a cone, with angle γ's (made up from two angles, φ_1 and φ_2) apex located at the imaginary crystal's center. The angle of the cone should be

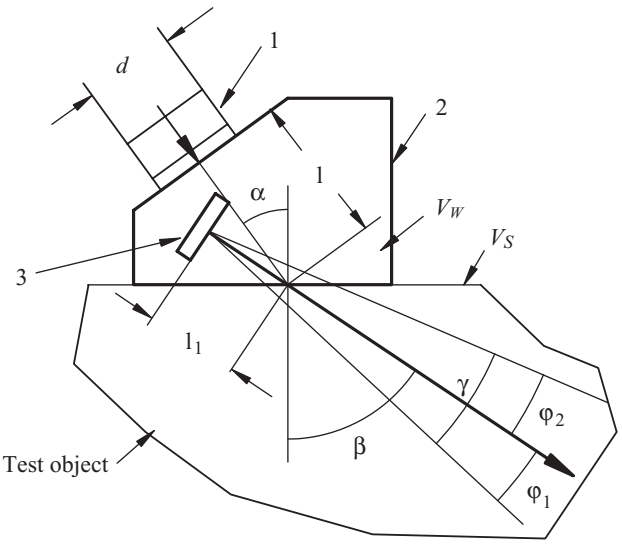

Figure 3.2 An imaginary crystal position in a wedge.

calculated for a given decibel level. The angle β is equal to the refracted angle of the main lobe.

The imaginary crystal size d_1 and its new distance from the exit point l_1 can be calculated as follows:

$$d_1 = d\frac{\cos\beta}{\cos\alpha} \tag{3.2}$$

$$l_1 = l\frac{V_W \times \cos\beta}{V_S \times \cos\alpha} \tag{3.3}$$

where V_W is the longitudinal wave (L-wave) velocity in the wedge material and V_S is the S-wave velocity in the test object material.

Thus, the portion l_1 of the wedge material was replaced by the test object material.

The other consideration is connected to the correction of the refracted angle. The most frequently used zone of refracted S-wave angle is the zone between the first and the second critical angles. Refracted angles calculated by Snell's law should be adjusted by correcting the wedge angle α.

The corrected angle depends on the frequency and the size of the transducer's crystal. The basic factor influencing this dependence is the coefficient of transmission of ultrasonic energy through the interfaces, that is, the wedge–couplant–metal. Each of the rays in the divergent ultrasonic beam has its own coefficient of transmission. For the Plexiglas–steel boundary, the coefficient of transmission for the refracted L-wave and S-wave is a function of the angle of incidence of the L-wave, which is shown in Figure 3.3.

Between the first cr_1 and the second cr_2 critical angles, the coefficient of transmission is maximized at the angles of incidence $\alpha_{max} \approx 31–32°$. When the ultrasonic beam propagates through the Plexiglas–steel interface, the rays located further from the maximum on either side will have a lower coefficient of transmission. For probes with wedge angles greater than α_{max}, the experimental refracted angle β, corresponding to the maximum energy or signal amplitude, will be less than β_{sn} as calculated in accordance with Snell's law. For a probe having a wedge angle less than α_{max}, the experimental refracted angle will be greater. The angle of deviation $\Delta = |\beta - \beta_{sn}|$ will increase with the decreasing frequency f and the crystal size d. Conversely, with the increase of the $d \times f$ parameter, that is, the narrowing of the directional characteristic,

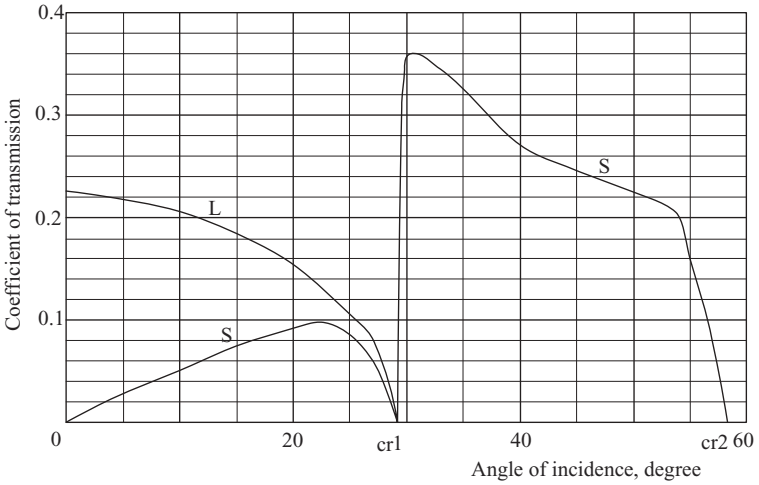

Figure 3.3 Coefficient of transmission for the Plexiglas–steel boundary (for illustration only).

this effect will be less. Graphically, for the sake of simplicity, this trend is depicted in Figure 3.4.

3.3. MEASUREMENT OF REFRACTED ANGLES

The $d \times f$ parameter describes only the deviation tendency of the refracted angle. To determine the value of the deviation, it is practical to measure these values for several of the most common sizes, angles, and frequencies of probes, and then to extrapolate these data to other probe parameters. To obtain reliable measurement results, the following conditions should be met:

1. The sound velocity in the wedge material has to be measured correctly.
2. The exit point of the wedge has to be determined.
3. The measurements have to be performed on the same test block.

The *sound velocity* in the wedge material is a major factor for the wedge angle calculation, and it is very important to measure it correctly, as shown in Section 2.2.

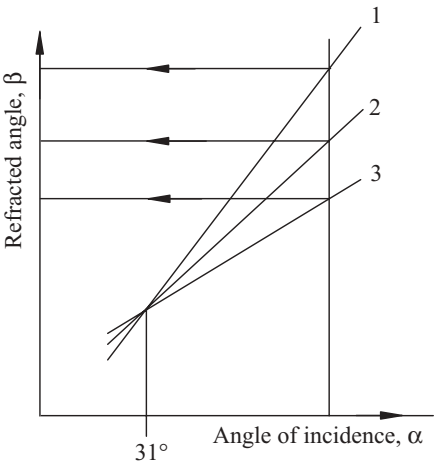

Figure 3.4 Overall trend of an experimental refracted angle deviation from the calculated angle by Snell's law (line 1). For lines 2 and 3: $d \times f\,(2) > d \times f\,(3)$.

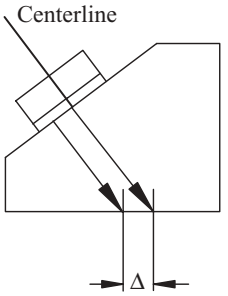

Figure 3.5 The exit point deviation Δ of an angle beam probe.

The *exit point* of any angle beam wedge is not necessarily located on the central line of the transducer or crystal assembly (Figure 3.5).

Deviation of the exit point, or the index, depends on the wedge angle, crystal size, and transducer frequency, and generally shifts to the lower end of the wedge. This happens mostly due to the wedge material attenuation.

As an example of the deviation of the probe's exit point, the measured indexes on the probe with a 70°S refracted angle are presented in Figure 3.6. The geometrical center point of the transducer on the wedge

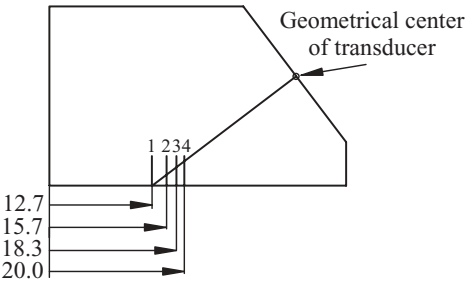

Figure 3.6 Deviation of the exit points. Exit point positions: (1) Calculated, (2) for 1.0 MHz transducer, (3) for 2.25 MHz transducer, (4) for 5.0 MHz transducer.

and its central ray line should be determined graphically from the wedge drawing. The graphically calculated index in this case is 12.7 mm. Indexes measured for three transducers with frequencies 1.0, 2.25, and 5.0 MHz are shown in the same figure. As expected, the actual indexes do not coincide with the predicted (theoretical) index. The higher the transducer frequency, the greater the deviation of the exit point.

Of course, this example (Figure 3.6) is one of the worst cases due to the steep wedge angle and the long wave path (approximately 37 mm). This is shown here as a visual illustration. However, this phenomenon is relevant to any wedge.

The International Institute of Welding's *IIW Reference Block* is most usable for transducer exit point and refracted angle measurements. The main problem with these blocks, fabricated according to old specification, such as ISO 2400, is the inconsistency in the material characteristics. It has been found that the sound velocity and attenuation in the metal used may vary significantly even in blocks fabricated by the same manufacturer (see Section 11.2.1). Thus, the measurement should be performed using the same block.

Results of refracted angle measurements on the same block in graphical form are shown in Figure 3.7 along with the calculated line, according to Snell's law. This is for a transducer 9.5 mm in diameter and for three frequencies: 5.0, 2.25, and 1.0 MHz.

One can see that the lower the frequency and the higher the refracted angle, the greater the deviation from the nominal (calculated) parameters. Graphs like this can be used to calculate corrections for a wedge angle.

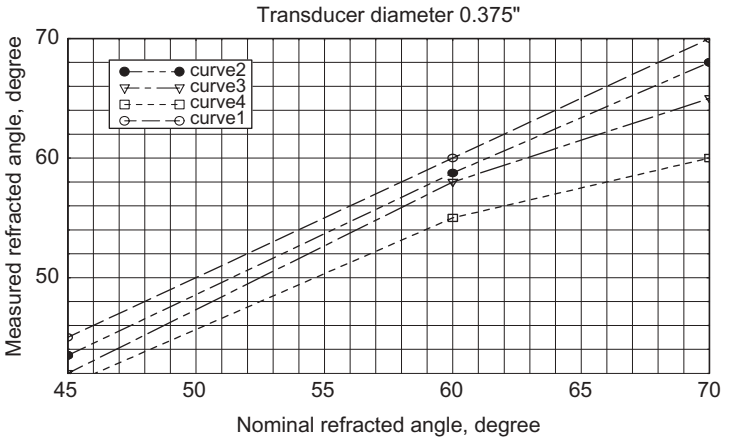

Curve no.		1	2	3	4
Transducer frequency, MHz	Calculated by Snell's law		5.0	2.25	1.0

Figure 3.7 Measured versus nominal refracted angle for the transducer diameter 9.5 mm.

A graph showing the angle of incidence versus the refracted angle, calculated according to Snell's law, can also be used for wedge angle correction. As an example, calculating the deviation angle for a nominal refracted angle of a 70°S, 2.25 MHz, 12.7 mm diameter transducer can be seen plotted on the graph in Figure 3.8: The measured refracted angle is 66°; the difference between calculated and measured angles is –4°. The difference in the incident angle is 2.0°.

The angles of incidence, based on experimental data and the calculations, are summarized in Table 3.1 for probes with refracted angles 45°S, 60°S, and 70°S.

The wedge material is Plexiglas with an average velocity V_{av} = 2.735 mm/μs +/– 0.005 mm/μs. The S-wave velocity in the test sample is 3.24 mm/μs +/– 0.02 mm/μs.

All these measurements should be performed using the same IIW Reference Block Type 1 or 2 or other test blocks with the reflector at a fixed depth. For refracted angles from 35° to 60°, the reflector, usually a side-drilled hole (SDH), has to be located at a depth of approximately

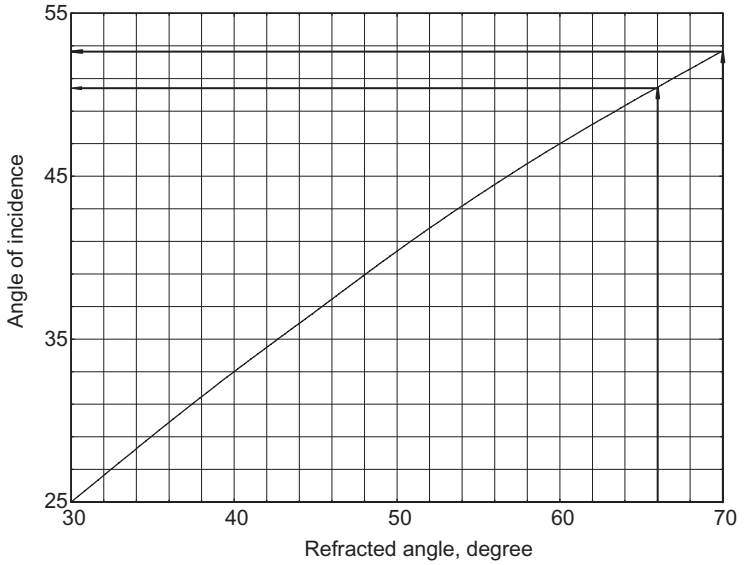

Figure 3.8 Example of the graph using angle of incidence correction.

50 mm, but for the refracted angle of 70°, this depth should not exceed 20 mm.

3.4. DEVIATION OF REFRACTED ANGLE RELATED TO THICK WALL TEST OBJECT INSPECTION

A wedge angle correction is especially important for test objects with wall thicknesses greater than approximately 100 mm. As shown earlier, the measured deviations of refracted angles are influenced by two factors: $d \times f$ parameter and deviation of the wedge exit point. Practically, it is almost impossible to separate their influences.

The previous section contains the explanation for the deviation of the experimental refracted angle from the calculated angle according to Snell's law. This phenomenon is correct for reflectors located at any depth. The reference or test blocks have reflectors for refracted angle measurement located at a specified depth. But if the measurement is performed using a reflector located at a depth other than in the test block, a different value of the refracted angle will be obtained. It is

Table 3.1
Experimental Angles of Incidence

f, MHz	1.0			1.5			2.25			5.0		
β°	45	60	70	45	60	70	45	60	70	45	60	70
	Angles of incidence calculated according to Snell's law											
	36.5	47	52.5	36.5	47	52.5	36.5	47	52.5	36.5	47	52.5
	Experimental angles of incidence											
6.35 mm	38.5	49	56	38.25	48.75	55.5	38	48.5	55	37.75	48.25	54
12.7 mm	38.25	48.75	55	38	48.5	54.75	37.75	48.25	54	37	48	53
25.4 mm	37.5	48	54.25	37.25	47.75	54	37	47.5	53.5	36.75	47	52.5

especially true for reflectors (SDH) located at depths more than 75–100 mm. In this case, the following phenomenon is observed.

Let us assume that the maximum signal amplitude from the reflector located at a depth h_1 will be achieved at the probe position 1 (Figure 3.9). It is more likely that the SDH at this depth will reflect the beam central ray at the refracted angle β_1. For the reflector located at the depth $h_2 > h_1$, the maximum signal amplitude will be achieved at the probe position 2. It is more likely that this SDH will reflect the beam rays located at the smaller refracted angle $\beta_2 < \beta_1$.

The explanation for this phenomenon is as follows. In an ultrasonic field, represented by the main lobe (Figure 3.10), the intensity of rays in the direction and at the distance r_1 is less than in the direction and the distance r, which is the central ray of the lobe. But the attenuation for the distance r_1 is less than for the distance r. So, the loss in intensity is less than the loss in attenuation. If a reflector is placed at point 1, the reflected energy from it, as well as the signal amplitude, will be larger than from the reflector positioned in point 2.

When reflectors are located at relatively shallow depths, the differences between attenuation and intensity losses are negligible. But for a longer distance, this effect is significant.

In nuclear power plants, where test objects have wall thicknesses up to 250 mm, the effect of this phenomenon is noticeable. During calibration and beam spread measurements, the refracted angle β_3 is

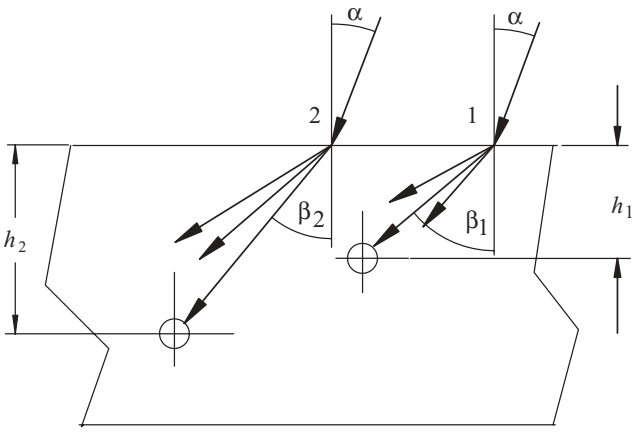

Figure 3.9 Refracted angles of rays as a function of the reflector depth.

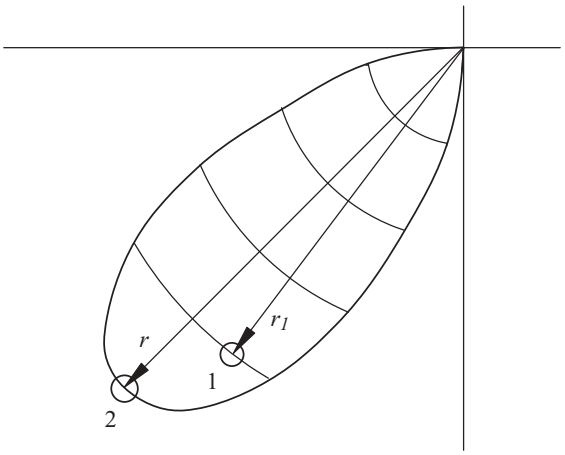

Figure 3.10 Possible position of reflectors in the main lobe.

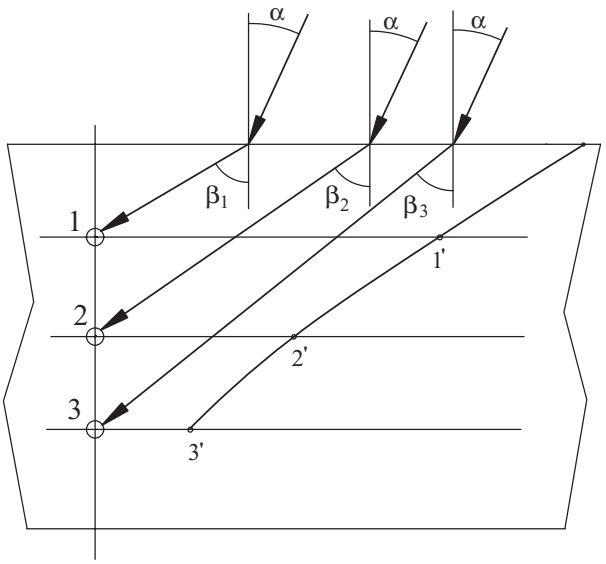

Figure 3.11 Refracted angles and quasi-bent central ray 1′, 2′, 3′.

less than β_2, and β_2 is less than β_1 (Figure 3.11). When the measured data are plotted, the line, connecting the three points1′, 2′, and 3′, becomes curved instead of straight. This creates an impression of a bent central ray of the lobe, which in reality is a quasi-bend.

CHAPTER 4

Dual Straight and Angle Beam Probe Design

4.1. PRINCIPLES OF DUAL STRAIGHT BEAM PROBE DESIGN

The main purpose of using a dual straight beam probe is to eliminate the dead zone, which is typical for single crystal straight beam transducers. Dual straight beam probes are mainly used for measuring wall thickness (corrosion mapping), for detecting and depth measuring of internal flaws close to the inspection surface.

These probes can also be used for concentrating an ultrasonic energy practically at any distance beyond the dead zone and even further than the near field.

The probe contains two identical sections: One is a transmitter *T* and the other is a receiver *R* (Figure 4.1).

The principles of a wedge design for the dual straight beam probes are almost the same as for the angle beam probes. The only difference is in defining the refracted angle. For dual probes, refracted longitudinal waves (L-waves) are used in most cases. The L-wave refracted angle should not exceed approximately 12–14° to avoid generating a strong

Ultrasonic Inspection Technology Development and Search Unit Design: Examples of Practical Applications, First Edition. Mark V. Brook.

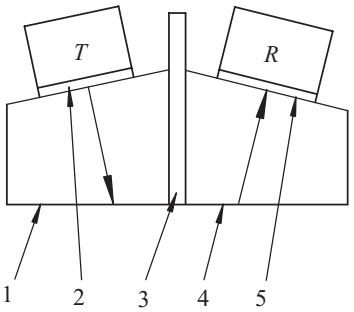

Figure 4.1 Conceptual design of a dual straight beam probe. 1, a transmitter wedge; 2, and 5, crystal assemblies; 3, electric and acoustic insulator; and 4, receiver wedge.

refracted shear wave (S-wave). But if generating a strong refracted S-wave is not a problem, the L-wave refracted angle can be as high as 20–22°, that is, less than the first critical angle.

4.2. SEQUENCE OF WEDGE CALCULATION

The two important parameters to consider (see Figure 4.2A) are the depth t of the central ray's intersection with the central line of the probe, which approximately determines the point of maximum signal amplitude, and distance c, which hereafter will influence the crystal size. As a rule, the crystal size d should be not greater then $2c$.

The exact acoustic field parameters can be defined by calculating the directional characteristics for both the transmitter and the receiver. For everyday calculations, it is sufficient to perform geometrical calculations for only one of the sections, either the transmitter or the receiver, and substitute the main lobe with the angle of divergence at the level of −6 dB or other specified decibel levels. This geometrical calculation is easier to perform by using the concept of an imaginary crystal for the transmitter and the receiver. The sequence of calculation is as follows:

the refracted L-wave angle β_l:

$$\beta_l = \arctan\frac{c}{t}; \tag{4.1}$$

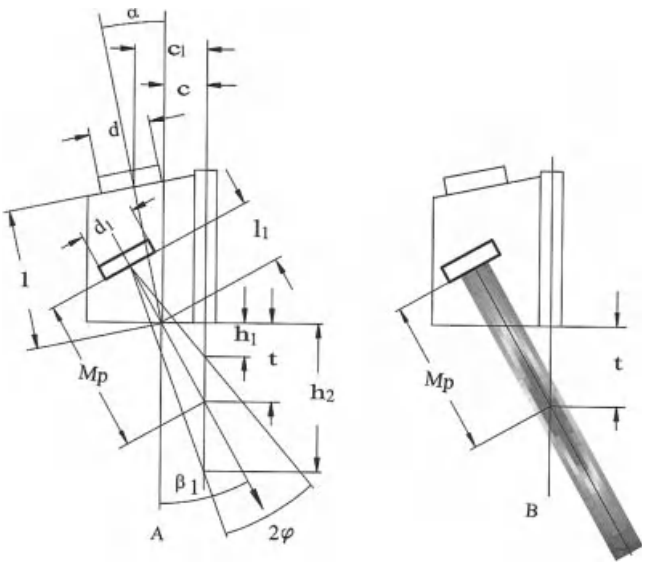

Figure 4.2 A dual straight beam probe wedge: (A) a schema of calculation, (B) position of the near field.

the angle of incidence α:

$$\alpha = \arcsin\left(\sin\beta_l \frac{V_W}{V_L}\right) \tag{4.2}$$

where V_W is the L-wave velocity in the wedge material, mm/μs

V_L is the L-wave velocity in the test object material, mm/μs;

the refracted S-wave angle

$$\beta_s = \arcsin\left(\sin\alpha \frac{V_S}{V_W}\right) \tag{4.3}$$

where V_S is the S-wave velocity in the test object material, mm/μs;

the diameter of the imaginary crystal d_1

$$d_1 = d\cos(\beta_l - \alpha); \tag{4.4}$$

the angle of divergence φ at a level of –6 dB

$$\varphi = \arcsin K \frac{V_L}{f \times d_1}; \tag{4.5}$$

the distance l_1 from the imaginary crystal to the test object surface

$$l_1 = l \frac{V_W}{V_L} \cos(\beta_l - \alpha) \tag{4.6}$$

where l is the height of the wedge center line;

the crystal position c_1

$$c_1 = c + l \times \sin\alpha; \tag{4.7}$$

the minimum depth of measurement h_1 at the level of –6 dB

$$h_1 = \frac{c_1}{\tan(\beta_l + \varphi)} - l_1 \cos\beta; \tag{4.8}$$

the maximum depth of measurement h_2

$$h_2 = \frac{c_1}{\tan(\beta_l - \varphi)} - l_1 \cos\beta; \text{ and} \tag{4.9}$$

the range of measurement $h_3 = h_2 - h_1$.

This calculation gives good results if

$$\beta_l < 22°;$$

$$\varphi < 10°;$$

$$c > 3.0 \text{ mm; and}$$

$$f \geq 2.25 \text{ MHz.}$$

One of the variations of dual straight beam probes is a probe without a wedge angle. This design may be preferable in some "unusual" cases, (for example, for the inspection of a test object with a concave surface). The conceptual design of this probe is shown in Figure 4.3.

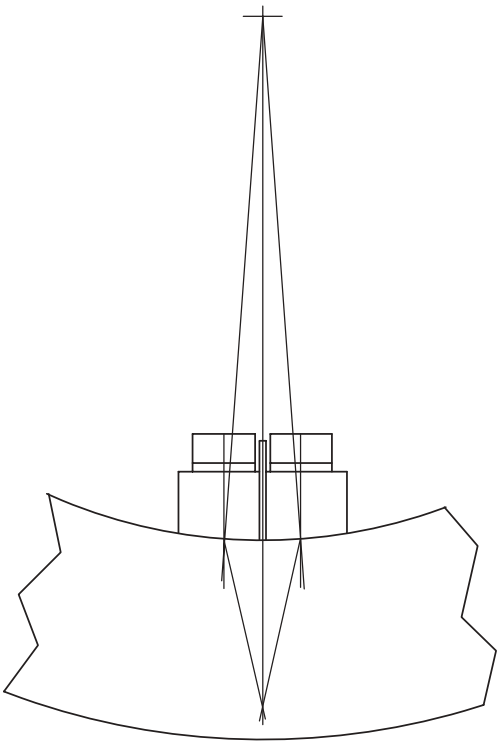

Figure 4.3 An example of conceptual design of a dual straight beam probe for a test object with a concave surface.

4.3. SENSITIVITY CURVES

The performance of the dual straight beam probes can be characterized by their sensitivity curves. These curves are constructed experimentally and plotted as the signal amplitude versus the depth of a reflector. The apogee of the curve corresponds with the point of the acoustic field's maximum energy reflected from a reflector at a given depth. The shorter the distance of the central ray's intersection ("focus"), the "sharper" the sensitivity curve. It is one of the drawbacks of dual probes. As an example, the sensitivity curve for the probe with a "focus" equal to 10 mm is shown in Figure 4.4. The dream of a probe designer is to equalize the probe sensitivity at a relatively long distance.

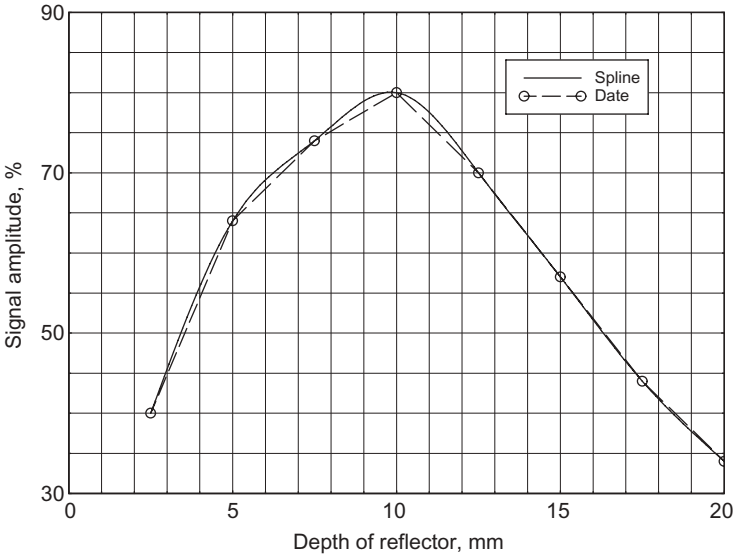

Figure 4.4 Sensitivity curve for the "focal" distance 10 mm.

4.4. EXAMPLE OF DUAL STRAIGHT BEAM PROBE DESIGN

The following parameters for a probe design are given (Figure 4.2A):

- t = 12.7 mm—depth of the central ray's intersection;
- c = 3.2 mm—distance from the centerline of the probe to the exit point; and
- d = 6.35 mm—crystal diameter.

The refracted L-wave angle β_l is

$$\beta_l = \arctan\frac{c}{t} = \arctan\frac{3.2}{12.7} = 14°.$$

The angle of incidence α is

$$\alpha = \arcsin\left(\sin\beta_l \frac{V_W}{V_L}\right) = \arcsin\left(\sin 14\frac{2.735}{5.85}\right) = 6.5°.$$

The diameter of imaginary crystal d_1 is

$$d_1 = d\cos(\beta_l - \alpha) = 6.35 \times \cos(14 - 6.5) = 6.3 \text{ mm}.$$

The angle of divergence φ at a level of –6 dB is

$$\varphi = \arcsin K\frac{V_L}{f \times d_1} = \arcsin 0.7\frac{5.85}{5 \times 6.3} = 7.5°.$$

Distance l_1 from the imaginary crystal to the test surface is

$$l_1 = l\frac{V_W}{V_L}\cos(\beta - \alpha) = 9\frac{2.735}{5.85}\cos(14 - 6.50) = 4.1 \text{ mm}$$

where l is the height of the wedge center line.

Crystal position c_1 is

$$c_1 = c + l \times \sin\alpha = 3.2 + 9 \times \sin 6.5 = 4.2 \text{ mm}.$$

The minimum depth of measurement h_1 at the level of –6 dB is

$$h_1 = \frac{c_1}{\tan(\beta_l + \varphi)} - l_1\cos\beta = \frac{4.2}{\tan(14 + 7.5)} - 4.1 \times \cos 14 = 6.7 \text{ mm}.$$

The maximum depth of measurement h_2 is

$$h_2 = \frac{c_1}{\tan(\beta_l - \varphi)} - l_1\cos\beta_l = \frac{4.2}{\tan(14 - 7.5)} - 4.1 \times \cos 14 = 32.8 \text{ mm}.$$

The range of measurements h_3 is

$$h_3 = h_2 - h_1 = 32.8 - 6.7 = 26.1 \text{ mm}.$$

It is a good practice, in some cases when the maximum possible signal amplitude from a given reflector has to be achieved, to verify the transmitter near field length relative to the metal path.

The metal path for the given example of the probe design is

$$Mp = l_1 + \frac{t}{\cos\beta_1} = 4.1 + \frac{12.7}{\cos 14} = 17.19 \text{ mm}.$$

The near field length for the crystal diameter 6.35 mm and the frequency 5.0 MHz is

$$N = \frac{d^2}{4\lambda} = \frac{6.35^2}{4 \times 1.17} = 8.62 \text{ mm}$$

where $\lambda = 1.17$ mm in steel for 5.0 MHz frequency.

The near field length is almost two times shorter than the metal path. This shows that the design of the probe is not optimized. If the near field length is equal to the metal path, one can expect that the gain can be drastically reduced to obtain the same signal amplitude from a given reflector. There are two options to equalize these parameters: to increase the frequency or to increase the crystal diameter.

Let us increase the frequency to 7.5 MHz with the same crystal diameter

$$N = \frac{6.35^2}{4 \times 0.78} = 12.92 \text{ mm}$$

where $\lambda = 0.78$ mm in steel for 7.5 MHz frequency.

This is better but not quite enough. Let us increase the crystal diameter to 9.5 mm with the same frequency of 5.0 MHz:

$$N = \frac{9.5^2}{4 \times 1.17} = 19.29 \text{ mm.}$$

This near field length is almost equal to the metal path. This position of the near field relative to the metal path is shown in Figure 4.2B.

Thus, the best performance of the probe will be achieved by using a 9.5-mm crystal diameter, but the original probe design was made for the crystal diameter 6.35 mm. The probe has to be recalculated until the metal pass and the near field are in a desirable agreement.

An example of the probe design is shown in Figure 4.5. The housing 3 contains wedges 1 with two crystal assemblies 2. The wedges are separated by an acoustic and an electrical insulator 8. Tubing 4 inserted in the fitting 5 supplies couplant liquid to the probe footprint. On the top of the housing is the cover 7 with two connectors 6.

The experimental sensitivity curves for dual straight beam probes designed for different depths F of the central ray's intersection are shown in Figure 4.6.

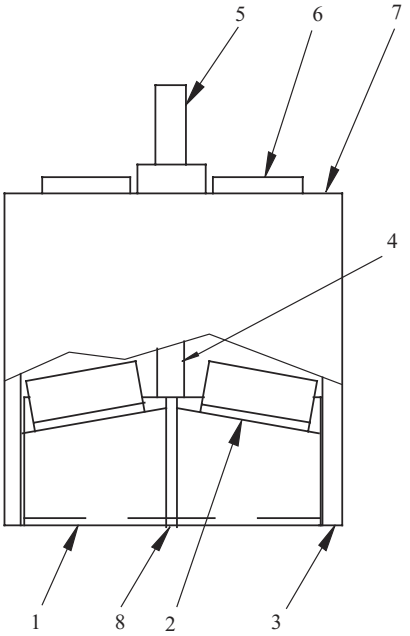

Figure 4.5 Example of a dual straight beam probe design.

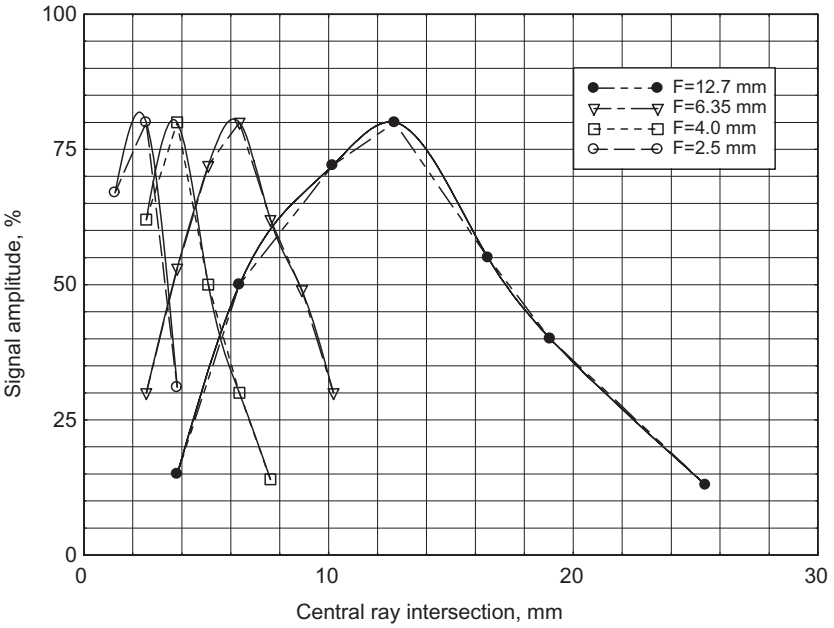

Figure 4.6 Central ray intersection distance vs. signal amplitude (sensitivity curves).

4.5. BASICS OF DUAL ANGLE BEAM PROBE DESIGN

The dual angle beam probes are used for refracted S-wave or L-wave generation in test objects. These probes are also suitable for "creeping" and other specific wave generation when the wedge angle is equal or close to the first critical angle.

The dual angle beam probe contains two wedges with transducers: a transmitter and a receiver. There are two possibilities to arrange wedges for dual angle beam probes: by using either a skew angle δ or a "roof" angle γ. Figure 4.7 shows these arrangements. If arrangement

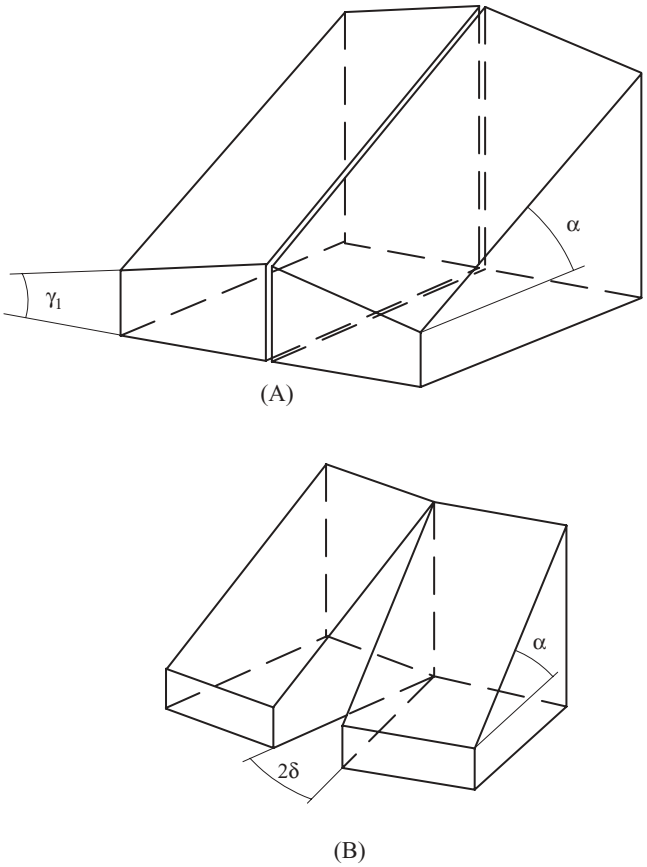

Figure 4.7 Wedge arrangement of a dual angle beam probe: (A) using a "roof" angle, (B) using a skew angle.

B is chosen, only the skew angle δ should be calculated and wedges with the angle of the incidence α should be rotated at this skew angle. If arrangement A is chosen, the angle of incidence α has to be corrected and the "roof" angle γ calculated.

4.6. WEDGE CONCEPTUAL DESIGN

In both cases of the design, using either the skew or the "roof" angles, the intention is to direct the refracted beam central ray from point ***o*** to point ***c*** (Figure 4.8). The first possibility (Figure 4.8A) is to rotate both wedges with the angle of incidence α on a skew angle δ around point ***o*** in order to make the wedge angle plane o_1-a_1-o-d_1 coincide with the required refracted angle plane *o-a-c-d*. Thus, the refracted beam center ray will lie in the plane *o-a-c-d*. In this case, each wedge will have only a single wedge angle, but all of its sides have to be machined at the same skew angle δ to make the wedges suitable for assembly in the smallest possible size of housing. In any case, the wedges itself and the probe will be larger than in the wedge design with the "roof" angle.

The second possibility is to make the wedges with a compound angle: the wedge angle α and the "roof" angle γ (Figure 4.8B). This

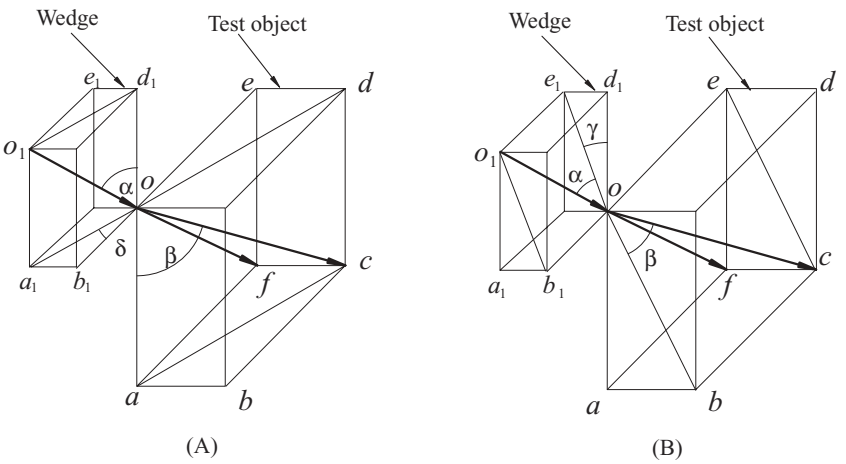

Figure 4.8 Two conceptual designs of a dual angle beam probe.

design is more compact. In this case, the wedge surface at angle α has to be inclined on angle γ. The refracted beam center ray will lay in the plane *o-b-c-e*.

The sketches that are shown in Figure 4.8 represent only the transmitter wedges of the probes and the refracted beam in the material of a test object. The rectangle o_1-a_1-b_1-*o*-d_1-e_1 shown in both sketches is the left wedge, and the rectangle *o-a-b-c-d-e-f* corresponds to a portion of the test object.

4.7. WEDGE DESIGN FOR INSPECTION OF A TEST OBJECT WITH FLAT AND PARALLEL SURFACES

The schema of calculation is shown in Figure 4.9, where

T is the wedge transmitter;

R is the wedge receiver;

t is the depth of the refracted beams' intersection or thickness of the test object;

α_1 is the angle of incidence in the central plane A;

α is the angle of incidence in the plane B;

β_1 is a refracted angle in the central plane A;

β is a refracted angle in the plane B;

δ is the skew angle;

c is the distance between the exit point of the transmitter (or receiver) and the center line of the probe; and

γ is the "roof" angle.

Let us consider the case of a rectangular transducer, the footprint of which is shown in Figure 4.10. This kind of transducer is common for phased array probes.

The purpose of a dual angle beam wedge calculation is to determine its acoustic and geometric parameters for a given refracted angle and the transducer to be used.

Before the calculation can be performed, several probe parameters, along with the test object data, must be specified, such as (Figures 4.9–4.11):

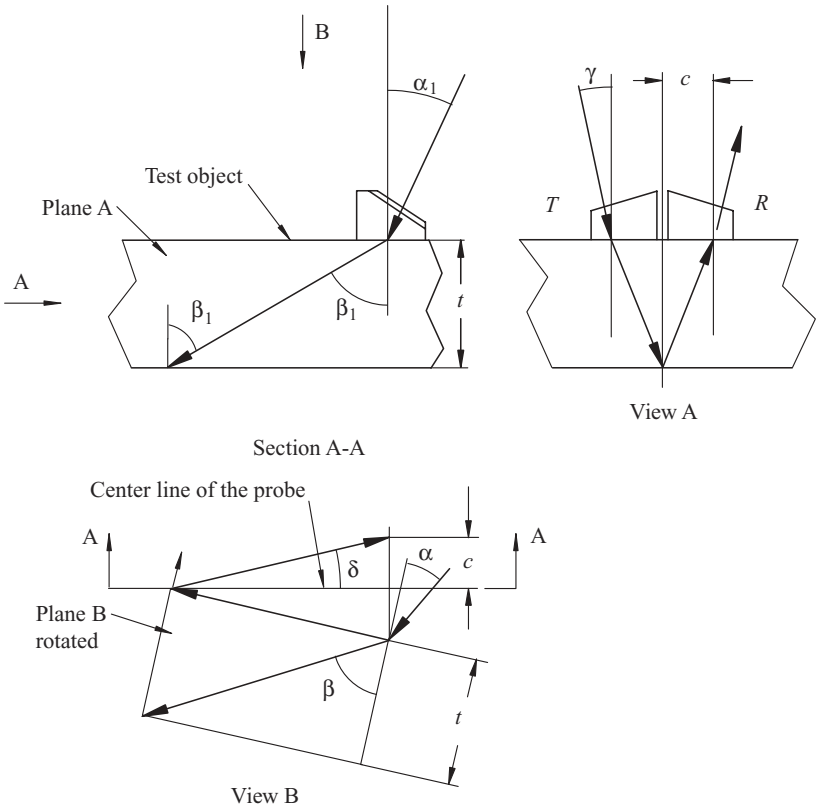

Figure 4.9 Diagram related to the calculation of a dual angle beam probe.

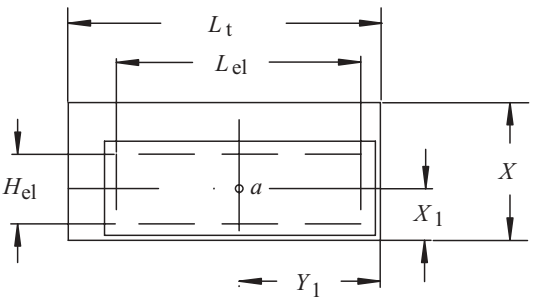

Figure 4.10 Foot print of a phased array transducer.

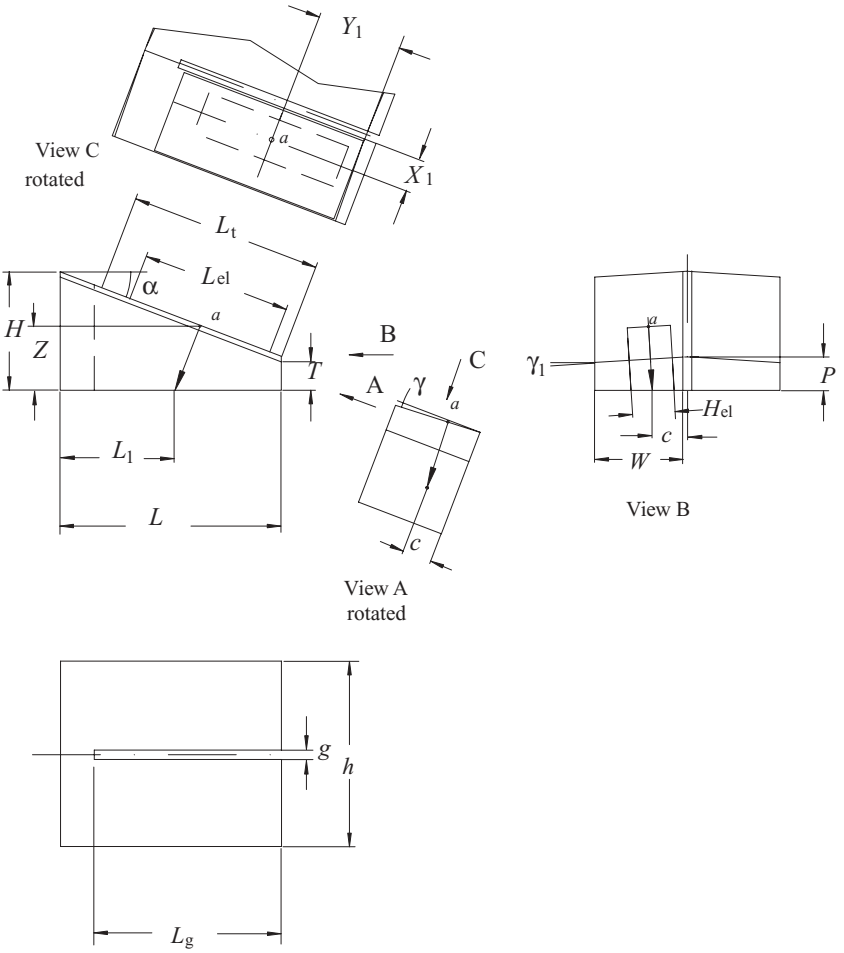

Figure 4.11 Geometrical parameters of the wedge with a flat footprint.

sound velocity in wedge material V_W;
sound velocity in test material V_M;
transducer length L_t;
transducer width X;
element length L_{el};
element width H_{el};
coordinates of the element center (point "a") X_1 and Y_1; and
one of the wedge dimension, for example, T.

The following are the wedge parameters to be determined (Figure 4.9):

the refracted angle β in the plane B,
the angle of incidence α in the plane B, and
the skew δ and "roof" γ angle.

4.7.1. The Wedge Calculation for the Inspection of Test Objects with Flat and Parallel Surfaces

Distance c between the centerline of the probe and the exit point should be chosen as $c \geq X_1$.

The skew angle δ is

$$\delta = \arctan \frac{c}{t \times \tan \beta_1}. \tag{4.10}$$

The skew refracted angle is

$$\beta = \arctan\left(\frac{\tan \beta_1}{\cos \delta}\right). \tag{4.11}$$

The angle of incidence is

$$\alpha = \arcsin\left(\sin \beta \frac{V_W}{V_M}\right). \tag{4.12}$$

The "roof "angle is

$$\gamma = \arctan(\sin \alpha \times \tan \delta). \tag{4.13}$$

The "roof "angle in view B (Figure 4.11) is

$$\gamma_1 = \arctan\left(\frac{\tan \gamma}{\cos \alpha}\right). \tag{4.14}$$

The geometric parameters of the wedge can be calculated as follows:

$$P = W \times \tan \gamma_1 + T \tag{4.15}$$

where $W \geq X$,

$$L = \frac{L_t}{\cos \alpha} + P \times \tan \alpha + n \tag{4.16}$$

where L_t is the length of the transducer.

n is an addition to the wedge length (0.25 ÷ 0.30 in.) as a space for refracted central ray deviation and couplant delivery system, if it is necessary:

$$\begin{aligned} H &= L \times \sin\alpha + P \\ L_g &= L_t \times \cos\alpha \\ h &= 2W + g \end{aligned} \qquad (4.17)$$

where g is the thickness of the acoustic insulator

$$Z = P \pm \left[(Y_1 \times \sin\alpha \pm X_1 \times \sin\gamma)\cos\alpha \right]. \qquad (4.18)$$

The distance between the front edge of the wedge and the exit point is

$$L_1 \cong L - \left(Z \times \tan\alpha + \frac{L_t}{2\cos\alpha} \right). \qquad (4.19)$$

To verify dimension "c,"

$$c = \frac{W}{2} - Z \times \tan\gamma. \qquad (4.20)$$

4.8. WEDGE DESIGN FOR THE INSPECTION OF A TEST OBJECT WITH A CURVED SURFACE

4.8.1. Wedge Calculation for the Inspection of a Test Object with Concentric Surfaces

The Case of Axial Direction of Beam Propagation

The wedge designed for the inspection of the test object with the flat and parallel surfaces cannot be used for the inspection of the test objects with concentric surfaces only by countering the wedge according to the pipe diameter, due to the fact that the desired directions of the central ray will be changed.

Figure 4.12 shows the roof angle γ and the central ray in the plane B (Figure 4.9) calculated for inspection of a test object with a flat surface, and the desirable distance T of the central ray's intersection at point o. In this example, the distance T is equal to the wall thickness. If this wedge will be contoured for a pipe with a certain radius and the same wall thickness T, and the pipe's central angle $\varphi = \gamma$, there will be no beam "refraction" in the test object due to the roof angle. The central

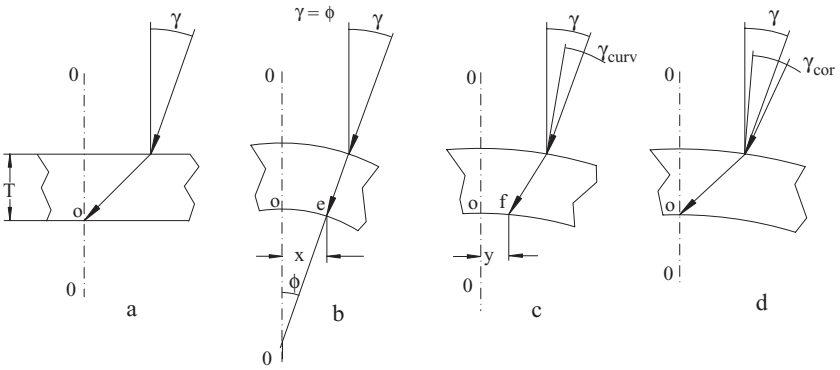

Figure 4.12 Sketches related to wedge design for test objects with concentric surfaces.

ray's intersection will be at distance x (Figure 4.12B). The second possibility of beam redirection will occur if the wedge will be contoured for a pipe with a certain radius and the roof angle for this curvature γ_{curv} will be less than γ. In this case also the distance central ray's intersection will be at distance y (Figure 4.12C).

Thus, the roof angle should be corrected (γ_{cor}) to direct central ray's intersection to point o (Figure 4.12D). To correct the roof angle, one has to calculate parameter Δh and then angle ϕ for given R (Figure 4.13):

$$\Delta h = R\left[1 - \cos\left(\arcsin\frac{W}{R}\right)\right] \tag{4.20}$$

$$c_c = c + \Delta h \times \tan\gamma \tag{4.21}$$

$$\phi = \arcsin\frac{c_c}{R} \tag{4.14}$$

So, the corrected roof angle is

$$\gamma_c = \gamma + \varphi \tag{4.15}$$

The Case of Circumferential Direction of Beam Propagation

For pipe inspection with dual angle beam probes, the sequence of calculations is different. In the previous case (testing of an object with flat and parallel surfaces), the angle of attack is equal to the refracted angle. In the case of testing pipes, the angle of attack β_a is not equal to the

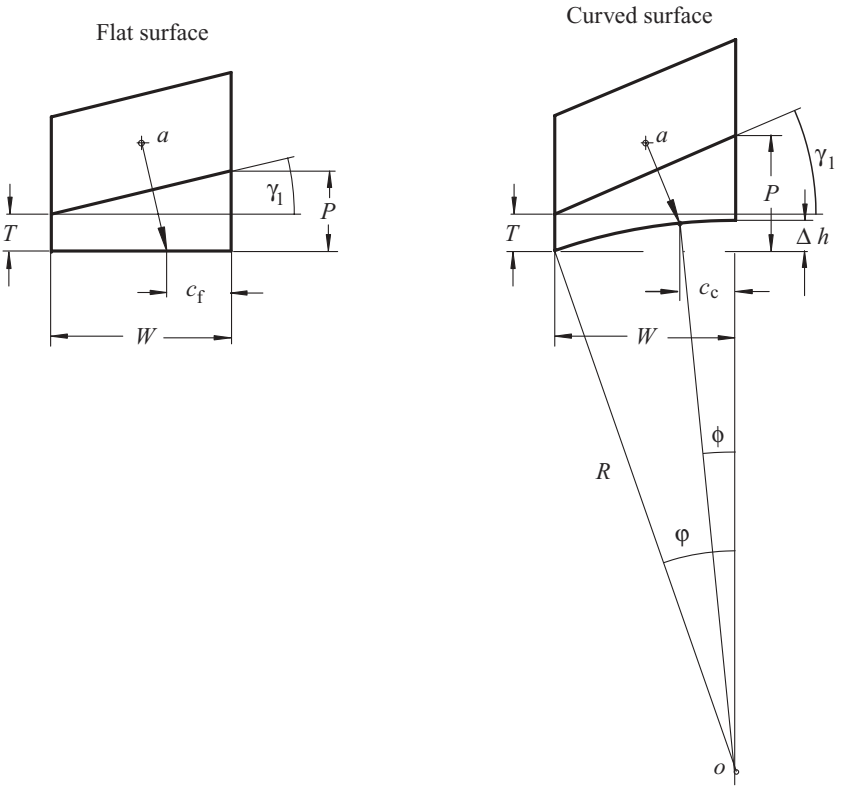

Figure 4.13 Diagrams related to wedge calculation for test objects with concentric surfaces.

refracted angle β_1 (Figure 4.14). So, assuming that the angle of attack is known, the values to be calculated are the refracted angle, and then the angle of incidence, the skew, and the "roof" angle. Figure 4.14 (view C) shows positions of the exit points of the transmitter *T* and the receiver *R* on the outer pipe surface. Section A-A is the plane of the transmitter refracted angle central ray propagation. The pipe section by inclined plane is an ellipse. Its small axis b is equal to the pipe outside radius *R* and its larger axis is $\boldsymbol{a} = R/\sin\delta$. The angle of incidence, and then the roof angle, can be calculated at first approximation, as follows. Let us assume that the transducer exit point O_2 on the ellipse and O_3 on the cylinder surfaces are coincident (Figure 4.14,

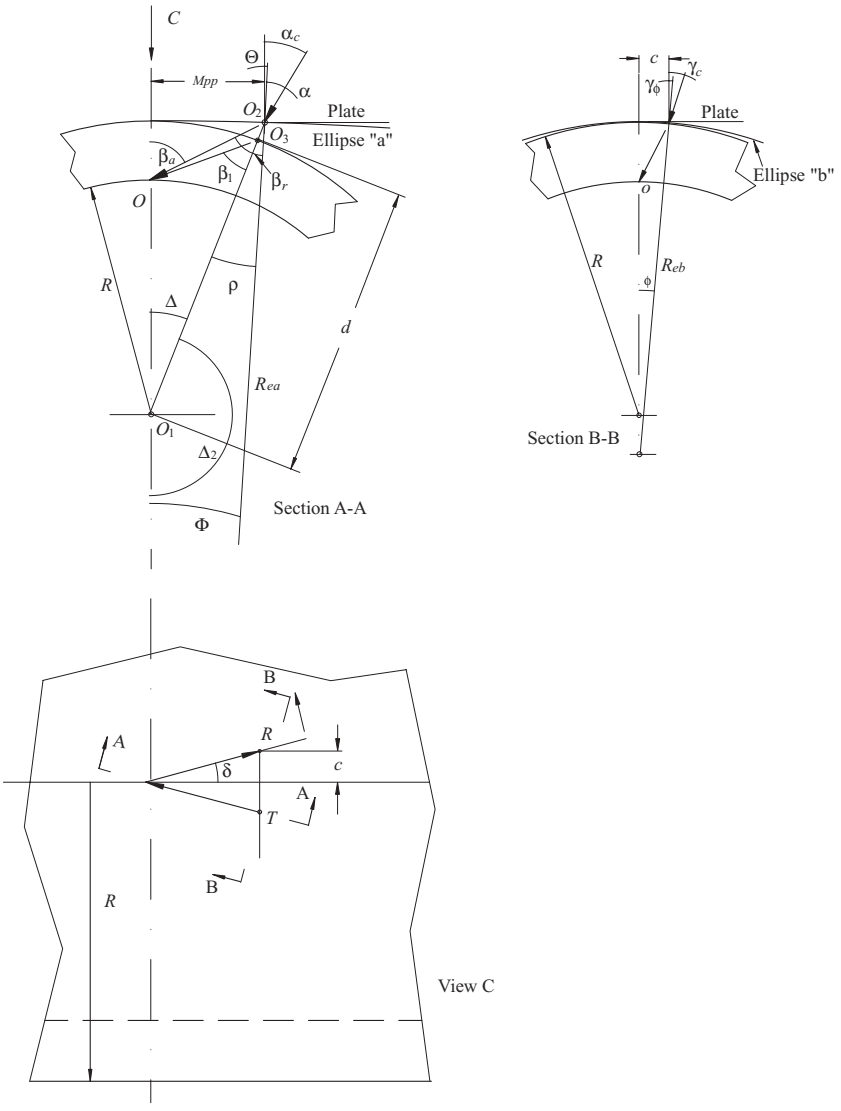

Figure 4.14 Diagram for calculation of a dual angle beam probe oriented in the circumferential direction of a pipe.

section A-A). Then the angle β_1, which is a portion of refracted angle βr is

$$\beta_1 = \arcsin\left(\sin\beta_a \frac{r}{R}\right) \tag{4.16}$$

and the central angle

$$\Delta = \beta_a - \beta_1 \tag{4.17}$$

The adjacent angle

$$\Delta_2 = 180 - \Delta$$

The "metal path" (distance O-O_3)

$$M_P = r\frac{\sin\Delta}{\sin\beta_1} \tag{4.18}$$

Projection of "metal path" on flat plane $Mpp = Mp(\cos 90 - \beta_a)$

The skew angle

$$\delta = \arctan\frac{c}{Mpp} \tag{4.19}$$

The radius of the ellipse curvature at point O_2 is

$$R_{ea} = \frac{\sqrt{(a^2\sin^2\Delta_1 + b^2\cos^2\Delta_1)^3}}{a \times b} \tag{4.20}$$

The parameter a (ellipse "a") can be calculated as

$$a = \frac{R}{\cos(90 - \Delta_1)} \tag{4.21}$$

The angle Δ_1

$$\Delta_1 = \arccos\frac{Mpp}{a} \tag{4.22}$$

The definition of Δ_1 is clear from Figure 4.15.

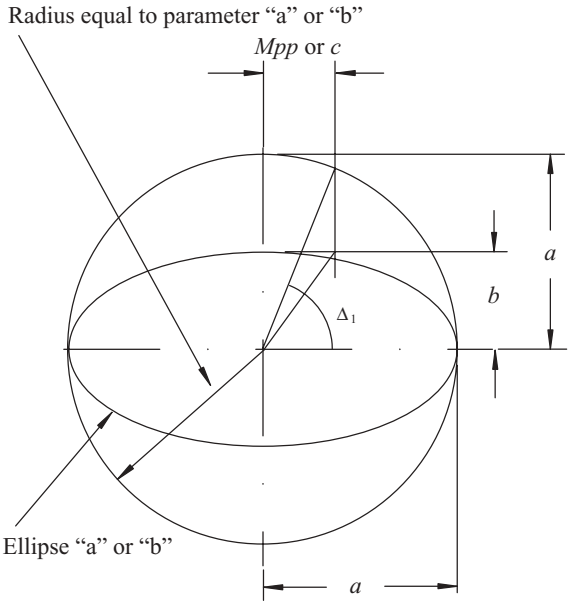

Figure 4.15 Definition of Δ_1.

The distance d (O_1O_2) can be calculated as

$$d = \frac{a \times b}{\sqrt{\left(a^2 \sin \Delta_{1a} + b^2 \cos^2 \Delta_{1a}\right)}} \tag{4.23}$$

The distance $O\text{-}O_2$ is the second approximation of the metal path.

Using the distance d, the angle between vertical diameter of the pipe and the radius of the ellipse curvature can be determined as:

$$\Phi = \arcsin\left(\sin \Delta_2 \frac{d}{R_{ea}}\right) \tag{4.24}$$

Knowing this angle, the second portion ρ of refracted angle can be calculated as $\rho = \Delta - \Phi$.

Then the refracted angle

$$\beta_r = \beta_1 + \rho \tag{4.25}$$

Finally the angle of incidence

$$\alpha = \arcsin\left(\sin\beta_r \frac{V_W}{V_S}\right) \tag{4.26}$$

The angle θ, which is equal to the angle Φ, has to be added to the angle of incidence. So, the corrected angle of incidence is: $\alpha_c = \alpha + \Phi$.

Finally, the "roof" angle should be calculated. This angle can be calculated the same way as it was done in the case of a flat surface, and then corrected by adding angle φ (Figure 4.14, section B-B). Basically, the correction angle φ should be determined by using the same procedure as for the angle Φ calculation, using curvature radius of ellipse, but not the radius of circle *R*.

The parameter a_1 which is not shown on the Figure 4.15, (ellipse "b") is:

$$a_1 = \frac{R}{\cos\delta} \tag{4.27}$$

In this case $\Delta_{1b} = \arccos\dfrac{c}{a_1}$

Radius of curvature for ellipse "b"

$$R_{eb} = \frac{\sqrt{\left(a_1^2 \sin^2\Delta_{1b} + b_1^2 \cos^2\Delta_{1b}\right)^3}}{a_1 \times b_1} \tag{4.28}$$

$$\varphi = \arcsin\frac{c}{R_{eb}} \tag{4.29}$$

The corrected "roof" angle is

$$\gamma_c = \gamma + \varphi \tag{4.30}$$

CHAPTER 5

Multiple Crystal Probe Design

5.1. CONCEPT OF "PACKAGING"

The conventional automated ultrasonic inspection systems are usually multichannel systems. To make the system maximally effective, as many channels as possible should be activated during one scan. At the same time, the number of separate probes should be kept to a minimum. This will increase positioning accuracy and simplify the scanners and the probes holding fixtures.

These opposing requirements should be considered during probe *packaging*, that is, the placement in the same housing as many crystal assemblies and using a minimum of separate wedges as is possible. A system of multiple probes can be created. The package should have a built-in couplant delivery system and wear protection. Special attention should be given to wedge(s) noise elimination.

These multiple crystal probes are a step toward linear and phased array probes. In many cases, the phased array probes cannot replace the multiple crystal probes, which can have a unique combination of

Ultrasonic Inspection Technology Development and Search Unit Design: Examples of Practical Applications, First Edition. Mark V. Brook.

the crystal assemblies. There is variety of multiple crystal probe designs. Several examples are shown below.

5.1.1. Triplex Probes

There are several designs of the *triplex probes*. The diagram of one of these probes is shown in Figure 5.1. The probe consists of three crystal assemblies located on one wedge. The angle of incidence or the wedge angle α provides, for example, the 70°S refracted angle, and the wedge angle α_1 provides a 60°S or a 45°S refracted angle in a test object. Any other combination of the angles may be used. On the top of the wedge is a crystal assembly for the straight beam portion of the probe. The wedge height *h* limits the thickness of the test object that can be inspected with a straight beam. The maximum allowable thickness should be determined in accordance with a delay line calculation. It is desirable that the probe index should be the same for each crystal assembly.

Another schema of a triplex probe package is shown in Figure 5.2.

This probe contains two wedges and four crystal assemblies: two for 45°S and 60°S refracted angles (or other modes and angles) single probes and two (T and R) for a dual straight beam portion of the probe. The design is compact and satisfies the requirements of many specifications for inspection.

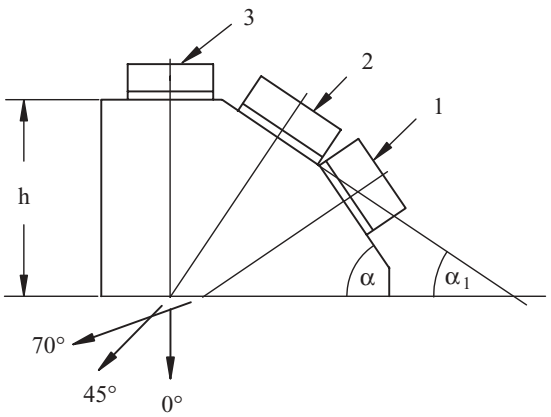

Figure 5.1 A triplex probe conceptual design to generate beams with the refracted angles: (1) 70°S single, (2) 45°S (60°S) single, and (3) 0°L single.

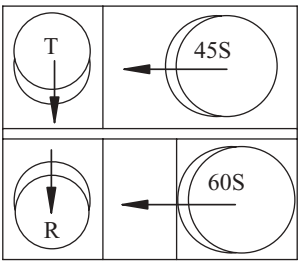

Figure 5.2 Conceptual design of a triplex probe to generate beams with refracted angles: 45°S single, 60°S single, and 0°L dual.

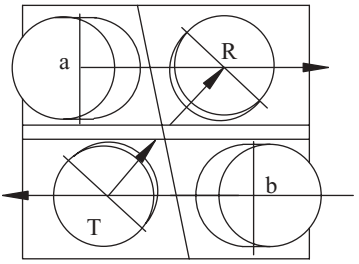

Figure 5.3 Conceptual design of a triplex probe: a and b are single probes oriented in the opposite directions, T and R are crystal assemblies for the dual 0°L portion of the probe.

The next illustration of design (Figure 5.3) is also a triplex probe, but two single probes (a and b) are aimed in the opposite directions. These types of probes can be designed, practically, for any wave mode and any refracted angle. The dual straight beam portion of the probe consists of crystal assemblies T and R, positioned at an angle of approximately 45° to the probe longitudinal axis.

5.1.2. Dual Duplex Angle Beam Probes

The combination of two dual angle beam probes is shown in the diagram of Figure 5.4. Each probe comprises two crystal assemblies T and R, or T_1 and R_1, and can be of L- or S-mode. This probe is very compact. Each of the two wedges has approximately the same size as one wedge for a single angle beam probe. The wedge noise is practically eliminated due to the fact that each crystal assembly acts as an absorber material.

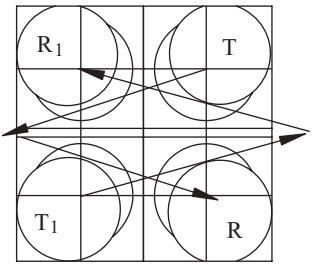

Figure 5.4 Conceptual design of a dual duplex probe: two dual angle beam probes oriented in the opposite directions.

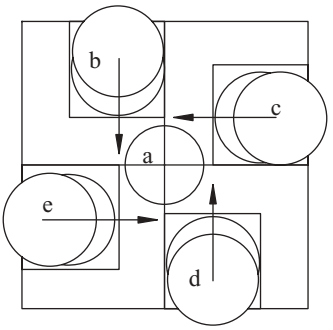

Figure 5.5 Conceptual design of a five crystal assembly probe: four single angle beam probes (b, c, d, and e) and one single straight beam probe (a).

5.1.3. Five Crystal Assemblies Probe

The probe plan shown in Figure 5.5 is a five crystal assembly probe. It consists of one wedge with four cutouts for the crystal assemblies b, c, d, and e. Each of these cutouts form a single crystal assembly wedge with the specified angle of incidence.

The crystal assembly a, which represents the straight beam portion of the probe, is located in the center of the wedge. This probe can be used on a test object with flat or curved surfaces. Staggering the crystals prevents wedge noise and cross talk between crystals.

5.2. EXAMPLE OF TRIPLEX PROBE DESIGN

5.2.1. Requirements for Triplex Probe Design

As an example, the triplex probe to be designed for the inspection of test objects is made from carbon steel. The probe should contain two single crystal probes with refracted angles of 45°S and 60°S oriented in the same direction, along with dual straight beam probe. The maximum wall thickness of the test object to be inspected is $T = 130$ mm and the average wall thickness is $T_{AV} = 115$ mm.

The first step in the design is to determine the maximum metal path and, based on this, a crystal size and frequency. The maximum metal path is

$$Mp = \frac{T}{\cos 60} = \frac{130}{\cos 60} = 260 \text{ mm}$$

Based on the experimental data, an adequate crystal size for this metal path is d = 19 mm with a frequency of 2.25 MHz.

The conceptual design of this probe is shown in Figure 5.6. To make a compact and lightweight probe, the crystal assemblies for the

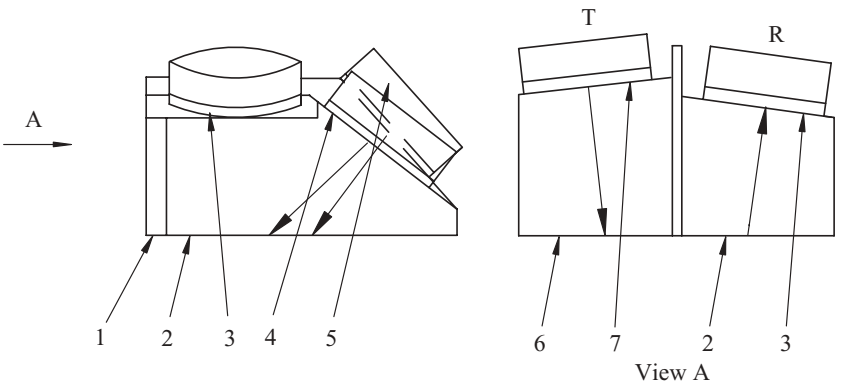

Figure 5.6 Conceptual design of a triplex probe. (1) Serration, (2) wedge 45°S, (3) crystal assembly for dual 0°L portion for the probe (receiver), (4) crystal assembly for 45°S portion for the probe, (5) crystal assembly for 60°S portion for the probe, (6) wedge 60°S, (7) crystal assembly for the dual 0°L portion for the probe (transmitter).

dual probes should be placed on the front top of the angle beam wedges. The wedge design for the 60°S refracted angle should be made first, because its size will be larger than the 45°S refracted angle wedge and, thus, will dominate the overall size of the triplex probe.

5.2.2. Wedge Design for 60°S Refracted Angle

The wedge angle calculated by Snell's law is

$$\alpha = \arcsin \beta \frac{V_{wl}}{V_s} = \arcsin 60 \frac{2.735}{3.23} = 47.16°,$$

where V_{wl} is L-wave velocity in the wedge material,

V_s is S-wave velocity in the test object material.

From the experimental graph (similar to 3–8) for crystal size d = 19 mm, the wedge angle is $\alpha = 48°$.

Ray tracing in the wedge is shown in Figures 5.7 and 5.8.

The next step in wedge design is to determine preliminarily the heights h_1 and h and then to verify their correctness with the following calculations. Assume that $h_1 = 4.0$ mm. From a practical point of view, the height $h = 2h_1 = 8$ mm.

The minimum height of the wedge is

$$h_2 = d_2 \times \sin \alpha + h,$$

where $d_2 = 20$ mm—diameter of crystal assembly.

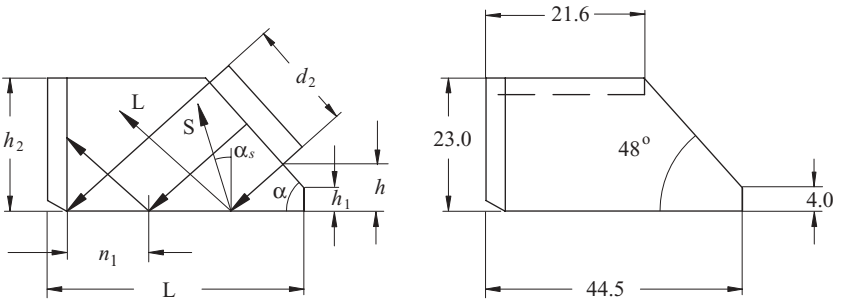

Figure 5.7 Ray tracing in the 60°S refracted angle wedge (A) and final dimensions of the wedge (B).

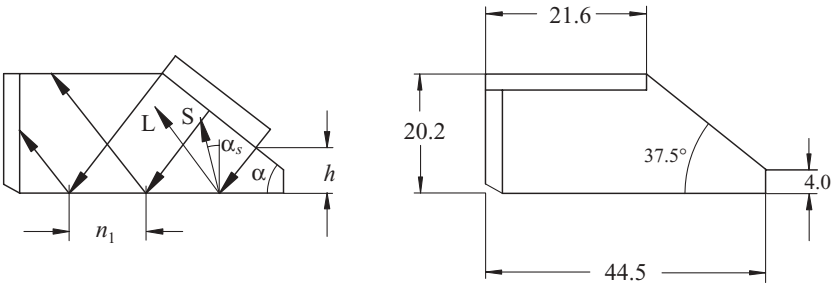

Figure 5.8 Ray tracing in the 45°S refracted angle wedge (A) and final dimensions of the wedge (B).

Therefore,

$$h_2 = 20\sin 48 + 8 = 22.9 \text{ mm}.$$

The first step in the wedge length determination is to calculate the probe index n_1.

$$n_1 = \frac{d}{2\cos\alpha} = \frac{19}{2\cos 48} = 14.2 \text{ mm}.$$

Then, the total wedge length is

$$L = 2n_1 + 1.5h\tan\alpha + 2.5,$$

$$L = 2\times 14.2 + 1.5\times 8\times\tan 48 + 2.5 = 44.23 \text{ mm},$$

where 2.5 mm is the depth of the serration.

Assume that the wedge length is 44.5 mm and the wedge height is 23 mm.

The next important requirement for the wedge design is to prevent L- and S-wave reflection inside the wedge to be directed back to the crystal. For L-wave (which is more important than S-wave), this can be achieved if $2\alpha \geq 90°$. In our case, $2 \times 48° = 96° > 90°$.

As to the S-wave, it is a desirable but not a mandatory requirement, because the attenuation of S-wave is more than the L-wave. This requirement will be met if

$$h \geq d\frac{\cos\alpha}{\tan(\alpha + \alpha_S)},$$

where α_s is the angle of S-wave reflection (see Figure 5.7A):

$$\alpha_s = \arcsin \alpha \frac{V_{ws}}{V_l} = \arcsin 48 \frac{1.13}{2.735} = 17.88°,$$

where V_{ws} = 1.13 mm/μs is S-wave velocity in Plexiglas. In this case,

$$h = 19 \frac{\cos 48}{\tan(48 + 17.88)} = 5.7 \text{ mm}.$$

This dimension is less than h = 8.0 mm in the designed wedge, so the desirable requirement is satisfied. Thus, the 60°S wedge design meets the requirements. The final dimensions of this wedge is shown in Figure 5.7B.

5.2.3. Wedge Design for 45°S Refracted Angle

The wedge angle calculated by Snell's law is

$$\alpha = \arcsin 45 \frac{2.735}{3.23} = 36.78°.$$

From the experimental graph (similar to 3–8) for crystal size diameter d = 19.0 mm, the wedge angle is α = 37.5°.

The dimension of the wedge low end should be equal 4.0 mm, the same as for the 60°S wedge; therefore, the minimum height of this wedge is

$$h_2 = d_2 \times \sin \alpha + h = 20 \sin 37.5 + 8 = 20.2 \text{ mm}.$$

The wedge length is also to be the same as for the 60°S wedge (Figure 5.8).

The probe index for this wedge will not be more than for the 60°S wedge, due to the same length.

The criterion $2\alpha \geq 90°$ is not fulfilled in this case ($2\alpha = 2 \times 37.5 = 75°$). This means that the criterion based on distance $h \geq h_1 \cos\alpha$ has to be checked for L- and S-waves reflections (Figure 5.8A).

For L-wave,

$$h_l = d\frac{\cos\alpha}{\tan 2\alpha} = 19\frac{\cos 37.5}{2\times\tan 37.5} = 4.0 \text{ mm},$$

which is the same as the actual dimension and, therefore, satisfies the requirement.

For S-wave,

$$h_s = d\frac{\cos\alpha}{\tan(\alpha+\alpha_s)} = 19\frac{\cos 37.5}{\tan(37.5+14.57)} = 11.8 \text{ mm},$$

where α_s is an angle of S-wave reflection:

$$\alpha_s = \arcsin\alpha\frac{V_{ws}}{V_{wl}} = \arcsin 37.5\frac{1.13}{2.735} = 14.57°,$$

where V_{ws} = 1.13 mm/μs is S-wave velocity in Plexiglas.

The real dimension h = 8.0 mm is less, which does not satisfy the requirements.

There are two options for correction: to increase the wedge height and make it the same as in 60°S wedge, which will satisfy the requirements, or to leave it as is. If the latter is the case, this may result in wedge noise.

The final dimensions of this wedge are shown in Figure 5.8B.

5.2.4. Dual Straight Beam Probe Design as Portion of Triplex Probe

The crystal assemblies for the dual straight beam portion of the probe should be located on the front of the probe at the top of the wedges. The transmitter T is located on top of the 60°S wedge and the receiver R is located on the top of the 45°S wedge as shown in Figure 5.6. The intention of the dual straight beam portion of the probe calculation is to determine the roof angle to satisfy the inspection requirements.

The test objects have thicknesses from 100 to 130 mm. It is desirable that one dual straight beam probe will detect reflectors located at

any depth of these thicknesses. The average thickness for the calculation is T_{AV} = 115 mm. The specified parameters of the probe are

- Crystal diameter—d = 19.0 mm
- L-wave velocity in Plexiglass—V_w = 2.735 mm/μs
- L-wave velocity in the metal—V_l = 5.85 mm/μs
- Average thickness—T_{AV} = 115 mm
- Central ray exit point distance—c = 10.0 mm
- Height of the transmitter wedge—l = 23.0 mm
- Frequency f = 2.25 MHz
- Distance of rays intersection H_0 = 51 mm.

The refracted angle

$$\beta = \arctan\frac{c}{H_0} = \arctan\frac{10.0}{51.0} = 11.1^\circ$$

The angle of incidence or roof angle

$$\alpha = \arcsin\left(\sin\beta\frac{V_w}{V_l}\right) = \arcsin\left(\sin 11.1\frac{2.735}{5.85}\right) = 5.16^\circ$$

The diameter of the imaginary crystal

$$d_1 = d\cos(\beta - \alpha) = 19.0\cos(11.1 - 5.16) = 18.9 \text{ mm}$$

The angle of the divergence for a free field at the –6 dB level

$$\varphi = \arcsin K\frac{V_i}{f \times d_1} = \arcsin 0.70\frac{5.85}{2.25 \times 18.9} = 5.52^\circ$$

The distance from the imaginary crystal to the test surface

$$l_1 = l\cos(\beta - \alpha)\frac{V_w}{V_l} = 23.0\cos(11.1 - 5.16)\frac{2.735}{5.85} = 10.23 \text{ mm}$$

The position of the imaginary crystal from the center line of the probe

$$c_1 = c + l_1 \sin\beta = 10 + 10.23 \sin 11.1 = 12.0 \text{ mm}$$

The minimum depth of measurements at the –6 dB level

$$h_1 = \frac{c_1}{\tan(\beta + \varphi)} - l_1 \cos\beta$$
$$= \frac{12.0}{\tan(11.1 + 5.52)} - 10.23 \cos 11.1 = 30.5 \text{ mm}$$

The maximum depth of measurements at the –6 dB level

$$h_2 = \frac{c_1}{\tan(\beta - \varphi)} - l_1 \cos\beta$$
$$= \frac{12.0}{\tan(11.1 - 5.52)} - 10.23 \times \cos 11.1 = 112.6 \text{ mm}$$

This maximum depth is slightly less than the average thickness (the distance at which a flaw is to be detected and measured) at the –6 dB level. If the angle of incidence, or the roof angle, is to be equal to 5.0° instead of 5.16°, this will slightly increase the maximum depth of measurements at the –6 dB level.

Let us compare metal path in the test object at the distance H_0 with the length of the near field (Figure 5.9).

The metal path is

$$Mp = \frac{H_0}{\cos\left(\arctan\frac{c}{H_0}\right)} = \frac{51}{\cos\left(\arctan\frac{10}{51}\right)} = 52 \text{ mm}.$$

The near field length at the frequency 2.25 MHz is

$$N = \frac{d^2 \times f}{4 \times V_L} - l_1 = \frac{19^2 \times 2.25}{4 \times 5.85} - 10.23 = 24.48 \text{ mm}.$$

One can see that the near field length is much less then the metal path. As was mentioned earlier, the optimum performance of a dual straight beam probe is when the metal path is equal to the near field length. Let

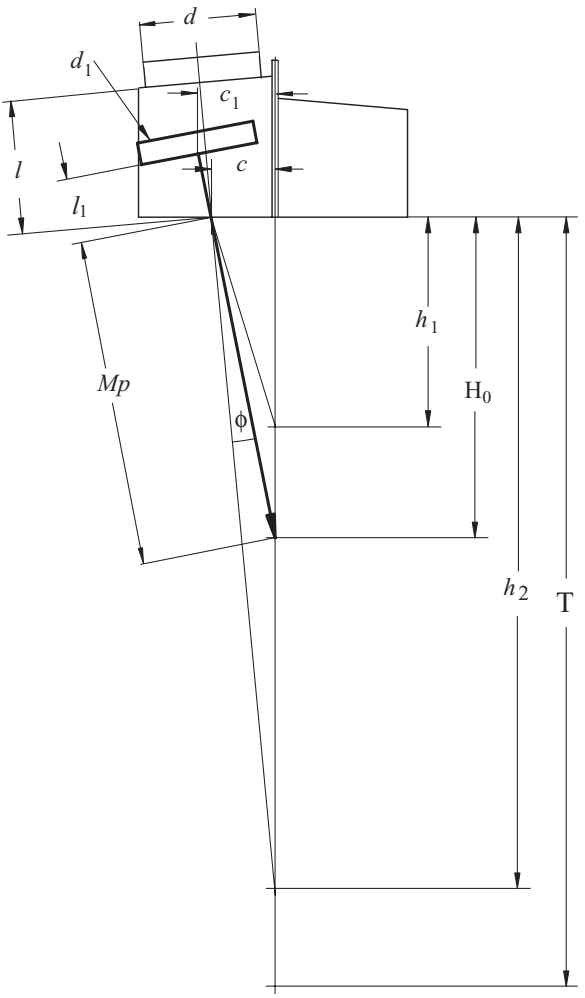

Figure 5.9 The dual straight beam portion of the probe calculation.

us change the frequency to 3.50 MHz. In this case, the near field length in the test object is

$$N = \frac{19^2 \times 3.5}{4 \times 5.85} - 10.23 = 54.0 \text{ mm}.$$

Thus, changing the frequency from 2.25 to 3.50 MHz will improve the performance of the dual portion of the probe.

CHAPTER 6

Technique Development and Probe Design for TOFD Method Application

6.1. INTRODUCTION TO TECHNIQUES BASED ON DIFFRACTION PHENOMENA

The time of flight diffraction (TOFD) techniques are used primarily for detection and sizing the depth of crack-like flaws [25–28]. Briefly and in a very simplified manner, the phenomenon of crack tip diffraction can be described as follows (Figure 6.1).

When an ultrasonic beam interacts with a crack-like flaw, the major amount of its energy reflects and possibly, mode converts, according to well-known laws. In the vicinity of sharp crack tips, a small portion of energy radiates in the form of diffracted waves.

The crack tip functions as a point source, and the front of the diffracted wave is circular.

Basically, the amount of energy converted into diffracted waves depends on the angle of attack relative to the plane of the crack, as well as the frequency and the wave mode. The mathematical and,

Ultrasonic Inspection Technology Development and Search Unit Design: Examples of Practical Applications, First Edition. Mark V. Brook.

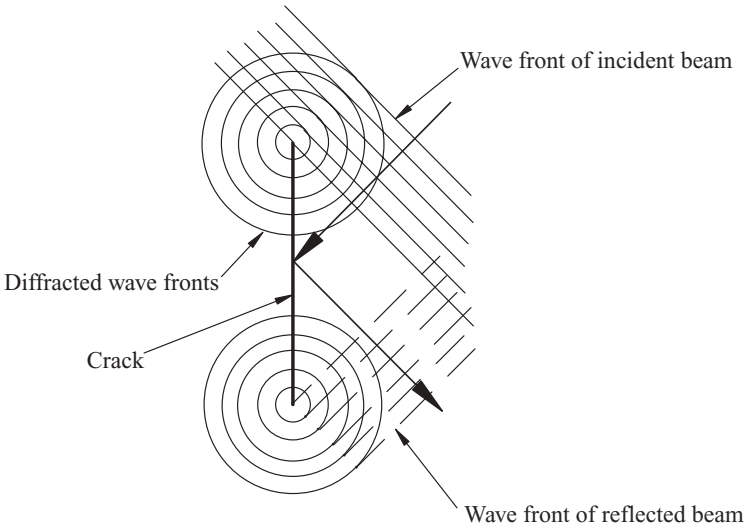

Figure 6.1 Interaction of an ultrasonic beam with a crack-like flaw.

particularly, the quantitative description of the tip diffraction process is complicated. Therefore, it is mostly the experimental data that provide us with the information regarding the influence of the different ultrasonic parameters on the tip diffraction signal amplitude. Practically, the wedge design and analysis of the received signals are based on geometrical calculations.

The purpose of any technique development, and especially if based on the diffraction phenomenon, is to increase the amplitude of the relevant signals (in this case, usually a weak tip diffraction signal) and eliminate any noise and irrelevant signals.

There are several techniques based on the diffraction phenomenon. The sketches in Figure 6.2 show the probe locations for several commonly used techniques. There is some confusion in the definition of the different techniques based on the diffraction phenomenon. We will use the following terminology.

In the case of the front surface breaking crack detection and depth sizing (Figure 6.2, A), several positions of the receiver R are possible relative to the transmitter T. When the combination of probes T and R_1 is used, the technique is commonly referred to as TOFD. It is better to refer to this technique as "forward scattering symmetric TOFD" (combination of T and R_1).

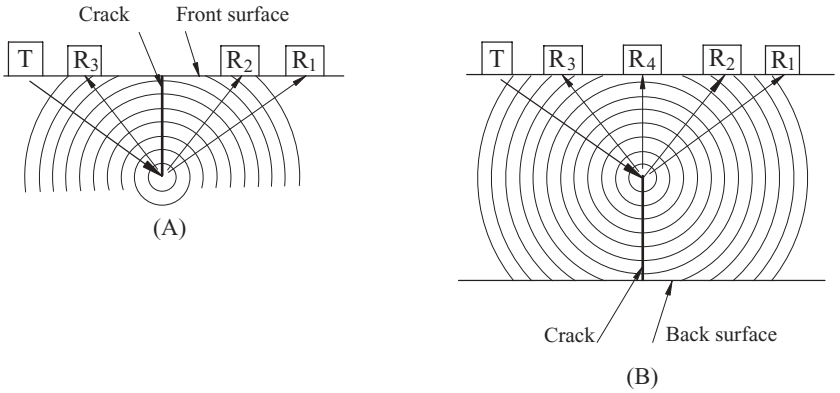

Figure 6.2 TOFD technique definitions.

When the transmitter and receiver are located not at the same distance from the crack opening, the technique is known as "forward scattering asymmetric TOFD" (combination of T and R_2). In the case of the combination T and R_3, the transmitter and the receiver are on the same side of the crack, and the technique can be referred to as "back scattering TOFD". When sizing a crack which is initiated from the surface opposite to the scanning (front) surface (Figure 6.2, B), the same combination of probes can be used plus one more combination, T and R_4. When the receiver is located over the crack, this technique is known as "delta TOFD".

6.2. TOFD FORWARD SCATTERING TECHNIQUE

The first official document describing the principles of this technique, calibration, and estimation of a flaw size is the British Standard BS 7706:1993 [29].

This technique is most commonly used for crack sizing during the inspection of butt bevel welded joints. It has several advantages over the other TOFD techniques. For example (Figure 6.3IIIa), in the absence of a front surface breaking crack, two signals will be present on the screen at all times during scanning: signal L generated by lateral wave L_L and signal B generated by and reflected from the opposite (back) surface wave L. These signals serve as reference signals to verify flaw

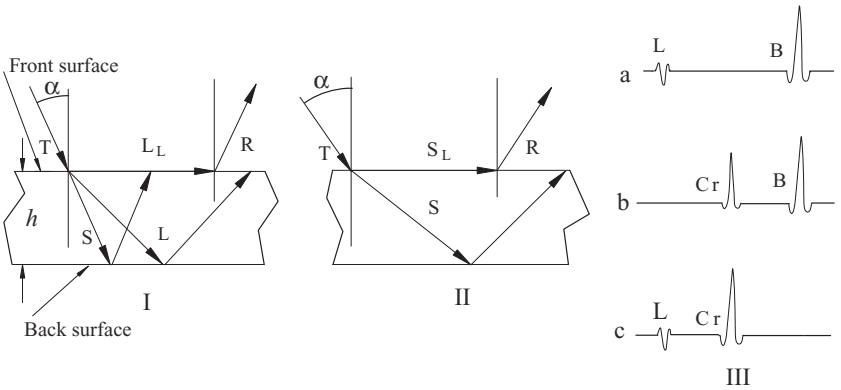

Figure 6.3 The wave modes generated by an oblique incident beam in a test object with the flat and parallel surfaces.

detection, and also as a sign of proper system operation. Therefore, the intention of the probe design for this technique is not only to optimize a tip diffraction signal, but also to generate meaningful lateral and back wall signals.

It should be kept in mind that when an oblique incident beam strikes a test surface, the acoustic field has a horizontal component L_L or S_L (Figure 6.3, I and II).

If the L-wave angle of incidence α is slightly less than $\alpha_{cr1,}$ then the L_L wave is known as a lateral wave (Figure 6.3I). This wave propagates at the shortest path between the transmitter T and receiver R on flat or convex surfaces. The lateral wave becomes a "creeping" wave when it propagates on a flat or a concave surface and when the incident angle α reaches the first critical angle α_{cr1} or slightly greater. When the angle of incidence $\alpha_{cr1} < \alpha < \alpha_{cr2}$, S_L is a shear lateral wave (Figure 6.3II). This lateral wave becomes a surface wave at the second critical angle and slightly beyond it.

Sketch III of Figure 6.3 shows several combinations of signals. As mentioned earlier, sketch a shows a lateral wave signal L and a back wall signal B in the absence of a front surface breaking crack. Sketch b shows the signal C_r from the front surface breaking crack tip and the back wall signal B. Sketch c shows the lateral wave signal L and the signal C_r from a back wall surface breaking crack tip.

The probes for this technique can be made as one combined unit or as two separate units using L-waves or S-waves, depending on the

test objective. During the development of this technique, the calculations should be performed to determine, among other things, the probe's parameters such as the wedge angle and the wedge exit points separation, to size crack depth in a specified range. The calculations are different for the test objects with flat and curved surfaces.

6.2.1. Flat Surface Test Object Inspection

Figure 6.4 shows the variables for calculation of the probe's parameters to inspect a flat surface test object with a crack initiating from the front surface.

First of all, the angle of incidence α should be calculated. This can be accomplished in the same manner as for a dual straight beam probe, using the concept of an imaginary source. Two parameters should be predetermined: an average depth h of a crack to be sized and the angle of attack β_1. In the case of a flat test surface, the angle of attack is equal to the refracted angle β and should be in the range of 45°–60°. Experiments show that in this range of angles, it is more probable to receive a relatively high amplitude of a tip diffraction signal. The half distance c between the exit point of the transmitter and the receiver is a function of crack depth h. So, for a given refracted angle β,

$$c = h \tan \beta. \tag{6.1}$$

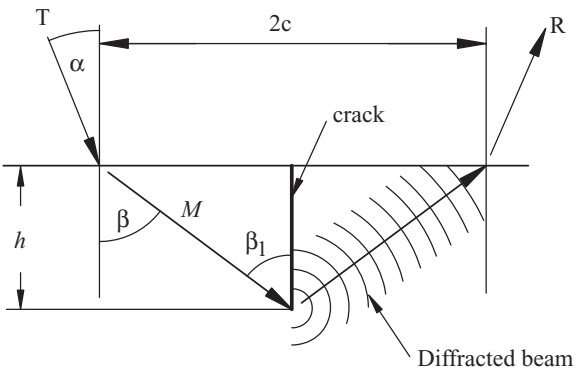

Figure 6.4 Diagram of probe calculation for TOFD forward scattering technique for inspection of a test object with a flat front surface.

The angle of incidence is

$$\alpha = \arcsin\left(\sin\beta\frac{V_w}{V_s}\right). \tag{6.2}$$

where V_w is the wave velocity in the wedge material and V_s is the wave velocity in metal material.

The range of the crack depth measurement at the −6 dB levels can be determined the same way as in the case of a dual straight beam probe.

It is useful to make graphs for these calculations where $h = \phi(c)$, and β = const.

The final step in the calculation is to determine the crack depth as function $h = \phi(\tau)$ after the time of flight (TOF) (τ) is measured, and c = const. From the geometry of a symmetrical system, it is clear that

$$h = \sqrt{M^2 - c^2}. \tag{6.3}$$

The metal path M can be expressed by means of the measured time τ and the sound velocity V_s in the test object metal, as

$$2M = \tau V_s$$
$$M = \frac{\tau V_s}{2}$$
$$M^2 = \left(\frac{\tau V_s}{2}\right)^2.$$

Thus, the final equation is

$$h = \frac{1}{2}\sqrt{\left[(\tau V_s)^2 - 4c^2\right]}. \tag{6.4}$$

This equation is used mostly in the case when the lateral wave signal is absent. In many cases, when the lateral wave signal is apparent, the other equation can be used. It is based on the difference in TOF between the signals from the crack tip and the lateral wave (τ_L):

$$h = \frac{V_s}{2}\sqrt{(\tau^2 - \tau_L^2)}. \tag{6.5}$$

Analogous equations can be derived for an asymmetric position of the probes.

For both probes positions, the symmetric and the asymmetric, the maximum signal amplitude is determined by the divergent diagram of the receiver.

6.2.2. Curved Surface Test Object Inspection (Figure 6.5)

Consider the case of an inspection of a hollow cylinder with the inner radius r and the wall thickness T. The first step in designing a probe for axial crack detection and sizing by scanning from the inside of the cylinder is to determine the limitations caused by the cylinder inner radius. One of the limitations is associated with an angle of attack β_1 which should be chosen from 45° to 60°, as mentioned earlier. The second limitation is related to the depth of the crack which can be sized. The crack initiation can be from either the outside or inside surface of the cylinder; what is important is the location of the crack tip.

The crack with the depth h in Figure 6.5 is initiated from the inside surface of the cylinder. If the crack is initiated from the outside surface, the distance h is a ligament (remaining wall thickness). The sequence of calculations is the same in both cases. In practice, the range of the crack depth to be sized is specified. So, the maximum (or minimum) crack depth h at the recommended minimum angle of attack should be calculated. If the minimum achievable angle of attack appears to be less than preferable, it may be a problem to determine the depth of the

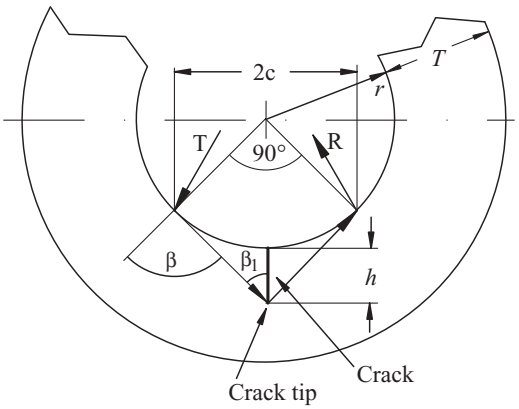

Figure 6.5 Diagram for calculation of minimum crack depth, which can be sized.

detected crack. The diagram in Figure 6.5 is helpful to understand the theoretical and practical limitations of the transmitter T and receiver R positions for sizing the depth of the crack.

One of the limitations is that the refracted angle β theoretically cannot be more than 90° (in practice approximately 75°). The other limitation is the inside diameter of the hollow cylinder. For example, the inside diameter of the cylinder is such that required position of the exit points of the transmitter T and the receiver R are 90° apart. In this case, the angle of attack β_1 is equal to 45°, which is the minimum recommended angle. Thus, the distance $2c$ can be calculated as $2c = r\sqrt{2}$.

The minimum depth of a crack that can be sized is

$$h = r\left(\sqrt{2} - 1\right) = 0.41r. \tag{6.6}$$

In the other case, when the inside diameter of the cylinder is larger and the wall is thinner, the angle of attack β_1 can be selected in the desirable range (Figure 6.6). The sequence of calculations is presented in Section 6.3.

6.3. EXAMPLES OF PROBE CALCULATION FOR CURVED SURFACE TEST OBJECT INSPECTION

6.3.1. Axial Crack Detection and Sizing

As an example, let us calculate the probe parameters for the inspection of a hollow cylinder fabricated from stainless steel, to detect and size

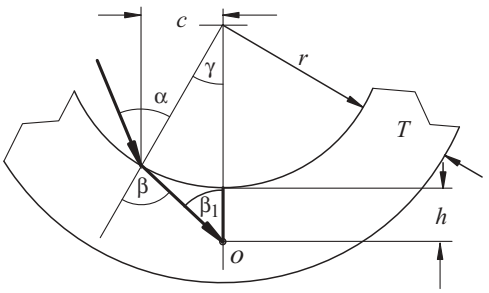

Figure 6.6 Diagram for calculation probe parameters for detection and sizing of an axial oriented crack (inspection from inside a cylinder).

an axial crack. The method of inspection is immersion with the probes located inside the cylinder.

The assumption is (Figure 6.6) that the tip of the crack is located at the point *o* at the distance *h* from inner surface (it can be a crack initiated from either inner or outer surface). The following data are given:

$r = 38$ mm

$T = 12.5$ mm

$c = 10$ mm

V_w = sound velocity in water 1.49 mm/μs

V_l = L-wave sound velocity in stainless steel 5.72 mm/μs

The depth *h* of the crack should be calculated for different angels of attack. Then the probe parameters should be chosen to satisfy the specification for inspection.

The practical way to calculate the angle of attack β_1 is to choose an arbitrary refracted angle β and then calculate the relative value of *h*. The sequence of calculation is as follows.

The central angle γ

$$\gamma = \arcsin\frac{c}{r} \tag{6.7}$$

The angle of attack

$$\beta_1 = \beta - \gamma \tag{6.8}$$

The angle of incidence

$$\alpha = \arcsin\beta\frac{V_w}{V_l} \tag{6.9}$$

The probe angle

$$\alpha_1 = \alpha - \gamma \tag{6.10}$$

Table 6.1
Parameters for Probe Design for Axial Crack Sizing

	Axial crack sizing				
β, degree	55	60	65	70	75
β_1, degree	39.53	44.53	49.53	54.53	59.53
α, degree	12.30	13.00	13.63	14.14	14.54
α_1, degree	–3.17	–2.47	–1.84	–1.33	–0.93
h, mm	10.90	8.93	7.27	5.84	4.59

The position of a crack tip

$$h = r\left(\frac{\sin\beta}{\sin\beta_1} - 1\right) \tag{6.11}$$

The central angle is the same for all refracted angles

$$\gamma = \arcsin\frac{10}{38} = 15.26°.$$

The calculations performed for refracted angles from 55°L to 75°L, and obtained parameters for the probe design are summarized in Table 6.1.

The data in the table show that for the reliable sizing of an axial crack, the refracted angle β should be at least 65°. At this angle, the maximum depth of the crack that can be sized is 7.27 mm.

For deeper crack sizing, parameter *c* would have to be increased.

6.3.2. Circumferential Crack Detection and Sizing (Figure 6.7)

The probe parameter calculations for circumferential crack detection and sizing can be performed assuming that the surface is flat (focusing effect of the cylinder curved surface in axial direction is negligible). The initial data are the same as in the previous case.

In this case $\beta = \beta_1$,

and the angle of incidence is

$$\alpha = \arcsin\beta\frac{V_w}{V_l}. \tag{6.12}$$

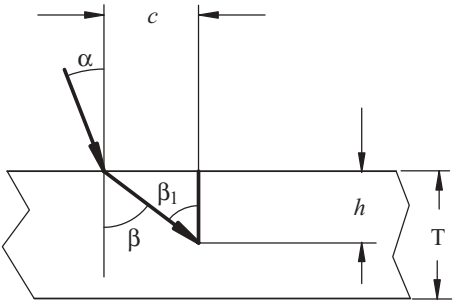

Figure 6.7 Sketch related to calculation of probe parameters, for circumferential crack detection and sizing (inspection from inside a cylinder).

Table 6.2
Parameters for Probe Design for Circumferential Crack Sizing

	Circumferential crack sizing				
β, degree	55	60	65	70	75
α, degree	12.30	13.00	13.63	14.14	14.54
h, mm	7.00	5.77	4.66	3.64	2.68

The crack depth is

$$h = \frac{c}{\tan \beta}. \tag{6.13}$$

The parameters for the probe design intended for circumferential crack sizing are presented in Table 6.2.

As a rule, the depth of the crack to be sized is the same for both the axial and circumferential cracks. Let us assume that the depth of the crack to be sized is 5.80 mm. If the crack is axial, the angle of incidence is 14.14°. But if the crack is circumferential, the angle of incidence is 13.0°.

6.3.3. Probe Design

The necessity of the probe angle α_1 (Table 6.1) calculation becomes obvious from the sketch in Figure 6.8A. The best way to drill holes in the probe (transducers holder) for transducers is to measure the probe

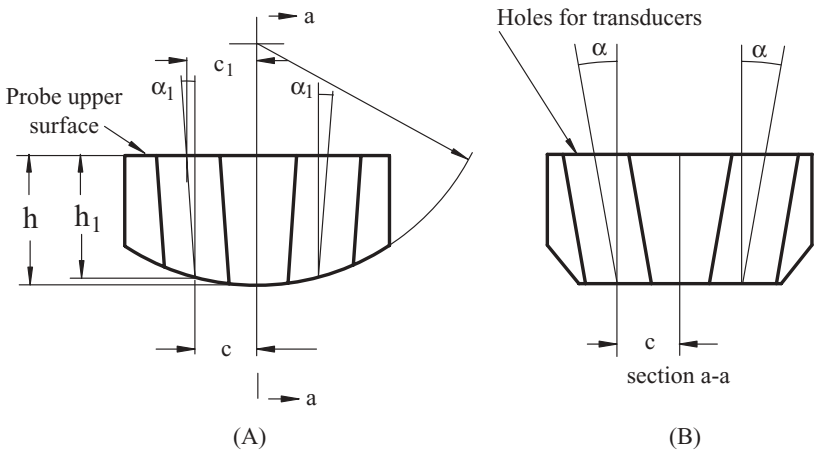

Figure 6.8 Conceptual design of the probe: (A) holes position of transducers for axial crack detection and sizing, (B) holes position of transducers for circumferential crack detection and sizing.

angle relative to the perpendicular to the transducers holder upper flat surface. The distance c_1 should be calculated as

$$c_1 = c + h_1 \times \tan \alpha_1. \tag{6.14}$$

6.3.4. Comments

The abovementioned British Standard BS 7706:1993 recommended using longitudinal waves "as these arrive first, simplifying the interpretation of the responses." And further: "The normal shear wave (vertically polarized) should rarely be used in this search and size role. . . . "

In many cases, the use of S-wave probes can be preferable [51]. For example, inspection of a steel hollow cylinder (ID = 75 mm, wall thickness 15 mm) to detect and size an axial notch revealed that shear waves produce more reliable results (Figure 6.9). On the left side in this figure are screen captures obtained by using L-waves, on the right side, by using S-waves. To achieve the same signal amplitude from the tip of the notch (approximately 50% for L-waves TOF is 8.520 μs; for S-waves TOF is 22.940 μs), the system using L-waves required 20 dB more gain than the system using S-waves (compare pictures A and B). The noise level is approximately the same (pictures C and D). The lateral wave is stronger and more distinguishable in the case of the

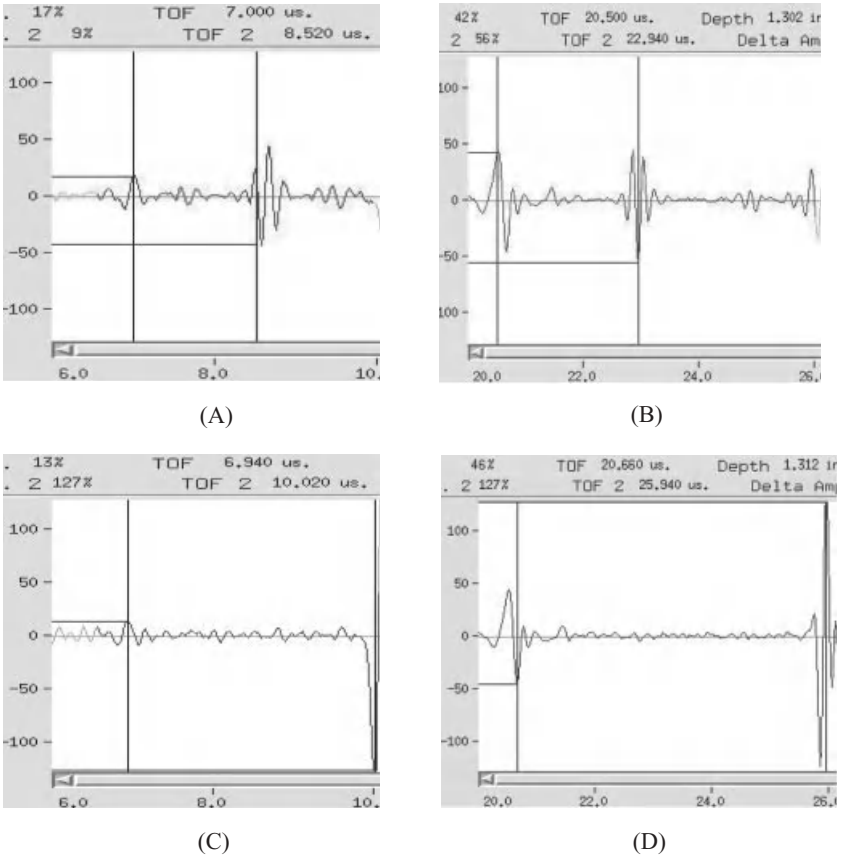

Figure 6.9 Comparison of the results obtained during the inspection of the same test object by using longitudinal waves (A and C) and shear waves (B and D).

system using S-waves (TOF is 20.66 μs). The shorter wave length for S-waves helps in the detection of the shallower reflectors.

Accuracy of sizing is comparable.

6.4. PROBE DESIGN FOR TOFD BACK SCATTERING TECHNIQUE

6.4.1. Basics of TOFD Back Scattering Technique

As was previously mentioned, when a transmitter and a receiver of a probe is located on the same side of the crack, the technique is named

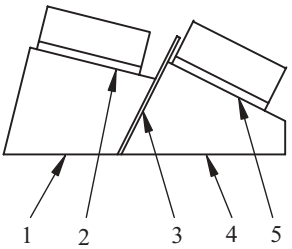

Figure 6.10 A tandem probe conceptual design: (1) wedge receiver with (2) crystal assembly, (3) acoustic and electric insulators, (4) wedge transmitter with (5) crystal assembly.

"back scattering TOFD." One of the designs based on this probe combination is known as *Tandem*.

A Tandem probe consists of two wedges with crystal assemblies: receiver and transmitter (Figure 6.10). As a rule, the receiver is placed in front of the transmitter and separated from it by acoustic and electric insulators [30, 31].

Generally, the Tandem probe can be considered as another arrangement of a dual angle beam probe, and therefore can be designed for a variety of refracted angles. In the most common designs, the wedge angle of the transmitter is calculated to produce a high angle refracted L-wave. This can be done if the angle of incidence is equal or close to the first critical angle. In this case, several "specific" waves can be recognized in the refracted acoustic field in the metal test object (Figure 6.11). A strong longitudinal wave *L* propagates at the refracted angle β_L of approximately 75°–80°, depending on the transducer frequency and the crystal size and shape. It is the same "longitudinal surface wave" which must propagate at the 90° refracted angle according to Snell's law.

In reality, a "creeping" wave C_R propagates along the front surface. This wave has a short path due to the radiation of "indirect" shear waves (shown in the sketch by the small arrows).

A "direct" shear wave S propagates at the refracted angle β_s, calculated by Snell's law. When the "indirect" shear waves strike the back surface parallel to the front surface, the same set of "specific" waves is observed, only in a mirror image (marked by subscript 1). Each of the "specific" waves can carry out its own function. The interaction of these waves with a crack (notch) of height *h* is shown in Figure 6.12.

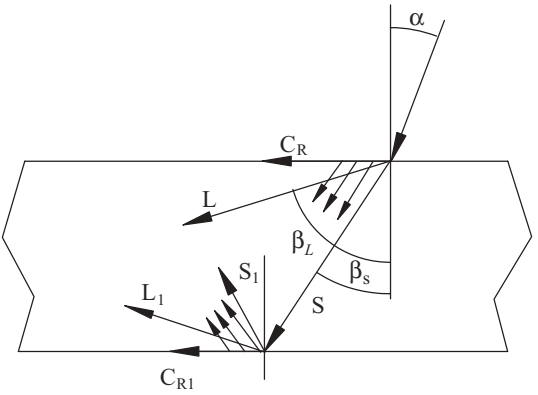

Figure 6.11 An acoustic field in a steel test object when an angle of incidence α is equal or close to the first critical angle.

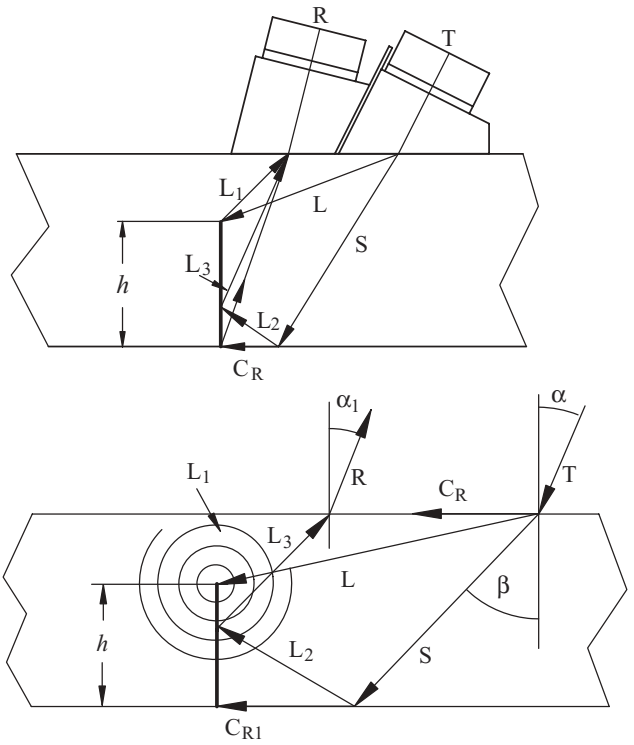

Figure 6.12 Interaction of waves with a crack of height *h*.

For example, very small surface breaking flaws can be detected by using "creeping" waves. The longitudinal wave L, when it interacts with a crack tip, produces diffracted waves (L_1) and is very useful for crack depth sizing. The combination of S-L_2-L_3 waves provides additional information about the crack size and serves as a flaw reconstruction tool. It is practically convenient to use this terminology. In reality, a "creeping" wave is a "portion" of an ultrasonic field, generated by a probe with an incident angle close to the first critical angle [32, 33].

The typical signals obtained by the abovementioned combination of waves are shown in Figure 6.13A. Signal #l (A ≈ 33%) is from the tip of the notch (the position of the probe is not optimized to receive the signal of maximum amplitude). This signal is produced by the L-L_1 wave. Signal #2 (A ≈ 30%) is from the corner trap of the notch, produced by the "creeping" wave. Signal #3 (A ≈ 127%) is produced by the combination of S-L_2-L_3 waves. The maximum signal amplitude (signal #1, A ≈ 55%) from the notch tip is shown in Figure 6.13B at the optimized position of the probe. The best method for crack sizing is to measure TOF between the initial and tip diffraction signals.

If a not deep crack is initiated from the scanning surface, the picture is quite different and the signals are produced by the waves shown in Figure 6.14. The combination of L-L_1 waves is responsible for a strong

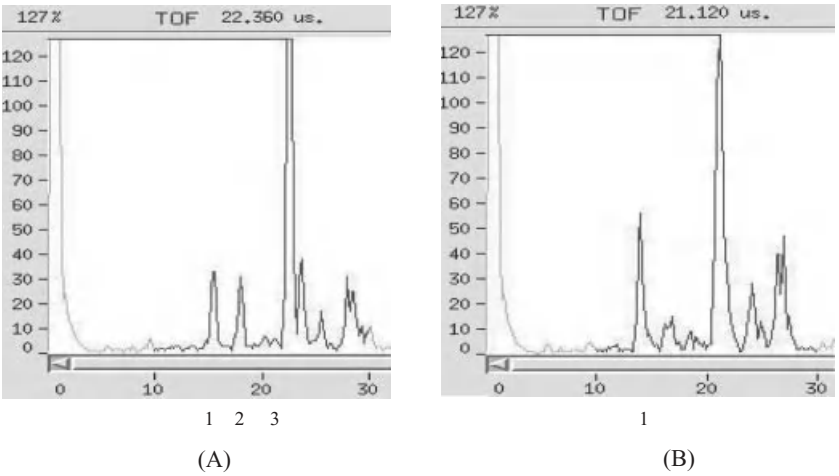

Figure 6.13 Typical signals produced by a tandem probe in the vicinity of a crack, initiated from a test object opposite surface.

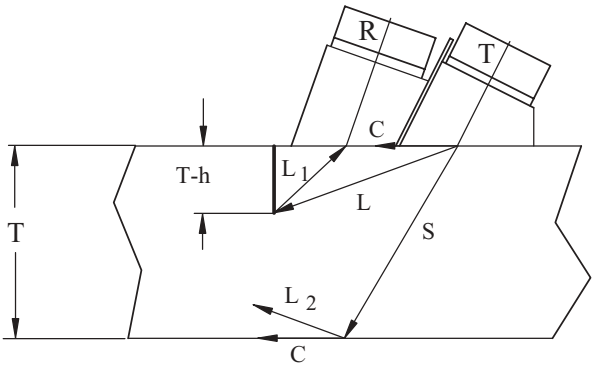

Figure 6.14 Waves in the vicinity of a crack, initiated from a scanning surface.

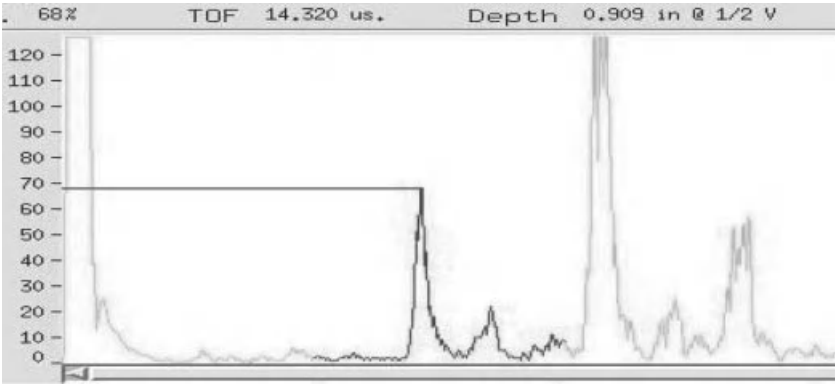

Figure 6.15 Typical signals produced by a tandem probe in the vicinity of a crack, initiated from scanning surface (signal 1 is from the crack's tip).

tip diffraction signal. A "creeping" wave can produce a signal from the crack's face. It is possible to receive a second tip diffraction signal from S-S or S-L_2 waves if the crack is deep enough. A typical tip diffraction signal (#1) produced by the Tandem probe in a 25-mm thick plate from a notch 12.5 mm deep, initiated from scanning surface, is shown in Figure 6.15.

6.4.2. Examples of Tandem Probe Design

There are two ways to calculate wedges for Tandem probes. The first way is to specify the wedge angles for the transmitter and receiver and

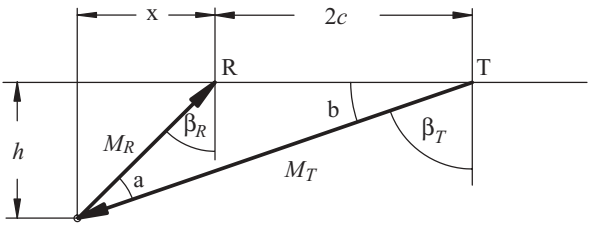

Figure 6.16 Sketch related to calculation of optimum wedges for a tandem probe.

then determine the depth of the crack, which will produce the tip diffraction signal of maximum amplitude by L-L_1 waves. If the refracted angles β_T and β_R along with the distance $2c$ are given (Figure 6.16), then

$$\alpha = \beta_T - \beta_R \tag{6.15}$$

$$b = 90 - \beta_T \tag{6.16}$$

$$M_T = 2c\frac{\sin\beta_R}{\sin\alpha} \tag{6.17}$$

$$h = M_T \times \cos\beta_T \tag{6.18}$$

An example of the calculation is presented below for a probe with the following parameters:

the refracted angle of the transmitter—$\beta_T = 70°$
the "refracted" angle of the receiver—$\beta_R = 45°$
the distance $2c$—17 mm

$$a = 70 - 45 = 25°$$

$$b = 90 - 70 = 20°$$

$$M_T = 17\frac{\sin 45}{\sin 25} = 28.45 \text{ mm}$$

$$h = 28.45\cos 70 = 9.73 \text{ mm}$$

The results of the experiments to confirm this probe design are presented in Table 6.3 and partly for three side-drilled holes (SDH) in

Table 6.3
The Results of Experiments to Confirm Tandem Probe Design

SDH depth, mm	2.5	5.0	7.5	10	12.5	15	17.5	20	22.5
Amplitude, %	40	52	74	80	70	56	42	32	26
TOF, μs	8.44	9.73	11.3	12.3	13.5	14.8	15.84	17.39	18.85
Distance X, mm	17.8	21.6	22.9	25.4	28	30.5	33.0	35.5	38.1
Refracted angle, $\beta°_T$	83	78	73	70	66	64	62	61	60

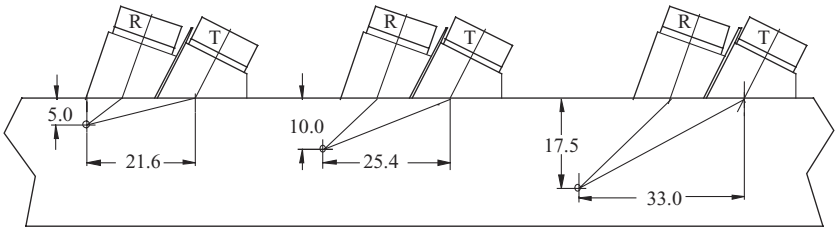

Figure 6.17 Position of a tandem probe to measure refracted angles.

Figure 6.17. One can see that the maximum signal amplitude is from the SDH at the depth of 10 mm which is very close to the calculated data.

Distance X in this table is the distance between the exit point of the transmitter and the SDH.

The angles of rays in the refracted beam, which are reflected from each of the holes, are different. The deeper the hole, the lower is the refracted ray's angle of the transmitter beam that is involved in a tip diffraction wave generation (Figure 6.18).

At the same time, only a portion of the diffracted waves, close to the nominal "refracted" angle of the receiver β_R (Figure 6.16), will produce the signal with maximum amplitude from the reflector at a given depth, with exception of the reflectors very close to the front surface. Thus, to produce the maximum possible signal amplitude from a crack tip at the specified depth, the "refracted" angle of the receiver has to be calculated.

The second way to design wedges is to specify the crack depth h to be measured and then to calculate the "refracted" angle of the receiver and then the wedge angle.

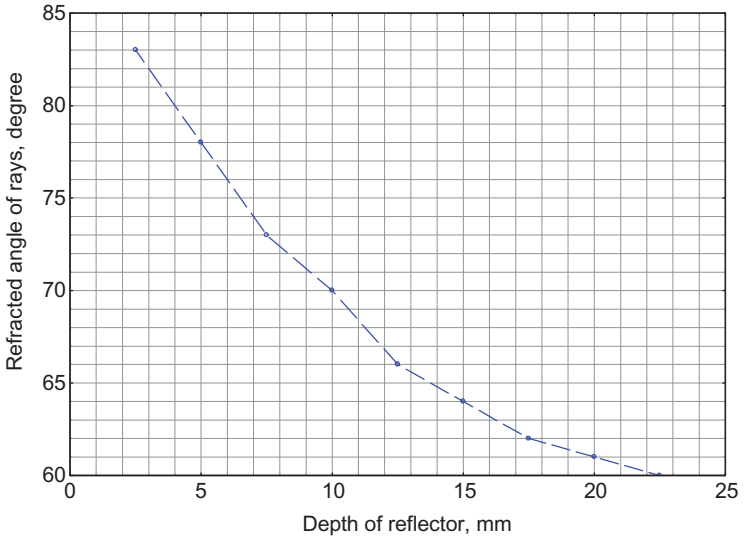

Figure 6.18 Dependence of refracted rays from depth of reflectors.

The metal path can be calculated as

$$M_T = \frac{h}{\cos \beta_T} \tag{6.19}$$

The distance x

$$x = M_T \times \cos(90 - \beta_T) - 2c \tag{6.20}$$

And the refracted angle of the receiver is

$$\beta_R = \arctan \frac{x}{h}. \tag{6.21}$$

The waves which may be involved in the detection and sizing of cracks initiated from the scanning surface are shown in Figure 6.19.

In the probe position A, the crack will be detected by the "creeping" wave C. No tip diffraction signal will be generated. In the position B, three not optimized signals will be visible: the signal from the crack wall generated by wave C, the tip diffraction signal that will be produced by L-L_1 wave, and a second tip diffraction signal by S-S wave. In the probe position C, the wave L-L_1 produces the optimized tip

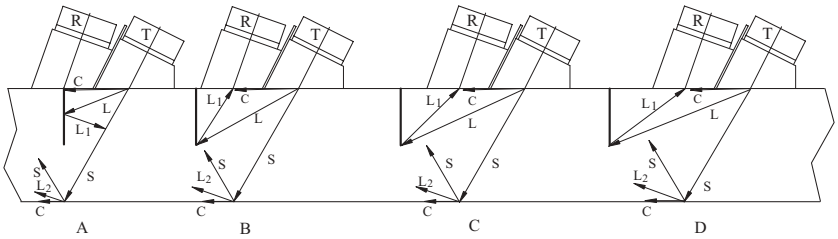

Figure 6.19 The waves which may be involved in detection and sizing cracks initiated from the scanning surface.

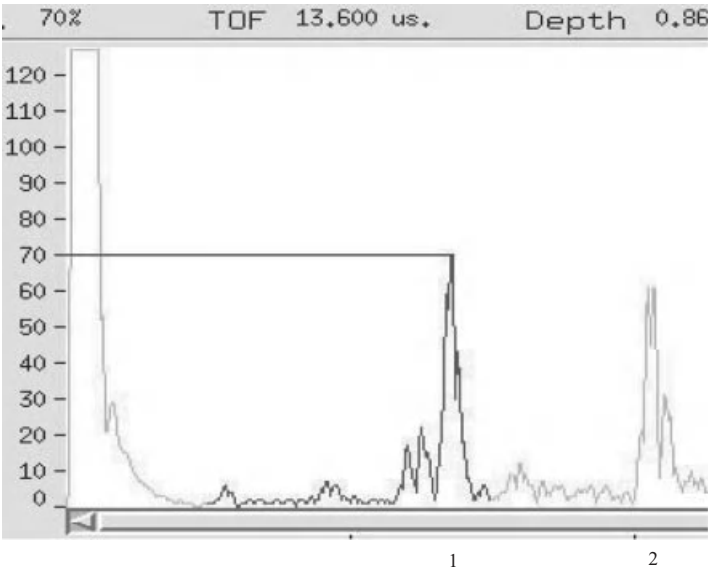

Figure 6.20 Tip diffraction signals produced by L-L_1 and S-S waves (position C in Figure 6.19).

diffraction signal, and the unoptimized tip diffraction signal is produced by S-S wave. In the probe position D, an unoptimized tip diffraction signal by L-L_1 is produced, as well as by S-S wave. The tip diffraction signals generated by L-L_1 (signal #1 with amplitude A = 70%) and S-S wave (signal #2) when the probe is in position C are shown in Figure 6.20.

The data from Table 6.3 were used to create the graphs presented in Figure 6.21A–C. The first graph shows the signal

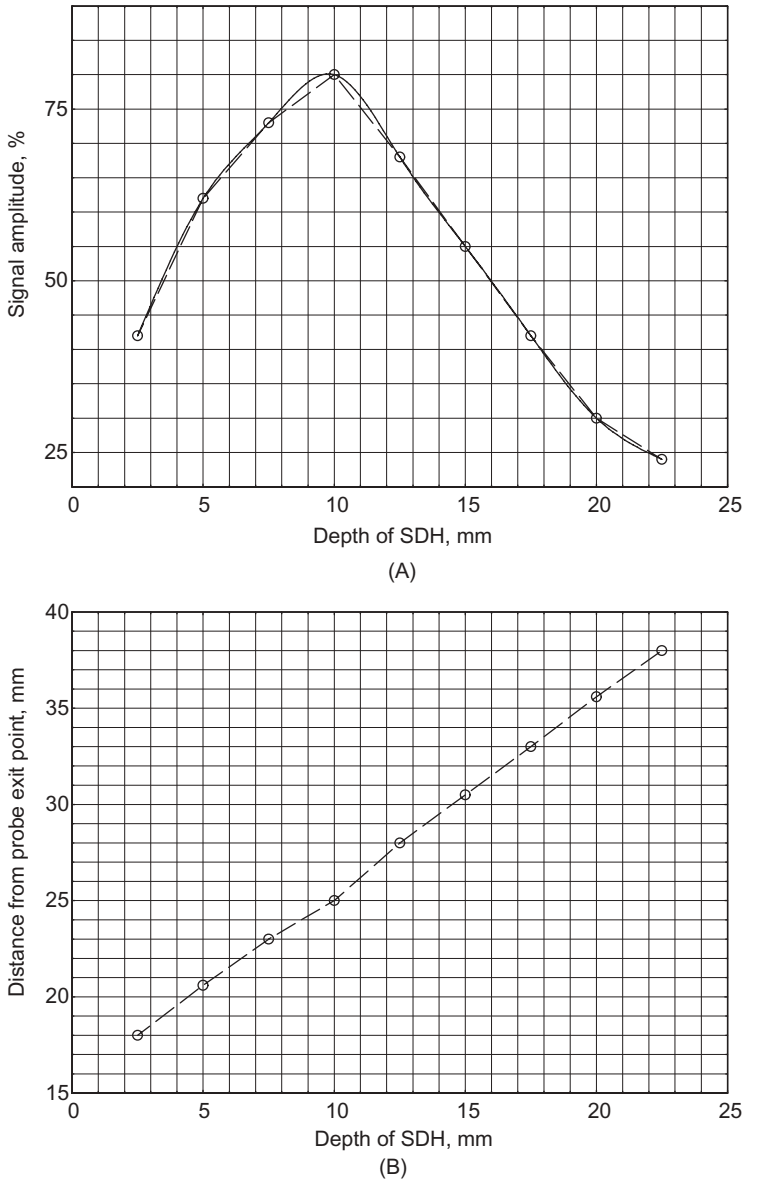

Figure 6.21 Tip diffraction signals parameters versus SDH depth (A, B, C).

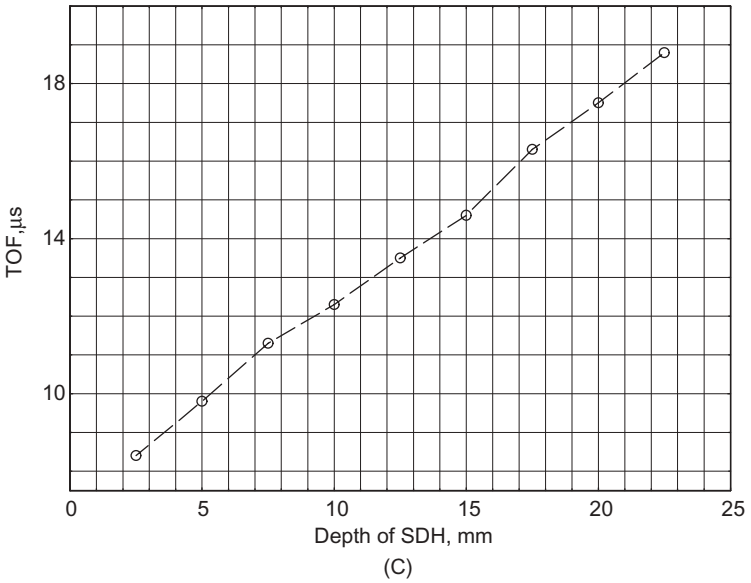

Figure 6.21 Continued.

amplitude dependence on the depth of SDH. The second graph shows the dependence of the distance from SDH to the exit point of the transmitter at the depth of the SDH to obtain the highest signal amplitude. The dependence is linear, which confirms the regular shape of the transmitter field. The third graph shows the TOF dependence on the metal path, as a function of SDH depth. This dependence is also linear. All these graphs confirm that the probe is designed correctly.

One of the Tandem probes application is described in Reference 34.

6.4.3. Gliding Diffracted Waves Technique

Sometimes, another type of diffracted waves, so-called gliding waves, is used in ultrasonic nondestructive testing (NDT).

When an oblique incident beam strikes a side-drilled hole, some of the rays, which are tangent to the hole surface (#1 in Figure 6.22A) produce a "band round waves." These waves, in turn, produce the gliding diffracted waves (#2 in Figure 6.22A). This technique can be

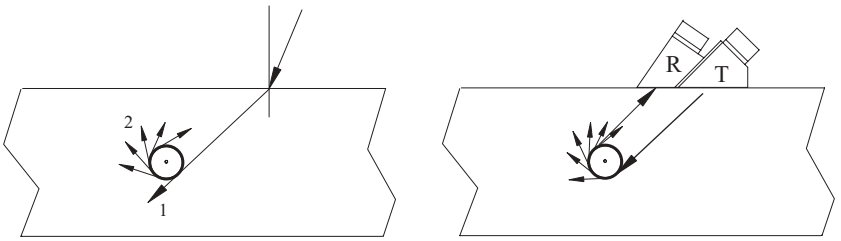

Figure 6.22 Generation of gliding waves (A) and conceptual design of gliding wave probe (B). 1, Oblique beam; 2, Gliding diffraction waves.

used for detection of a crack located on the opposite side of the hole, which is not accessible for direct inspection. The band round waves and the gliding diffraction waves will be interrupted by the crack, and the signal, representing these waves on the screen, disappears. This indicates the presence of a crack located in a "shadow" zone of the hole.

The presence of this signal also can be used for a hole diameter calculation by measuring the TOF of the band round wave. In this case, a tandem type probe generating a shear wave is recommended. The refracted angle of the probe should be in the region of 50°–60°. The conceptual design of such probe is shown in Figure 6.22B.

Like any other diffracted wave, the gliding diffraction waves are weak. Its signal amplitude depends on the hole diameter. Compared with a bulk wave reflected signal amplitude from an SDH 12.7 mm in diameter, the gliding diffraction wave signal amplitude will be less by approximately 20–25 dB.

CHAPTER 7

Technique Development and Probe Design for Cylindrical Rod Inspection

7.1. BOUNDARY EFFECT

The ultrasonic inspection of a test object with a thick wall can be treated as an inspection of a semi-infinite medium. In this case, the only possible cause for a beam propagation distortion is a reflector located inside the volume, limited by the lobe's boundaries (Figure 7.1).

This is the simplest example of an inspection, and the results obtained are easy to interpret. When the diameter of the lobe exceeds the dimension of the test object perpendicular to the beam propagation, the rays of the ultrasonic beam are confined by the test object walls, and the boundary effect will take place. It is known that the boundary effect produces mode conversion and beam rays redirection. These two phenomena will alter the normal beam propagation—the ultrasonic beam becomes *guided*. The interpretation of the inspection results becomes more complicated.

When the test object is a round cylinder with a relatively small diameter (in comparison to its length) and the wavelength is greater than the diameter of the rod, cylindrical *rod waves* will be created with

Ultrasonic Inspection Technology Development and Search Unit Design: Examples of Practical Applications, First Edition. Mark V. Brook.

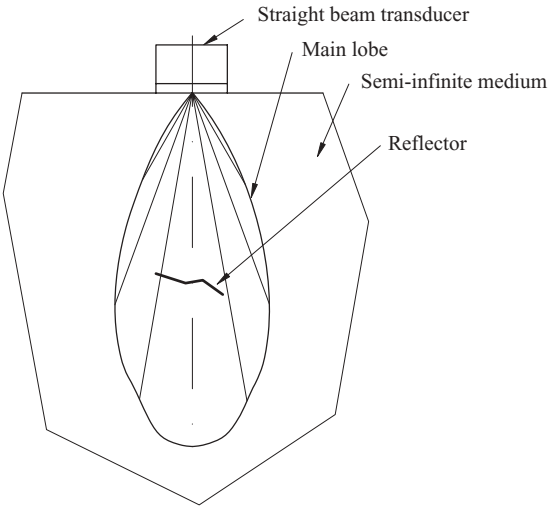

Figure 7.1 Main lobe of a straight beam transducer in a semi-infinite medium.

bar wave velocity, which is dispersive [9]. In a rod with larger diameter (more than several wavelengths) the multiple L-wave reflection and mode conversion will produce only a wave guide effect (Figure 7.2A). A similar wave guide effect can be observed in bars of different shapes: square, rectangular, and so on.

If a transducer is located close to the test object wall (not necessary a cylindrical rod) at some distance c, the peripheral rays of the ultrasonic beam at the side of the wall can touch the wall (Figure 7.2B). As a result, the direction of the rays propagation changes, and the phenomenon of mode conversion occurs. When the L-wave ray L at the angle φ strikes the wall, the portion of the ultrasonic energy will be reflected as an L-wave at the same angle, and the other portion will be converted into S-wave, which will propagate at an angle β. These two phenomena will interfere with the normal propagation of the beam and create problems for flaw detection in the wall region.

7.2. SYMMETRIC AND ASYMMETRIC CYLINDRICAL ROD-GUIDED WAVES

Two cases will be discussed: symmetric and asymmetric cylindrical rod-guided waves, as shown in Figure 7.3. It is possible that in both

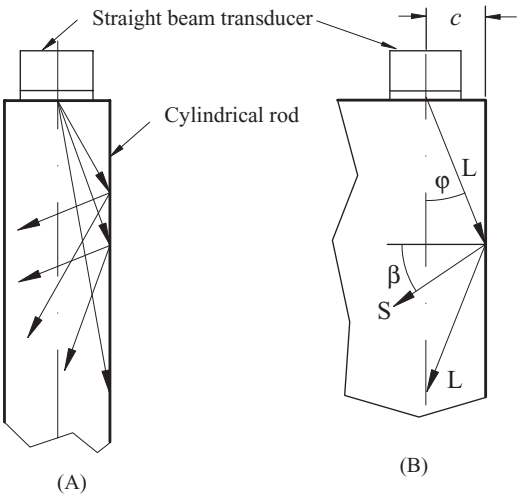

Figure 7.2 Illustration of wave guide effect in a cylindrical rod (A) and near a test object wall (B).

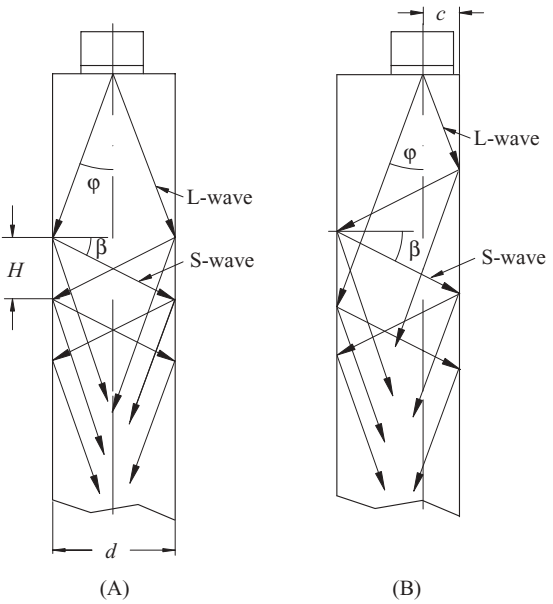

Figure 7.3 Beam propagation in a cylindrical rod: (A) symmetric and (B) asymmetric rod wave.

Table 7.1
Beam Divergent Angle φ and Angle β of Mode Converted S-wave

Crystal	Angles, degree	Transducer frequency, MHz			
diameter, mm		1.0	2.25	5.0	10.0
19	φ	12.3	5.4	2.44	1.22
	β	32.75	33.31	33.45	33.48
25.4	φ	9.2	4.1	1.8	0.9
	β	33.0	33.39	33.47	33.48

cases, a portion of L-wave will propagate along the rod axis and reflect from the bottom of the rod. The other portion of L-wave rays will strike the wall and the wave guide effect will take place.

To analyze the beam propagation, the beam divergent angles and the reflected angles of the mode converted S-wave should be determined. The beam divergent angles, calculated according to the well-known formula (Eq. 7.1), are summarized in Table 7.1, along with the angle β of mode converted S-wave, calculated according to Snell's law.

The divergent angle for the free field at the level of –6 dB is

$$\varphi = \arcsin K \frac{V_L}{f \times d} \tag{7.1}$$

If the transducer is located at the center of the rod (Figure 7.3A), the rod wave is symmetric. A screen capture of the signals from the symmetric rod waves reflected from the bottom of the rod has typically distinguished characteristics (Figure 7.4A, B).

Signal #1 here is from the back of the rod. Signals #2, 3, and 4 are the secondary signals created by the mode converted L-S waves. The distance *t*, or the time difference between each of the signals, is constant. It can be calculated as follows (see Figure 7.3).

The time of flight (TOF) for mode converted S-wave is

$$t_S = \frac{d}{\cos\beta \times V_S}. \tag{7.2}$$

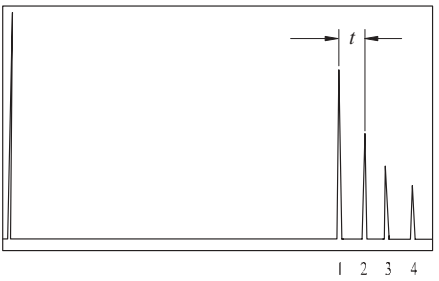

(A)

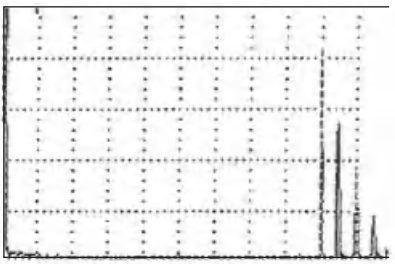

(B)

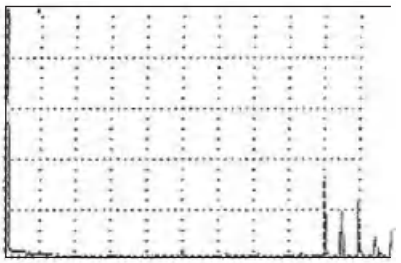

(C)

Figure 7.4 Screen pattern of the symmetrical rod wave (A), screen capture of signals generated by the symmetrical (B) and the asymmetrical (C) rod waves.

The TOF of the L-wave on distance L is

$$t_L = \frac{d \times \tan\beta}{\cos\varphi \times V_L}, \tag{7.3}$$

where d is the rod diameter,

V_S is shear wave velocity,

V_L is longitudinal wave velocity.

The TOF t_S has to be added to the total TOF, but TOF on the distance H has to be subtracted from it. The difference between these two times of flight is $t = t_S - t_L$,
and

$$t = \frac{d}{\cos\beta \times C_S} - \frac{d \times \tan\beta}{\cos\varphi \times V_L} = d\left(\frac{1}{\cos\beta \times V_S} - \frac{\tan\beta}{\cos\varphi \times V_L}\right). \tag{7.4}$$

For carbon and stainless steels, this difference in time is equivalent, approximately, to the time propagation of the distance equal to 0.7d [35]. This formula can be used for the verification and confirmation of the existence of the rod-guided wave.

When the transducer is located at some distance from the rod's centerline, the symmetry of the rod wave will be disturbed (Figure 7.3B), along with its typical arrangement of signals (Figure 7.4C), but the time differences between the signals will remain approximately the same.

Both rod-guided waves, symmetric and asymmetric, are useful for flaw detection in long cylindrical objects: bolts, studs, shafts, and so on. The application of either one of the techniques depends on the test object geometry. The symmetric technique does not allow for distinguishing the position on the circumference where the detected reflector is located and does not permit resolution of reflections, if several of them are located in close proximity to each other in the same cross section of the rod. When this is a requirement, the asymmetric technique application is preferable.

A single straight beam transducer with a wear plate can be used to generate the rod waves. There are no special requirements for these transducers except for the damping and frequency. The bandwidth should not exceed 20–30%. As to the frequency selection, one should remember that any test object material is a frequency filter, especially a long test object. Thus, it makes no sense to use high frequency transducers. The practical solution is to perform Spectral Fourier Fast Transform (FFT) analysis of the reflected signal from the back surface of the rod and to compare its center frequency to the nominal frequency of the transducer used. If the measured center frequency is less than one-half of the nominal transducer frequency, a different transducer should be used with its nominal frequency close to the measured frequency of the previous transducer.

7.3. TECHNIQUE DEVELOPMENT AND PROBE DESIGN FOR INSPECTION OF STEPPED SHAFT

As an example, configuration of the shaft to be inspected has the geometry of a long cylindrical rod with multiple changes in the diameter (Figure 7.5).

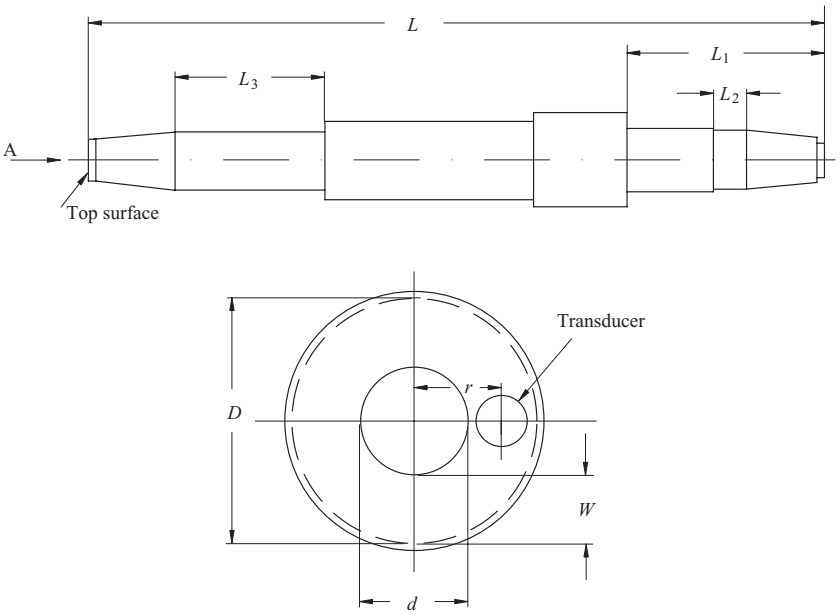

Figure 7.5 Simplified geometry of the stepped shaft and a geometry of a shaft top surface.

Any cracks would most likely be located in zone L_2 near the bottom of the shaft. The inspection should be performed from the top end of the shaft, which has the geometry shown in the same figure. At the center of the top end is a shallow hole, which restricts the inspection zone to a ring. Let us assume that the outside inspection diameter D of the ring is 160 mm, and the diameter of the shallow hole d is 100 mm. Thus, the width of the ring W is 30 mm. It restricts the transducer's crystal diameter to a maximum of 25 mm. The distance between the shaft's centerline and transducer center is in the range of $r \cong 65$ mm.

So, the distance between the central ray of the ultrasonic beam and the shaft's wall is small and, therefore, the boundary effect will influence the ultrasonic beam propagation. The illustration of ray tracing in cylindrical rod of the same length as the stepped shaft is shown in Figure 7.6.

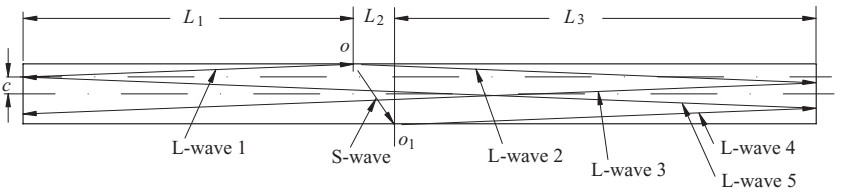

Figure 7.6 Example of ray tracing in a cylindrical rod.

In this case, when the transducer is located at the distance c from the rod centerline, the possible tracing of a ray may be as follows:

1. L-wave 1 to point o at the rod side,
   L-wave 2 from point o to the rod end,
   L-wave 3 back to the top.
2. L-wave 1 to point o at the rod side,
   S-wave from point o to point o_1,
   L-wave 4 from point o_1 to the rod end,
   L-wave 5 back to transducer.
3. Direct L-wave from the transducer to the rod end and back to the top (not shown in Figure 7.6).

The routine calculation of TOF consists of the following steps:

Step 1: Calculate the length of selected rays up to intersection with the rod surface or rod end (L_1, L_2, L_3).

Step 2: Calculate the metal path for each of the rays.

Step 3: Calculate TOF for each of the rays, and the total TOF.

An example of TOF calculation for a shaft with dimensions as illustrated in Figure 7.7 is presented below. A calculation is performed for a transducer 25.4 mm in diameter and a nominal frequency of 2.25 MHz. The results of this calculation, along with the measured data, are summarized in Table 7.2.

Predicted geometrical reflectors are

K1—from the upper keyway,

A—from the shoulder,

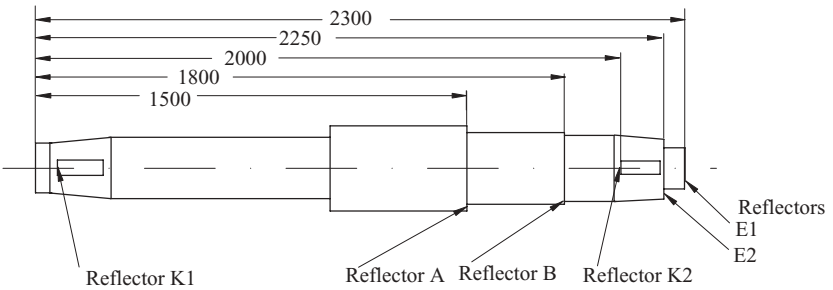

Figure 7.7 Simplified sketch of the shaft to be inspected.

Table 7.2
Calculated and Measured TOF

Distance to reflector, mm	Calculated TOF, μs	Measured TOF, μs
2300	806.0	802.4
2250	785.0	781.6
2000	721	724.4
1800	655.0	657.6
1500	532.0	537.6

B—from the step,

K2—from the lower keyway,

E1 and E2—from the shaft end.

The signals from all these reflectors can be used as reference signals to isolate a signal from a crack, the position of which is more likely to be between the reflections B and K2.

It may be confusing to make an interpretation of the signals on a C-scan and B-scan, due to the fact that the reflections may be caused by the rays located on both sides of the beam center line. For example, the reflections from the upper keyway and lower keyway will be 180° apart. The reflection from the crack will be shown at 180° apart from the transducer position.

7.4. TECHNIQUE DEVELOPMENT AND PROBE DESIGN FOR STUD INSPECTION

7.4.1. Stud Inspection from the Top Surface

Inspection of studs with two threaded ends (Figure 7.8) requires special attention to crack detection in the threaded zones. To make the stud inspection as sensitive as possible, a probe with two transducers should be used: the beam from the first transducer will cover the upper zone of the stud L_1, and the second transducer beam will provide coverage of the lower threaded zone L_2. Such an arrangement permits the use of the first transducer with the highest possible frequency and to extend the inspection range separately for each of the zones.

The screen presentation during the inspection is very handy. As an example, the screen capture in Figure 7.9 shows the signals from the

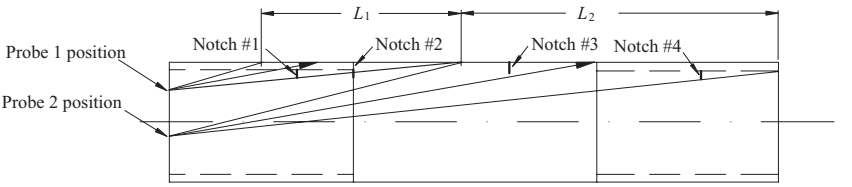

Figure 7.8 Inspection zones of the stud and locations of the reflectors.

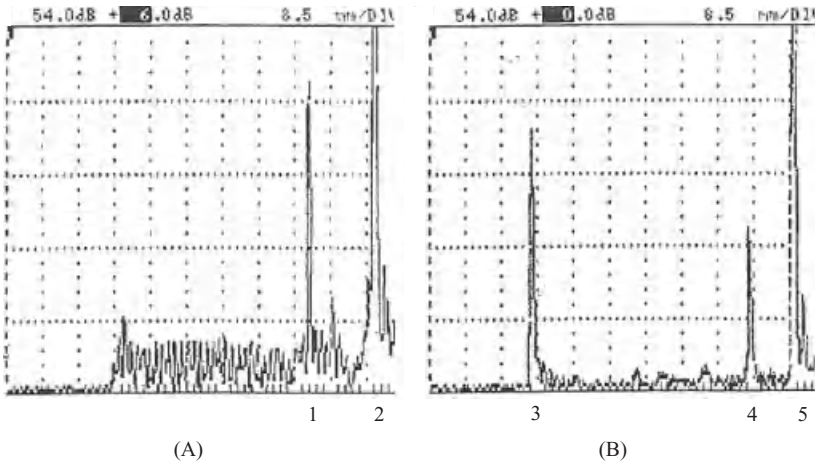

Figure 7.9 Screen captures of signals: (A) flaws in the upper threaded zone, (B) flaws in the second zone of the stud.

reflectors (notches) in the calibration standard, located in the zones as illustrated in Figure 7.8.

The difference in the signal responses from the threaded and shank zones is helpful in crack detection and identification. Reflector #1 is located in the upper threaded zone (Figure 7.9A) and is the higher amplitude signal in the area on the background of reflections from the threads. Signal #2 is from the reflector located at the thread to shank intersection (notch #2). Signal #3 is from the notch, located in the shank zone. Signal #4 is from the notch in the lower threaded zone, and finally, signal #5 is from the stud end.

An example of a probe design for stud inspection is shown below. Figure 7.10 illustrates the zones of the stud to be inspected. Circumferential cracks may occur in the upper and/or lower threaded zones as well as in the shank. The stud's length is divided into two inspection zones L_1 and L_2 and are inspected using two separate probes. The zone L_1 begins at distance H_1 from the top, and zone L_2 starts at distance H_2 from the top of the stud. The exit point of the first probe will be located at point a at distance c, and the second probe exit point will be located at point b at distance c_1 from the stud centerline.

The following is a probe design for the inspection of a stud with the following dimensions: length L = 250 mm and diameter D = 50 mm.

The dimensions for the first inspection zone are:

$$L_1 = 47 \text{ mm}$$

$$H_1 = 44 \text{ mm}$$

$$c = 13.0 \text{ mm}$$

The diameter of the crystal d and the wedge angle α_W is to be calculated.

Figure 7.11 shows schematically the first inspection zone geometry. The calculation can be performed in the following sequence.

The angle δ

$$\delta = \arctan \frac{H_1}{c_0} = \arctan \frac{44}{12} = 74°,$$

where

$$c_0 = \frac{D}{2} - c = \frac{50}{2} - 13 = 12 \text{ mm}.$$

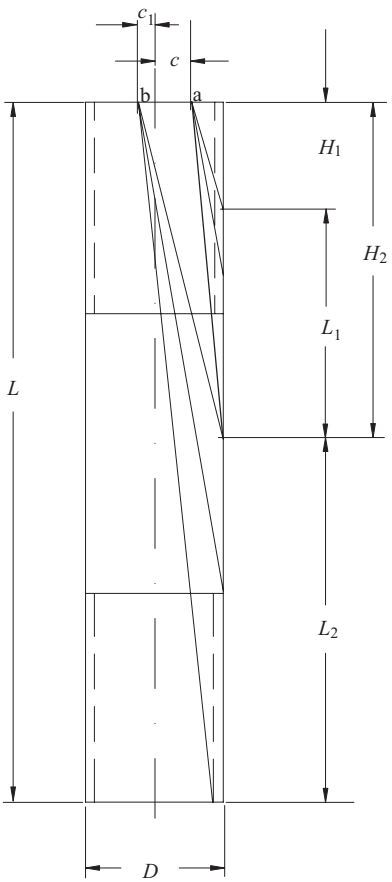

Figure 7.10 The zones of the stud to be inspected.

The length of the triangle side A is

$$A = \frac{H_1}{\sin \delta} = \frac{44}{\sin 74} = 45.8 \text{ mm}$$

The angle $\Delta = 90 + \delta = 90 + 74 = 164.0°$.

Then the triangle side C is

$$C = \sqrt{\left(A^2 + L_1^2 - 2 \times A \times L_1 \times \cos \Delta\right)}$$
$$= \sqrt{\left(45.8^2 + 47^2 - 2 \times 45 \times 47 \times \cos 164\right)} = 92.2 \text{ mm}.$$

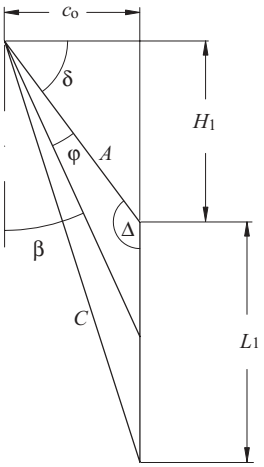

Figure 7.11 The stud first inspection zone parameters.

The divergent angle φ

$$\varphi = \arcsin\left(\sin\Delta\frac{L_1}{2C}\right) = \arcsin\left(\sin 164\frac{47}{2\times 92.2}\right) = 4.0°$$

The crystal diameter d can be calculated as

$$d = K\frac{V_L}{\sin\varphi\times f} = 0.7\frac{5.85}{\sin 4\times 5} = 11.74 \text{ mm},$$

where $f = 5.0$ MHz is the transducer frequency,

$V_L = 5.85$ mm/μs is the L-wave velocity in steel.

A crystal diameter of 12.0 mm is acceptable.

The refracted angle β is

$$\beta = 90 - (\delta + \varphi) = 90 - 74 - 4 = 12°.$$

And finally, the wedge angle α is

$$\alpha = \arcsin\left(\sin\beta\frac{V_W}{V_L}\right) = \arcsin\left(\sin 12\frac{2.735}{5.85}\right) = 5.58°,$$

where $V_W = 2.735$ mm/μs is the wave velocity in the Plexiglas wedge.

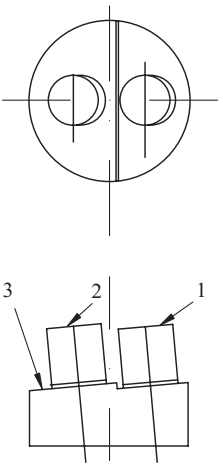

Figure 7.12 Duplex probe conceptual design: (1) transducer for the first zone inspection, (2) transducer for the second zone inspection, (3) a wedge.

The parameters for the second probe can be calculated in the same manner as for the first probe.

The conceptual design of the duplex probe is shown in Figure 7.12.

To perform the stud inspection, the probe should be positioned on the top of the stud in the holding fixture and rotated 360° to cover the entire volume of the stud to be inspected.

7.4.2. Stud Inspection from a Center-Drilled Bore

The guided wave technique for cylindric rod inspection produces reliable results when applied to studs with a relatively good outside surface condition. When the stud is severely corroded, this technique does not produce reliable results. In Figure 7.13A, a severely corroded stud is shown. This corrosion damage was not detected by an examination from the top surface of the stud. The corroded zone becomes a trap for an ultrasonic beam, as schematically shown in Figure 7.13B.

If the stud has a center-drilled bore, it is better to use conventional straight or angle beam techniques, applying the probe from the bore side. It makes the stud inspection not only more reliable, but also more sensitive. The probe design can vary depending on the inspection requirements, but the technique basics remain the same. The straight

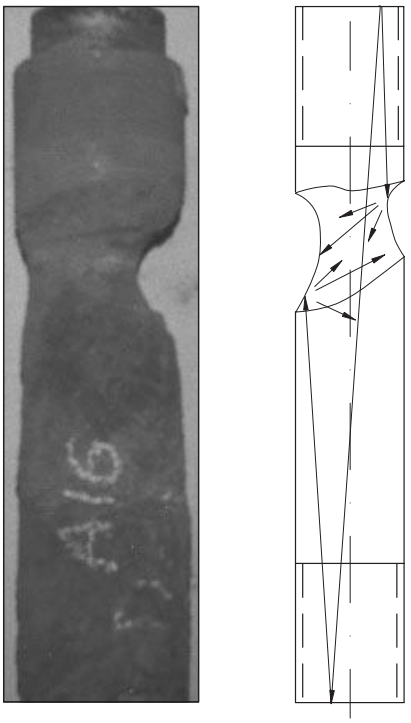

(A) (B)

Figure 7.13 Severely corroded stud (A) and corroded zone trap (B).

beam technique can be used for mapping corrosion on the outside stud surface. The angle beam technique can be used for the detection and sizing of cracks that are located on the outer stud surface and oriented in the circumferential direction.

Especially important, and at the same time challenging, is to detect cracks in the threaded zones. One of the probes designed for stud inspection from the bore side is shown in Figure 7.14.

The same angle beam probe can be utilized as either pulse–echo or shadow techniques, as illustrated in Figure 7.15.

At the probe position A in the shank zone, the reflection from crack a has a usual pattern (pulse–echo technique). The typical pattern of the reflections from the threaded zone (probe position B) consist of signals with different amplitudes (seven signals are shown). The central portion of the beam (ray 4) produces the highest signal. These signals are the

Figure 7.14 Example of probe design for a stud inspection from the bore side. Reprinted by permission of Westinghouse Electric Company LLC.

background *noise* from which the useful signal from crack b should be differentiated when the probe is in position C.

In order to obtain reliable inspection results, the signal-to-noise ratio should be at least 2 to 1. However, it is very difficult to achieve this ratio by a positive signal, which is the signal above the noise level. It is more reliable to choose a negative signal, which is the signal below the noise level. For example, in the case when the crack **b** is located in the valley of the thread (thread #4), a portion of the ultrasonic beam will not penetrate through the crack, and threads #2 and #3 will be in the *shadow*. The signal's amplitude from thread #4 will have slightly higher amplitude, but the signal's amplitude from threads #2 and #3 will be drastically reduced. This is a reliable indication of the presence of a crack. The screen captures at the two probe positions B and C, are shown in Figure 7.15D, E.

Several probe designs can be employed: single straight and angle beam immersion transducers, or a mirror system, depending on the bore diameter, number of transducers, and the inspection requirements.

The design of the mirror system requires special attention. The system can consist of from at least one mirror M and one transducer T (Figure 7.16). The mirror directs the ultrasonic beam at the desirable angle of incidence α. Sketch 1 illustrates the direction of the straight beam. Sketch 2 illustrates the direction of the aft oriented angle beam, and sketch 3 illustrates the direction of the forward oriented angle beam. Only the central rays of the beams in the plane of incidence are shown in the Figure 7.16 sketches.

The mirror angle α_M (Figure 7.17) can be calculated as

$$\alpha_M = \frac{90 \pm \alpha}{2}, \tag{7.5}$$

where α is the angle of incidence.

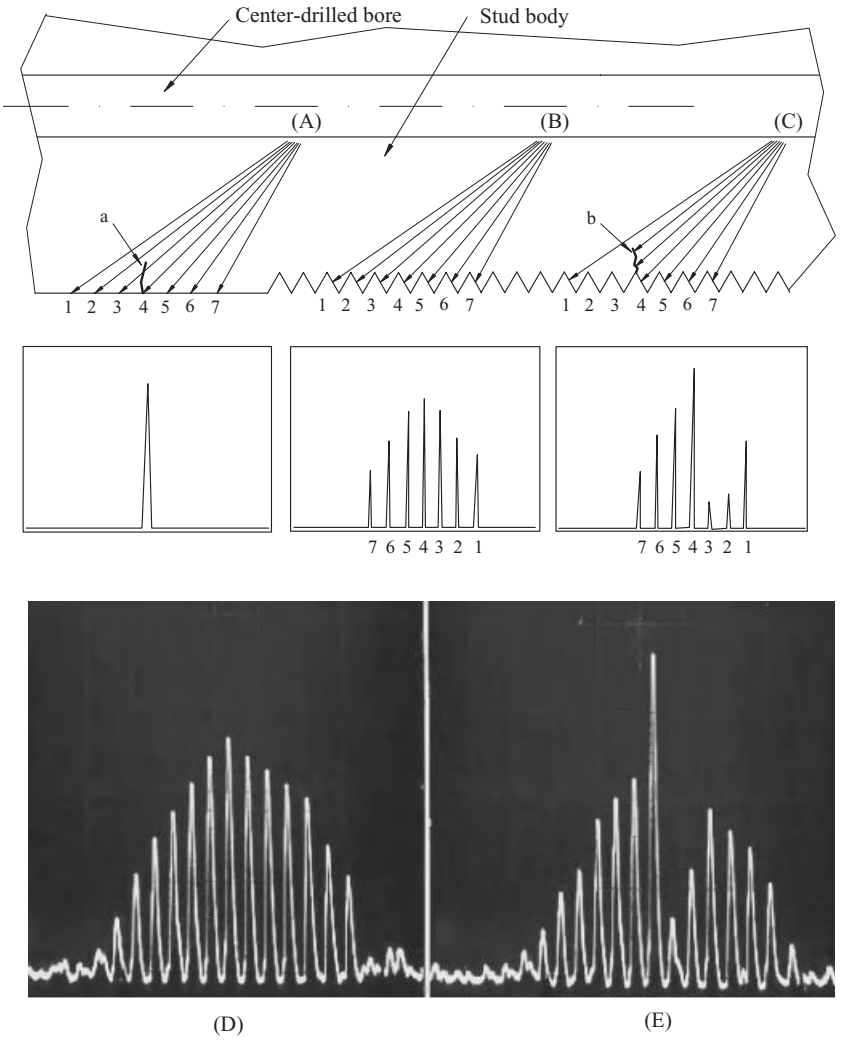

Figure 7.15 Position of the probe and signals from reflectors: (A) in the shank zone with crack, (B) in the threaded zone without crack, (C) in the threaded zone with crack. a, a crack in the shank zone; b, a crack in the threaded zone. Screen captures: (D) no crack, (E) crack in threaded zone.

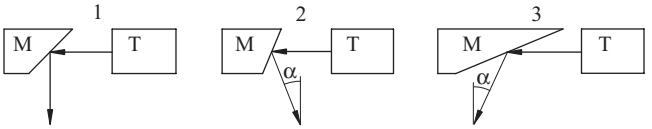

Figure 7.16 Directions of ultrasonic beams reflected from mirrors: (1) a straight beam, (2) a back oriented angle beam, (3) a forward oriented angle beam. M, mirror; T, transducer.

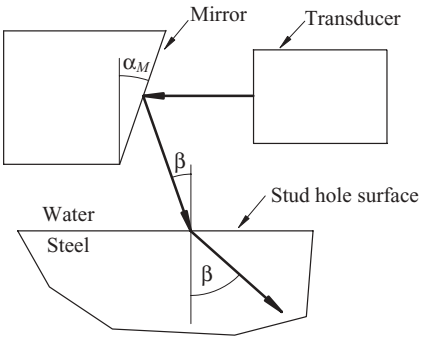

Figure 7.17 A mirror angle calculation for detection of a circumferential crack.

The sign "–" applies to the aft oriented angle beam mirror system, and the sign "+" to the forward oriented angle beam mirror system.

The angle of incidence as usual is

$$\alpha = \arcsin \beta \frac{V_W}{V_M} \tag{7.6}$$

where: β is given refracted angle in the test object,

V_W is sound velocity in water,

V_M is sound velocity in test object material.

The sketch in Figure 7.17 represents the beam central rays in the plane of incidence. The ray's direction in the plane of incidence and perpendicular to the incident plane are shown in Figure 7.18A for the straight beam. Circle D is the projection of the crystal diameter on the mirror face. The bore surface of the stud acts as a cylindrical focusing lens. The section A-A in Figure 7.18A shows the direction of the rays from three points of the strip L of the flat mirror. Ray 1 will not refract. Rays 2 and 3 will refract into the stud body at different

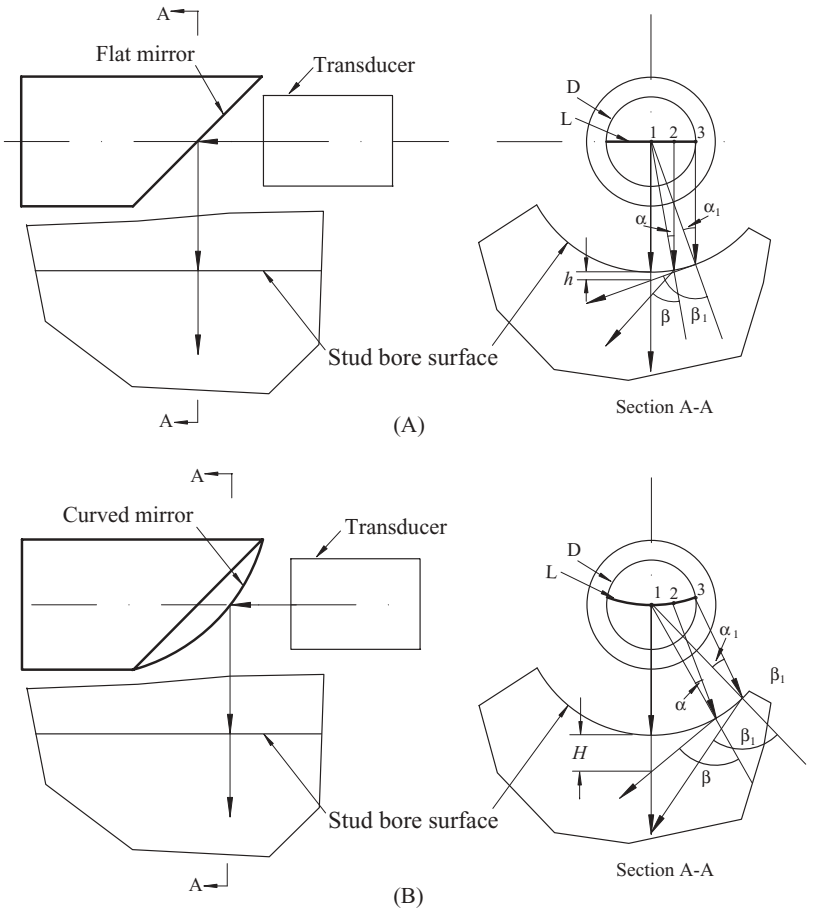

Figure 7.18 Comparison of reflections from flat (A) and curved mirrors (B).

angles, β and β_1. Ray 3, for example, intersects the central axis of the stud at distance *h*, which is a minor portion of the stud wall thickness to be inspected.

In many cases of stud or thick wall tube inspection, it is necessary to concentrate the ultrasonic energy at a specified distance of the stud or tube wall in order to increase the detection sensitivity. This can be achieved by profiling the mirror.

For example, a convex mirror increases the distance of the rays' intersection (Figure 7.18B). By calculating the mirror radius, it is possible to achieve the desirable distance *H*.

To calculate the distance H, it is practical to arbitrarily prescribe the mirror radius R_g, then calculate R_m (Figure 7.19). The profile of the mirror at any section is an ellipse with dimensions $2a = 2\,R_g$ and $2b = 2\,R_g \cos \alpha_M$. To simplify the fabrication of the mirror, the ellipse can be substituted by a circle. As a good approximation, this circle radius $R_m = 2b$ (Figure 7.20).

At this time, the angle of the mirror α_M and a point on the mirror for which the ray tracing has to be performed should be chosen. The diagram for ray tracing is shown in Figure 7.21.

Now assume that the ray tracing starts from the point 0_3 at the distance $d/4$ from the center line of the mirror (d is diameter of the

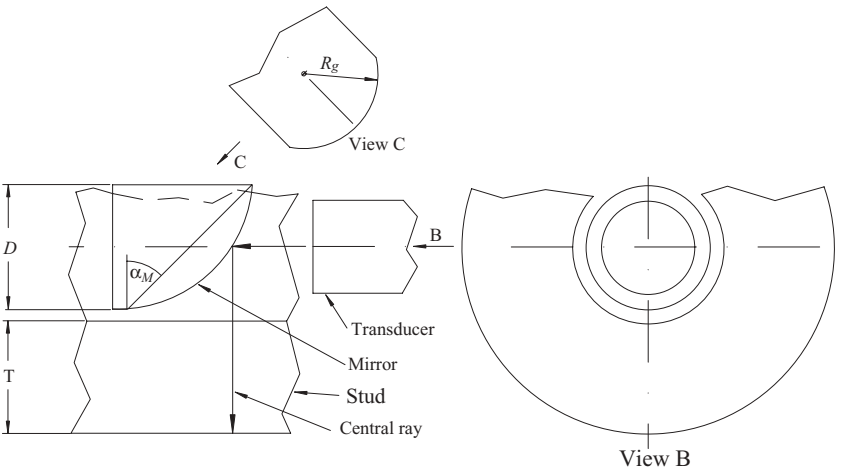

Figure 7.19 Relative positions of a convex mirror and a transducer in a stud bore.

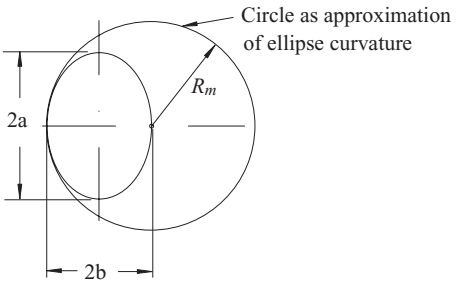

Figure 7.20 Profile of the mirror at a section of 45° (See Figure 7.19).

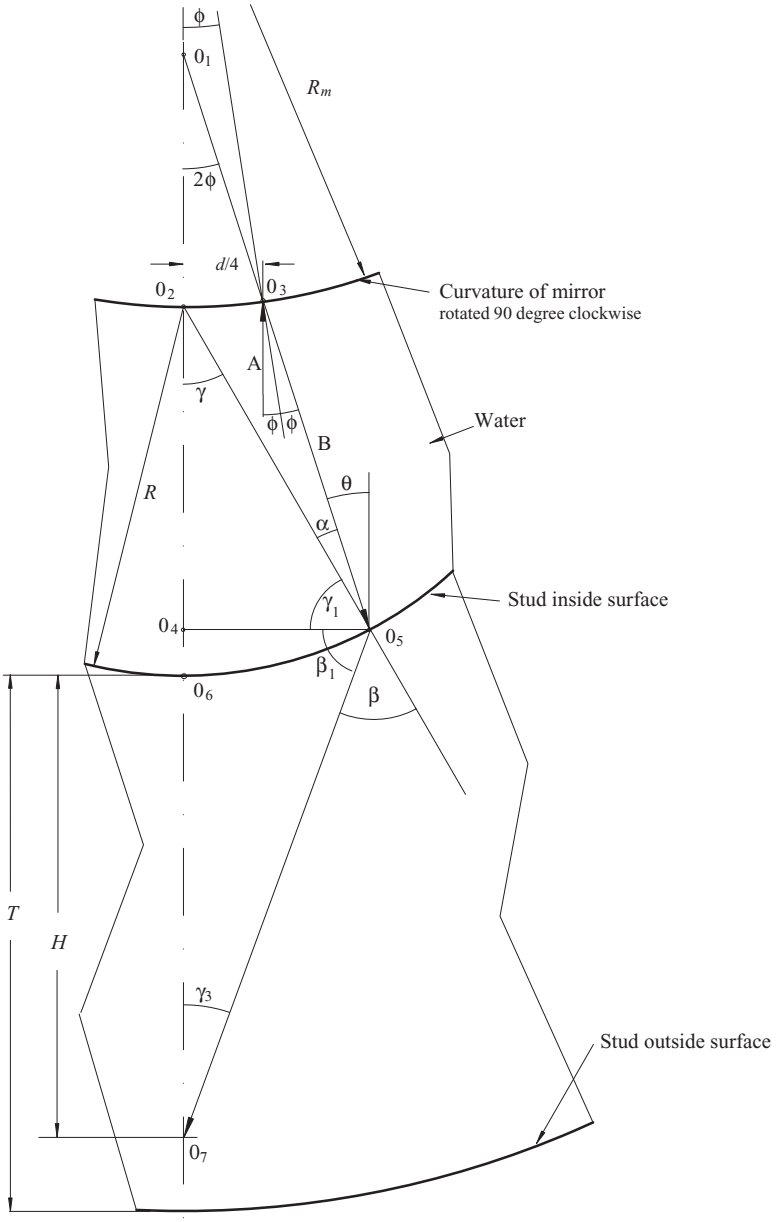

Figure 7.21 Ray tracing reflected from a curved mirror.

crystal). If the incoming ray A strikes the mirror at point 0_3, the angle ϕ is

$$\phi = \arctan \frac{d}{4R_m}. \tag{7.7}$$

The refracted ray B from the mirror strikes the inside surface of the tube also at the angle ϕ at point 0_5. The angles to be calculated are γ, θ, α, and finally β. To determine the angle γ, let us assume that $0_30_5 = 0_20_5 = R$.

Then,

$$0_10_3 = \frac{d}{4\sin 2\phi}. \tag{7.8}$$

As a first approximation, the length $0_10_5 = 0_10_3 + R$. The distance 0_40_5 is

$$0_40_5 = 0_10_5 \times \sin 2\phi.$$

So, the angle γ is

$$\gamma = \arcsin \frac{0_40_5}{R}. \tag{7.9}$$

Then the angle θ is

$$\theta = \arctan \frac{0_40_5 - \dfrac{d}{4}}{0_50_7}, \tag{7.10}$$

where $0_50_7 = R \times \cos \gamma$.

And then $\alpha = \gamma - \theta$.

Finally,

$$\beta = \arcsin\left(\sin \alpha \frac{V_M}{V_W} \right). \tag{7.11}$$

The next step is to determine the intersection point of the refracted ray with the axes, which is the distance H. To do this, the following angles have to be calculated:

$$\gamma_1 = 90 - \gamma,$$

$$\beta_1 = 90 - \gamma - \beta,$$

$$\gamma_3 = 90 - \beta_1.$$

And finally

$$H = \frac{0_4 0_5}{\tan \gamma_3} - R(1 - \cos \gamma). \tag{7.12}$$

The point 0_7 is at the intersection of the refracted ray with the tube axis. As an example, calculation was performed for the tube with wall thickness *T*. The distance *H* has to be slightly less than *T*. One can see that this requirement is met. This proves that the curvature of the mirror was calculated correctly.

7.5. NOTCH DIMENSION CALCULATION FOR STUD CALIBRATION STANDARDS

As is well known, the system for any ultrasonic test shall be calibrated. For bolt and stud inspection, circumferentially oriented reflectors as notches shall be machined in the threaded zones of the calibration standards. Requirements for the dimension of the notches are specified in appropriate documentation.

Three types of notch reflectors are practically applicable in the stud calibration standards. They are segment (A), ring sector (B), and "Lentil" (C) as shown in Figure 7.22.

For a given outside radius *R* of a stud, two parameters of the notch are specified: the maximum depth *T* and maximum area *S*. Occasionally, the shape of the notch is also specified.

The length of the notch 2L needs to be calculated, and for the *Lentil* notch, the radius of the cutter as well.

A. Segment notch parameter calculation

The segment notch area can be calculated as the difference between the area of the sector and area of triangle.

$$S_{SEG} = S_{SEC} - S_{TR}. \tag{7.13}$$

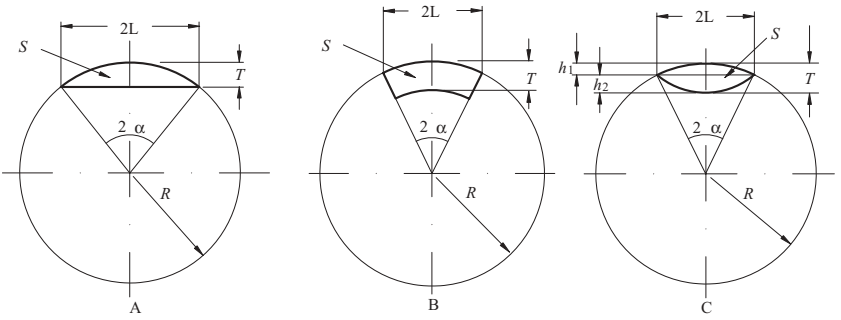

Figure 7.22 Shape of the notches for studs calibration standards: (1) a segment, (2) a ring sector, (3) a lentil.

$$S_{SEG} = \frac{\pi R^2}{180}\alpha - L(R-T). \tag{7.14}$$

The half of the sector angle

$$\alpha = \arcsin\frac{L}{R}.$$

The dimension L equals

$$L = \sqrt{T(2R-T)}.$$

B. Ring sector notch parameter calculation

For this notch reflector, the central angle 2α should be calculated first for given S and T:

$$2\alpha = \frac{360 \times S}{\pi\left[R^2 - (R-T)\right]}. \tag{7.15}$$

And then the length of the notch is

$$2L = R \times \sin\frac{\alpha}{2}. \tag{7.16}$$

C. "Lentil" notch parameter calculation

In this case, the depth of the notch area has to be divided into two segments with heights h_1 and h_2

$$T = h_1 + h_2.$$

To determine the length of the notch, the following equation can be used:

$$2L = \frac{3 \times \sum S}{2 \times T}, \tag{7.17}$$

where

$$\sum S = S_1 + S_2,$$

$$S_1 \cong \frac{2}{3} 2L \times h_1,$$

$$S_2 \cong \frac{2}{3} 2L \times h_2,$$

$$\sum S = \frac{2}{3} 2L \times T.$$

The height of each segment of the notch can be determined as

$$h_1 = R \pm \sqrt{\left(R^2 - L^2\right)}$$

$$h_2 = T - h_1$$

And finally, the radius of the cutter is

$$r = \frac{L^2 + h_2^2}{2 \times h_2}. \tag{7.18}$$

Examples of calculations

As an example, let us calculate the notch parameters for a 6.0-in. diameter stud. According to ASME Code Section XI, Appendix VIII, 2007 Edition, two parameters are specified: the maximum notch depth and the maximum notch reflective area. For example, for a stud greater

than 4.0 in. in diameter, the maximum notch dimensions are depth $T = 0.157$ in. and area $S = 0.059$sq in. The shape of the notch is not specified. The specified notch dimensions in ASME Code are presented in English Units; therefore, the calculation shown below is in the same units.

(a) Segment notch parameter calculation

To calculate the segment notch area for the maximum notch depth $T = 0.157$ in.

$$L = \sqrt{0.157(2\times 3.00 - 0.157)} = 0.958 \text{ in.}$$

$$\alpha = \arcsin\frac{0.958}{3.00} = 18.62^\circ$$

$$S_{SEG} = \frac{\pi 3.00^2}{180} 18.62 - 0.958(3.00 - 0.157) = 0.200 \text{ sq in.}$$

This area far exceeds the maximum allowable area.

Thus, the depth of the notch should be reduced and the calculation repeated by the trial-and-error method up to the point where $S_{SEG} = 0.059$ sq in.

The calculation shows that the maximum allowable notch area has to be at $T = 0.07$ in. At this depth, the length of the notch is 1.289 in.

The typical ratio $2L/T$ for a fatigue crack is from 3 to 5. For this notch, the ratio is 18.4, and thus the shape of the notch cannot represent a fatigue crack.

(b) Ring sector notch parameter calculation

The central angle is

$$2\alpha = \frac{360\times S}{\pi\left[R^2 - (R-T)\right]} = \frac{360\times 0.059}{\pi\left[3^2 - (3-0.157)^2\right]} = 7.38^\circ.$$

The notch length

$$2L = R\times \sin 2\alpha = 3\times \sin 7.38 = 0.385 \text{ in.}$$

The ratio of the notch length to the depth is

$$\rho = \frac{2L}{T} = \frac{0.385}{0.157} = 2.45.$$

The ratio and the shape of this notch cannot represent a fatigue crack either.

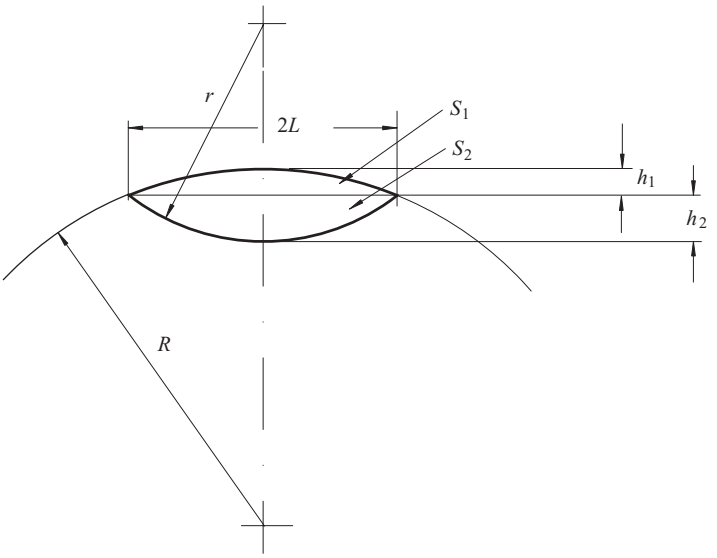

Figure 7.23 Diagram related to "Lentil" notch area calculation.

(c). "Lentil" notch parameter calculation
The length of the notch is (Figure 7.23)

$$2L = \frac{3\times\sum S}{2\times T} = \frac{3\times 0.059}{2\times 0.157} = 0.564 \text{ in.}$$

The height of each segment is

$$h_1 = R \pm \sqrt{\left(R^2 - L^2\right)} = 3 \pm \sqrt{3^2 + 0.282^2} = 0.0133 \text{ in.}$$

$$h_2 = T - h_1 = 0.157 - 0.0133 = 0.1437 \text{ in.}$$

Now the radius of the cutter (to machine the notch) can be determined as

$$r = \frac{L^2 + h_2^2}{2\times h_2} = \frac{0.282^2 + 0.1437^2}{2\times 0.1437} = 0.384 \text{ in.}$$

The ratio of length to depth is

$$\rho = \frac{2L}{T} = \frac{0.564}{0.157} = 3.6.$$

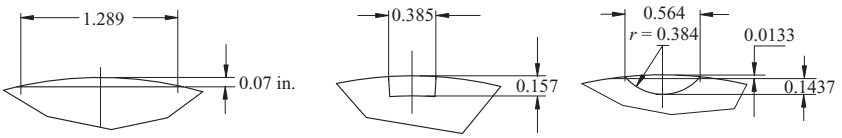

Figure 7.24 Real shape and calculated dimensions of the notches.

The shape and ratio 2L/*T* of the *Lentil* notch represents a fatigue crack much better than the other two notches.

Figure 7.24 shows the real shapes and dimensions of the all three notches.

CHAPTER 8

Technique Development and Probe Design for Hollow Cylinder Inspection

8.1. LAMB WAVE GENERATION

An ultrasonic inspection of a test object with a thick wall can be treated as an inspection of a semi-infinite medium. In this case, as it was mentioned in Chapter 7, the only possible cause of beam propagation distortion is a reflector located inside the beam lobe's volume, limited by its borders (Figure 8.1).

When the volume of the lobe exceeds the volume or thickness of the test object, the rays of the ultrasonic beam are confined by the object's walls, and the boundary effect will take place. As is known, the boundary effect causes mode conversion and beam redirection. These two phenomena will interfere with the normal propagation of the beam and the ultrasonic beam becomes *guided*.

An example of what happens with an angle beam propagation in a flat plate when its wall thickness is decreased is shown in Figure 8.2.

Ultrasonic Inspection Technology Development and Search Unit Design: Examples of Practical Applications, First Edition. Mark V. Brook.

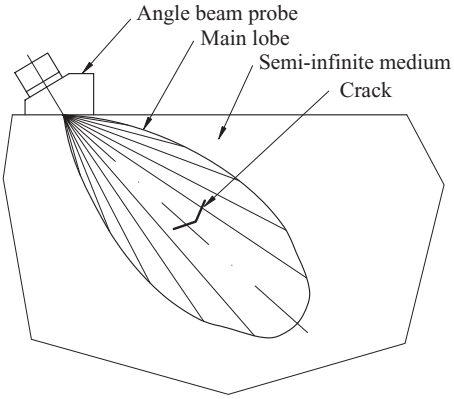

Figure 8.1 An angle beam probe main lobe position in a semi-infinite medium.

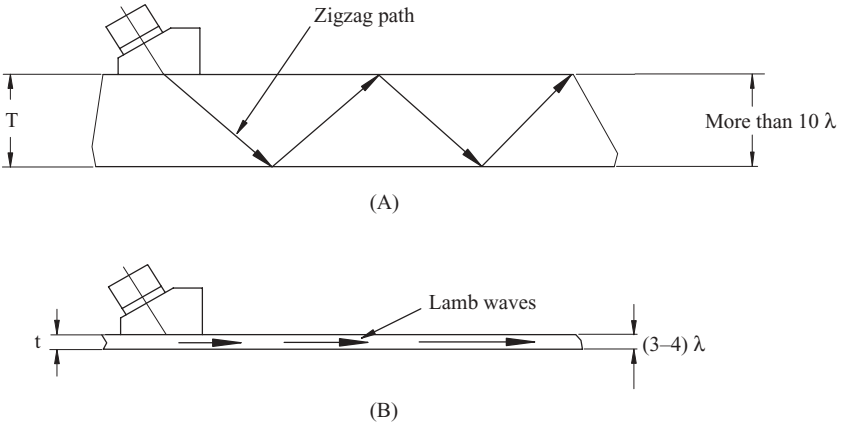

Figure 8.2 Illustration of beam propagation change when the wall thickness decreases: (A) thick wall, (B) thin wall.

When the wall thickness is much greater than the wavelength ($T >> \lambda$) (Figure 8.2A), the beam will propagate in a zigzag path, and the mode will not change. In instances where the wall thickness is $t \cong (3–4)\ \lambda$, a new phenomenon will be observed—*plate* or *Lamb* waves can be generated (Figure 8.2B). Lamb waves are one of a variety of *guided waves*.

Approximately, a similar but more complicated phenomenon will occur during ultrasonic wave propagation in thin wall tubing: axially

symmetric and non-axially symmetric *Lamb-type* modes may be created.

Lamb waves are defined as the *elastic vibration propagating in a solid plate with free boundaries for which displacement occurs both in the direction of wave propagation and perpendicularly to the plane of the plate* [13].

To distinguish waves in a plate from waves in a hollow cylinder, the latter can be named *Lamb-type guided waves*.

In order to design probes for Lamb-type guided wave generation in a hollow cylinder, it is necessary to know, in some detail, conditions for the formation and propagation of ultrasonic waves in thin plates. An effective way of generating Lamb waves is by using the same type of angle beam probes as for bulk wave generation, but with specific angles of incidence and size of crystals.

Propagation of ultrasonic waves in thin plates is completely different from propagation of bulk waves in thick plates. The definition of a thin and a thick plate for Lamb wave application is stricter than in the case of bulk waves. A thin plate can be defined as a plate with the thicknesses commensurable with the wavelength. Thick plates, by definition, have thickness much greater than the wavelength.

The best application for Lamb waves is for the inspection of plates (or tubes) with thicknesses ranging from 0.10 to 5.0 mm with the transducer frequency varying from 1.0 to 10 MHz. The height of a crack that can be detected is approximately 30% of the plate thickness for thinner plates (0.2 mm) and 5% for thicker plates (up to ≈5 mm).

In general, the transformation from bulk waves to Lamb waves occurs due to the reflection and mode conversion inside the thin plate. In a very simplified case, the condition for the formation of Lamb waves can be illustrated by substituting a solid plate with a liquid layer or thin film. In this case, only a longitudinal wave will propagate in the layer, and no mode conversion will occur [3].

Let us assume that an incident plane wave with a front AB at an angle of incidence α strikes the surface of the liquid layer with a thickness d (Figure 8.3). The refracted wave with a front CD at an angle β will propagate in the layer and will be repeatedly reflected from the layer's boundaries. Under a certain angle of incidence, the wave reflected from the back surface of the layer will be in phase with the incident wave. This is the condition where "Lamb waves" are created in a liquid layer as well as in the thin solid plate.

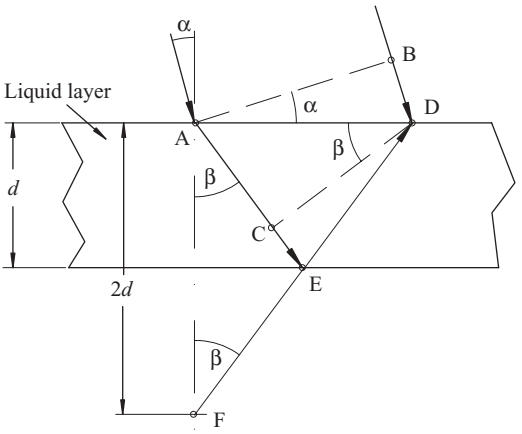

Figure 8.3 Formation of "Lamb waves" in a liquid layer.

In order to find the phase differences between the incident and the refracted waves, it is necessary to calculate differences in their paths.

In Figure 8.3, AE = ED = FE. The angles marked by β are equal.

The path from point A to point D by the refracted wave is equal to

$$\mathrm{AED} = \frac{2d}{\cos\beta}, \tag{8.1}$$

which is obvious from triangle AEF.

The path AC is

$$\mathrm{AC} = 2d \times \tan\beta \times \sin\beta. \tag{8.2}$$

The condition for the incident and the refracted waves to be in phase is

$$\frac{\mathrm{AED}}{\lambda_2} - \frac{\mathrm{AC}}{\lambda_2} = n. \tag{8.3}$$

Substitute AED and AC from Equations 8.1 and 8.2 into Equation 8.3,

$$\frac{1}{\lambda_2}\left[\frac{2d - (2d \times \tan\beta \times \sin\beta)}{\cos\beta}\right] = n, \tag{8.4}$$

where λ_2 is the wavelength in the liquid layer,

$n = 1,2,3\ldots$ is the number which represents the phase lag.

Substitute $\tan\beta$ and $\sin\beta$ by $\cos\beta$, Equation 8.4 can be rewritten as

$$\frac{2d\times\cos\beta}{\lambda_2} = n. \tag{8.5}$$

Thus, the angle at which the incident and the refracted waves will be in phase is

$$\beta = \arccos\frac{\lambda_2}{2d}n. \tag{8.6}$$

Replacing wavelength λ with wave velocity V_2 and frequency f as $\lambda_2 = V_2/f$ we will obtain

$$\frac{2d\times\cos\beta\times f}{V_2} = n. \tag{8.7}$$

By solving the equation against the wave velocity, it becomes clear that the wave velocity in the thin liquid layer depends on its thickness, frequency, and the refracted angle of the probe:

$$V_2 = 2d\times f\times\cos\beta\frac{1}{n}. \tag{8.8}$$

This is in general agreement with Lamb wave propagation in a solid thin plate.

8.1.1. Phase and Group Velocities

When Lamb waves propagate in a thin layer, two separate velocities of wave propagation should be considered: *phase velocity* and *group velocity*. In general terms, the velocity of the point of constant phase on the wave front is the *phase velocity* $\boldsymbol{V}_{\mathbf{ph}}$. The direction of $\boldsymbol{V}_{\mathbf{ph}}$ vector is perpendicular to the wave front. The *group velocity* $\boldsymbol{V}_{\mathbf{gr}}$ is the velocity of energy flow and is measured in the direction of beam propagation. The notation of the phase and group velocities is borrowed from physical optics. In the previous sections, when we considered a longitudinal or shear wave propagation, we did not distinguish between the

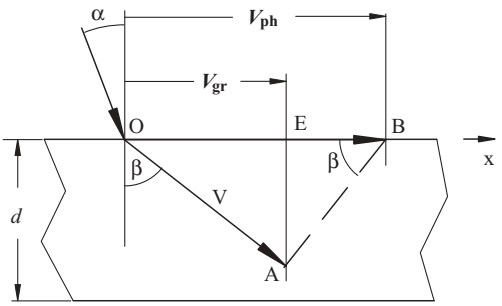

Figure 8.4 Relationship between bulk V, phase V_{ph}, and group V_{gr} velocities.

phase and the group velocities. This is due to the fact that in a thick, solid, acoustically isotropic material, these velocities of bulk waves are equal, independent of beam angle and constant for a given material.

This is not the case for Lamb waves. A plate, or, in our case, liquid layer, serves as a guide. The direction of "bulk" velocity $\boldsymbol{V}$ in the layer is along line O-A with wave front A-B (Figure 8.4). The phase and group velocities are measured along the x-axis. When the low point of the wave front vector is at point A, the upper corner of the front will reach point B. So, at given time τ the wave will propagate distance O-B with velocity $\boldsymbol{V}_{ph.}$

At the same time τ the energy front will move only from point O to point E with group velocity $\boldsymbol{V}_{gr}$. So, the physical meaning of the group velocity can be described as follows: the wave front is moving along line O-A with velocity $\boldsymbol{V}$, but under angle β to the liquid layer (plate) surface, and undergoes multiple reflections from the liquid layer (plate) boundaries; thus, the energy front relative to the plate surface moves with the group velocity. The phase and group velocities for the same liquid layer as mentioned above can be calculated by using the corresponding formulas:

The phase velocity is $\boldsymbol{V}_{ph} = \mathbf{V}/\sin\beta$ or because $\sin^2\beta = 1 - \cos^2\beta$,

$$\boldsymbol{V}_{ph} = \frac{\boldsymbol{V}}{\sqrt{1-\left(n\dfrac{\lambda_2}{2d}\right)^2}}. \tag{8.9}$$

The group velocity is $\boldsymbol{V}_{\mathbf{gr}} = \mathbf{V} \times \sin\beta$ or

$$\boldsymbol{V}_{\mathbf{gr}} = \boldsymbol{V}\sqrt{1-\left(n\frac{\lambda_2}{2d}\right)^2}. \tag{8.10}$$

Thus, the phase and group velocities depend on the plate thickness d and the wavelength λ_2 of the refracted wave.

The phase velocity is approximately equal to the group velocity if the plate thickness is more than 10 wavelengths, that is $d/\lambda_2 \geq 10$.

Dispersion of the velocities is one of the main characteristics of Lamb waves. In instances where $d/\lambda \to \infty$, that is, for a thick plate, the velocities tend to achieve velocity of bulk waves.

According to physical optics, the relation between phase and group velocities can be established by considering the groups formed by superposition of two (or more) waves with slightly different parameters. For example, when two waves with slightly different frequencies f and f_1 propagate in some medium, their interference leads to the creation of wave groups as illustrated in Figure 8.5. At position A_{min}, a group minimum amplitude (node of the wave) will exist, and at position A_{max}, a group maximum amplitude (crest) will exist. The resultant waves have an average wavelength, but the amplitude is modulated to form groups. The wavelength of the group is greater than the wavelength of each of the original waves, but the velocity of the group

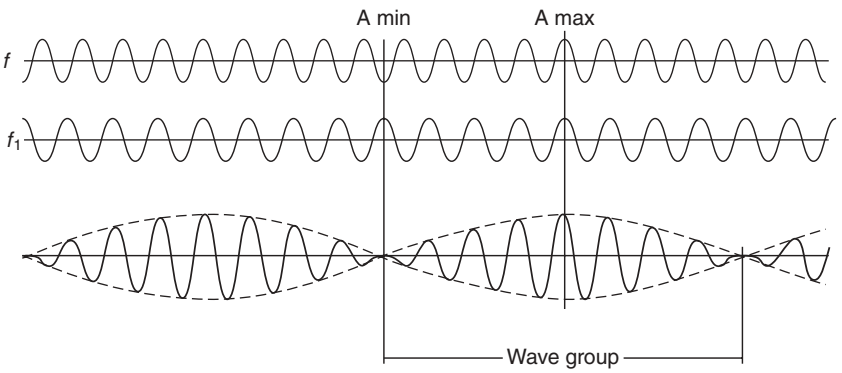

Figure 8.5 Creation of the wave groups.

propagation is less. The relationship between phase and group velocities is

$$V_{gr} = V_{ph} - \lambda \frac{dV_{ph}}{d\lambda}, \tag{8.11}$$

where λ is actual wavelength in the medium.

Although this equation was derived for simple (sinusoidal) types of waves, it can be applied to more complicated wave types. It is also correct for frequencies in the ultrasonic diapason.

The energy flow is carried out by the wave group pockets and is represented by the group velocity. This velocity can be measured and therefore compared with the calculated group velocity. This can help in the identification of the Lamb wave mode and also in the determination of the detected reflector position.

8.1.2. Lamb Wave Propagation Parameters

In case of a thin solid layer, the formation of Lamb waves is much more complicated due to the existence of shear waves and mode conversion. Consequently, the equations of the phase and the group velocities became complicated and unsuitable for hand calculations.

Lamb wave propagation parameters are given usually as a set of dispersion curves that present phase and group velocities of selected modes, along with angles of incidence, as a function of the product: transducer frequency by the plate thickness $f \times d$. The dispersion curves are calculated by using a special computer program. The plate material parameters, such as bulk velocities and densities, along with the same parameters of the wedge material, are the components used in the programs. The calculated dispersion parameters are very sensitive to these values, especially to the longitudinal and shear wave velocities of the test object and wedge materials. Their values should be measured on samples that represent the actual material of the test object and the wedge.

To determine the correct wedge angle, it is necessary to use the measured values of the plate and the wedge material parameters to calculate the dispersion curves. However, the calculated parameters do not ensure the best results for generating the selected Lamb wave mode.

Practically, the parameters, especially the wedge angle, have to be verified experimentally by using a calibration standard.

Two separate graphs of the dispersion curves are shown in Figure 8.6 to determine the phase and group velocities (only several most usable modes are marked). The phase velocity value V_{ph} is used for wedge (incident) angle calculation according to Snell's law, as

$$\alpha = \arcsin \frac{V_w}{V_{ph}}, \tag{8.12}$$

where V_w is velocity in the wedge material.

Each curve on each graph represents one mode which is traditionally marked by the letters A_0, S_0, A_1, S_1, and so on. The letter A is designated for asymmetric modes and the letter S for symmetric modes. The subscript $_0$ marks the lower modes that transform into surface wave when the plate thickness increases. The modes of higher orders, as 1st, 2nd, and so on, arise under specific values d/λ for each of the modes. These values correspond to resonance vibrations of given thickness for longitudinal or shear waves. For example, the mode A_1 will arise starting from the half wave resonance of the shear wave, and S_1 will arise starting from the half wave resonance of the longitudinal wave. These modes will transform into the shear waves when the plate thickness increases.

Symmetric Lamb waves are named as such because the particle displacement is symmetrical relative to the neutral axis of a plate, and along this axis, the particles are vibrating only in the longitudinal direction. Lamb asymmetric waves are flexural waves, and the particles along the neutral axis of a plate are vibrating strictly in the transverse direction.

The procedure for angle of incidence determination is simple. For a given thickness of plate, only the frequency of a transducer has to be selected. On the graph of phase dispersion curves from the point on the abscissa axis, equal to the product of plate thickness by frequency, a perpendicular has to be drawn. This line will cross one or more of the dispersion curves, representing the Lamb wave's modes that could be generated. Then, the chosen mode, and related to it, phase velocity, are the inputs to determine angle of incident. The wedge design process is similar to a wedge design for a surface wave wedge, with one exception related to the crystal diameter. As a rule of thumb, the crystal diameter

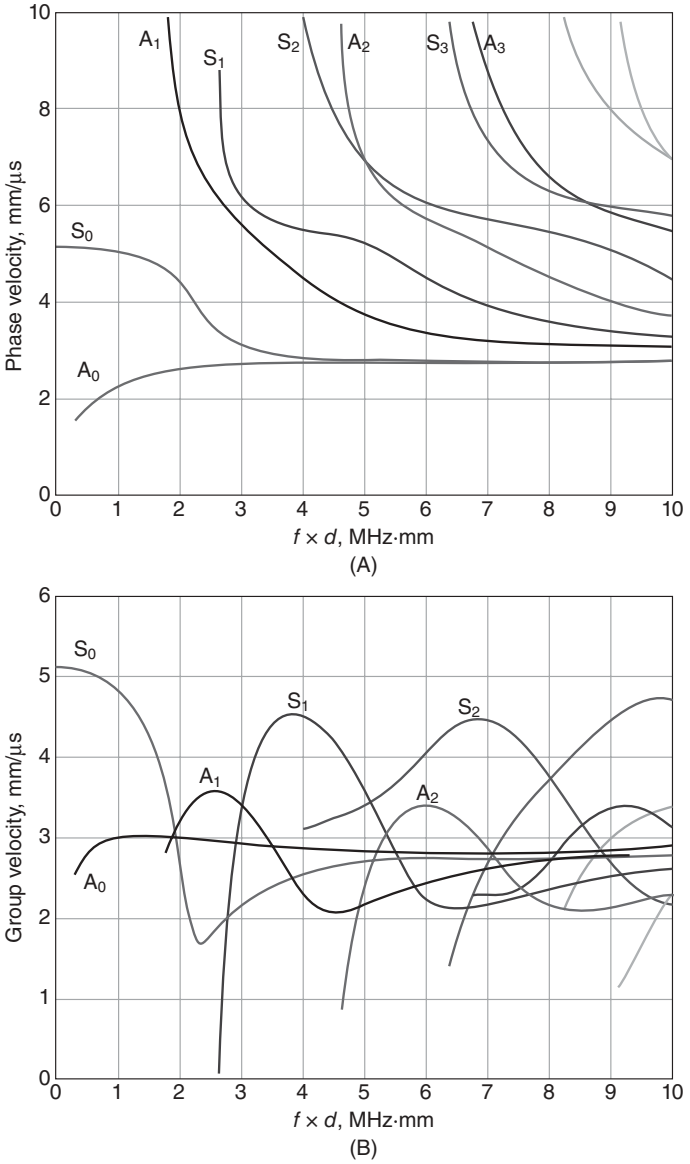

Figure 8.6 Phase (A) and group (B) dispersion curves.

has to be at least from 3 to 4 times more than the plate thickness to be tested.

In choosing the correct transducer frequency and the mode of propagation, several factors have to be considered.

Mode of propagation has to be at as low order as possible. The preferable modes are A_0, S_0, A_1, S_1. For crack detection, it is better to use the symmetric modes. The cracks on either free surface, scanning or opposite, will be detected at approximately the same sensitivity. So, Lamb wave inspection cannot distinguish at which surface of the plate the crack is located.

If possible, a zone of the phase velocity dispersion curve with a minimum slope should be chosen for selecting the mode. The phase velocity dispersion curve with a minimum slope indicates that the wedge angle is less critical, which is important for the wedge design. And vice versa, if the chosen portion of the curve is extremely steep, the wedge angle is very critical. In this case, deviation from a calculated angle of ±1.0° can drastically reduce the amplitude of the reflected signal or even cause a loss of mode.

Transducer frequency has to be as high as practically possible. Usually, this is in the range from 1.0 to 10 MHz depending on the plate thickness and the reflector to be detected. The thinner the plate, the higher the frequency that should be selected, in order to remain in the range of the first four mode orders. It is very important to use *actual* (not *nominal*) transducer frequencies to calculate the product of wall thickness by frequency. Each transducer has to be evaluated before use. Interchangeable transducers must be fabricated with a very tight frequency tolerance of not more than ±2%. The bandwidth tolerance is not as critical as the frequency tolerance, but should be not more than ±5% of selected value. A gain tolerance of ±2 dB is acceptable.

Selection of the Best Modes and Frequencies

The best modes for the detection of reflectors in water-loaded test objects are mainly symmetric modes. According to Reference 13, *for symmetric modes, when the phase velocity reaches the value of the velocity of bulk longitudinal waves, the vertical (normal to the sample surface) component of the displacement vector vanishes on the free surface*. This means that the leaks of energy in water will be minimized.

Based on this statement, the equation given in Reference 9 to calculate the *fd* parameter of the symmetric modes is

$$fd = \frac{n \times V_S}{\sqrt{1 - \left(\frac{V_S}{V_L}\right)^2}} \tag{8.13}$$

where: n = number of mode,

V_S = shear wave velocity, mm/μs

V_L = longitudinal wave velocity equal to phase velocity $\boldsymbol{V}_{\mathbf{ph}}$, mm/μs.

For a given wall thickness, the appropriate frequency can be calculated as

$$f = \frac{fd}{d}. \tag{8.14}$$

Then, the incident or wedge angle can be calculated according to Equation 8.12.

Lamb Wave Attenuation

One of the practical considerations for selecting the mode is its ability to propagate over a relatively long distance. Attenuation of Lamb waves is determined by two factors: absorption of energy in the material of the test object, as in any ultrasonic wave propagation, and due to leakage of energy in an environment, for example, in water surrounding a test object. The loss of energy in a material due to absorption is comparatively less than that attenuated due to leakage of energy in water, which depends on the relationship between the vertical and the longitudinal displacement of the particle within the thickness of the plate. As an illustration, the dimensionless coefficient of attenuation vs. *fd* (leakage in water) is presented in Figure 8.7.

Any *fd* parameter defines only one point on the attenuation curve. A minor change in this parameter can lead to a substantial increase or decrease in the coefficient of attenuation.

For example, for a 1.5 mm thick Inconel plate and a transducer frequency of 2.25 MHz (*fd* = 3.375), attenuation is practically zero for

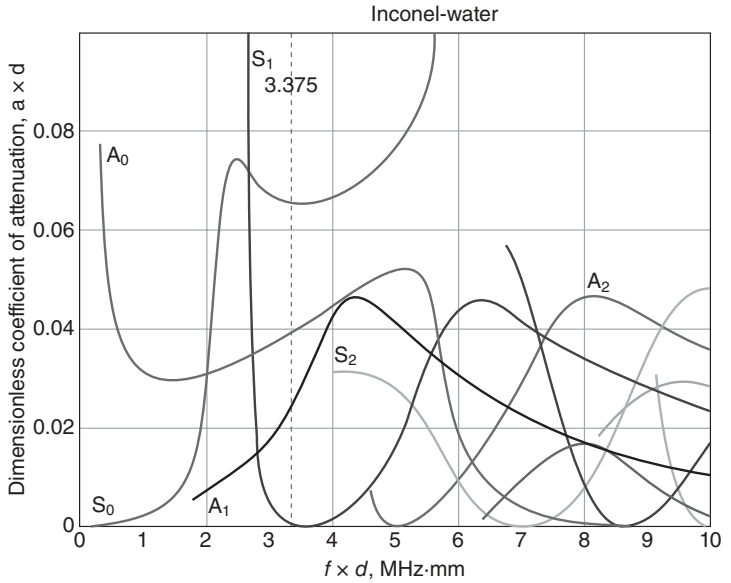

Figure 8.7 Dimensionless coefficient of attenuation.

the S_1 mode propagation. But, for a transducer frequency of 1.80 MHz, the coefficient of attenuation rises sharply.

Reflected Signal Shape

The signal shape is an important parameter in the assessment of Lamb wave propagation. It characterizes that the selected mode is chosen correctly (or not correctly) for the given inspection conditions and that the probe frequency is coincident with test object wall thickness. The typical shape of "good" signals is shown in Figure 8.8. These signals are from the same reflector, but at a different analog to digital (A/D) ratio. It is interesting to note that the signal comprises high frequency components. When the probe is moving relative to the reflector, these oscillations travel over the signal apogee.

Technique development for the inspection of hollow cylinders using Lamb-type guided waves are based in many cases on the same principles that are used for Lamb wave generation. The propagation parameters specific for Lamb waves are also correct for Lamb-type guided waves.

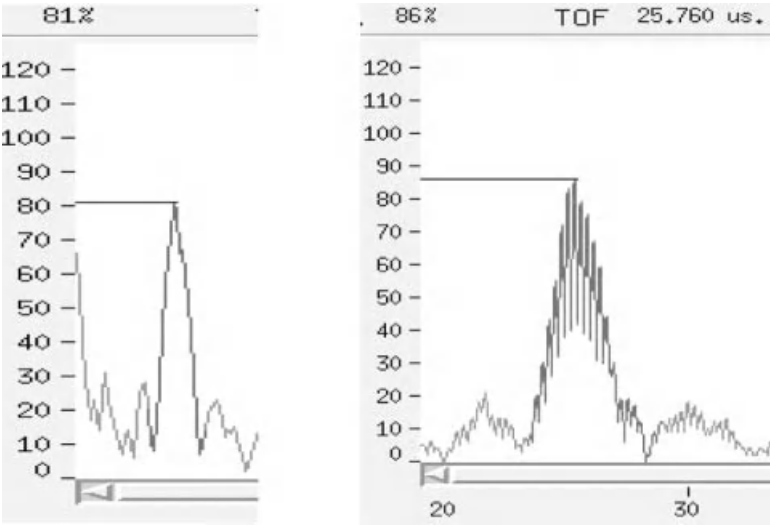

Figure 8.8 Typical shape of Lamb wave reflected signal.

In the following sections, technique development for the inspection of hollow cylinders will be discussed. Each of the sections is dedicated to different types of hollow cylinders, which have unique characteristics.

8.2. TECHNIQUE DEVELOPMENT AND PROBE DESIGN FOR THE INSPECTION OF HOLLOW CYLINDERS FROM THE INSIDE SURFACE

8.2.1. Test Object Description and Inspection Consideration

One of the first applications of Lamb-type guided waves was used in steam generator tubing (SGT) inspection of the type generally used in nuclear power plants and other power generating facilities. In nuclear power plants, for example, the tube diameters range from 16 to 25 mm with wall thickness in the range of 1.0 to 1.5 mm. These tubes are perfect candidates for inspection using Lamb-type guided waves.

Mathematically, tubing is treated as a thin hollow circular cylinder with the ratio of average wall thickness h to a mean radius r of much less than the unit $h/r << 1$.

Assume that the average mean radius for the SGT is 10 mm with an average wall thickness of 1.25 mm, so 1.25/10 = 0.125. This complies with the definition of a thin hollow circular cylinder.

One of the steam generator designs uses vertically mounted tubing assembled in bundles of several hundred or even a thousand tubes with a $\cap$-bend on the top. The lower ends of each tube are expended in a tube sheet. Several plates support the tube bundles along their length. The distance between tubes is in the range of 3 to 6 mm.

SGT degradation is divided in two broad categories: chemical corrosion and mechanical degradation. Corrosion degradation includes thinning, pitting, stress-corrosion cracking and intergranular attack/stress-corrosion cracking. Mechanical degradation includes wear, fatigue, and erosion-corrosion.

The primary test method used in SGT so far is eddy current. An eddy current probe is placed inside the tube and rotated providing a helical scan with a small pitch, to inspect the tube wall. Interfering signals can exist due to possible tube deformation during the installation and expansion process at the tube sheet, as well as for deposits on the tube walls that can be either magnetic or conductive.

As an alternative method, Lamb-type guided wave inspection is used to overcome the problems associated with the false positive indications from sludge and other issues caused by the tube expansion in the transition region.

Similar to the case of eddy current inspection, the ultrasonic probe should be inserted inside the tube. One of the expected problems for ultrasonic wave propagation over a relatively long distance is the existence of water outside the tubes.

SGT can be inspected with Lamb-type guided waves, both axisymmetric and non-axisymmetric. The axisymmetric waves cover the full circumference of the cylinder (i.e., cylindrically guided). Non-axisymmetric waves are localized and travel in a double spiral pattern along the hollow cylinder. Although the structure of axisymmetric waves is preferable, a real crack will produce a reflected wave that is non-axisymmetric. Therefore, from a practical point of view, the advantage of generating axisymmetric waves is questionable. On the other hand, the wave structure of non-axisymmetric waves is more

complicated, and the energy distribution in particular sections along the cylinder is variable.

Wave propagation in a thin wall hollow cylinder is more complicated than in a plate [36]. Three different wave modes need to be considered: longitudinal, torsional, and flexural. The notation of these modes is:

- L(0,m)—for longitudinal modes,
- T(0,m)—for torsion modes, and
- F(0,m)—for flexural modes.

These notations are less familiar among practitioners than the notations used in the Lamb wave description, such as A_n or S_n. The dispersion curves for L(0,m) modes correspond to those of Lamb wave modes. The phase velocities of longitudinal modes are primarily determined by the hollow cylinder's wall thickness and diameter. It was shown that in the case of when $h/r << 1$, the dispersion curves for Lamb waves in thin plate are practically not distinguishable from the dispersion curves for a thin wall hollow cylinder, particularly in the most usable region of the product $fd \geq 1$. This means that one can use either of the two sets of dispersion curves, calculated for thin plate or for thin wall hollow cylinders. The program designed to calculate dispersion curves in hollow cylinders provides good results for cylinders with diameters of approximately 6.0 mm and up.

The best modes and frequencies to be calculated for symmetric modes are indicated by Equation 8.13. If the longitudinal wave velocity V_L is equal to the phase velocity $\boldsymbol{V_{ph}}$, no leakage in water is expected. This equation can be used to assess the possibility of leakage for given bulk velocities. For example, for Inconel with velocities $V_S = 3.1$ mm/μs and $V_L = 5.66$ mm/μs, the best frequencies are as follows:

For S_1 mode,

$$fd = \frac{1 \times 3.10}{\sqrt{1 - \left(\frac{3.10}{5.66}\right)^2}} = 3.71 \text{ mm}/\mu\text{s}$$

For a given wall thickness of 1.22 mm, the appropriate frequency can be calculated as

$$f = \frac{fd}{d} = \frac{3.71}{1.22} = 3.04 \text{ MHz}.$$

For S_2 mode,

$$fd = \frac{2 \times 3.10}{\sqrt{1 - \left(\frac{3.10}{5.66}\right)^2}} = 7.41 \text{ mm}/\mu\text{s}$$

$$f = \frac{fd}{d} = \frac{7.41}{1.22} = 6.07 \text{ MHz}.$$

The incident or wedge angle can be calculated according to Equation 8.12.

With these parameters, one can expect a minimum energy leakage in water. Particle displacement calculation in wall thickness confirms this statement. For example, normalized particle displacement for S_1 mode in Inconel with a wall thickness of 1.22 mm is shown in Figure 8.9. The out-of-plane displacement, that is, particle displacement

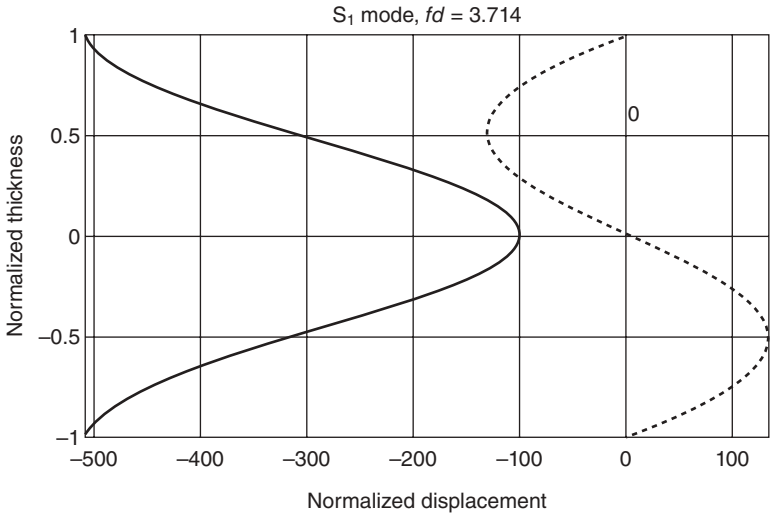

Figure 8.9 Normalized particle displacement: S_1 mode, the wall thickness 1.22 mm.

perpendicular to the sample surfaces (dotted line), is practically zero on both sides of the sample wall. The in-plane displacement, that is, particle displacement parallel to the tube surfaces (solid line), reaches its maximum on both sides of the tube wall and its minimum in the middle of the tube wall thickness. This is the best combination of particle displacement possible for water-loaded hollow cylinder.

The calculated frequencies of 3.04 MHz and 6.07 MHz are not commonly used by transducer manufacturers. Let us add another parameter $fd = 5 \times 1.22 = 6.1$ MHz mm for the common frequency of 5.0 MHz to extend the choice of phase velocities and wedge angles.

The phase velocity dispersion curves for selected *fd* parameters are shown in Figure 8.10A, B. The obtained data from these curves, along with calculated wedge angles, are summarized in Table 8.1.

The next step in the technique development and the probe design is to fabricate wedges with selected angles, inspect tube test samples in the dry and water-loaded conditions, and finally select the best performing probes.

One of the advantages of Lamb-type guided waves is their ability to propagate over long distances. For example, in SGT not loaded by water (dry tubes), these waves can extend for many feet, including around a ∩-bend. This phenomenon is very desirable to save inspection time. The problem is the decrease in sensitivity for the detection of

Table 8.1
Phase Velocities and Wedge Angles for Selected Modes

Parameter *fd*, MHz·mm	Phase velocities mm/μs for modes					
	A_0	S_0	A_1	S_1	A_2	S_2
3.714	2.733	2.902	4.822	5.628	–	–
7.41	2.788	2.786	3.178	3.738	4.893	5.62
6.1	–	–	3.333	4.43	5.648	5.988
	Wedge angle, degree for modes					
3.714	–	–	34.55	29.08	–	–
7.41	–	–	59.38	47.12	33.98	29.12
6.1	–	–	55.14	38.13	28.96	27.18

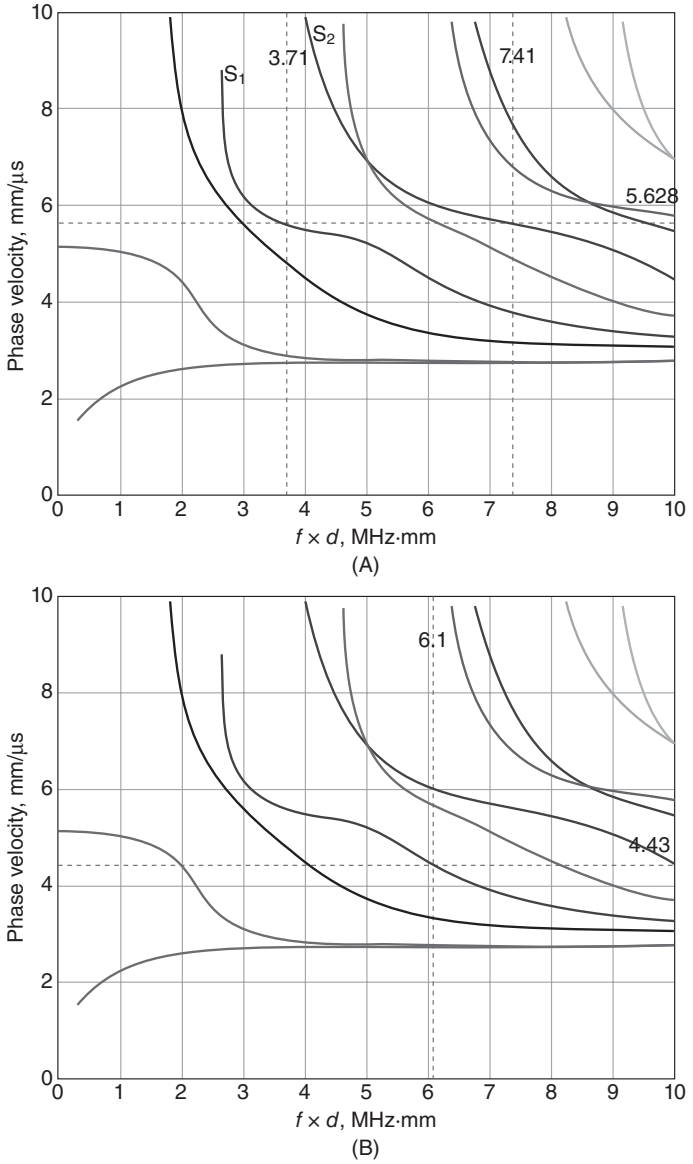

Figure 8.10 Phase velocity determination for selected *fd* parameters.

small reflectors and their position in the tube circumferential direction at a long distance [37, 38].

The more practical approach is to inspect relatively short lengths (approximately from 75 to 150 mm) of the tubes in the critical regions of stress concentration, such as the tube transition zone and zones in the vicinity of the support plates. This approach will reduce the influence of energy leakage in water on the inspection sensitivity. The advantage of this technique is to provide improved sensitivity and high resolution measurements of crack length along with discrimination of intermittent ligaments between short crack segments. The crack length and existence of ligaments are essential factors to assess tube structural integrity and to predict tube rupture strength [39].

As an example, let us discuss the inspection of a tube in a transition zone of a tube sheet (Figure 8.11A). To detect circumferentially oriented cracks, the probe is inserted in the tube from the bottom of the tube sheet, with the ultrasonic beam directed down (Figure 8.11B). One of the positive side effects is the possibility to assess the quality of the tube expansion. When the probe is located in the tube expended zone, and if a tube is expended correctly into the tube sheet, the S-wave beam will propagate into the tube sheet and will reflect from the nearest reflector (adjacent tube or corner of tube sheet).

One of the probe assembly designs is shown in Figure 8.12. On the left is the probe mounted in the fixture, which centers the probe and provides local couplant supply. This fixture can be attached to a flexible shaft, the length of which depends on the distance to the region to be inspected. After setup at the inspection region, the probe can be rotated and, if necessary, indexed.

8.2.2. Lamb-Type Guided Wave Mode Selection for Practical Application

Theoretically, six modes can be utilized for SGT inspection (Table 8.1), but two of these modes, A_0 and S_0, cannot be considered for practical application in water-loaded tubes. Moreover, the wedge angles for generating these modes are in the range of 70°, which makes it difficult to utilize them in probes for the small diameter tubes.

The modes S_1 and S_2, as was mentioned above, are most likely to produce desirable results. It could be difficult to omit mode A_2 during the generation of the S_2 mode. The reason is wedge angles for these

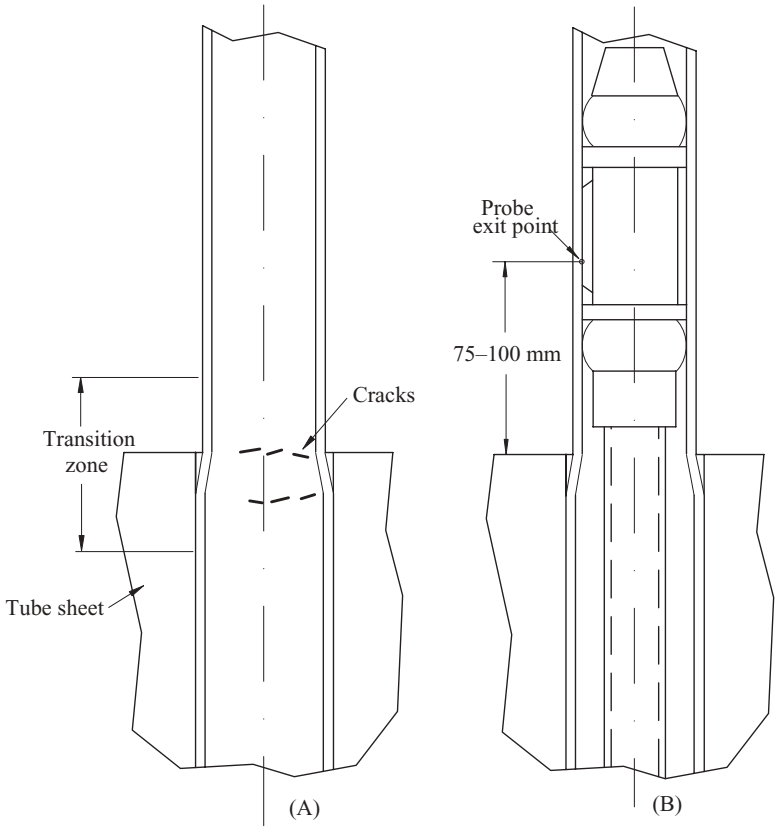

Figure 8.11 Tube transition zone (A) and the probe position during inspection (B).

Figure 8.12 Example of a probe assembly for SGT inspection. Reprinted by permission of Westinghouse Electric Company LLC.

modes are close to each other. Wedge angles for selected modes and chosen frequencies are shown in Table 8.2.

One of the reasons to generate several modes at different frequencies is to compare signal response amplitudes, shapes, and to assess the attenuation.

Table 8.2
Wedge Angles for Selected Modes and Chosen Frequencies

Frequency, MHz	Wedge angles for modes, degree			
	A_1	S_1	A_2	S_2
3.0	34.55	29.08	–	–
5.0	55.14	38.13	28.96	27.18
6.0	59.38	47.12	33.98	29.12

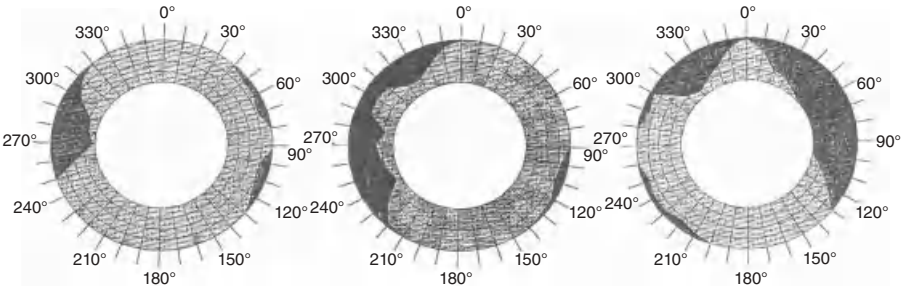

Figure 8.13 The circular diagrams showing the results of the tube inspection.

The results of the inspection can be presented in the form of a circular diagram, as shown in Figure 8.13 for three different sections of tubes. The dark areas represent cracks of different depth and length.

8.3. TECHNIQUE DEVELOPMENT AND PROBE DESIGN FOR THE INSPECTION OF HOLLOW CYLINDERS FROM THE OUTSIDE SURFACE

8.3.1. Technique Development and Probe Design for Inspection of Cylinders with Welded Adapters

Test Object Description and Inspection Consideration

Consider the case of an inspection using Lamb-type guided wave to inspect a stainless steel hollow cylinder with the following dimensions:

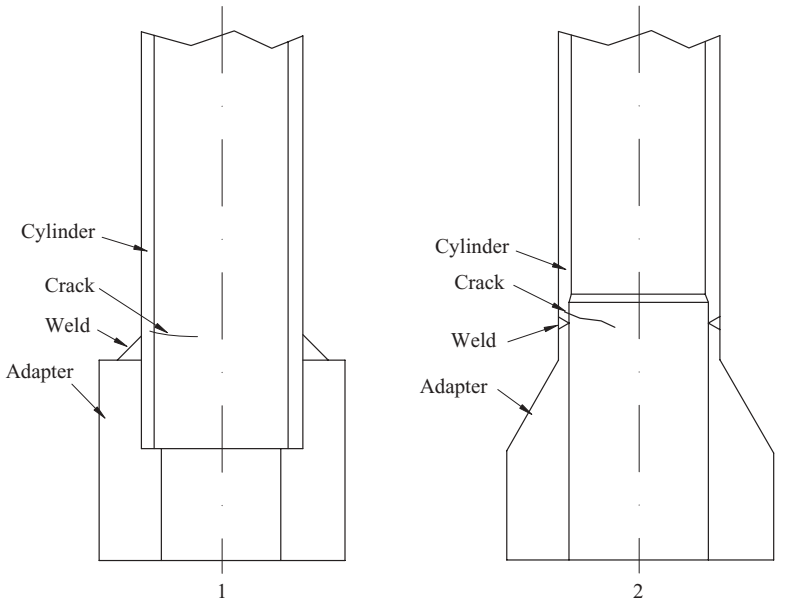

Figure 8.14 Hollow cylinders with the welded on adapters.

- outside diameter of the hollow cylinder—30.0 mm
- wall thickness—2.50 mm.

These cylinders are part of the penetration system in pressure vessels. At one end of each cylinder, the adapter is welded with a different weld type: fillet (1) and butt bevel (2) (Figure 8.14). The hollow cylinder wall is only a wave guide for delivering ultrasonic energy to the zone to be inspected. Usually, the inspection zone itself is a weld region (as in this case), a rolled transition to a different diameter, a step on the hollow cylinder, and so on.

These locations have different grain structure, wall thickness and, as a result, different wave velocity and attenuation. These are the locations where cracks would most likely be initiated.

The other end of the cylinder penetrates the pressure vessel, heat exchanger, or some other structure. Inside the cylinder, some kind of instrumentation or a heater in the shape of a round bar is located (not shown in Figure 8.14).

There is a water gap in the radial direction of approximately 0.10–0.3 mm between the inside surface of the hollow cylinder and outside surface of the heater or instrumentation. A crack can initiate from the inside surface of the hollow cylinder and may propagate most likely in the circumferential direction, following the heat-affected zone of the weld. Thus, the task of the inspection is to detect a crack located on the inside surface of the hollow cylinder from its outside surface.

The conditions of ultrasonic inspection can be formulated as follows:

1. The heater or the instrumentation will remain in the cylinder during the inspection.
2. The outside surface of the hollow cylinder is accessible for a distance of approximately 50–100 mm from the inspection zone.
3. The probe should be positioned only on the outside surface of the cylinder and be able to rotate 360°.

These hollow cylinders comply with the definition of a *thin* hollow circular cylinder. The average mean radius is 13.75 mm and the wall thickness is 2.5 mm, so $h/r = 2.5/13.75 = 0.1818$.

Selection of the Best Modes and Frequencies

The best modes to detect reflectors in water-loaded test objects, as mentioned above, are mainly symmetric modes. For known wall thickness d, the Equation 8.13 is to be used for calculating the fd parameters for symmetric modes.

The velocities in this test object are

- $V_S = 3.10$ mm/μs is shear wave velocity,
- $V_L = 5.80$ mm/μs is longitudinal wave velocity.

For a given wall thickness, the appropriate frequency can be calculated as $f = fd/d$.

For S_1 mode,

$$fd = \frac{3.10}{\sqrt{1-\left(\frac{3.10}{5.80}\right)^2}} = 3.67 \text{ mm}/\mu\text{s}$$

$$f = \frac{fd}{d} = \frac{3.67}{2.50} = 1.468 \text{ MHz}.$$

For S_2 mode,

$$fd = \frac{2\times 3.10}{\sqrt{1-\left(\frac{3.10}{5.80}\right)^2}} = 7.337 \text{ mm}/\mu\text{s}$$

$$f = \frac{fd}{d} = \frac{7.337}{2.50} = 2.93 \text{ MHz}.$$

With these values, one can expect minimum energy leakage in water.

The calculated frequencies 1.468 MHz and 2.93 MHz are not common for standard transducers.

Figure 8.15 shows phase velocities with transducers having the standard frequencies of 1.0 MHz. and 2.25 MHz. The calculated phase velocity is 6.28 MHz for A_2 and S_2 modes, as shown in Figure 8.15.

The S_1 mode cannot be used at the frequency of 1.0 MHz. So, let us consider only the S_2 mode. The phase velocity of the S_2 mode is very close to the phase velocity of A_2 mode. Therefore, particular attention has to be given to the wedge design in order to prevent generation of the A_2 mode.

The incident or wedge angle for S_2 mode can be calculated according to Equation 8.12

$$\alpha = \arcsin\frac{2.735}{6.28} = 25.82°.$$

The calculated group velocities for S_2 and A_2 modes from Figure 8.16 are shown in Table 8.3.

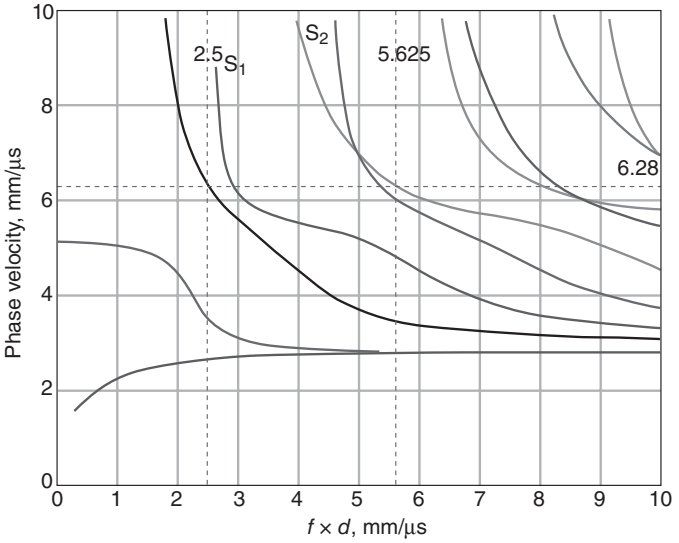

Figure 8.15 Phase velocity dispersion curves for 1.0 MHz and 2.25 MHz transducers.

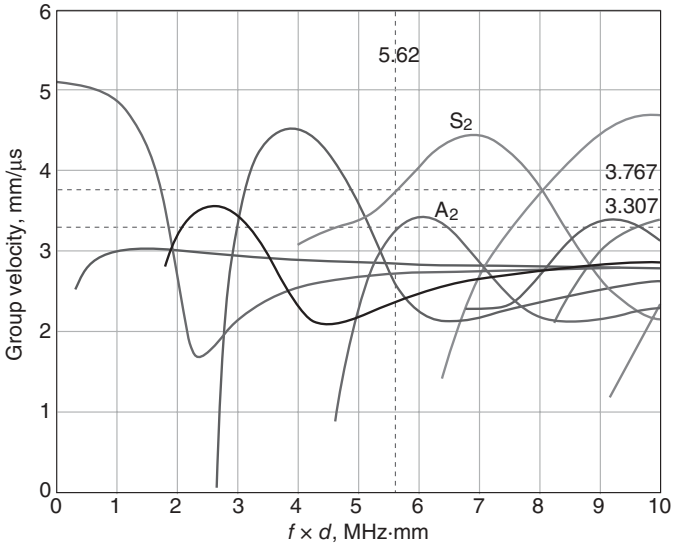

Figure 8.16 Group velocity dispersion curves.

Table 8.3
Calculated Phase and Group Velocities for S_2 and A_2 Modes

Parameter *fd*, MHz·mm	Velocities, mm/μs for modes			
	Phase velocity		Group velocity	
	A_2	S_2	A_2	S_2
5.62	6.009	6.28	3.307	3.767
Wedge angle, degree		25.82		

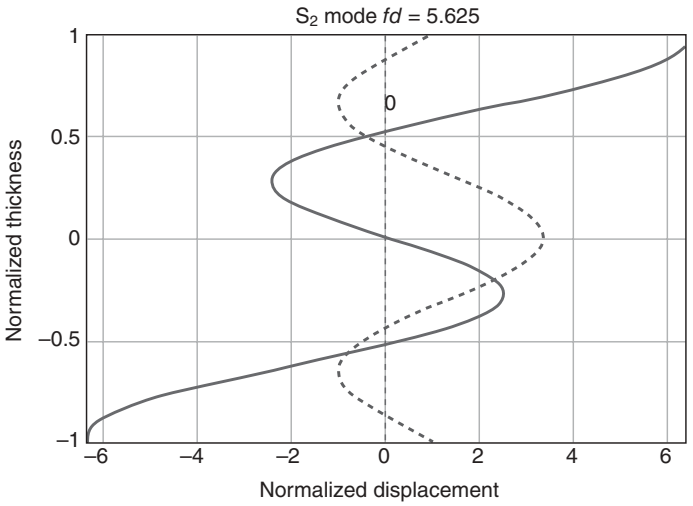

Figure 8.17 Normalized particle displacement.

Normalized particle displacement is shown in Figure 8.17. It shows that at the frequency 2.25 MHz, small leakage of ultrasonic energy in water is possible due to out-of-plane particle displacement.

Group Velocity Measurement

As mentioned in Section 8.2.1 the non-axisymmetric waves travel along the hollow cylinder in double spiral lines, which are the same as helical lines.

So, to measure a group velocity, two parameters should be determined: a length of a helical line and a transit time between two

reflectors. The helical line length S of one revolution (360°) can be calculated as:

$$S = 2\pi\sqrt{r^2 + \frac{h^2}{(2\pi)^2}}, \tag{8.15}$$

where r is the radius of a cylinder,

h is the lead of a helix.

To understand the meaning of this expression, multiplier 2π has to be introduced under the radical

$$S = \sqrt{(2\pi r)^2 + h^2}. \tag{8.16}$$

It means that the helical line length of one revolution is equal to the hypotenuse of a triangle, one side of which is $(2\pi r)$ and is equal to the circumference of the cylinder base, and the other side (h) is equal to the lead of the helix (Figure 8.18).

To mark the beginning and the end of the helical line, two or three reflectors (side-drilled holes), located 50 mm or 100 mm apart in the axial direction and 90° or 180° apart in the circumferential direction of the test sample can be used. To determine a fraction of one revolution of a helical line length, it is easier to calculate the total arc length of one revolution and then divide the obtained data according to the

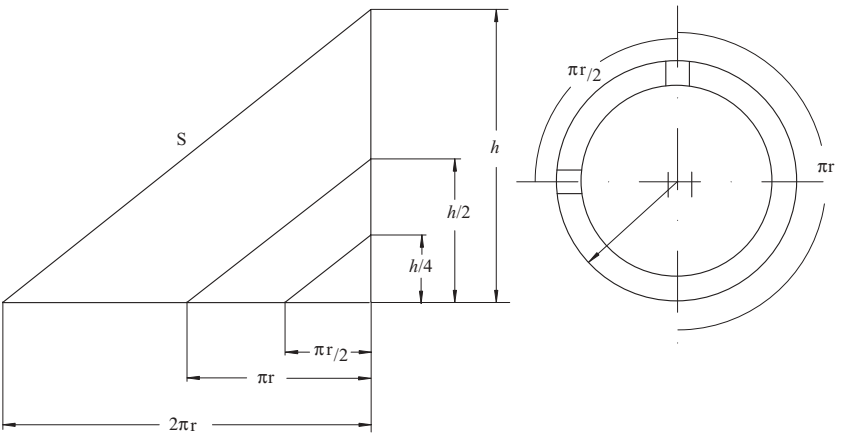

Figure 8.18 An arc length measurement.

location of the reflectors. For example, if the are reflectors located 90° apart in the circumferential direction, $S_{90} = S/4$.

Let us calculate the arc length of a hollow cylinder 30 mm diameter with two holes 90° apart and $h/4 = 50.8$ mm:

$$S = \sqrt{(2\pi \times 15)^2 + 203.2^2} = 223.98 \text{ mm},$$

where $h = 50.8 \times 4 = 203.2$ mm.

Therefore, the arc length is $S/4 = 223.98/4 = 56$ mm.

The group velocity of the generated mode should be determined by measuring time of flight (TOF). For example, the TOF (τ) between signals from two reflectors is 32.64 μs (Figure 8.19). Thus, the group velocity is

$$V_{gr} = \frac{S}{4\tau} = \frac{56 \times 2}{32.64} = 3.43 \text{ mm}/\mu\text{s}.$$

Most likely that S_2 mode was generated, which calculated group velocity is 3.767 mm/μs.

Finally, water influence on inside notch detection should be determined in order to accept or reject the chosen mode. For this purpose,

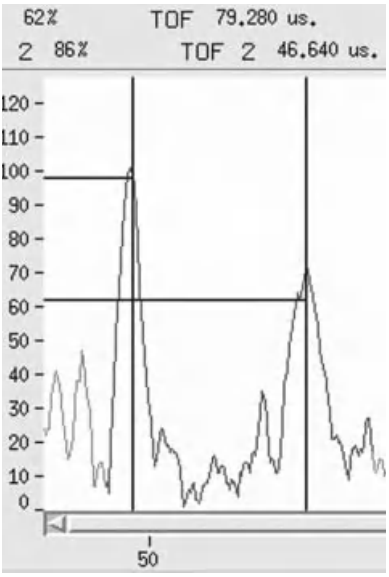

Figure 8.19 The signal from two reflectors 50.8 mm apart.

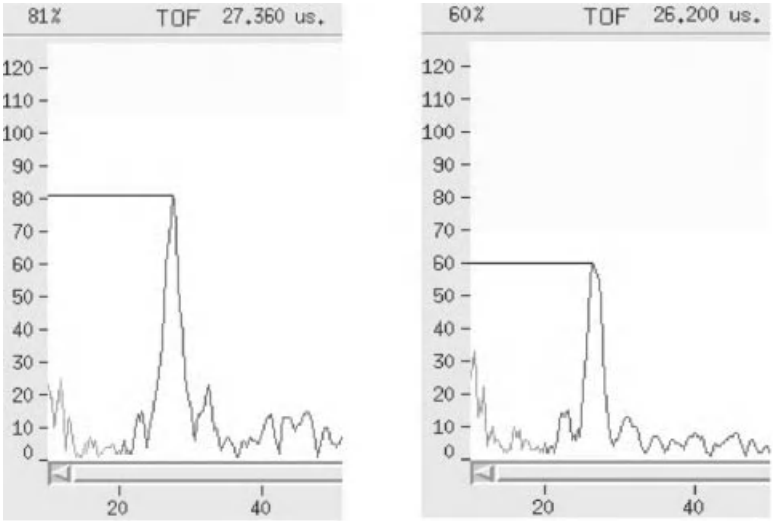

Figure 8.20 Reflected signals from a notch: (A) the dry cylinder #1, (B) water in the gap.

test samples of the hollow cylinder with a notch on the inside surface should be inspected. The reflections from the notch located in the test sample 1 is presented in Figure 8.20. The difference in signal amplitudes between the dry cylinder (A) and with water in the gap (B) is approximately minus 20%. The signal-to-noise ratio is more than 5/1. Approximately the same difference in signal amplitudes was observed during the inspection of test sample 2.

Conclusion

1. As predicted by the calculations, the S_2 mode was generated in the test samples.
2. Water gap has minimal influence on S_2 mode propagation.
3. There is no need to fabricate a special transducer with a calculated best frequency.

8.3.2. Technique Development and Probe Design for Heater Sleeve Inspection

Test Object Description and Inspection Consideration

Many heat exchangers include sleeves welded into the exchanger shell. The sleeves are relatively short cylinders (200–300 mm) that serve as

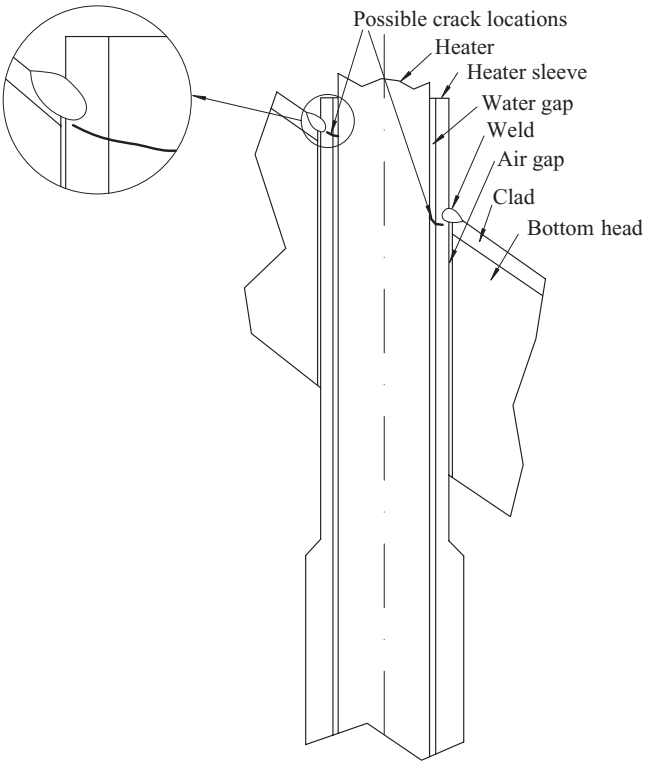

Figure 8.21 Simplified configuration of the heater sleeve.

penetrations for the insertion of heat exchanger instrumentation and other devices. For example, in nuclear power plant pressurizers, there are pressurizer heater sleeves. The sleeve is essentially a hollow cylinder with a step on outside surface (Figure 8.21). The heater sleeve is welded to the cladding of the bottom head of the pressurizer. Heaters are located inside the heater sleeves. There is an air gap between outside surface of the sleeve and the penetration into the bottom head. There is also a water gap between the inside diameter of the sleeve and outside diameter of the heater.

The water gap between inside surface of the sleeve and outside surface of the heater in the radial direction is approximately 0.12–0.15 mm. When cracking occurs, the crack is initiated from an inside surface of the hollow cylinder, progressing most likely in an inclined circumferential direction, following the heat-affected zone of the weld.

The conditions for ultrasonic inspection are usually as follows:

1. The heater will remain in the sleeve during the inspection.
2. A water gap exists between the inside surface of the hollow cylinder and the outside surface of heater.
3. The outside surface of the hollow cylinder is unobstructed.
4. The probe can be positioned only on the step of outside surface of the sleeve and be able to rotate on 360°,
5. Non-axisymmetric waves should be used.

The average distance between the probe exit point and the possible crack location is approximately from 200 to 300 mm depending on the sleeve location at the bottom head. Outside diameters of the sleeve can be in the range of 30–40 mm and wall thickness in the range of 3–5 mm.

As mentioned before, mathematical tubing treated as thin hollow circular cylinder with ratio of average wall thickness h to mean radius r much less than unit $h/r << 1$. The dimensions of the heater sleeves comply with the definition of a thin hollow circular cylinder.

In the case of inspection of a water-loaded hollow cylinder, it is preferable to utilize symmetrical S_n modes, in which case the in-plane particle displacement is maximized on both the inside and outside surfaces.

Calculation of the fd parameter in this case provides the following results (Eq. 8.12).

As known, if V_L is equal to phase velocity $\boldsymbol{V_{ph}}$, no leakage in water is expected.

For example, for Inconel with velocities $V_S = 3.10$ mm/μs and $V_L = 5.66$ mm/μs, the best frequencies are

for S_1 mode,

$$fd = \frac{1 \times 3.10}{\sqrt{1 - \left(\frac{3.10}{5.66}\right)^2}} = 3.71 \text{ mm}/\mu\text{s}.$$

For a given wall thickness, the appropriate frequency can be calculated as

$$f = \frac{fd}{d} = \frac{3.71}{3.2} = 1.159 \text{ MHz}.$$

For S_2 mode,

$$fd = \frac{2\times 3.10}{\sqrt{1-\left(\frac{3.10}{5.66}\right)^2}} = 7.41\,\text{mm}/\mu\text{s}$$

$$f = \frac{fd}{d} = \frac{7.41}{3.2} = 2.316\,\text{MHz}.$$

From this, it appears that common transducers can be used in this case with a nominal frequency 1.0 MHz. and 2.25 MHz. With these parameters, one can expect minimum energy leakage into the water gap. The incident or wedge angle can be calculated, according to Equation 8.12.

Lamb-Type Guided Wave Mode Selection

The sleeve geometry with a step on the outside surface presents a challenge for inspection. The probe can be positioned only on the surface of the step whose wall has a thickness of 4.4 mm; however, the inspection of the thinner portion of the sleeve has to be performed with a wall thickness of 3.2 mm. If the probe is positioned at an arbitrary distance from the step, the strong reflection from the step will drastically reduce the energy which should be propagated in the thinner section. The wall thicknesses of this sleeve at its transition is shown in Figure 8.22.

Distance X should be such that the reflection from the step does not occur. This will allow the ultrasonic energy to propagate mainly in the thinner portion of the sleeve.

The best modes in this case will be S_1 or S_2. Dispersion curves for the phase velocity shows that for a 1.0 MHz transducer, the phase velocity V_{ph} = 5.906 mm/μs and for a 2.25 MHz transducer, phase

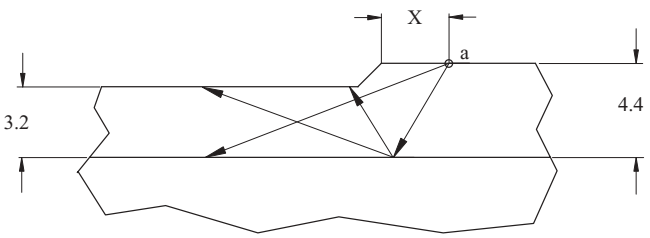

Figure 8.22 Beam propagation in the step region. a, probe exit point.

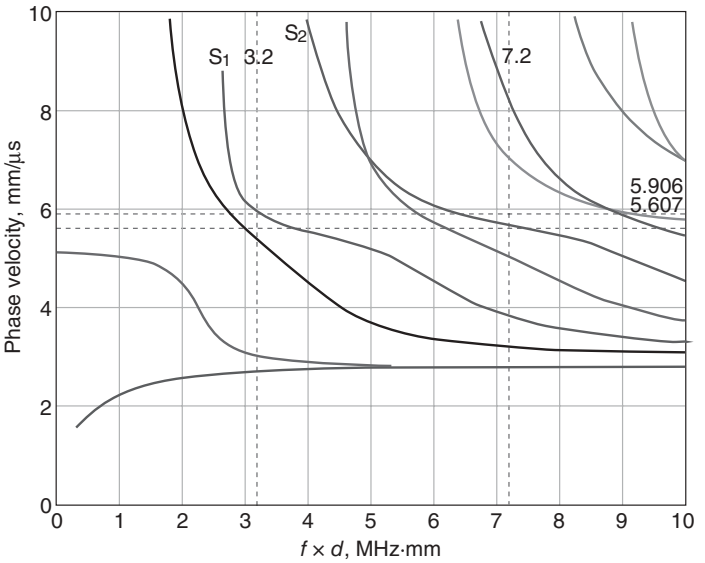

Figure 8.23 Phase velocity dispersion curves.

velocity is 5.667 mm/μs (Figure 8.23). The dispersion curves for the group velocity are shown in Figure 8.24.

The group velocity for 1.0 MHz. is 4.01 mm/μs and for 2.25 MHz is 4.384 mm/μs.

The data obtained from the dispersion curves are summarized in Table 8.4.

Energy leakage in water gap for these two modes will not be zero which is clear from the particle displacement graphs (Figure 8.25) for 1.0 MHz frequency and for 2.25 MHz (Figure 8.26).

Two potential problems should be addressed before Lamb-type guided wave modes can be properly selected in this case. The first one is the directivity pattern of Lamb-type guided waves propagating in a hollow cylinder. The second one is the reflectivity from reflectors which are not perpendicular to the cylinder axes.

Experiments to Measure Wave Propagation Parameters

a. Sound energy or signal amplitude distribution along the hollow cylinder

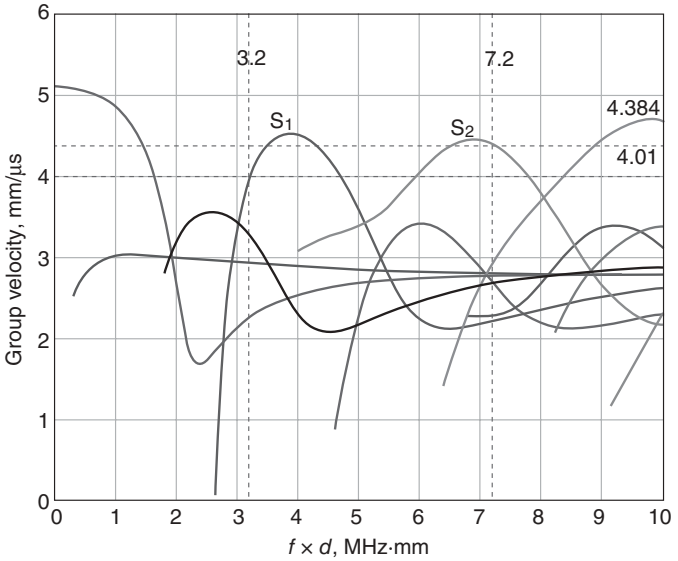

Figure 8.24 Group velocity dispersion curves.

Table 8.4
Phase and Group Velocities for Selected Modes

$f \times d$, MHz·mm	Frequency 1.0 MHz			$f \times d$, MHz·mm	Frequency 2.25 MHz		
	Mode	V_{ph} mm/μs	V_{gr} mm/μs		Mode	V_{ph} mm/μs	V_{gr} mm/μs
3.2	S_1	5.906	4.01	7.2	S_2	5.667	4.384
Wedge angle		27.58°		Wedge angle		28.86°	

The directivity pattern of Lamb waves in a plate is well known; however, the directivity pattern of Lamb-type guided waves in a hollow cylinder is more complicated and is less investigated, especially for non-axisymmetric waves. Generation of non-axisymmetric waves leads to generation of not only longitudinal, but also torsion modes. Due to the small differences in the phase velocities for each of the modes, the acoustic field varies from section to section along the cylinder. This leads to a pattern of energy distribution in the cylinder wall as if its sections rotate.

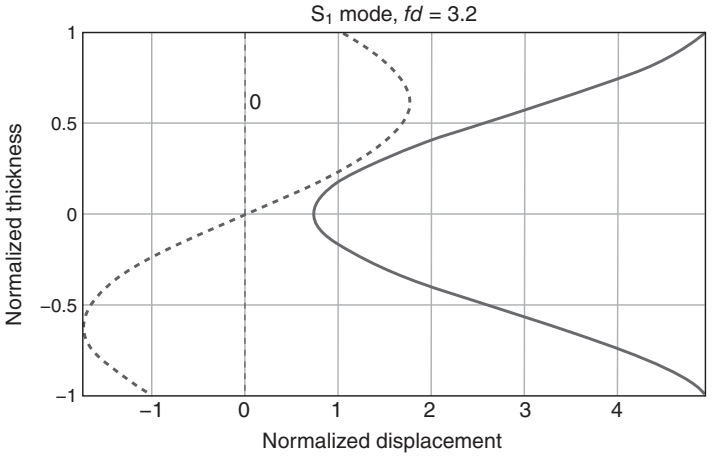

Figure 8.25 Particle displacement graph for S_1 mode.

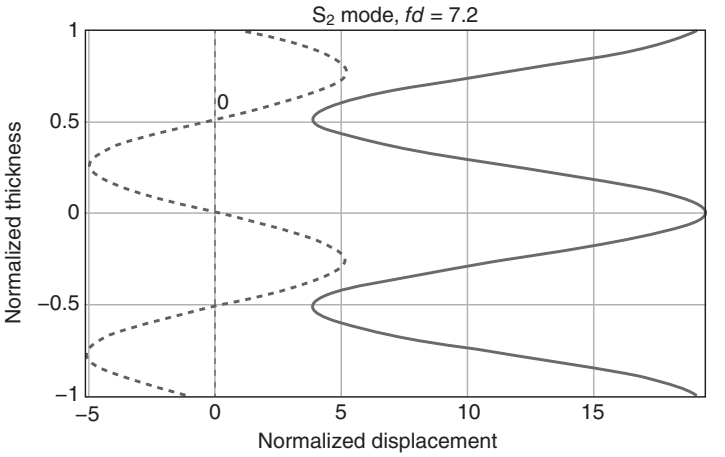

Figure 8.26 Particle displacement graph for S_2 mode.

At a relatively short distance from the probe, the difference in energy distribution in a circumferential section of the hollow cylinder, from section to section along the axes, can be distinguished. As the distance from the probe increases, the differences tend to diminish. One of the practical ways to assess approximate energy distribution along the hollow cylinder is to conduct a simple experiment.

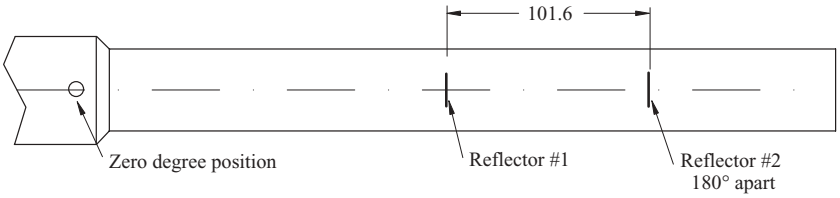

Figure 8.27 Diagram related to the signal amplitude distribution measurements.

An example of the experimental setup for these experiments is shown in Figure 8.27. The cylinder should contain two or more reflectors: for example, reflector #2 is on 101.6 mm from reflector #1 in the axial direction and 180° in the circumferential direction.

The probe is placed on the hollow cylinder at the zero degree position, which is in line with the first reflector. The probe should be rotated around the cylinder at a fixed distance from the reflectors.

Similar test samples with different types of reflectors can be used for different purposes. For example, side-drilled holes should be used to assess the energy distribution, and to collect information in order to calculate the group velocity. Notches should be used to assess detectability and for system calibration. Experiments show that from one probe locality, two reflectors can be detected simultaneously: the first signal at 61.680 μs is from reflector #1 at the gain of 47 dB (Figure 8.28A), the second signal at 108.48 μs is from reflector #2 180° from reflector #1. For S_2 mode, the same signals at the gain of 58 dB are shown in Figure 8.28B.

These screen shots were obtained with the probe at position 0°, that is, the probe is in line with the center of the reflector #1 (notch) (Figure 8.29). In two other circumferential probe positions, signal amplitudes are different (see Table 8.5).

Note that the distinctive feature of the reflected signal of Lamb-type guided wave propagation is the widening of the signal as the distance from the probe increases which is common for Lamb waves.

Note that the difference in signal amplitude at each of the probe circumferential positions is greater for notch #1, which is located close to the probe (see Figure 8.27).

b. Group velocity measurement

The group velocity should be determined in the same way as shown earlier in the section on "Group Velocity Measurement." Let us

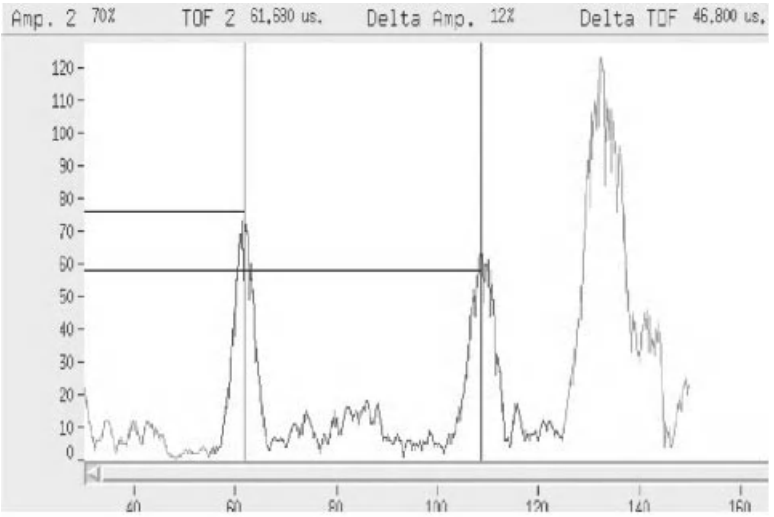

(A)

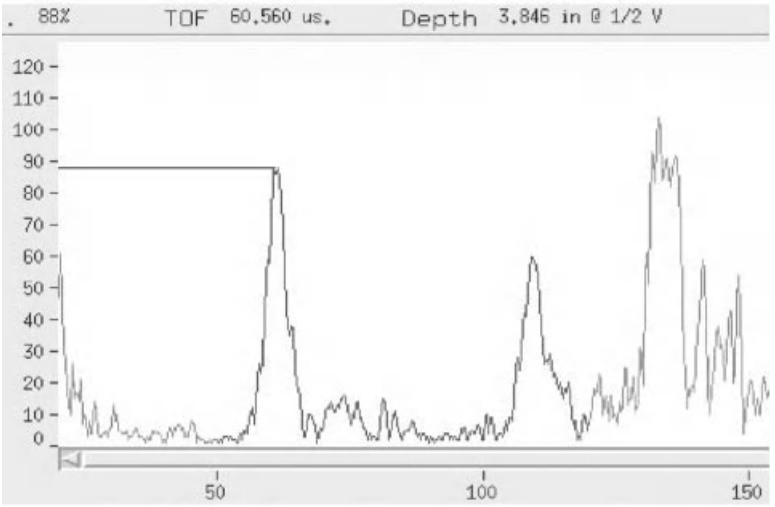

(B)

Figure 8.28 The signals reflected from two notches: (A) S_1 mode, (B) S_2 mode.

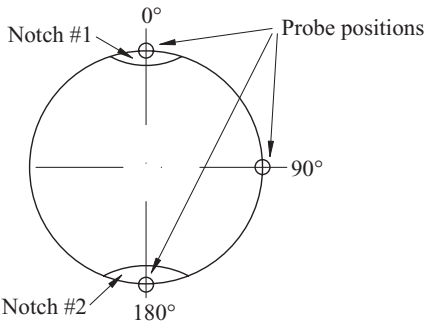

Figure 8.29 Relative position of the notches and the probe.

Table 8.5
Signal Amplitudes in Probe Positions 0, 90, and 180°

Notch #	Signal amplitude, %		
	0 degree	90 degree	180 degree
1	90	20	60
2	64	45	38

calculate the arc length of a hollow cylinder 29 mm in diameter with two holes 180° apart and $h/2 = 101.6$ mm:

$$S = \sqrt{(2\pi \times 14.5)^2 + 203.2^2} = 222.67 \text{ mm},$$

where $h = 101.6 \times 2 = 203.2$ mm.

So, the arc length is $S_{180} = 222.67/2 = 111.34$ mm.

For S_2 mode, measured TOF (τ) between signals from two holes is 48.0 μs (pulse-echo method was used). Thus, the group velocity is

$$V_{gr} = \frac{S_4}{\tau} = \frac{111.34 \times 2}{48} = 4.64 \text{ mm}/\mu\text{s}$$

This confirms that the S_2 mode was generated (calculated group velocity is 4.384 mm/μs).

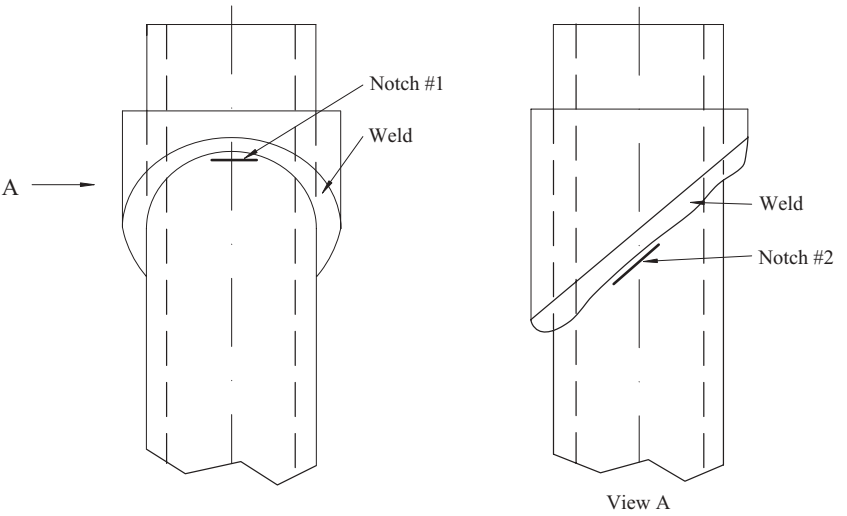

Figure 8.30 Upper end of the test samples, representing location of two notches in heat-affected zone.

It is very important to asses the influence of a water load on wave propagation in the cylinder. Experiments have shown that the water load slightly influences the S_1 wave mode propagation. The wave mode S_2 propagation is slightly affected by the water load as well: the signal amplitude is slightly reduced and changed in shape.

The final test for the probe to be selected is its ability to detect notches that represent the location and size of real cracks. Figure 8.30 shows the positions of two notches that simulate real crack orientation in the weld's heat-affected zones. Reflections from these notches are shown in Figure 8.31.

One can see that both notches were detected. Especially important is the detection of the notch that is inclined at 45°. It confirms once again that the beam propagation follows a spiral path.

The probe design in this case is a much easier task than the technique development. The wedge angle for both S_1 and S_2 modes can be chosen as the same at 28° and then corrected, if necessary. Figure 8.32 shows one of the wedge geometry.

Conclusion

1. Comparison of the two modes shows that both of them are acceptable for practical applications.
2. The S_1 mode needs less gain and slightly more gain than S_2 mode sensitive to water load.

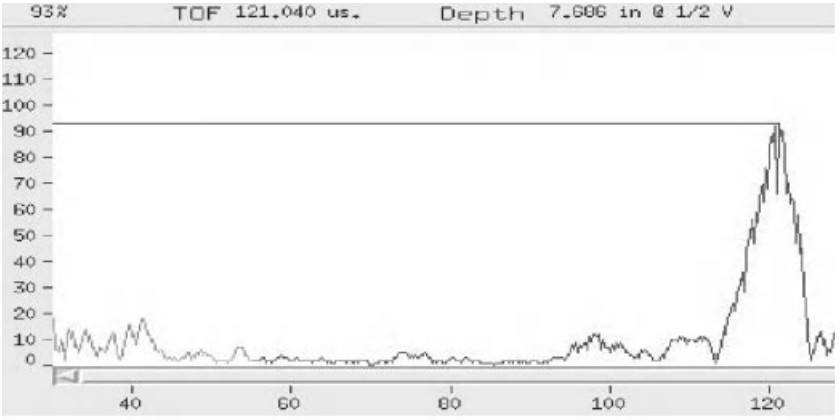

(A)

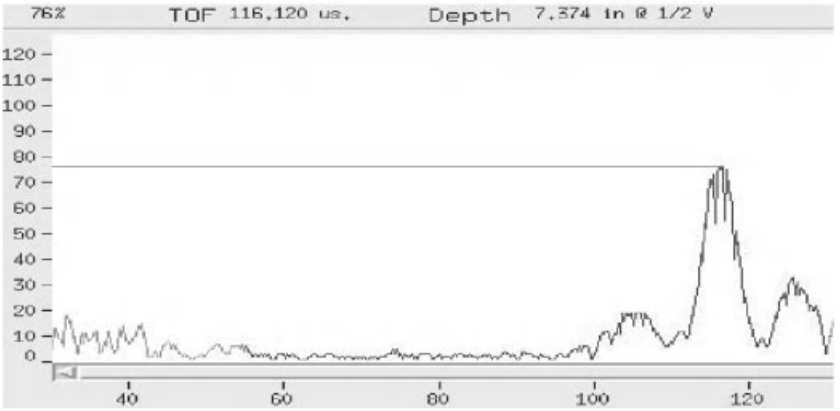

(B)

Figure 8.31 Reflections from the notches that represent the location and size of the real cracks (S_2 mode). (A) Reflection from notch #1, (B) reflection from notch #2.

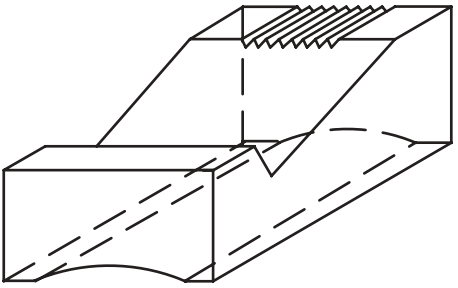

Figure 8.32 Example of a wedge design for Lamb-type guided wave generation for the inspection of a cylinder.

3. The reflected signals have shape (see Figure 8.8), which confirms that the frequency of the transducer matches the theoretical calculations.

8.3.3. Technique Development and Probe Design for a Thick Wall Hollow Cylinder Inspection

Test Object Description

Consider the case of an inspection with Lamb-type guided waves of a hollow cylinder, fabricated from Inconel, with the following dimensions:

- Outside diameter of the hollow cylinder—33.5 mm
- Inside diameter—20.8 mm
- Wall thickness—6.35 mm.

This hollow cylinder does not match with the definition of a *thin* hollow circular cylinder. Let us name it a *thick* hollow circular cylinder. It is very possible that the inspection of these cylinders will present difficulties.

This hollow cylinder (Figure 8.33) is welded to the cladding of the bottom head of the vessel. Inside the cylinder an insert is located. There is an air gap between outside surface of the cylinder and the penetration into the bottom head. There is also a water gap between the inside diameter of the cylinder and outside diameter of the bar.

The water gap in the radial direction is approximately 0.15 mm. The air gap is approximately at the same magnitude as the water gap. The minimum available distance between the probe exit point and a possible crack location is approximately 180 mm.

The locations of possible cracks to be detected are shown in Figure 8.33. A crack may start on the inside surface of the cylinder and propagate in the wall toward the outside surface and in the circumferential direction following the heat-affected zone of the weld.

First, let us calculate the *fd* parameter of the symmetric modes which may not be sensitive to a water load.

For example, for an Inconel cylinder with a wall thickness of 6.35 mm, $V_S = 3.10$ mm/μs and $V_L = 5.66$ mm/μs, the symmetric S_1 mode *fd* parameter is

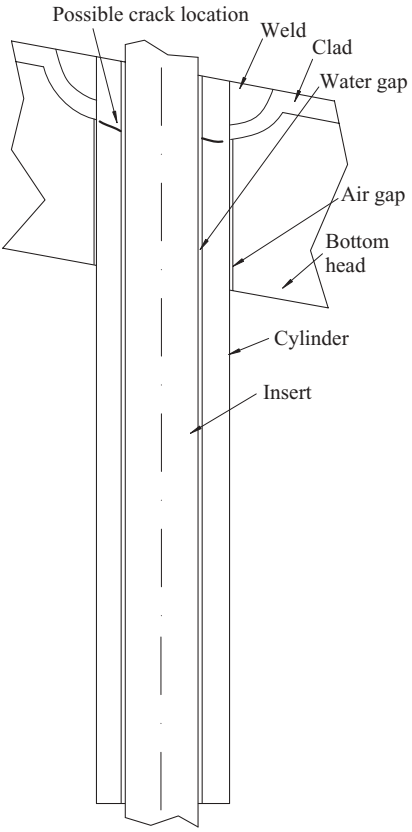

Figure 8.33 Simplified geometry of thick wall hollow cylinder.

$$fd = \frac{1 \times 3.1}{\sqrt{1 - \left(\frac{3.1}{5.66}\right)^2}} = 3.71 \text{ MHz} \cdot \text{mm}.$$

For a given wall thickness of 6.35 mm, the frequency can be calculated as

$$f = \frac{fd}{d} = \frac{3.71}{6.35} = 0.584 \text{ MHz}.$$

Then the incident or wedge angle can be calculated according to Equation 8.12.

Table 8.6
Calculation Results for Two Modes: S_1 and S_2

Parameter	Wall thickness d, mm	Frequency f, MHz	
fd, MHz·mm		S_1 mode	S_2 mode
3.71	6.35	0.584	
7.41	6.35		1.167
Wedge angle, degree		28.89	28.89

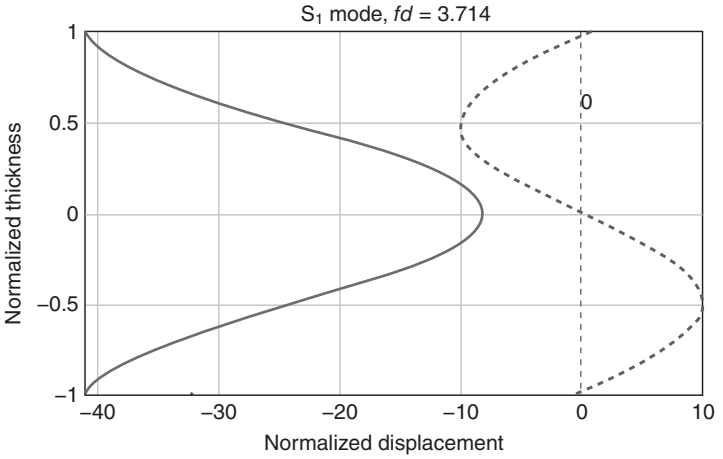

Figure 8.34 Normalized particle displacement: S_1 mode, wall thickness 6.35 mm.

Calculation results for the two modes are presented in Table 8.6.

If it will be possible to fabricate a transducer with exactly the same frequency as calculated (0.584, 1.167 MHz.), the out-of-plain particle displacement should be zero. Particle displacement calculation for the wall thickness confirms this statement. For example, the normalized particle displacement for the S_1 mode in Inconel with wall thickness 6.35 mm is shown in Figure 8.34.

The out-of-plane displacement, which is the particle displacement perpendicular to the test sample surfaces, is almost equal to zero on both sides of the test sample wall. The in-plane displacement, which is the particle displacement parallel to the test sample surfaces, reaches maximum on both sides of the test sample wall and minimum in the

middle of the sample wall thickness. The frequencies shown in Table 8.6 are uncommon for transducer manufacturers. To find a desirable combination of the frequency and the dependence on water load, the analysis should be performed for several other modes.

For 0.5 MHz and 1.0 MHz frequencies, the following modes can be generated (Table 8.7) according to the dispersion curves (Figure 8.35).

Table 8.7
Modes Which Can Be Generated at 0.5 MHz and 1.0 MHz Frequencies

Frequency, MHz		Phase velocities, mm/μs and wedge angles for modes					
		A_0	S_0	A_1	S_1	A_2	S_2
0.5		2.707	3.008	5.344	5.906	–	–
1.0		2.786		3.291	4.252	5.503	5.953
Wedge angle, degree	0.5 MHz	–	65.4	30.78	27.59	–	–
	1.0 MHz	78.7		56.2	40.0	29.8	27.66

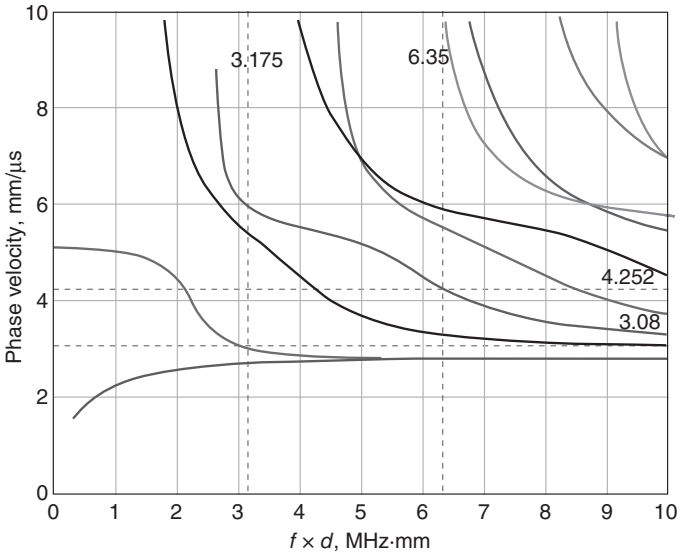

Figure 8.35 Phase velocity dispersion curves for wall thickness 6.35 mm frequency 0.50 and 1.0 MHz.

Particle displacements for S_1, S_2, and S_0 modes for wall thickness 6.35 mm are shown in Figure 8.36A–C. In this case, the out-of-plane displacement is not equal to zero. This means that the energy will leak into the water. It is not clear if these modes can be utilized practically. The in-plane displacement is maximized on both surfaces of the test sample wall, and only experiments can show the applicability of these modes.

Group velocities for modes at the 0.5 MHz and 1.0 MHz frequencies are summarized in Table 8.8. An example of the group velocities calculation for 1.0 MHz transducer and S_1 and S_2 modes is shown in Figure 8.37.

Mode Selection for Transducers with Standard Frequencies

To assess the applicability of modes, as a first approximation, it is much easier to generate modes in flat strips instead of a hollow cylinder, with the same metal and wall thickness. Propagation in the Inconel strip, which contains notches on both sides, can be performed experimentally by using the setup as shown in Figure 8.38.

The following modes were generated by using a standard 1.0 MHz 0.500 in. diameter transducer for a given wall thickness (Table 8.9). The generated modes should be evaluated by using the following practical performance criteria: influence of water load, noise level, gain level, and signal shape.

The reflections generated by A_0 and S_0 modes are the best according to abovementioned criteria. The parameter "water influence" shows the gain in decibel necessary to increase the signal amplitude to the level of amplitude with no water in the gap. Water should be present only on one side of the strip, "inside" surface, opposite to the surface where the probe is positioned. This should simulate a real water gap.

Examples of signals generated in a 6.35-mm thick strip are shown in Figure 8.39 (no water gap). In Figure 8.39, the first signal is from the first notch: for S_0 mode at 148.000 μs, and for S_2 mode at 86.600 μs (TOF 2 in Figure 8.39). The signal amplitude from the second notch in both cases is not more than 20%. The signal-to-noise ratio in the area of the second notch is unacceptable.

The two modes A_0 and S_0 were selected for thick wall hollow cylinder inspection. For the group velocity measurement, the sample with

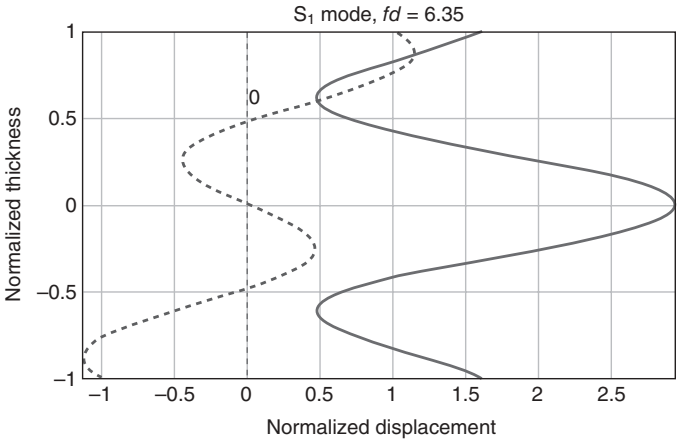

(A)

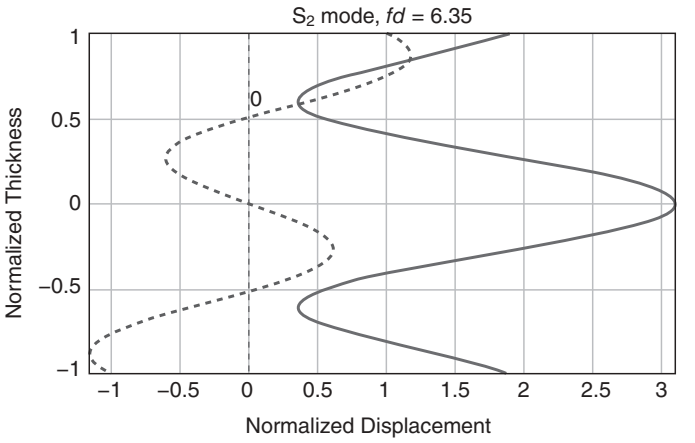

(B)

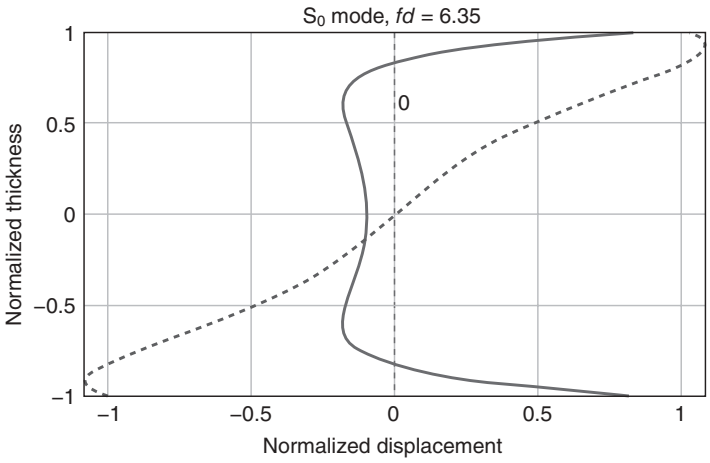

(C)

Figure 8.36 Normalized particle displacement: S_1, S_2, and S_0 modes for 6.35 mm wall thickness.

Table 8.8
Group Velocities for Modes at 0.5 MHz and 1.0 MHz Frequencies

Frequency, MHz	Group velocities, mm/μs					
	A_0	S_0	A_1	S_1	A_2	S_2
0.5	2.923	2.265	3.306	4.01	–	–
1.0	2.748		2.541	2.123	3.34	4.309

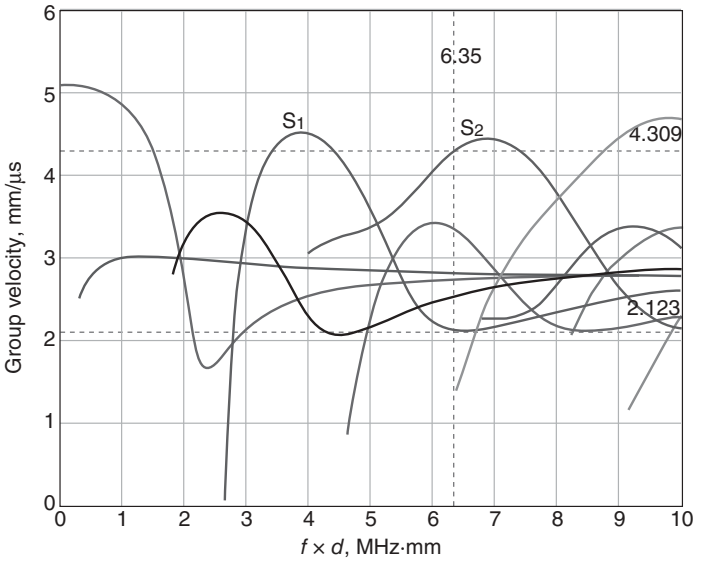

Figure 8.37 Group velocity dispersion curves for modes at 1.0 MHz.

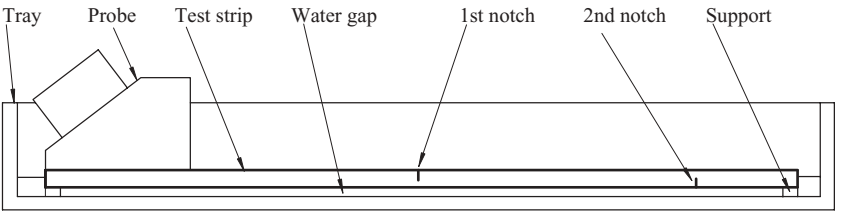

Figure 8.38 An experimental setup.

Table 8.9
Calculated and Generated Modes and Their Parameters

Incident angle, degree		Group velocity, mm/μs		Signal-to-noise ratio, dB	Water influence, dB	Comments
Calculated	Measured	Calculation	Measurement			
78.7—A_0, S_0	73	2.748	2.8	>20	+8	Acceptable
56.2—A_1	56	2.541	2.73	>20	+13	Acceptable
40.0—S_1	39	2.123	2.17	≅12	+20	Acceptable
29.8—A_2	29	3.34	3.12	≅4	+12	Not acceptable
27.66—S_2	27	4.309	3.96	≅4	+6	Acceptable

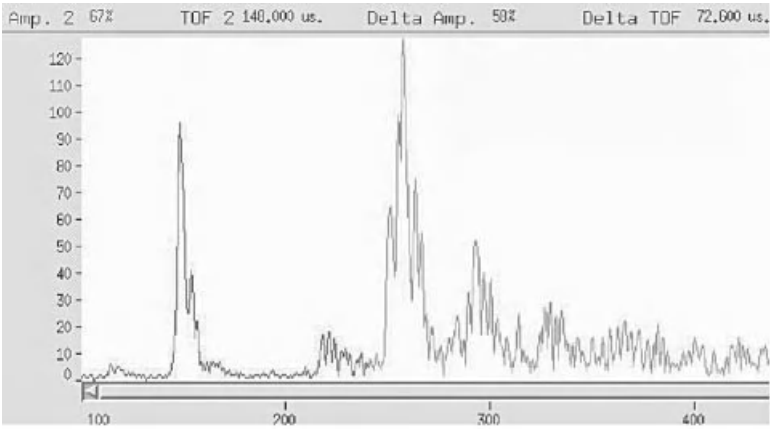

S_0 mode

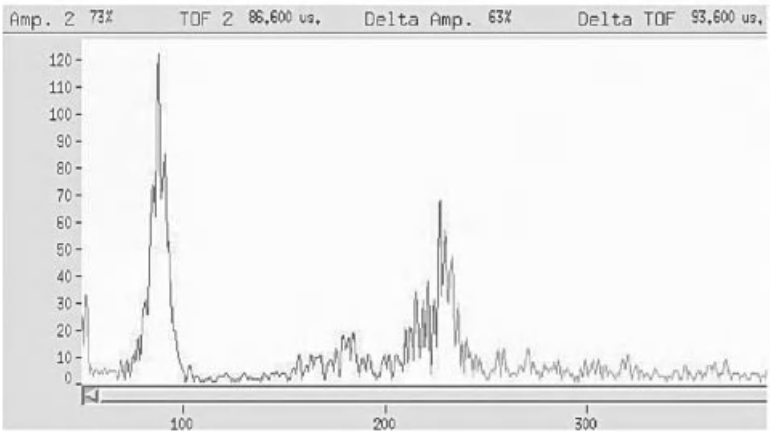

S_2 mode

Figure 8.39 Examples of signals generated in 6.35 mm thick strip.

three holes 90° apart in circumferential direction and $h = 50.8$ mm apart in axial direction was selected. The procedure of arc length calculation is the same as in "Group Velocity Measaurement" section.

Cylinder outside diameter is 33.5 mm, therefore $2\pi r = 105.19$ mm:

$$S = \sqrt{105.19^2 + 203.2^2} = 228.8 \text{ mm}$$

$$S/4 = 2\pi/4 = 228.8/4 = 57.2 \text{ mm}.$$

The average $\tau = 37.7$ μs. So, the group velocity is

$$V_{gr} = \frac{2S/4}{\tau} = \frac{2\times 57.2}{37.7} = 3.03 \text{ mm}/\mu\text{s}$$

It appears that the S_0 mode was generated, of which the calculated group velocity is 2.748 mm/μs.

Energy Distribution along the Hollow Cylinder

The signal amplitude distribution along the circumference of the hollow cylinder can be measured approximately on the test sample with two reflectors 180° apart in the circumferential and 100 mm apart in the axial direction (Figure 8.40).

At the zero degree position, the probe should be aligned with the center of the first reflector. Then the probe should be rotated around the circumference, and the signal amplitude from each reflector should be measured at, for example, every 45°. As an example, results are summarized in Table 8.10 and are plotted in Figure 8.41 for the S_0 mode and the 6.35 mm hollow cylinder wall thickness.

It is known that Lamb waves in plate have a sharp directivity pattern. One can see that in a hollow cylinder, the signal amplitude distribution depends on the probe position along the circumference and

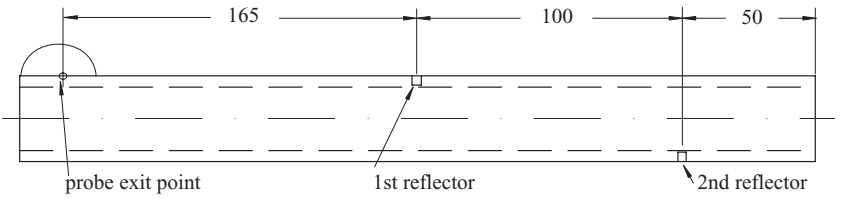

Figure 8.40 Position of the reflectors for a signal amplitude distribution measurement.

Table 8.10
Signal Amplitudes, % for S_0 Mode

Probe position, degree	0	45	90	135	180	225	270	315
1st reflector, A (Figure 8.41)	80	22	20	24	36	20	18	30
2nd reflector, B (Figure 8.41)	38	60	54	50	70	42	56	45

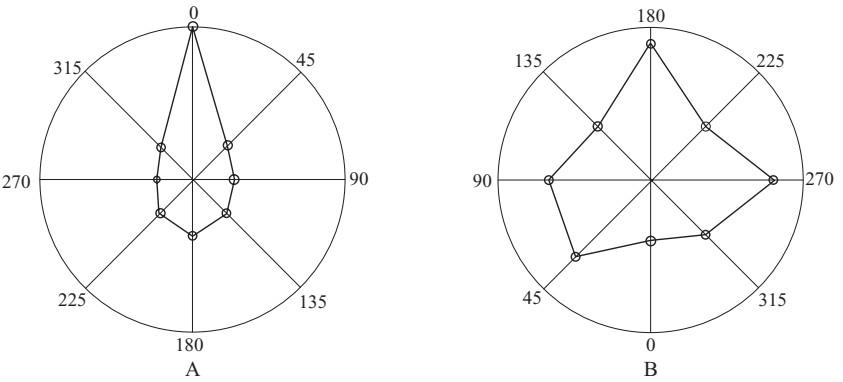

Figure 8.41 Normalized circumferential signal amplitude distribution on the outside surface of the hollow cylinder. S_0 mode.

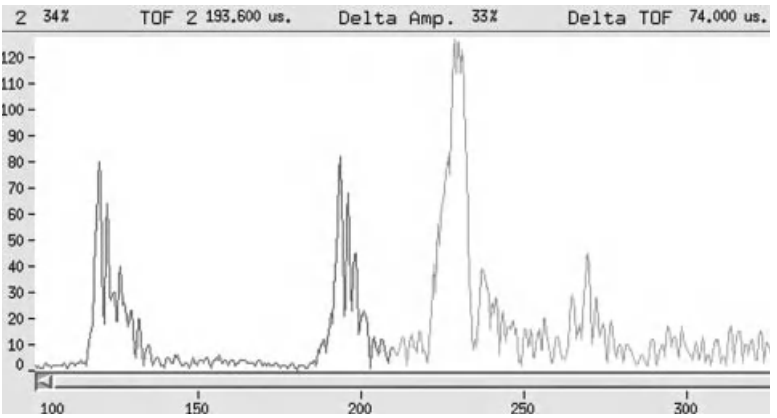

Figure 8.42 Signals reflected from the notches in the hollow cylinder. S_0 mode.

its distance from any reflectors. For example, at a distance of 165 mm from the probe, the distribution is more or less sharp (Figure 8.41A), but at a distance of 265 mm from the probe, the energy is more evenly distributed around the circumference (Figure 8.41B). It would appear that at some distance from the probe the wave propagation becomes axisymmetric, even though it originated as non-axisymmetric.

The first signal at 119.6 μs in Figure 8.42 is a reflection from the first reflector, and the second signal at 193.6 μs from the second reflector. The drawback of the almost even signal amplitude distribution

(Figure 8.41B) is the problem of locating the exact position of the reflector along the circumference.

Influence of Water Gap Thickness on Wave Propagation for S_0 Mode

Analysis of the modes reveals that the S_0 and/or A_0 modes demonstrate the best results, both in signal shape and signal-to-noise ratio for a non-water loaded strip. To assess the influence of water gap thickness on wave propagation, the experimental setup as shown in Figure 8.38 can be used.

The strip should be placed in the tray on two supports forming a water gap of approximately 3.0 mm, which is equal to ≈2 wavelengths at 1.0 MHz. The probe is fixed on one end of the strip. The distance between the exit point of the probe and the edge of the strip has to be the same as in the case of actual inspection of the test object. To compare the results, experiments should be performed with no water in the gap and with water in the gap. The typical results for transducer frequency 1.0 MHz, 6.35 mm thick strip, S_0, or A_0 mode are

1. With no water in the gap both notches are detected.
2. With water in the gap the second notch (imitation of an "inside" notch in the hollow cylinder) cannot be detected.

At the same time, the wave propagation showed some dependency from the reduction of the water gap thickness.

The water gap between the inside surface of the sleeve and the outside surface of the heater in the radial direction is much less than 3.0 mm, approximately, 0.13–0.2 mm, which is, by order of magnitude, less than the wavelength in water. It is possible that a drastic reduction in the thickness of water gap will have a beneficial effect on the Lamb-type guided wave propagation.

To address wave propagation in the hollow cylinder with a real water gap thickness, the notch should be machined on the inside surface of the test samples. Measurements were made with a rod inside the hollow cylinder, which simulated a real condition. The gap in the radial direction was approximately 0.2 mm.

Several modes were generated in the test sample with a water gap by using a 1.0 MHz transducer. No influence of the water gap on the

detectability of the inside notch was noticed. So, if the water gap is much less than the wavelength (in this case the water gap is $\cong 0.1\lambda$), practically, all the generated modes will probably provide acceptable signal amplitudes and shapes.

During the experiments with a 6.35 mm thick strip, it was noticed that not one but two modes propagate simultaneously. The explanation of this phenomenon was given in Reference 13. It is generally known that as the plate thickness varies from "zero" to infinity, the phase and group velocities of modes, S_0 and A_0, tend to have Rayleigh wave velocity V_R. It was shown that at plate thickness $d > \lambda_R$, the Rayleigh wave excites in two modes S_0 and A_0 (in this case $d \cong 3\lambda_R$). The waves of these modes are excited with approximately the same amplitudes and phase velocities. During the propagation the waves interfere. At some *fd* value, these two modes become like "one" wave. This "combined" wave is named the quasi-Rayleigh wave.

Rayleigh Wave Velocity Measurement

To confirm that S_0 mode was generated and to clarify the phenomenon of a quasi-Rayleigh wave propagation in a thick strip, Rayleigh wave velocity should be measured.

Rayleigh wave generation and velocity V_R measurements were performed on 304 stainless steel plate 25 mm thick. Strictly speaking, surface (Rayleigh) wave can propagate only along the flat surface of a half space, which is impossible to create in practice. But for the plate thickness $d >> \lambda_R$, the measurements should be acceptable.

S_0 mode generated at frequency 1.0 MHz was used for the experiment. The average measured surface wave velocity is $V_R = 2.93$ mm/μs. At this velocity, the wavelength for 1.0 MHz is $\lambda = 2.93$ mm. So, for the strip thickness $d = 6.35$ mm, $d = 2.17\lambda$ (1.0 MHz). These measurements confirm the statement in Reference 13.

The same phenomenon is correct for hollow cylinders. The program, designed to calculate dispersion curves for hollow cylinders, shows the same output as for plate at large product of *fd*. As the wavelength decreases, the hollow cylinder begins to resemble a half space: the phase velocity of A_0 and S_0 modes should approach the velocity of the Rayleigh wave. The program also shows that for large radii, the effect of curvature diminishes, and in the limit of an infinite radius, the effect of curvature vanishes. Figure 8.43 illustrates these statements. The

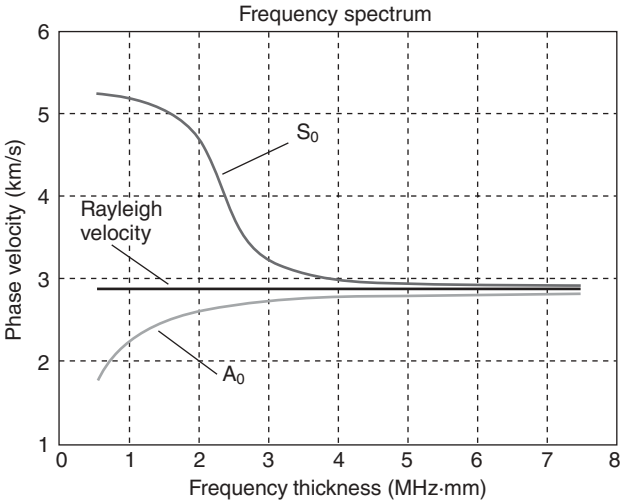

Figure 8.43 Phase velocity dispersion curves for two zero modes compared with Rayleigh wave velocity.

program provides good results of the calculation dispersion curves for hollow cylinders with diameters of approximately 6.0 mm and greater.

The previous experiments were performed with transducers having standard frequencies and did not show optimized reflected signal pattern. One of the reasons for this is inadequate frequencies for given wall thicknesses and modes to be generated. To optimize Lamb-type guided wave propagation in hollow cylinder, the frequency tuning is very helpful.

For example, when a standard transducer of 1.0 MHz is driven by tone-burst cycles at a close to excitation frequency, the shape of the signal improves, and the gain needed to achieve the same signal amplitude is drastically reduced. Figure 8.44B illustrates the best signal received from an inclined notch, generated by the S_0 mode, in the test sample with a wall thickness of 6.35 mm, without frequency tuning. Compare this signal with the signal from the same notch at the same distance but tuned (Figure 8.44A). The best signal was produced at frequency of 0.874 MHz. The signal shape is significantly different from untuned signal and, more importantly, the gain was reduced by 14 dB to achieve the same signal amplitude.

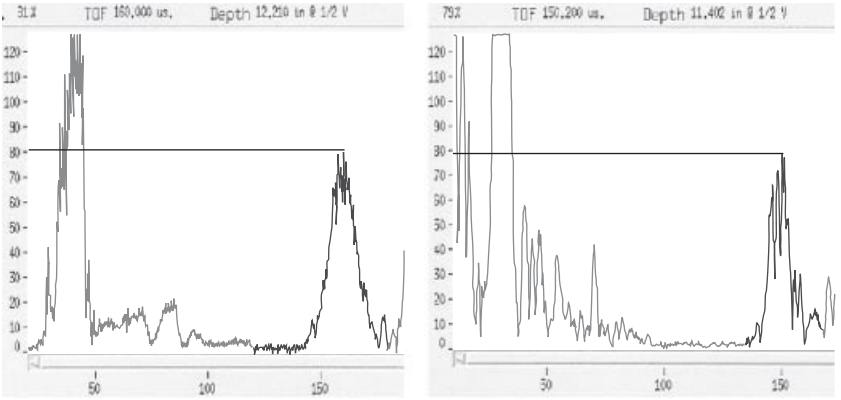

(A) 42 dB (B) 56 dB

Figure 8.44 Comparison between tuned (A) and untuned (B) signals.

Conclusion

1. The water load does not influence wave propagation of water-sensitive modes, if the layer thickness is much less than the wavelength.
2. It is most likely that a hollow cylinder with a wall thickness of about 6–7 mm is the maximum thickness of a hollow cylinder wall that can be inspected at frequencies close to 1.0 MHz.
3. Frequency tuning is very helpful to optimize the wave propagation.

CHAPTER 9

Technique Development and Focused Probe Design for Immersion Method Inspection

9.1. BASICS OF FOCUSED IMMERSION PROBE DESIGN

9.1.1. General Observation

Focused probes development and application for NDT reached its apogee in the late 1970s [40–43]. These focused probes were developed to improve the detection and sizing of flaws by concentrating the ultrasonic energy in a smaller focal zone using a relatively large diameter transducer. Currently, there are other techniques for an accurate detection and sizing of flaws, but focused probes are still valuable tools to aid in detection and sizing.

The focusing effect of an ultrasonic probe can be achieved, among other techniques, by attaching a lens to a flat crystal, or using a curved

Ultrasonic Inspection Technology Development and Search Unit Design: Examples of Practical Applications, First Edition. Mark V. Brook.

crystal, or using an annular transducer. The use of lenses is the most practical approach in many cases. The lens can be permanently attached to a flat crystal, or machined separately and made to be replaceable. The design of both types of the lenses is similar. Permanent lenses are usually fabricated from epoxy raisin compounds. The removable lenses are manufactured from acrylics or polystyrene.

The simplified diagrams of a single surface lens focused probes are shown in (Figure 9.1).

The straight beam probes (Figure 9.1A) are the most usable.

There are several approaches to the design of a straight beam focused probe. One approach is to use "precise," and therefore complicated, equations, starting from the determination of focal distance parameters (*Fm, L*, etc.) in a test object and then extrapolating them to parameters in water, such as a water path *L*, a focal length *Fa*, and others. In ultrasonic NDT, these "precise" equations often do not give precise results. The other approach is to use relatively simple equations to define the same parameters, and then adjust test parameters by using the experimental results. This approach will be described below.

To use the same type probe for an angle beam inspection is not recommended. The brief explanation is illustrated in Figure 9.1B. The angles of incidence for each of the inclined rays are different. For example, for two peripheral rays $\alpha_1 < \alpha < \alpha_2$, so are refracted angles also $\beta_1 < \beta < \beta_2$. This means that the central ray will be crossed by

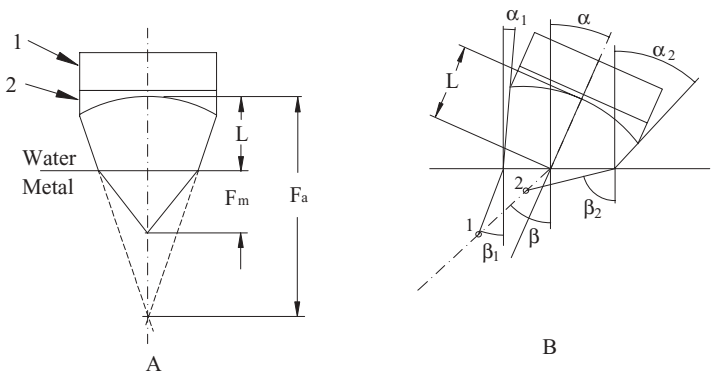

Figure 9.1 Focused immersion probe positions for (A) straight beam inspection and (B) angle beam inspection. 1, transducer; 2, lens.

other rays not in one focal zone, but in two, for example, 1 and 2. Thus, the interpretation of the test results can present difficulties.

9.1.2. Consideration Relative to Straight Beam Immersion Focused Probe Design

Spherical Aberrations Phenomenon

The easiest way to describe these aberrations is to follow the explanation given in the geometrical optics for a concave spherical mirror, which is also correct for a lens (Figure 9.2) [11]. The sketch shows a mirror with a radius r and a curvature radius R. The parallel rays of light, coming from the right, reflect and intersect the mirror axis not in one focus point, but in different points, depending on the distance h, at which a ray is reflected. This is an undesirable effect in optics and is known as spherical aberration. Instead of a singular focus, there is a focal zone of length L and diameter d.

The explanation of a spherical aberration of a mirror, given in optics, is simple (Figure 9.3).

If a ray, parallel to the axis of the spherical mirror with curvature radius R, is incident at point a, it will reflect at the angle α, which is equal to the angle of incidence, according to the law of reflection. Therefore, the triangle a-b-o is isosceles, and side ab = bo. Then of course, ao < ab + bo and therefore, $R < 2$bo. If point a moves toward

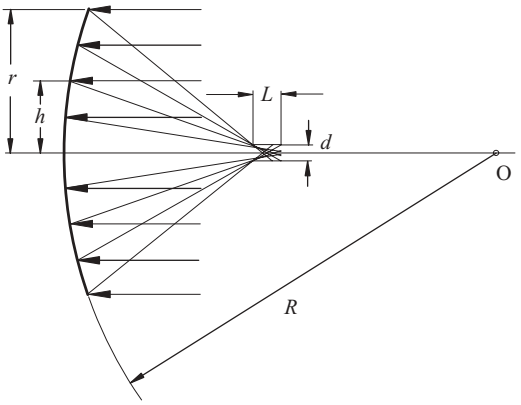

Figure 9.2 Spherical aberration of a concave spherical mirror.

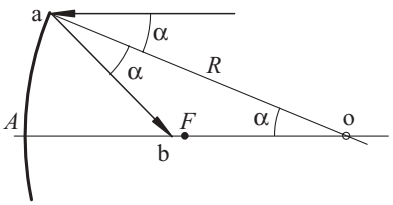

Figure 9.3 Aberration explanation of a concave spherical mirror.

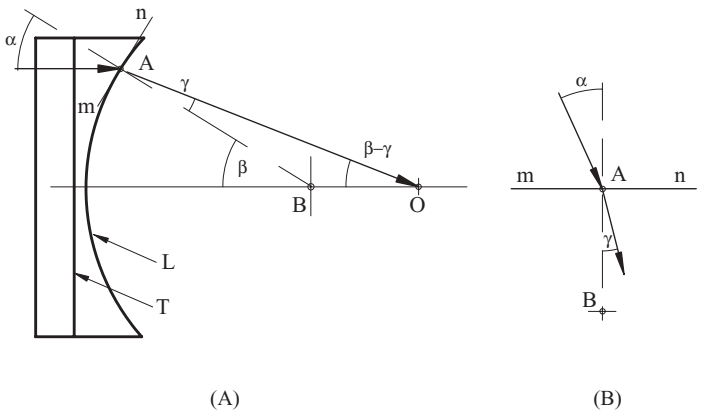

Figure 9.4 Single surface lens aberration (A) and restriction to ray propagation.

point *A*, point b will approach point *F*, which is the paraxial focus of the mirror. In the limit oF = ab = FA = 0.5R.

It is worth noticing that the magnitude of aberration is proportional to h^2, which is the square of the height of the ray above the mirror axis.

All of the abovementioned regarding mirror aberration is also correct for a single surface lens (Figure 9.4A). The only exception—the law of refraction—should substitute for the law of reflection.

The Figure 9.4 shows a spherical lens L attached to a flat transducer T. The lens curvature radius is AB, and line mn is perpendicular to the radius. The incoming ray is incident on the lens surface at point A at the angle of incidence α.

If it would be possible to refract all rays to the center of the lens curvature B, then no spherical aberration would occur (angle $\gamma = 0$). This would be an ideal case, but it is impossible due to the restriction

of Snell's law [44]. By rotating the portion of the sketch (angle of incidence α, along with lines mn and AB), as shown in Figure 9.4B, one can see that the refracted angle γ cannot be zero when the angle of incidence α is not zero.

9.1.3. Acoustic Parameters of Focused Probe

The maximum distance to the flaw, which has to be detected in the test object, is usually given in the inspection specifications, as well as its minimum dimensions to be sized. The ultimate goal of a probe design is to calculate the acoustic parameters in water, which would satisfy certain specification requirements.

The acoustic parameters are

1. the acoustical focal length in water or in a test object material, which defines the point of highest concentration of energy that is the acoustic focus,
2. the focal zone, which is the space around acoustic focus point defined by the length and the diameter.

The focal zone length is the distance on both sides of the focus point where signal amplitude decreases at 6 dB, as compared to the maximum amplitude. The focal zone diameter is defined as the distance from both sides of a probe acoustic field central line where the signal amplitude decreases at 6 dB, as compared to the maximum amplitude.

The desirable acoustic parameters of the probe can be calculated using its geometrical parameters, such as

1. the geometrical focus which defines the point, where all imaginary rays intersect the central axis of the probe,
2. the crystal radius, and
3. the lens curvature radius.

The parameters related to the focused probe geometry are illustrated in Figure 9.5.

The single-surface lens 2 with the curvature radius R_l is attached to the transducer 1 with the flat crystal of radius r. The geometrical

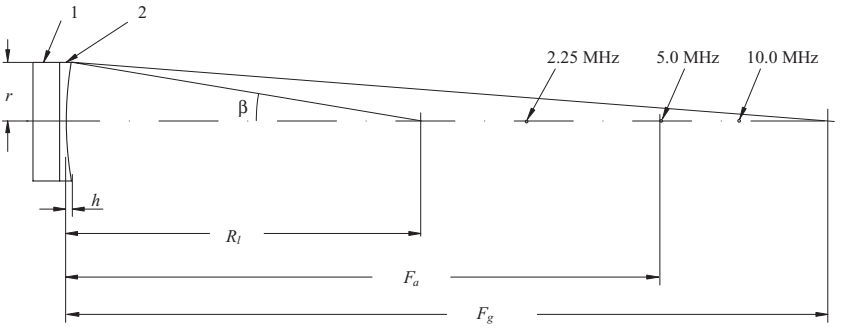

Figure 9.5 Focused probe geometrical parameters. 1, transducer; 2, lens.

focus length is F_g. Usually, the location of the acoustic focus is between the geometrical focus and the lens radius point, depending on the transducer frequency (for the same R_l and r). Possible positions of the acoustic foci for nominal transducer frequencies 2.25, 5.0, and 10 MHz are shown in Figure 9.5, where the acoustic focal length F_a defines the position of the acoustic focus of the transducer with a nominal frequency of 5.0 MHz.

Spherical and chromatic aberrations, typical in optical systems, are a great influence on the sound field of an ultrasonic focused probe. It is worth noting that aberrations in the sound field do not affect conventional straight beam inspections using focused probes. The aberrations are "responsible" for the creation of the focal zone. In several cases, when an extremely sharp focus spot is essential (acoustic microscope), there are techniques to eliminate the aberrations.

9.2. GEOMETRIC AND ACOUSTIC PARAMETER CALCULATION

The geometric focal point can be calculated as

$$F_g = R_l \frac{\cos\beta\left(1-\frac{h}{R_l}\right)+\frac{V_w}{V_l}\left(\frac{r}{R_l}\right)^2}{\cos\beta-\frac{V_w}{V_l}\left(1-\frac{h}{R_l}\right)}+h. \tag{9.1}$$

The following equation for the acoustic focal distance F_a calculation provides practically accurate results:

$$F_a = R_l \frac{1 - \left(\frac{\lambda}{2} - \frac{V_w}{V_l}\right)^2}{\frac{r^2 + h^2}{\left(1 - \frac{V_w}{V_l}\right) + \frac{\lambda}{2h}}}, \tag{9.2}$$

where R_l = lens curvature radius, mm

r = lens radius, mm

h = lens "depth", mm

λ = wave length, mm

V_w = sound velocity in water, mm/μs

V_l = sound velocity in lens material, mm/μs

The value of h can be calculated as $h = R_l(1 - \cos\beta)$.

For a flat transducer (or flat lens) $R_l = \infty$, $h = 0$, and this equation becomes the formula for near-field distance:

$$F_a = N_0 = \frac{r^2 - \frac{\lambda^2}{4}}{\lambda}. \tag{9.3}$$

The maximum and minimum acoustic focal distances can also be derived from this equation.

If $R_l >> r$, it is a condition for maximum acoustic focal distance, and $F_{a\,\max}$ can be calculated as

$$F_{a\max} = R_l \frac{1 - \frac{\lambda^2}{4}}{\left(1 - \frac{V_w}{V_l}\right) + \frac{\lambda}{2h}}. \tag{9.4}$$

If $R_l = r$, it is a condition for minimum acoustic focal distance and $F_{a\,\min}$ can be calculated as

$$F_{a\min} = \frac{r\left[1 - 0.5\left(\frac{V_w}{V_l}\right)^2\right] + \frac{\lambda}{2}\frac{V_w}{V_l} - \frac{\lambda^2}{8r}}{\left(1 - \frac{V_w}{V_l}\right) + \frac{\lambda}{2r}}. \tag{9.5}$$

For practical simplicity, the main equation for the acoustic focal distance can be reduced to the formula

$$F_a = R_l \frac{1}{\left(1 - \frac{V_w}{V_l}\right) + \lambda \frac{k}{r}}, \tag{9.6}$$

where $k = R_l/r$.

The following equation for the geometrical focal distance F_g calculation gives practically accurate results:

$$F_g = R_l \frac{1 + \frac{V_w}{V_l}\left(\frac{1}{k}\right)^2}{1 - \frac{V_w}{V_l}}. \tag{9.7}$$

The focal zone diameter d and length l at a level of –6 dB can be calculated as

$$d = \lambda \frac{F_a}{2r} \tag{9.8}$$

$$l = 4\lambda \left(\frac{F_a}{2r}\right)^2. \tag{9.9}$$

9.3. STRAIGHT BEAM SPHERICAL FOCUSED PROBE DESIGN

9.3.1. Assessment of Design Feasibility

To achieve the required acoustic focal distance in the test object, the acoustic focal distance in water can be calculated using the following equation (Figure 9.6):

$$F_a = F_m \frac{V_m}{V_w} + L \tag{9.10}$$

where F_a = acoustic focal distance in water, mm

F_m = acoustic focal distance in test object material, mm

L = water path, mm

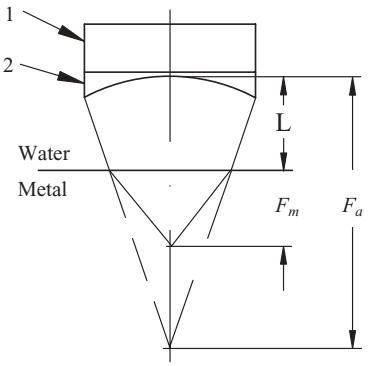

Figure 9.6 Focused straight beam immersion probe conceptual design.

V_w = wave velocity in water, mm/μs

V_m = wave velocity in test object material, mm/μs

The first step in focused probe design is to perform a rough preliminary assessment of the design feasibility. This would help to understand if the fabrication of a probe with a calculated acoustic focal distance and desirable focal zone parameters is possible. This can be done by a comparison of the focused transducer preferable sound field parameters with the near field ones.

The acoustic focal distance has to be considerably less than the near field length for the appropriate crystal diameter and frequency. The focal zone diameter has to be less than the minimum dimension of the flaw to be sized.

A quick feasibility study can be made by using the following graphs:

1. the near-field length versus the crystal diameter and frequency,
2. the crystal diameter versus the beam diameter at the near field.

As an example, the graph in Figure 9.7 shows the near field length versus crystal diameter for two frequencies. If the calculated acoustical focal distance F_a is equal to or less than approximately 0.7 of the near-field length N, then the probe fabrication is feasible.

The graph in Figure 9.8 shows the beam diameter in the near field of a flat transducer versus the transducer (crystal) diameter for

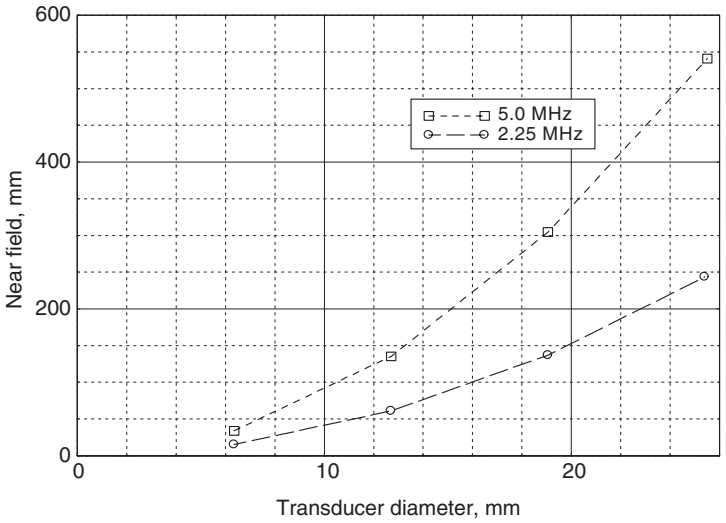

Figure 9.7 Near-field length versus crystal diameter for two frequencies.

all frequencies. If the desired focal zone diameter is less than approximately half of the beam diameter at the near-field length for appropriate transducer diameter and frequency, the probe fabrication is feasible.

9.3.2. Consequence of Calculation

After the necessary focal distance is determined, the geometrical focal distance can be calculated as

$$F_g = R_l \frac{1 + \frac{V_w}{V_l}\left(\frac{1}{k}\right)^2}{1 - \frac{V_w}{V_l}}. \tag{9.11}$$

The coefficient $k = R_l/r$. Its practical value varies from approximately 2 to 10.

For known sound velocities in the lens material V_w and steel V_l, this equation can be reduced to

$$F_g \cong R_l \times K_g \tag{9.12}$$

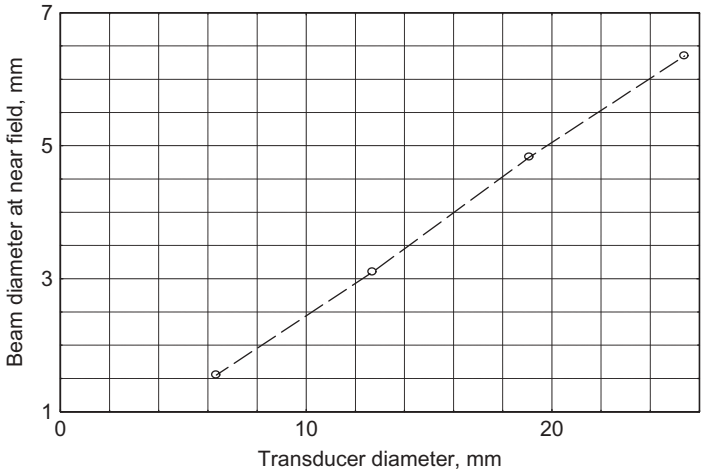

Figure 9.8 Beam diameter at near field versus crystal diameter.

The coefficient K_g can be determined from the graph in Figure 9.9 for a lens from Plexiglas with a sound velocity $V_w = 2.735$ mm/μs and steel with velocity 5.85 mm/μs. Similar graphs can be created for different combinations of velocities.

Figures 9.9 and 9.10 illustrate why the frequency independent geometric focus distance should be determined first. The lens curvature radius is approximately 2.2–2.3 times less than the geometric focus distance. The coefficient $k = R_l/r$ is used as a first approximation, keeping in mind that the crystal radius should not be more than approximately 25 mm for manufacturing reasons.

As is mentioned above, the acoustic focus distance cannot exceed the length of the near field, and there is a practical limit for the acoustic focal length and focal zone diameter. The acoustic focus distance increases sharply up to $k \cong 10$ with the increase of the lens curvature radius. Then, this increase slows down, and acoustic focus distance gradually approaches near field limit. The same phenomenon applies to the focal zone diameter. There is no reason to make a focused probe with a focal zone diameter more than half of the beam diameter in the near field zone.

As an example, Figure 9.10 illustrates the practical limitations of a spherical lens radius for a transducer diameter of 25.4 mm with frequency 2.25 MHz. The beam diameter at the near field is 3.1 mm.

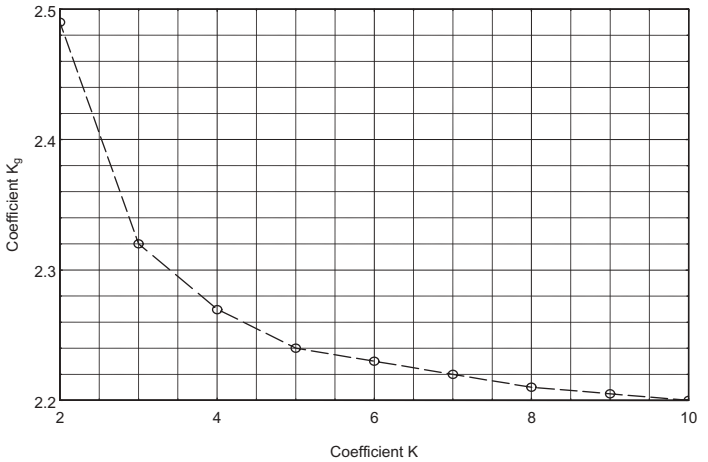

Figure 9.9 The coefficient K_g determination.

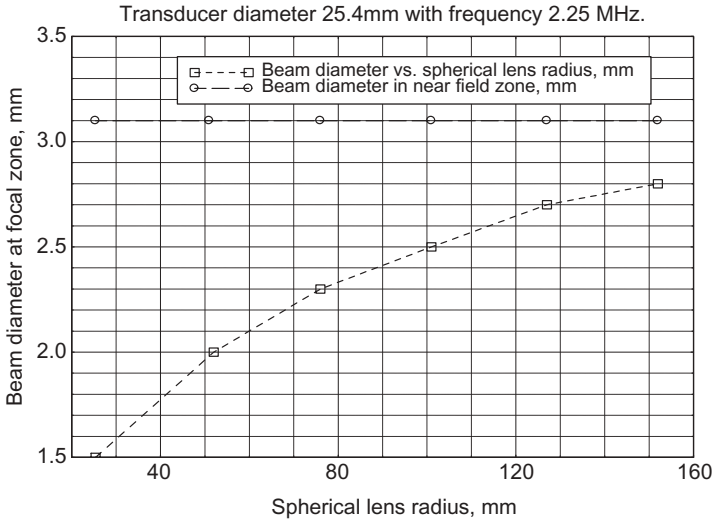

Figure 9.10 Beam diameter versus spherical lens radius.

Therefore, there is no reason to make the transducer with a spherical lens curvature radius more than 40 mm. At this radius, the beam diameter is approximately 1.77 mm.

To achieve the smallest possible focal zone diameter, the crystal diameter should be as large as practically possible, and the transducer frequency should be selected as high as possible.

As a rule of thumb, the acoustic focus distance is $F_a \cong (0.8 \div 0.9)F_g$, depending on frequency. Then, after defining the lens curvature radius, the acoustic focus distance can be calculated by using the equation

$$F_a \cong R_l \frac{1}{\left(1-\frac{V_w}{V_l}\right)+\lambda\frac{k}{r}}, \tag{9.13}$$

where λ = wave length, mm

k = coefficient.

Acoustic focus distance should be calculated for at least two appropriate frequencies.

Defining focal zone diameter d and length l by using the following formulas will complete the calculations:

$$d = \lambda\frac{F_a}{2r} \qquad l = 4\lambda\left(\frac{F_a}{2r}\right)^2.$$

These equations give values of d and l for a −6 dB level from the maximum signal amplitude in water, for the free field.

9.3.3. Example of Focused Immersion Probe Calculation with a Single-Surface Lens

Let us calculate the focused immersion probe for the inspection parameters (Figure 9.11):

- water path L = 25.4 mm
- acoustic focal distance in steel F_m = 44.45 mm

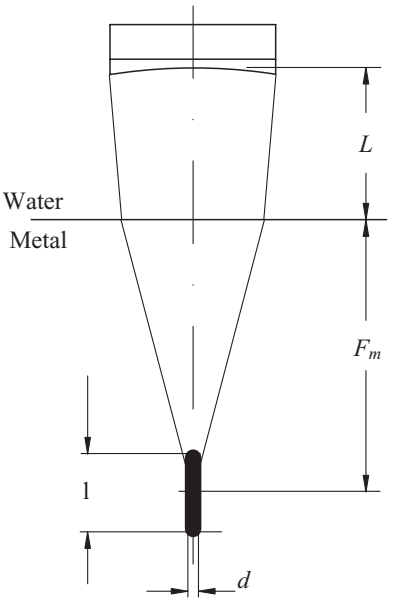

Figure 9.11 Focused immersion probe parameters for straight beam inspection.

- velocity in water $V_w = 1.49$ mm/μs
- L-wave velocity in steel $V_m = 5.85$ mm/μs

The calculation is performed for two transducers with $r_1 = 12.7$ mm and $r_2 = 19.05$ mm and frequencies $f_1 = 2.25$ MHz and $f_2 = 5.0$ MHz.

The acoustic focal distance in water, to satisfy the inspection parameters, should be

$$F_a = L + F_m \frac{V_m}{V_w} = 25.4 + 44.45 \frac{5.85}{1.49} = 200 \text{ mm}.$$

The geometrical focal distance in water can be approximately calculated as

$$F_g = R_l \times K_g.$$

Coefficient $K_g = 2.22$ is from the graph (Figure 9.9) for coefficient $k = 7$.

Then, the lens curvature radius can be calculated for the given lens radii:

$$R_l = k \times r.$$

$r_1 = 12.7$ mm	$r_2 = 19.05$ mm
$R_{l1} = 7 \times 12.7 = 89$ mm	$R_{l2} = 7 \times 19.05 = 133$ mm
$F_{g1} = 89 \times 2.22 = 196$ mm	$F_{g2} = 133 \times 2.22 = 295$ mm

The acoustic focal distance in water for the two frequencies is (coefficient $k = 7$)

	$r_1 = 12.7$ mm	$r_2 = 19.05$ mm
$f = 2.25$ MHz, $\lambda = 0.662$ mm	$F_{a1} = 108.5$ mm	$F_{a2} = 162.2$ mm
$f = 5.0$ MHz, $\lambda = 0.298$ mm	$F_{a1} = 143.5$ mm	$F_{a2} = 214.5$ mm

Finally, the focal zone diameter d and length l at the level of −6 dB should be calculated.

	F_{a1}		F_{a2}	
	d_1	l_1	d_2	l_2
$f = 2.25$ MHz, $\lambda = 0.662$ mm	2.83 mm	48 mm	2.83 mm	48 mm
$f = 5.0$ MHz, $\lambda = 0.298$ mm	1.68 mm	38 mm	1.68 mm	38 mm

The diameter of the focal zone remains the same in steel as in water, due to the fact that the wave length increases proportionally to V_m/V_w and $F_a/2r$ decreases in the same proportion.

The length of the focal zone does not remain the same in steel. It reduces proportionally to V_m/V_w because the wave length increases proportionally to V_m/V_w. At the same time, $F_a/2r$ decreases proportionally with the square of this ratio.

Therefore, the length of the focal zone will be $l_m = 48/3.93 = 9.7$ mm for 5.0 MHz probe, and $l_m = 48{:}3.93 = 12.2$ mm for a 2.25 MHz probe.

Thus, a focused probe with the crystal diameter 38.1 mm and a frequency of 5.0 MHz will completely satisfy the inspection requirements. A probe of the same diameter and a frequency of 2.25 MHz can also be used, but the water path should be reduced by approximately 12.5 mm.

Keeping in mind that the water path has a minimum value,

$$L_{\min} = F_m \frac{V_w}{V_m}.$$

In our case, the minimum water path is

$$L_{\min} = 44.45 \frac{1.49}{5.85} = 11.3 \text{ mm}.$$

Thus, to reduce the water path to 12.5 mm is possible.

This method of calculation can be applied when designing a focused probe for inspection of a test object with a curved surface, concave or convex, if the radius R_o of the object is much more than the probe's crystal radius. However, a correction is needed, if the ratio $R_o/r \leq 10$ (approximately).

It is a good practice to visualize the acoustic field of the designed focused probe after its fabrication. This can be done by scanning the probe in an immersion tank, using a target such as a thin wire or a small ball. The parameters that should be determined are the acoustic focal distance F_a, length l and diameter d of the focal zone. The focal zone diameter can be calculated after the focal zone length is measured by using the following equation:

$$d = \frac{l \times r}{2F_a}. \tag{9.14}$$

As an example, in Figure 9.12, the acoustic field of a focused transducer is shown. The transducer crystal diameter is 19.0 mm, and the nominal frequency is 5.0 MHz. This transducer's design parameters are:

- acoustic focal distance $F_a = 38.1$ mm,
- focal zone length $l = 4.8$ mm, and
- focal zone diameter $d = 0.62$ mm.

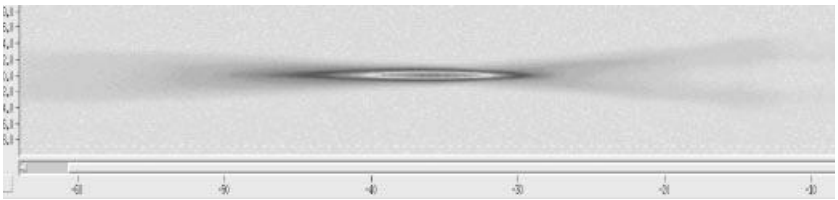

Figure 9.12 Screen capture of the acoustic field of a focused transducer.

The measured parameters are

- acoustic focal distance F_a = 39.24 mm,
- focal zone length l = 7.7 mm, and
- focal zone diameter d = 0.76 mm.

One can see that calculated and measured parameters are close enough. The deviation of the parameters can be explained by the influence of the pulsed mode of operation of the ultrasonic instrument. The length of the focal zone increases and becomes asymmetric, the maximum signal amplitude of the zone is shifting out of the transducer, and the focal zone diameter is also increasing.

CHAPTER 10

Technique Development and Probe Design for Reactor Pressure Vessel Nozzle Inner Radius Inspection

10.1. INSPECTION ZONE CONFIGURATION

Inspection of the inner radius zone of a reactor pressure vessel (RPV) nozzle for radial crack detection is one of the unique applications for ultrasonic inspection. The nozzle and the vessel are two cylinders perpendicular to each other. In most RPV designs, these two cylinder intersections are joined by welding. This creates blended zones in the shape of a saddle-like surface. In other RPV designs, the "blended zone" is machined as part of the nozzle (Figure 10.1).

The section of the inner radius inspection zones in the elevation view is shown in Figure 10.1. The inner nozzle radius zone 1, representing the corner, is the most difficult to inspect.

Ultrasonic Inspection Technology Development and Search Unit Design: Examples of Practical Applications, First Edition. Mark V. Brook.

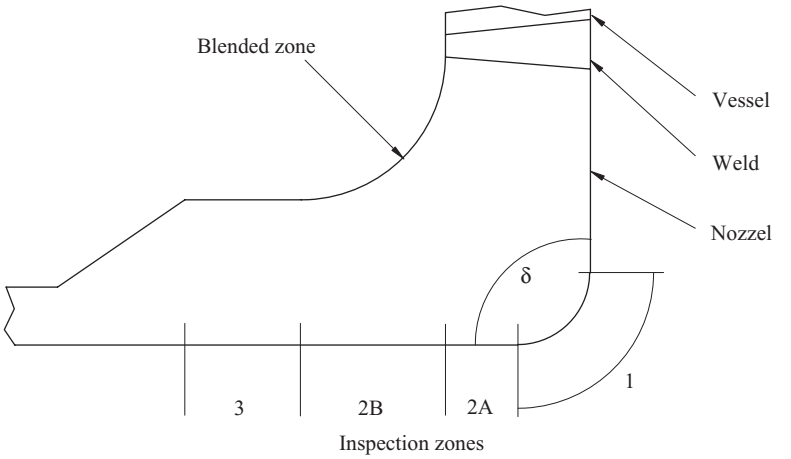

Figure 10.1 The inner radius inspection zones.

To detect possible flaws located in the inner radius zones, the inspection can be performed from the nozzle's outer or inside surfaces. These inspections have to be performed according to the requirements of the American Society of Mechanical Engineers Boiler and Vessel Code, Section XI.

10.2. INSPECTION FROM THE OUTSIDE NOZZLE SURFACES: CONTACT METHOD

The ultrasonic inspection of zone 1 is complicated by the fact that each point of the outside blended surface is oriented differently relative to the vessel and the nozzle coordinate system (Figure 10.2). This leads to a constant redirection of the sound beam with respect to the inner radius inspection zones during scanning.

Single crystal angle beam probes are usually used for this inspection. Calculation of the inspection and wedge parameters is complicated due to the shape of the blended zone.

Performing a ray tracing starting at the flaw to the probe and calculating the refracted and skew angles of the wedge manually are a difficult and very time-consuming process. Mathematical modeling speeds up this process and makes it much more reliable. Several companies, such as Electric Power Research Institute(EPRI), Weidlinger

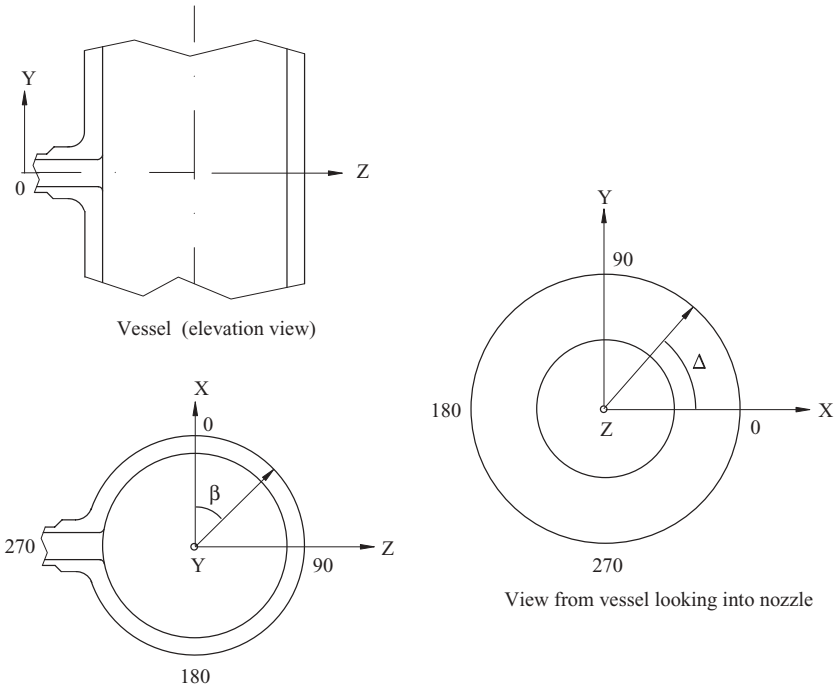

Figure 10.2 The coordinate system of a nozzle and a reactor pressure vessel.

Associates, and Westinghouse Electric, developed and use computer models.

For example, the computer model WARay3D developed by Weidlinger Associates, first of all, generates a 3D model of the nozzle to be inspected. The coordinate system of the nozzle and the RPV bring together flaw and probe positions. These positions will be defined by using, for example, the Z-axis and the angles β and Δ (Figure 10.2).

The next step in modeling is to create the flaw models (Figure 10.3), which should be located in the inspection zone. These flaw models are used for performing ray tracing from the flaw to the outside surface of the zone to be scanned.

A common inspection procedure usually defines the preferable angle of attack β_1 for radial flaw detection. The misorientation δ and skew γ angles should not exceed approximately $\pm 20°$. The position of the angles is clear from Figure 10.3. The computer model offers the

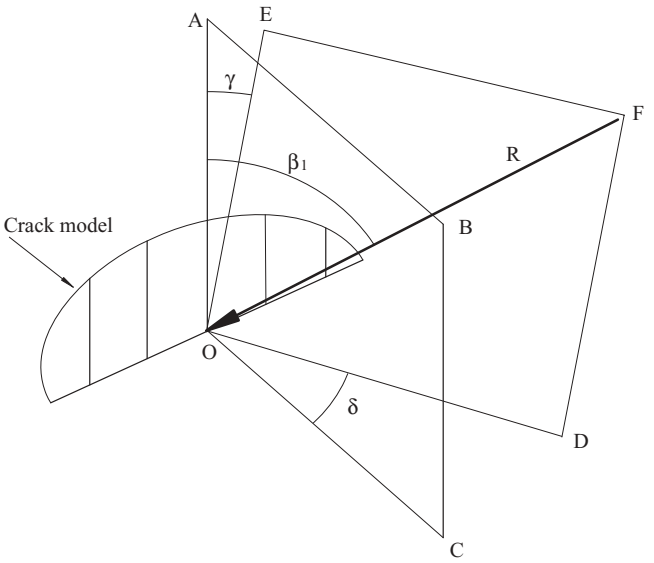

Figure 10.3 The inspection angles and a crack model.

opportunity to choose the best possible combination of the angles in order to achieve reliable inspection results. The selection is based on an analysis of each ray as it returns from the flaw model to the outer blended surface. The location and orientation of each ray with respect to the blended surface is defined by the angle of attack and by the skew and misorientation angles. The selected values of the angles are used for a wedge design.

Clearly, the best possible flaw detection results will be achieved when the central ray *R* of the refracted beam is located in plane OABC, which is perpendicular to the plane of the flaw model. In this case, the skew angle γ and the misorientation angle δ are equal to zero.

10.3. EXAMPLE OF WEDGE DESIGN FOR INNER RADIUS INSPECTION FROM THE OUTER SURFACE

Figure 10.4A shows the positions of probe 1 on the nozzle outer blend surface and flaw model 2 on the inner radius surface. Obviously, the refracted angle β_1 and the skew angle γ have to be calculated prior to the wedge design. The results of the calculations are the wedge angle

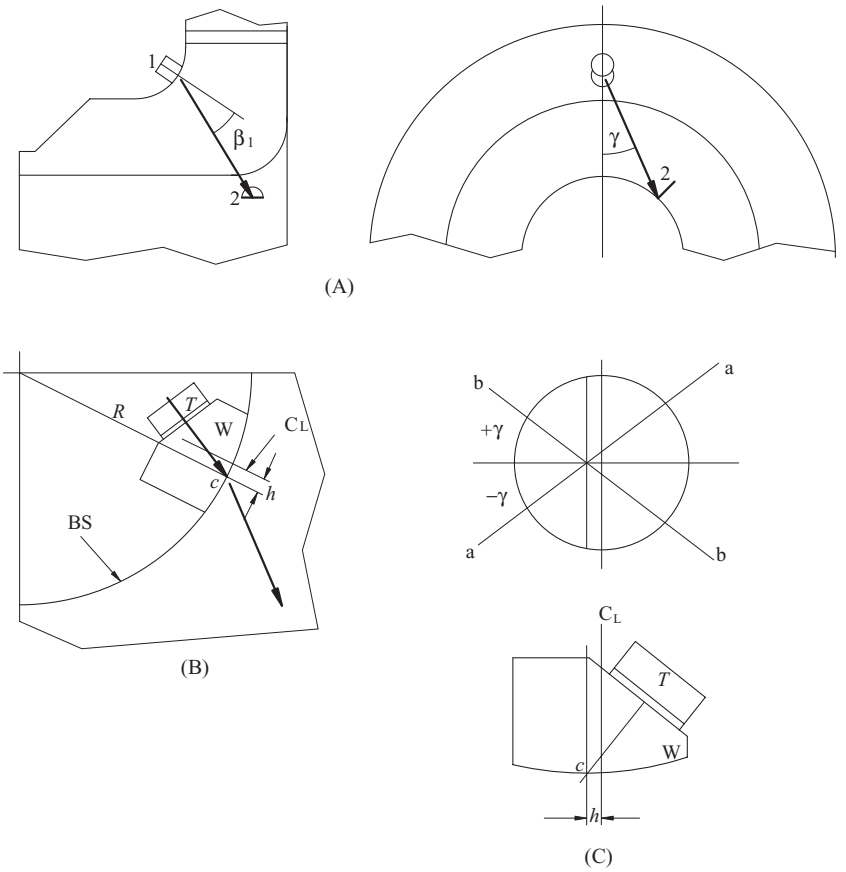

Figure 10.4 Sketches relevant to probe design for inner radius inspection. (A) Position of probe 1 on nozzle outer blank surface and flaw model 2; (B) position of wedge W with transducer T on the blend surface BS; (C) conceptual wedge design.

and ± skew angle, because the scans need to be conducted in the two opposite directions, clockwise and counterclockwise.

Figure 10.4B shows the position of the wedge W with the transducer *T* on the outer blend surface BS. The wedge exit point *c* has to coincide with the blend radius *R*.

The conceptual wedge design is shown in Figure 10.4C. The wedge blank is a round bar in order to reduce the wedge noise, machined of Plexiglas or the other wedge material in order. The wedge centerline CL does not pass though the probe exit point *c*. The distance between them is *h*. The skew angles +γ and −γ define two lines, a-a and b-b, as

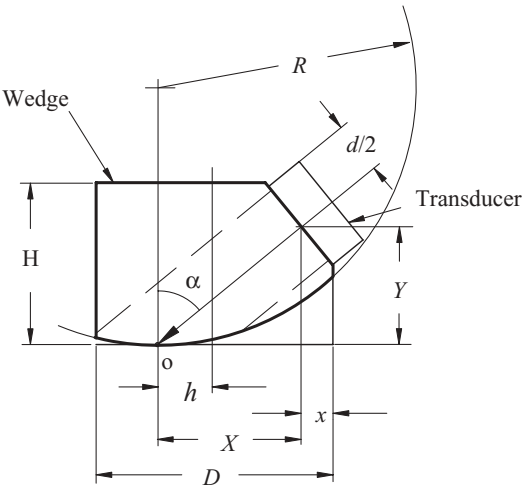

Figure 10.5 Example of a wedge calculation.

axis for cutting the wedge radius equal to the blend radius *R*. Thus, two wedges have to be used to inspect the nozzle inner radius in both directions. An example of a conceptual wedge design is presented in Figure 10.5.

Assuming that the calculations, which are performed by the computer model, determine the following wedge parameters:

the refracted angle 63°S and

the skew angles ±24°.

Thus, the angle of incidence is $\alpha = 49°$. The crystal diameter is 12.5 mm. The transducer housing diameter is $d = 14.5$ mm. The nozzle outside blend radius is $R = 38$ mm. The following wedge dimensions have to be determined (Figure 10.5):

the distance *h* between the exit point and the centerline of the wedge

the wedge diameter *D*

the wedge height *H*.

The design begins by drawing a line at the angle of incidence α, which indicates a beam center ray. The point o represents the exit point. The

circle at radius R, which was drawn through point o, represents the section of the blend surface. The dashed lines indicate the beam diameter. The distance Y has to be sufficient to prevent the transducer from touching the blend surface. In this case, $Y = 20$ mm. The simple calculation is then performed.

The distance X is

$$X = Y \times \tan \alpha = 20 \times \tan 49 = 23.0 \text{ mm}.$$

The distance x is

$$x = \frac{d}{2} \times \cos \alpha = \frac{14.5}{2} \times \cos 49 = 4.75 \text{ mm}.$$

Let us choose the wedge diameter $D = 38$ mm as the first approximation. Then the distance h is

$$h = X + x - \frac{D}{2} = 23 + 4.75 - 19 = 8.75 \text{ mm}.$$

The minimum wedge height is $H = 25.5$ mm.

The final wedge design is shown in Figure 10.6, and a photo of the wedge with the transducer is shown in Figure 10.7.

10.4. INSPECTION FROM THE INSIDE NOZZLE SURFACE: IMMERSION METHOD

The nozzle inside the corner region is at the intersection of a large vertical cylinder and a small horizontal cylinder, producing a bent saddle-shaped corner region, torus, wherein the angle of the corner δ (Figure 10.1) can vary from 90° up to approximately 130° depending on the radial displacement from the axis of the nozzle in the plan view (angle Δ in Figure 10.2).

The ultrasonic examination concept of the inner radius zone 1 consists of insonifying this region from the adjacent surfaces, not from the radius surface itself [45, 46]. This leads to a system design incorporating two separate transducers (Figure 10.8). One of these (transmitter T) is located on the side of the nozzle bore surface; the other (receiver R) is located on the side of the boss surface. The system is

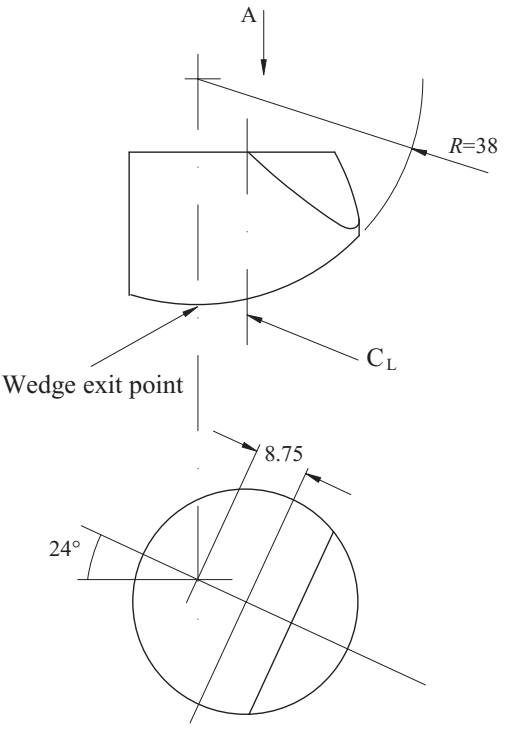

Figure 10.6 Example of the wedge design.

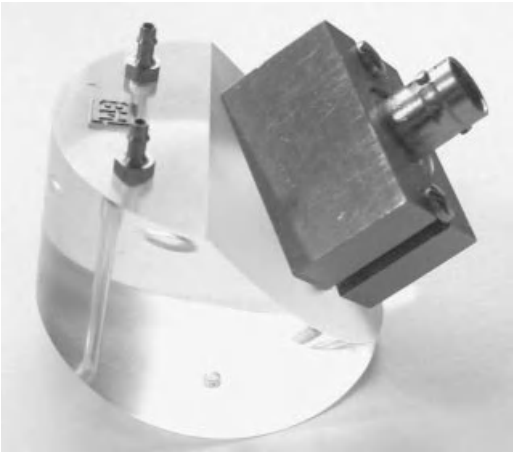

Figure 10.7 The wedge with the transducer.

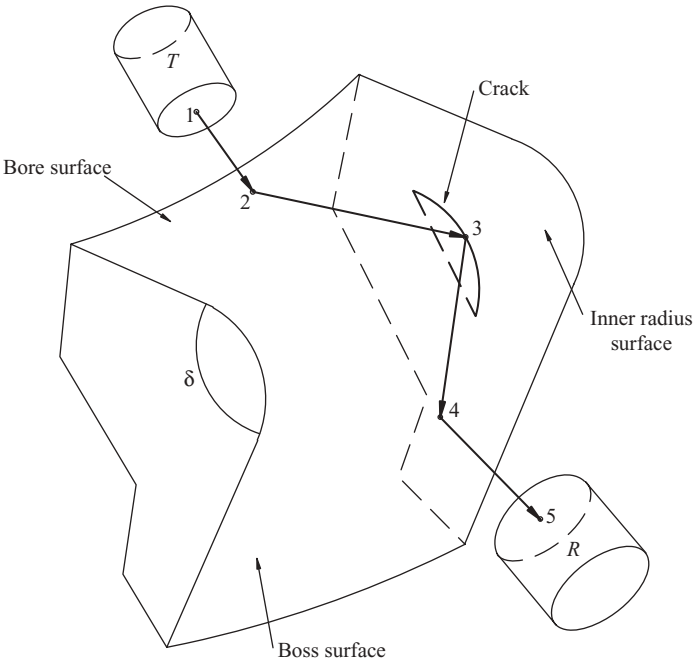

Figure 10.8 Conceptual design of an inner radius immersion technique inspection from the inside of the nozzle.

asymmetric due to the asymmetry of the nozzle inner radius region itself. Ray tracing has to be calculated separately for both the transmitter and the receiver. The central ray from point 1 of the transmitter refracts at point 2 of the bore surface, and has to be oriented to the curved corner, formed by the plane of the flaw and the surface of the inner radius (shooting from down up to point 3).

The reflected ray from the flaw's corner trap strikes the boss surface at point 4 (directed from up down), refracts to water, and orients toward point 5 of the receiver.

The main purpose of the transmitter path calculation is to determine the refracted angle and the orientation of the central ray for different flaw positions. The main purpose of the receiver path calculation is to determine the position and orientation of the receiving transducer, which will be more suitable for receiving the ultrasonic rays from radially oriented reflectors in the elevation and plan views.

Figure 10.9 shows the transducer's delivery system. The smaller transducer (on the left) is the transmitter. The larger transducer on the

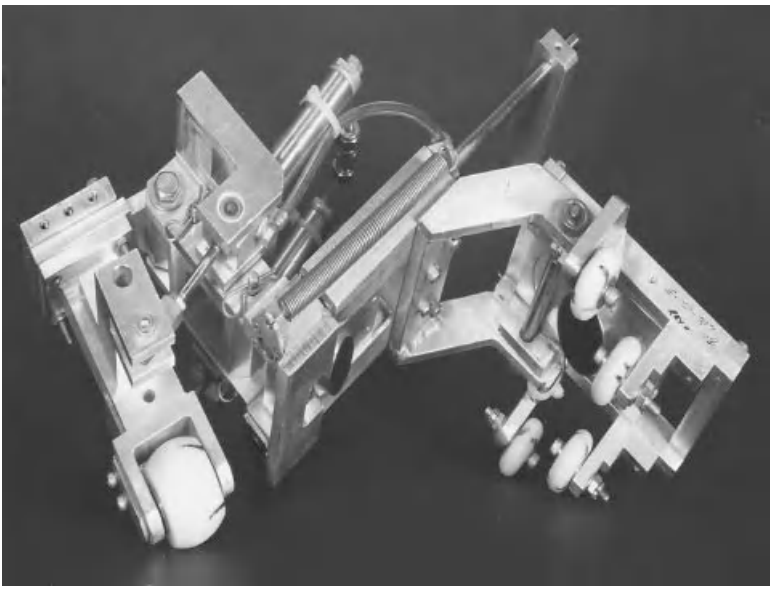

Figure 10.9 Actual transducer delivery system. Reprinted by permission of Westinghouse Electric Company LLC.

right is the receiver. The system is required to "track" the torus shape of the inner radius region. This action is provided by a computer-controlled coordinated system when the transducer's assembly rotates around the nozzle.

The other zones of the inner radius region connected to zone 1 can be inspected by one of the near surface testing methods; for example, see the method described in Reference 47.

CHAPTER 11

Search Unit Functioning Test

Generally, a new fabricated ultrasonic search unit is evaluated by the manufacturer and a test report is included with the search unit. It is a good practice to perform a review of this search unit as an incoming control before use. Both these evaluations should be performed according to an American Society for Testing and Materials (ASTM) standard or the other industry regulations.

A search unit functioning test consists of two measurements:

1. the measurement for evaluating certain characteristics of ultrasonic search units and
2. the measurement for obtaining the specific parameters of the selected ultrasonic search units.

11.1. EVALUATION OF CERTAIN CHARACTERISTICS OF A SEARCH UNIT

Evaluation of the certain characteristics of ultrasonic search units has to be performed in accordance with the ASTM E 1065-08 Standard Guide for Evaluating Characteristics of Ultrasonic Search Units.

Ultrasonic Inspection Technology Development and Search Unit Design: Examples of Practical Applications, First Edition. Mark V. Brook.

This guide provides a description of the measurement procedures for evaluating the certain characteristics of each unit, which may be used to define their acoustic responses. The obtained data should verify the designed characteristics of the search unit. There are many characteristics that describe probe performance. Some of these are only necessary for a probe designer to assess the correctness of the design parameters. For practitioners, not all but several *main* parameters are important.

Modern equipment and its software permit to perform and design an evaluation report that can include as much information of a search unit, test instrumentation parameters, and reference/test blocks as desirable.

The basic parameters to measure are

peak frequency, MHz;
center frequency, MHz;
bandwidth, %;
sensitivity, dB; and
waveform duration, μs.

The measured peak frequency (maximum frequency response) is to be compared with the nominal (designed) frequency of the search unit. The center frequency, which is the center of the bandwidth limits (at a specified dB level) can also be used for this comparison. In both cases, for the standard search units, the tolerance of ±10% from the nominal frequency is acceptable. It is preferable that both frequencies, peak and center, should be equal. There is no tolerance for this parameter.

The bandwidth is a critical parameter to obtain desirable resolution, but deviation from nominal at ±10% will not influence the probe performance.

One of the parameters to be included in the evaluation report is a pulse echo sensitivity. It shows the ratio in dB between the voltage applied to the crystal and the voltage received from a target. This is one of the indicators of the probe quality and, especially, of the matching layer's conformity to the design.

11.1.1. Definition and Examples of Bandwidth

The graphs in Figure 11.1 represent a typical screen capture obtained during the probe evaluation. On the left side are illustrations of

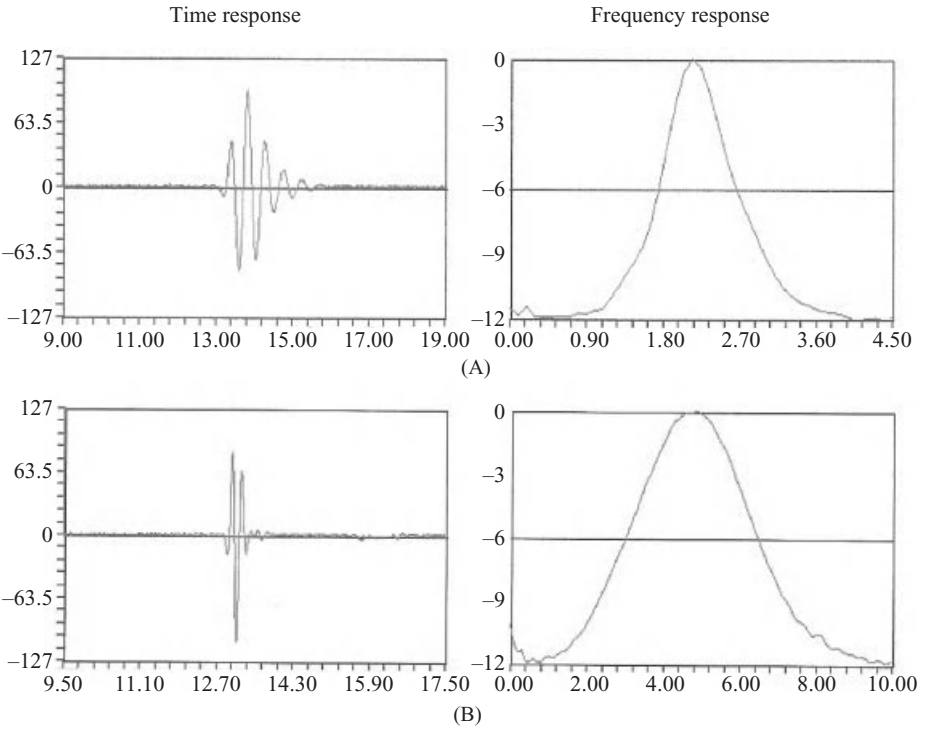

Figure 11.1 Time response and frequency response examples. (A) Medium damped transducer $BW = 36\%$, (B) high damped transducer $BW = 73.5\%$.

time response, and on the right side are illustrations of *frequency response*.

Time response is the waveform received from a specified reflector. It is a plot of signal amplitude versus time. From this response the waveform duration and frequency can be measured. It is also the basis for bandwidth parameter evaluation.

Frequency response, or frequency spectrum, is a plot of a signal amplitude versus frequency. The bandwidth parameters and sensitivity are calculated from this response.

In practice, two levels of transducer bandwidth are common: a broadband and a narrowband. The level of the bandwidth is defined by the mechanical damping of the piezoelectric element.

The three levels of damping are known as low, medium, and high. The measure of the damping characteristics is the number of cycles in

Table 11.1
Damping and Bandwidth Parameters

Parameters	Levels of damping		
	Low	Medium	High
Number of cycles	5–6	3–4	1–2
Bandwidth, %	less than 30	40–60	More than 60
Bandwidth definition	Narrowband	Broadband	

the waveform of the time response. The correlation between the number of cycles and the bandwidth is not strictly defined. Table 11.1 presents the average numbers of cycles and the bandwidth percentage related to different levels of the damping.

Figure 11.1A shows the evaluation results of a transducer with a bandwidth of 36%, and Figure 11.1B shows those of a transducer with a bandwidth of 73.5%.

11.2. MEASUREMENT OF SPECIFIC PARAMETERS OF SELECTED SEARCH UNITS

The specific parameters to be measured depend on the end use of the search unit.

Typically, the specific parameters of a selected ultrasonic search unit includes

1. the exit point and the refracted angle of a single or dual angle beam probe;
2. the depth of the ultrasonic beam's intersection point for a contact dual straight and angle beam probe, and other parameters for the construction of the sensitivity curves; and
3. the focal distance and the parameters of the focal zone for immersion-focused transducers.

Any commercial ultrasonic instrument can be used to perform these measurements.

Several test or reference blocks can be used for these measurements and evaluation.

11.2.1. IIW Reference Blocks

The most common reference block used for measuring the probe's exit point and refracted angle is the IIW Reference Block Type 1 or 2 [48, 49].

The IIW Reference Block is designed for the evaluation of a search unit as an individual component, as well as for the determination of the operating parameters of an ultrasonic test instrument or system. These blocks are relatively complicated and not convenient to use. Figure 11.2 shows the various setups for evaluating search units using the IIW Type 1 Reference Block.

Some problems with these blocks have been known in the ultrasonic nondestructive testing (NDT) profession for a long time. The main problems are inconsistency in the probe exit point position and refracted angle measurements when measured using different IIW blocks. The Material Science and Engineering Laboratory of NIST

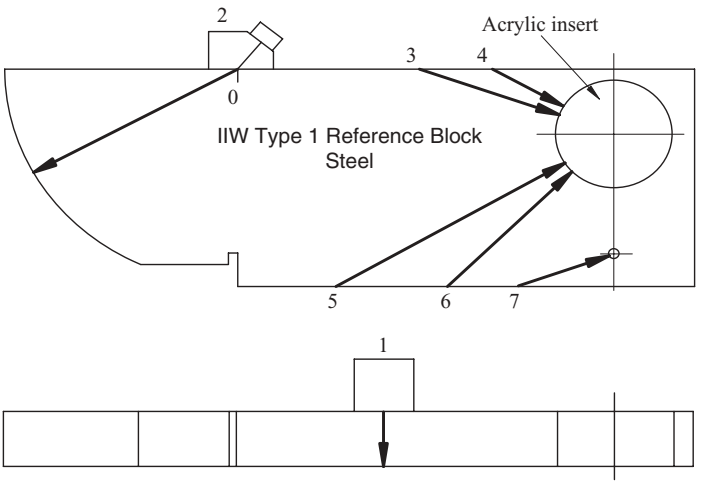

Figure 11.2 Setups for evaluating search units using the IIW Reference Block. (1) Setup for the evaluation of a single straight beam transducer with a wear plate, (2) setup to define the exit point of an angle beam probe, (3 and 5) setups to measure the refracted angle of a 60° angle beam probe, (4 and 6) setups to measure the refracted angle of a 45° angle beam probe, (7) setup to measure the refracted angle of a 70° angle beam probe.

prepared a presentation for the ASTM New Methods Seminar EO-7.98 describing the problems with these blocks [50]. The main conclusions are

> *Speed of sound and attenuation properties of the IIW type blocks may vary significantly. Manufacturers can make blocks without regard to microstructure, such as grain size, texture, dislocation density, etc., which depends on rolling direction, thickness and thermo-mechanical treatment of steel.*
>
> *ASTM E164-08 states, that "unless otherwise specified, low carbon steel such as UNS G10180 is suggested." Otherwise, "material must be selected by the using parties.*

It also does not stipulate the requirements and tolerances of the sound velocity and attenuation in the reference block metal (steel, stainless steel, or aluminum).

Accuracy of the measurements is influenced by these inconsistencies.

Several IIW blocks, fabricated by different manufacturers, were evaluated to assess the problem. Three standard angle beam probes with refracted angles of 45°S, 60°S, and 70°S were evaluated.

The results are summarized in Figure 11.3. The deviation is significant, especially for probes that create ultrasonic beams with near 70°S refracted angles.

Older IIW blocks included an acrylic (Perspex, Plexiglas) insert. The main reason for this insert was to provide a simulated ultrasonic dimension of 2.00 inch in steel (in the English version of the block, the thickness of the insert is 0.923 inch). There were other applications for the insert, for example, a measure of the aging of the crystal or loss of sensitivity. The block was internationally standardized in 1972.

Nowadays the insert is obsolete. Some manufacturers consider the insert optional. The unplugged hole is used for refracted angle measurement. Some users consider the hole very handy to carry this heavy block.

The relatively new standard for this block EN 12223 (1999) does not include the requirement for the acrylic insert. At the same time, an acrylic insert or a separate Plexiglas block is useful for the evaluation of straight beam transducers intended for use with wedges, and many transducers' manufacturers use the insert for this purpose.

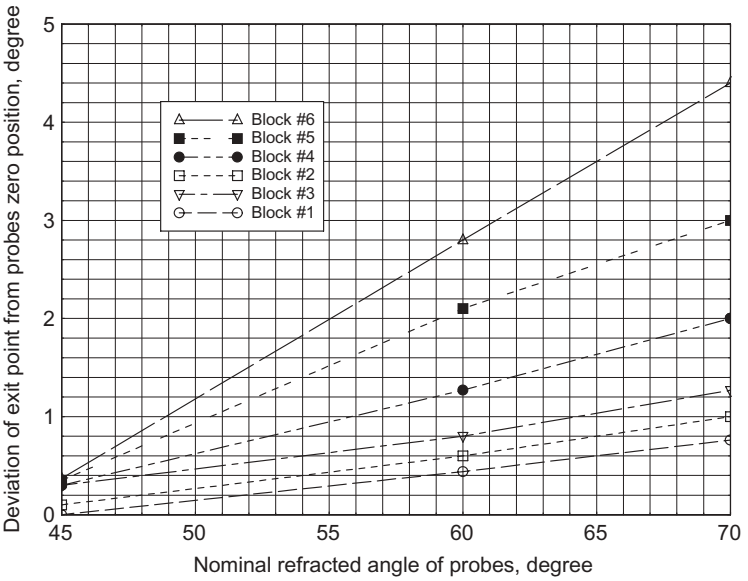

Figure 11.3 Deviation of the exit point of probes, measured on different reference blocks.

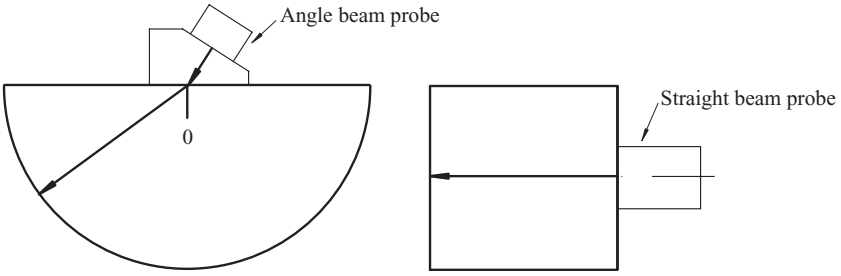

Figure 11.4 Simple test block for evaluation of straight and angle beam probes.

11.2.2. Additional Test Blocks

The problems with IIW blocks can be partly avoided by using simplified test blocks. The intention of one of these test blocks (Figure 11.4) is to make the simplest possible block for limited search unit evaluation. This test block, machined from the specific grade of steel, is "universal" in a sense that it can be used for the evaluation of almost all sizes of contact search units: Its width is twice the thickness of the IIW Type 1 block. This test block is very simple and recommended for

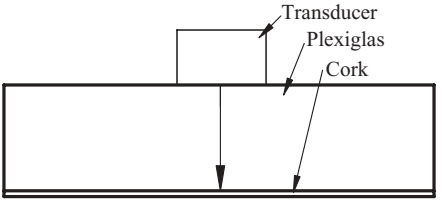

Figure 11.5 Test block for the evaluation of a single straight beam transducer with a matching layer for a Plexiglas wedge.

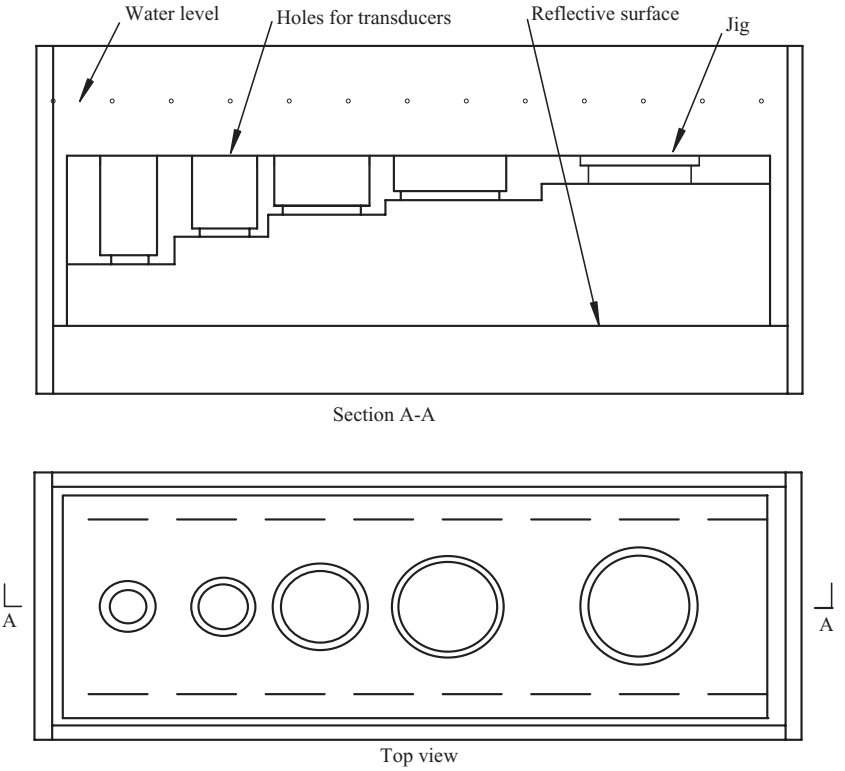

Figure 11.6 Small tank for the evaluation of immersion transducers.

the evaluation of single and dual angle beam probes when measurement of the refracted angle is not required. It can be used as well for a single straight beam probe evaluation.

The other useful test block is a plate of Plexiglas or other wedge materials with an attached cork layer (Figure 11.5). This block should be used for the evaluation of a straight beam transducer with a matching layer for a given material.

It is very handy to use a small immersion tank for the evaluation of flat and focused immersion transducers with diameters up to 12.7 mm and with frequencies up to 10 MHz (Figure 11.6). A fixture is placed inside the tank, with different diameter holes for a variety of transducer diameters, and different water paths.

APPENDIX A

System of Units and Symbols That Are Accepted for This Book

From seven base units in the International System of Units (SI), we used only three:

length—meter (m);
mass—kilogram (kg); and
time—second (s).

From many derived units and units outside the SI, the following are used:

area—square meter (m^2);
velocity—meter per second (m/s);
volume—cubic meter (m^3);
mass density—kilogram per cubic meter (kg/m^3);
frequency—hertz (Hz); and
sound pressure—bel (B).

Ultrasonic Inspection Technology Development and Search Unit Design: Examples of Practical Applications, First Edition. Mark V. Brook.

Some of these units are too large or too small for practical application when describing the data of results, obtained during experiments. So, the following units with prefixes are used:

length—mm;
mass—g;
time—μs;
area—mm^2;
velocity—mm/μs;
volume—mm^3;
mass density—g/cm^3;
frequency—MHz; and
sound pressure—dB.

The following symbols, summarized in Table A1, are used.

Conversion of metric to English units and English to metric units is presented in Table A2.

Table A1

Terminology		Symbol	Unit
Angles	Incident	α	degree
	Refracted	β	
	Attack	β_1	
	Other	γ, δ, φ, δ, θ, ϕ	
Area		S	mm^2
Coefficient of attenuation		δ	
Diameter		*D*, *d*	mm
Frequency		*f*	MHz
Gain		–	dB
Length		L, l	mm
Mass density		ρ	mm/cm^3
Near field		*N*	mm

(Continued)

Table A1
(Continued)

Terminology		Symbol	Unit
Radius		*R*, r	mm
Signal amplitude		A	%
Time		τ	μs
Thickness, distance		*T*, *H*, *h*, *d*	mm
Velocity		*V*	mm/μs
Wave (mode) type	Longitudinal	L	
	Shear	S	

Table A2

Measure	Metric to English units	English to metric units
Linear	1 mm = 0.0394 in = 39.4 mi	1 in = 25.4 mm
Area	1 mm^2 = 0.00155 $in.^2$	1 in = 645.16 mm^2
Volume	1 cm^3 = 0.061 $in.^3$	1 in^3 = 16.383 cm^3
Mass	1 kg = 2.205 lb	1 lb = 0.4536 kg
Mass density	1 g/cm^3 = 0.361 lb/in^3	1 lb/in^3 = 27.7 g/cm^3
Velocity	1 mm/μs = 39.4 mi/μs	100 mi/μs = 3.94 mm/μs

APPENDIX B

American Societies Engaged in Activities Related to Nondestructive Testing and Serving the Needs of NDT Professionals

The American Society for Testing and Materials (ASTM) is the standards development organization. The ASTM publishes books of standards each year.

The following Standard Practices from the *Annual Book of ASTM Standards*, Section 3, Volume 03.03, Nondestructive Testing, 2010, were referenced or quoted in this book:

E 114-10. Standard Practice for Ultrasonic Pulse-Echo Straight-Beam Examination by the Contact Method

Ultrasonic Inspection Technology Development and Search Unit Design: Examples of Practical Applications, First Edition. Mark V. Brook.

E 164-2008. Standard Practice for Contact Ultrasonic Testing of Weldments

E 494-2005. Standard Practice for Measuring Ultrasonic Velocity in Materials

E 587-10. Standard Practice for Ultrasonic Angle-Beam Contact Testing

E 664/664M-10. Standard Practice for the Measurement of the Apparent Attenuation of Longitudinal Ultrasonic Waves by Immersion Method

E 1065-08. Standard Guide for Evaluating Characteristics of Ultrasonic Search Units

E1316-10b. Standard Terminology for Nondestructive Examinations. Section I: Ultrasonic Testing (UT) Terms.

The American Society for Nondestructive Testing, Inc. (ASNT) is a technical nonprofit organization that serves nondestructive testing (NDT) professionals. The main ASNT activity is to provide technical information and training materials for the qualification and certification of NDT personnel. The ASNT publishes technical journals and books:

Materials Evaluation

Research in Nondestructive Evaluation

NDT Handbook

Recommended Practice SNT-TC-1A

ASNT Standard for Qualification and Certification of NDT Personal (CP-189)

The American Society of Mechanical Engineers (ASME) is the professional organization that serves mechanical engineers. It provides codes and standards for the fabrication of mechanical equipment.

From many codes published by the ASME, for NDT professionals working in the energy producing industry, the most important is the international Boiler and Pressure Vessel Code. This code establishes rules for the inspection of boiler and pressure vessel parts, including mechanisms of nuclear power plants. Sections of this code, related to NDT, are

Section III. Rules for Construction of Nuclear Power Plant Components

Section V. Nondestructive Examination

Section XI. Rules for Inservice Inspection of Power Plant Components

Section V. It provides recommendations for each of the nondestructive methods, including the ultrasonic method, which are referenced by other sections in the code.

This section provides requirements for search units such as nominal frequencies, refracted angles, and bandwidth for different ultrasonic techniques and different test objects such as weld joints, bolts, and studs.

Appendix VIII of Section XI provides requirements for performance demonstration for ultrasonic inspection. Among other things, this appendix specifies requirements for different types of search units, including essential variable tolerances. It also provides requirements for qualification test specimens, which can serve as calibration standards.

For example, it specifies maximum notch dimensions for bolt and stud test specimens:

If the bolt or stud diameter is greater than 4 in. (101.6 mm), the depth of the notch is 0.157 in. (3.98 mm) with a reflective area of 0.059 sq in. (38 mm^2).

If the bolt or stud diameter is between 2 and 4 in. (50.8–101.6 mm), the depth of the notch is 0.107 in. (2.72 mm) with a reflective area of 0.027 sq in. (17.4 mm^2).

It is interesting to note that the ASME 2007 Section V, Appendix IV, describes requirements for in-service examination of bolts that are different from the requirements of Appendix VIII of Section XI. Reflectors in the calibration standard shall be straight-cut notches with a depth of one thread if the bolt diameter is less than 50 mm, 2.0 mm deep if the bolt diameter is between 50 and 75 mm, and 2.5 mm deep if the bolt diameter is 75 mm and greater.

Note that in the first case, the area of the reflector is specified, but its shape is not. In the second case, the shape of the reflector is specified but not the area.

This example shows that the technique development engineer and probe designer should know, among other things, the requirements for the calibration standards in the industry they are working on.

The Institute of Electrical and Electronics Engineers (IEEE) has the section Ultrasonics, Ferroelectrics, and Frequency Control Society (UFFC). The ultrasonic section of this society is responsible for the organization of the annual International Ultrasonic Symposium, which includes the sections Nondestructive Evaluation and Transducers and Sensors. Articles presented in these sections are primarily dedicated to theoretical problems in NDT.

APPENDIX C

An Example of Applying the Third Critical Angle

Let us assume that a weld joint has a counterbore with the inclined angle $\gamma = 10°$ (Figure C1). A shallow crack in the heat-affected zone has to be detected by using a creeping wave. To generate the creeping wave on the surface of the counterbore, the shear wave angle of incidence should be equal to the third critical angle.

So, the refracted angle should be

$$\beta = \alpha_{3CR} + \gamma$$

$$\alpha = \arcsin\left(\sin\beta \frac{V_W}{V_S}\right).$$

Assuming that the third critical angle is equal to 33°, the longitudinal sound velocity in the wedge material is $V_L = 2.735$ mm/μs, and the shear velocity in the test object metal is $V_S = 3.23$ mm/μs, one can calculate the wedge angle:

$$\alpha = \arcsin\left(\sin 43 \frac{2.735}{3.23}\right) = 35.27°.$$

Ultrasonic Inspection Technology Development and Search Unit Design: Examples of Practical Applications, First Edition. Mark V. Brook.

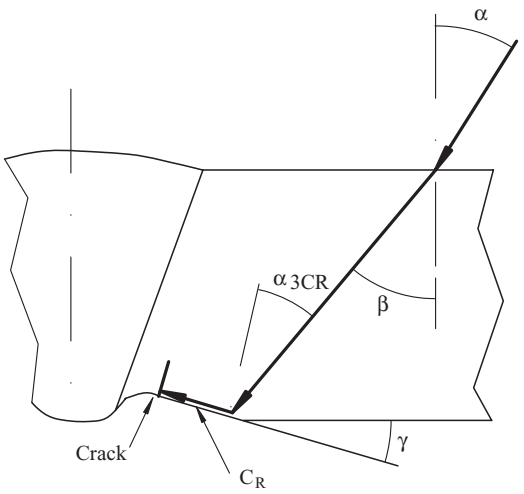

Figure C1 Sketch related to application of the third critical angle.

APPENDIX D

WesDyne International Computer Program for Lamb Wave Dispersion Curve Calculation*

The Lamb wave dispersion curve figures, presented in Chapter 8, were created by using, let us say, "common" computer programs. Each of the graphs—Phase Velocity, Group Velocity, and so on—were created separately. To determine the required Lamb wave parameters, each graph has to be displayed on the screen, the cursor placed on the desired curve, and the data read using additional manipulations. To make annotation or to edit titles, additional programs, for example Paint, may be used. In general, the programs are not user-friendly.

WesDyne International created the computer program that eliminates the aforementioned drawbacks and is much more user-friendly and time-saving.

There are five graphs available to render using this program:

Phase Velocity

Group Velocity

* Reprinted by permission of Westinghouse Electric Company LLC.

Ultrasonic Inspection Technology Development and Search Unit Design: Examples of Practical Applications, First Edition. Mark V. Brook.

Wedge Angle

Coefficient of Attenuation

Particle Displacement

Each of the first four graphs has a vertical "cursor." The user can move this cursor to a desired *fd* value location. These graphs also have horizontal cursors that move simultaneously with the vertical cursor and indicate the values of the ordinate of each graph.

The intersection of these two cursors, marked by a small circle, is the "main cursor." It allows the user to select the current mode as well as an *fd* position. The main cursor will "snap" to the desired curve, usually on the "phase velocity" graph. Simultaneously, the position of the main cursor will appear on the three other graphs at the selected mode, and each of the values will be saved and presented in the appropriate boxes. At the same time, the curves on the "particle displacement" graph will change. This graph is unique in that it is a slave to the other graphs and is re-rendered whenever the *fd* position or the current mode is changed by the user.

The "particle displacement" graph has two plots, "in plane" and "out of plane," graphed against normalized displacement and the normalized thickness of the test object wall. The title of this graph dynamically represents the current mode and the current *fd* position.

The screen contains all necessary windows and buttons to edit input and output parameters.

The upper-left corner of the screen contains text boxes that display parameters relevant to the current test object and wedge materials. All of this information is editable by the user.

These parameters are

Test object material

Thickness of the test object

Longitudinal and shear velocities of the test object material

Wedge material

Longitudinal velocity of the wedge material.

To the right of the text boxes is a set of boxes that contains the information relevant to the current cursor position, as well as the information

of two "points of interest" that the user may have saved. The boxes include names of the mode and the values of the following parameters:

fd;
Frequency
Phase Velocity
Group Velocity
Wedge Angle

The user can set (or replace) the current point of interest information with the information from the current cursor location by pressing the "Set" button next to either point of interest line.

The next set of buttons is "Editing buttons" (not shown in the screen capture). By clicking the "Edit Creation Settings" button, the user can change the current values for the dispersion curve calculation.

By clicking "Edit Graph Settings" button, the user can change any of the graph parameters, including the ability to set the *y*-axis minimum and maximum for the Phase and Group Velocity graphs. The user also has the ability to hide or show many graph parameters, as well as the ability to change the colors associated with those elements.

By clicking "Edit Plot Settings" button, the user can edit, for example, the color of each curve and write an annotation.

Pressing the "Create Mode Report" button will create a file containing information for all modes for the current *fd* position.

The upper-right corner of the screen contains a set of "radio buttons" named "Display Configuration" (not shown in the screen capture). By selecting the button, the user can arrange the screen to show a particular set of graphs. Once displayed, the user can change the particular graph rendered at a screen location to display the next available graph.

For example, the screen configuration shown in Figure D1 contains the following graphs:

Phase Velocity
Group Velocity
Coefficient of attenuation due to leakage in water
Particle motion

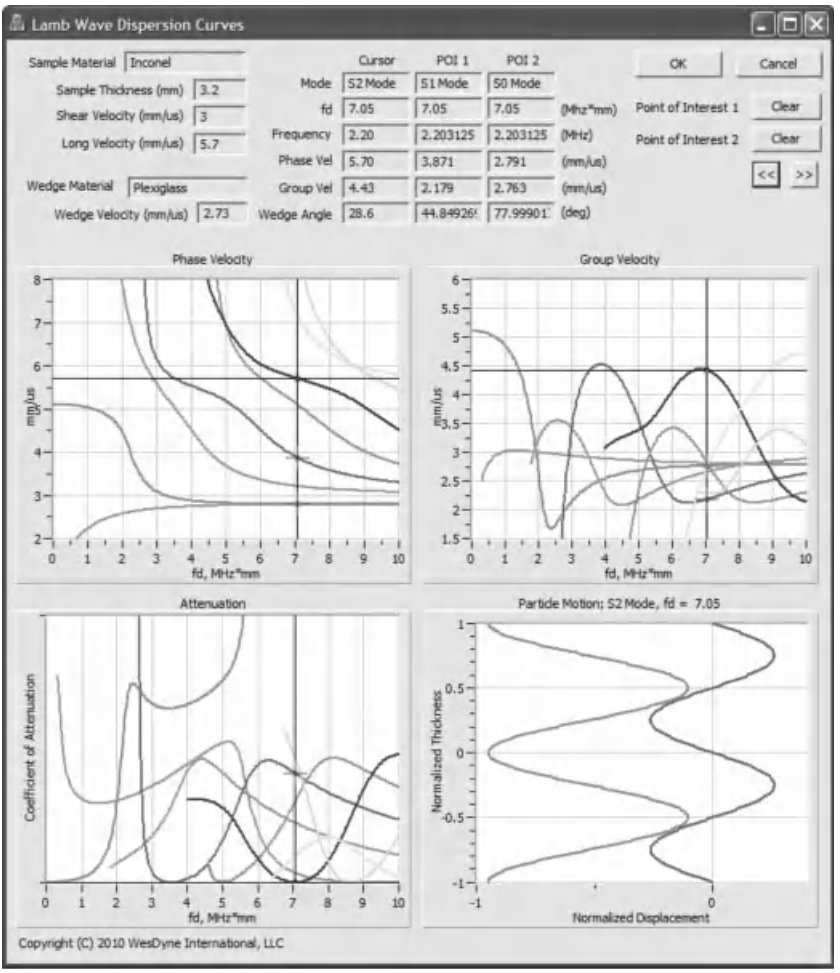

Figure D1 Lamb wave dispersion curves.

Each of the first three graphs contains four pairs of curves, representing the first four pairs of modes.

The graphs were created for the test object machined from Inconel with a wall thickness of 3.2 mm.

The main cursor position is on the S_2 mode curve. Two additional points of interest (POI 1 and POI 2) are S_1 and S_0 modes. All information obtained is presented in the POI boxes.

The program is based on the following equations that represent propagation in a plate symmetric *S* and asymmetric *A* Lamb waves:

$$\frac{\tanh \beta d}{\tanh \alpha d} = -\frac{4k^2 \alpha \beta}{\left(k^2 + \beta^2\right)^2}$$

$$\frac{\tanh \beta d}{\tanh \alpha d} = -\frac{\left(k^2 + \beta^2\right)^2}{4k^2 \alpha \beta}$$

where k is the Lamb wave number

$$\alpha^2 = k^2 - k_l^2$$

$$\beta^2 = k^2 - k_t^2$$

and k_l and k_t are the wave number for bulk longitudinal and shear waves:

$$k_l = \omega \sqrt{\frac{\rho}{\lambda + 2\mu}}$$

$$k_t = \omega \sqrt{\frac{\rho}{\mu}}$$

λ and μ are elastic Lamb constant.

$\omega = 2\pi/f$ = circular frequency and

f = transducer frequency.

The attenuation due to leakage into water is connected to the ratio of particle displacement on both sides of a test object wall. For example, in the case of

$$\frac{\Delta \perp}{\Delta =} = 0,$$

the leakage is nonexistent. If

$$\frac{\Delta \perp}{\Delta =} \to \infty,$$

the leakage is maximum.

$\Delta \perp$ is out-of-plane particle displacement and

Δ is in-plane particle displacement.

Glossary of Terms Specific to This Book

Acoustic impedance—The product of material density and ultrasonic velocity.

Angle beam—The beam axis oriented not perpendicular to the test object scanning surface.

Apparent attenuation—The observed ultrasonic energy loss during wave propagation through the test object material.

Area of interest—The section of the test object to be inspected.

Asymmetric waves—The Lamb waves with particles oscillating in the perpendicular direction along the neutral axis of a plate.

Axisymmetric waves—Cylindrically guided waves that cover the full circumference of the hollow cylinder.

Back-wall reflection—The signal that represents the reflection of ultrasonic energy from the back surface of a test object.

Band round wave—Waves that slide around a cylindrical or oval hole in solid media.

Beam axis—The acoustic centerline of the main lobe defined by the locus of points that represent maximum sound pressure.

Beam spread— A divergence of the ultrasonic beam as it travels through a test object.

Boundary effect—The phenomenon where the peripheral ultrasonic rays change direction when they impinge on the surface of a test object and cause mode conversion.

Ultrasonic Inspection Technology Development and Search Unit Design: Examples of Practical Applications, First Edition. Mark V. Brook.

Bulk waves—A wave propagating in semi-infinite media.

Couplant—A film-forming substance between a probe and a test object surface to enhance the transmission of ultrasonic energy when using a contact method.

Critical angle—A specific angle of incidence at which a certain mode of propagation "disappears" during refraction or reflection at the interface of two media.

Cross talk—The reception of ultrasonic energy by the receiver directly from the transmitter in a dual probe due to the breakdown of the dividing acoustic insulator.

Crystal—The piezoelectric element as a part of the search unit.

Crystal assembly—A portion of a transducer that contains the crystal, matching layer, backing, and tuning components.

Damping—A process of limiting signal duration by mechanical or electrical means.

Dead zone—A minimum distance after the ring dawns of the crystal measured from a surface of the test object after which a reflector can be resolved.

Decibel (dB)—A unit of sound pressure measurement.

Delay line—A column of substance between the transducer and the test object surface.

Delta TOF—A difference in time between two consecutive signals.

Dispersion—A phenomenon related to velocity dependence of a frequency.

Dual search unit (straight or angle beam)—A search unit containing two crystals located on separate wedges, oriented in the same general direction with central ray's intersection on specified depth in a test object.

Duplex search unit (straight or angle beam)—A search unit containing two crystals located on separate wedges, oriented in the same or opposite directions.

Examination—A process of nondestructive testing method application to inspect a test object.

Flaw—A potential defect or synonym of defect.

Free field—An acoustic field generated by a transmitter.

Frequency response (frequency spectrum)—A diagram that shows signal amplitude as a function of frequency.

Gliding diffracted waves—Waves produced by band round waves that are used to detect the presence of a discontinuity located in a "shadow" zone of a cylindrical reflector.

Group velocity—A velocity of groups of waves formed by the superposition of two (or more) waves with slightly different parameters.

Hollow circular thin wall cylinder—A tube that has a ratio of an average wall thickness to the mean radius much less than one.

Imperfection—A synonym of flaw.

Indication—A response (signal) during an examination that requires interpretation and evaluation.

In-plane particle displacement—A displacement of particles parallel to a plate surface in the case of Lamb wave propagation.

Inspection—An observation of a nondestructive testing operation to determine any imperfection in the test object.

Lamb-type guided waves—An elastic vibration similar to Lamb waves. For example, waves propagating in a thin wall hollow cylinder.

Lamb waves—An elastic vibration propagating in a solid plate with free boundaries, for which displacement occurs both in the directions of wave propagation and perpendicularly to the plane of the plate.

Lateral wave—An ultrasonic longitudinal surface and sometimes subsurface wave that travels at the shortest path directly between two probes when the time of flight diffraction forward scattering technique is used.

Lead of a helix—Length of a cylinder generating line of one revolution.

Leakage—The transmission of ultrasonic energy at the boundary between the test object and the environment, for example, water.

Line scan—The scan along a straight line without probe indexing.

Mode—A type of ultrasonic wave.

Mode conversion—A phenomenon of wave propagation related to a change of one type of ultrasonic wave to another in the process of reflection or refraction at an interface of two media.

Nonaxisymmetric waves—Localized waves that travel in a double spiral pattern along a thin wall hollow cylinder.

Out-of-plane particle displacement—A displacement of particles perpendicular to a plate surface in the case of Lamb wave propagation.

Particle displacement—An oscillation of particles during wave propagation.

Phase cancellation—A phenomenon based on the fact that Lamb wave modes become standing waves at the normal angle of incidence. A divided frequency spectrum permits the measurement of the resonant frequency.

Phase velocity—Propagation of velocity at a constant phase. For example, a velocity of the wave crest propagation along a surface of a plate (in the case of Lamb wave propagation).

Probe center spacing—A distance between exit points of two probes oriented toward each other.

Pulse tuning—The process used in order to optimize the reflected signal by adjusting the frequency spectrum of the transmitted pulse.

Radial vibration mode—Vibration of the piezoelectric disk in radial directions; one of the varieties of area expansion modes.

Rayleigh waves—Elastic vibrations propagating along a free surface of a solid medium and decaying with depth.

Sensitivity—The degree to which a probe responds to incoming ultrasonic energy from a reflector.

Scanning—A prescribed route of probe movement relative to the test object surface during inspection.

Scanning surface—The test object surface from which the inspection is performed.

Sensitivity curve—A graph showing signal amplitude versus depth of reflector. The apogee of the curve corresponds to the point of the acoustic field's maximum energy.

Tandem probe—A probe consisting of two wedges with crystal assemblies (or transducers). In most cases, the receiver is located in front of the transmitter.

Technique—A means of conducting an inspection within a specific method.

Test—A procedure of examination and observation.

Time of flight—The time interval between specified reflections.

Time of flight diffraction—A technique that uses tip diffraction signals to identify the ends (tips) of a flaw like a crack.

Time response—A diagram that shows a waveform received from a specified reflector as a function of time.

Triplex probe—A probe that generates three combinations of modes.

Wave front—A continuous surface drawn through the forwardmost points of a wave with the same phase.

NOTE

For more common terms, see the latest edition of the *American Society for Testing and Materials Standards*, Volume 03.03, Nondestructive Testing E 1316 Section I: Ultrasonic Examination.

Bibliography

1. Sokolov, S.J. 1997. Selected works. St-Petersburg.
2. Born, M. and Wolf, E. 1999. *Principles of optics*, 7th ed. Cambridge: Pergamon Press.
3. Brekhovskikh, L.M. 1980. *Waves in layered media*. San Diego, CA: Academic Press, Inc.
4. Dianov, D.B. 1965. Research into divergence characteristics of the angle beam probe. *Defectoscopiya*, pp. 8–22.
5. Hellier, C.J. 2001. *Handbook of nondestructive evaluation*. New York: McGraw-Hill Book Company.
6. Brook, M.V. and Lopierev, N.K. 1973. Nondestructive testing in shipbuilding and ship repairing. Moscow: Transport.
7. Nondestructive Testing Handbook 2009. *Ultrasonic testing*, Vol. 3. Moscow: Publishing House Spektr. Translated from Russian.
8. Nondestructive Testing Handbook 1991. *Ultrasonic testing*, Vol. 7. ASNT.
9. Rose, J.L. 1999. *Ultrasonic waves in solid media*. Cambridge, UK: Cambridge University Press.
10. Viktorov, I.A. 1981. *Sound surface waves in solid media*. Nauka.
11. Jenkins, F.A. and White, H.E. 1957. *Fundamentals of optics*. New York: McGraw-Hill Book Company.
12. Ermolov, I.N. and others. 1986. *The ultrasonic transducers for nondestructive testing*. Moscow: Mashinostroenie.
13. Viktorov, I.A. 1967. *Rayleigh and lamb waves*. New York: Plenum Press. Translated from Russian.
14. Aleshin, N.P., Ermolov, I.N., and Knjasev, V.D. 1990. Generation of Rayleigh waves by the angle beam probe. *Defectoskopiya*, 10, pp. 2–10.
15. Desilets, G.S., Fraser, J.D., and Kino, G.S. 1978. The design of efficient broad-band piezoelectric transducers. *IEEE Transactions on Sonics and Ultrasonics*, SU-25(3), May, pp. 115–125.
16. Kossoff, G. 1966. The effects of backing and matching on the performance of piezoelectric ceramic transducers. *IEEE Transactions on Sonics and Ultrasonics*, SU-13(1), pp. 20–30.

Ultrasonic Inspection Technology Development and Search Unit Design: Examples of Practical Applications, First Edition. Mark V. Brook.

17. Sayers, C.M. and Tait, C.E. 1984. Ultrasonic properties of transducer backings. Ultrasonics, 1984, 22(2).
18. Lach, M., Platte, M., and Ries, A. 1996. Piezoelectric materials for ultrasonic probes. NDTnet-September, Vol. 1, No.09.
19. Selfridge, A.R. 1982. The design and fabrication of ultrasonic transducers and transducers arrays. Dissertation, Stanford University.
20. Silk, M.G. 1984. *Ultrasonic transducers for nondestructive testing*. Bristol, UK: Adam Hilger Ltd.
21. Ermolov, I.N. 1981. *Theory and practice of ultrasonic testing*. Moscow: Mashinostroenie.
22. Aleshin, N.P. and others. 1989. *Methods of acoustic testing of metals*. Moscow: Mashinostroenie.
23. Gugvich, A.K. and Kuzmina, L.I. 1980. *Beam divergent diagrams of ultrasonic search units*. Kiev: Technica.
24. Wustenberg, H. 1972. Investigation for the sound field of angle test units for testing materials with ultrasound. Dissertation. Translated from German.
25. Basatskaya, L.V. and Ermolov, I.N. 1980. Theoretical study of ultrasonic longitudinal subsurface waves in solid media. *Defectoskopiya*, No. 7, pp. 58–65.
26. Erhard, A. 1982. Investigations into the propagation of longitudinal waves on surfaces during material inspection with ultrasonics. Dissertation, Translation from German.
27. Ermolov, I.N., Razygraev, N.P., and Sherbinskii, V.G. 1978. Study of shaping process for acoustic field of a head-type wave in a test medium. Translation from Russian, *Defectoskopiya*, No. 1, pp. 33–40.
28. Golan, S., Adler, L., Cook, K.V., Nanstad, R.K., and Bolland, T.K. 1980. Ultrasonic diffraction technique for characterization of fatigue cracks. *Journal of Nondestructive Evaluation*, 1(1), pp. 11–19.
29. Guide to calibration and setting-up of the ultrasonic time of flight diffraction (TOFD) technique for the detection, location and sizing of flaws. 1993. British Standard. BS 7706.
30. Brook, M.V. 1985. Ultrasonic method and device for detecting and measuring defects in metal media. Patent No. 4,658,649.
31. Brook, M.V. 1986. Ultrasonic transducers design for detection and characterization of cracks in nuclear primary pressure piping. Proceedings, 8th International Conference on NDE in the Nuclear Industry, Orlando, FL, November 1986.
32. Langenberg, K.L., Fellinger, P., and Marklein, R. 1990. On the nature of the so-called subsurface longitudinal wave and/or the surface longitudinal "creeping" wave. Paper submitted to research in Nondestructive Evaluation, University of Kassel, FRG.
33. Nikiforov, L.A. and Haritonov, A.B. 1981. Research into longitudinal creeping waves parameters generated by the angle beam probe. *Defectoskopiya*, No. 6.

34. Brook, M.V., Graig, S.M., and Hain, N.W., Jr. 1993. System for ultrasonic inspection of tension leg well platform tendons. *Russian Journal of Nondestructive Testing*, 29(10), pp. 18–23.

35. Krautkramer, J. and Krautkramer, H. 1977. *Ultrasonic testing of materials*. Springer-Verlag.

36. Gazis, D.C. 1959. Three-dimensional investigation of the propagation of waves in hollow circular cylinders. *The Journal of the Acoustical Society of America*, 31(5), pp. 568–578.

37. Brook, M.V. and Ngoc, Tran D.K., and Elder, J.E. 1989. Ultrasonic inspection of steam generator tubing by cylyndrical guided waves. Review of Progress in Quantitative NDE.

38. Lareau, J.P. and Brook, M.V. 1996. Ultrasonic inspection of steam generator tubing using lamb wave technique. EPRI Steam Generator Inspection Workshop.

39. Brook, M.V. and Lareau, J.P. 1998. Lamb wave ultrasonic probe for crack detection and measurement in thin-walled tubing. Patent No. 5,767,410.

40. Saglio, R. and Prot, A.C. 1985. Ultrasonic focusing techniques. Nondestructive Testing, Vol. 8.

41. Schlengermann, U. 1978. The focused sound field—a versatile tool for ultrasonic evaluation of meterials. Proceedings of the First International Symposium on Ultrasonic Materials Characterization.

42. Schlengermann, U. 1980. The characterization of focusing ultrasonic transducers by means of single frequency analysis. Materials Evaluation.

43. Wustenberg, H. 1977. Sensitivity calibration for the use of focusing probes in ultrasonic inspection at planer and curved surfaces. Translation from German, Materialpruf.

44. Kino, G.S. Acoustic waves: devices, imaging, and analog signal processing. 1987.

45. Brook, M.V. and Fox, J.R. 1984. Reactor pressure vessel nozzle inner radius UT inspection system.

46. Brook, M.V. and Wentzell, T.H. 1983. Corner region ultrasonic inspection device. Patent No. 4,532,808.

47. Brook, M.V., Kuljis, Z., and Lareau, J.P. 1983. Near surface inspection system. Patent No. 4,509,369.

48. Methods for assessing the performance characteristics of ultrasonic flaw detection equipment. BS 4331: Part 3:1974. British Standards Institution.

49. Specification for calibration blocks for use in ultrasonic flaw detection. BS 2704:1978. British Standards Institution.

50. Fortunco, C.M., Lerch, T.P., and Renken, M.C. 1998. Velocity measurements in IIW-Type Blocks. Prepared for ASTM New Methods Seminar E-7.98.

51. Golan, S. 1981. Optimization of the crack tip ultrasonic diffraction technique for sizing of cracks. *Materials Evaluation*, No. 2, pp. 168–169.

About the Author

Dr. Mark Brook received his doctoral degree from the Leningrad Waterway Transportation Institute. He has worked as an associate professor and was in charge of the Nondestructive Testing Laboratory in the same institute. He is the author of many articles and of the book *Nondestructive Testing in Shipbuilding and Ship Repair*.

In the United States, since 1979, he has worked for Combustion Engineering, ABB, and Westinghouse Electric Company as a consultant in the research and development of ultrasonic nondestructive testing. He holds four patents for techniques and designs in the industry. He is heavily involved in numerous projects for the development of techniques and probe designs for the ultrasonic inspection of test objects, mostly for nuclear power plants.

This book is based in part on lectures given by Dr. Brook for engineers at the NDE Products & Technology Department of Westinghouse Electric Company.

His hobbies are gardening and cooking.

Ultrasonic Inspection Technology Development and Search Unit Design: Examples of Practical Applications, First Edition. Mark V. Brook.

Index

Acoustic emission testing 1, 5
Acoustic field 17, 27, 52, 57–60, 61, 62, 65, 78, 81, 114, 124, 125, 197, 223, 234
Angle beam probe 14–17, 23–25, 36–38, 54–55, 64, 149, 164–165, 251–255
  single 65–76, 238, 250
  dual 77–98, 124, 250
  dual duplex 101–102
Angle of attack 115–118
Angle of divergence 58, 60–61, 62, 64, 78, 80, 83
Angle of incidence 10, 17–20, 39, 68–73, 79, 82, 887–88, 91, 94, 98, 100, 102, 108, 109, 114, 115, 116, 119, 120, 121, 124, 125, 150, 152, 165, 171, 221–223, 242, 265
ASME 159, 160, 262, 263
ASNT 262
ASTM 13, 38, 42, 48, 52, 53, 247, 252, 261
Asymmetric modes 9, 171
Attenuation measurement 24
  in wedge materials 42–52
Automated inspection (testing) 14, 15, 25–27,
Axisymmetric waves 177

Back scattering 113, 123–134
Backing material 34, 37
Bandwidth 17, 21, 34, 37, 140, 173, 248–250, 263
Band round wave 133–134
Best modes 173–174, 178, 186, 195
Boundary effect 10, 135, 141, 163
B-scan 143
Bulk waves 7–8, 134, 165–169

Calibration standard (block) 145, 157–162, 263–264
Center frequency 35, 40, 140, 248
Coefficient of attenuation 45–52, 174–175, 268, 269
Coefficient of transmission 68–69

Ultrasonic Inspection Technology Development and Search Unit Design: Examples of Practical Applications, First Edition. Mark V. Brook.

Combined wedges 26–27
Creeping wave 10–11, 114, 124, 126–127, 130, 265
Critical angles 10–11, 19–20, 30, 68, 78, 86, 114, 124–126, 265–266
Crystal assembly 15–17, 24, 32–36, 67, 70, 100–104, 124
Crystal size (diameter) 52–57, 68, 70, 78, 103, 104, 106, 124
Crystal (piezoelectric) materials 33, 35–36
Cylindrical rod inspection 135–162

Damping 34, 140, 249–250
Dead zone 77
Decibel 46–48, 63–64
Delay line 14–16, 20–23, 100
Delta TOFD technique 113
Deviation 66–75, 92, 173, 235, 248, 252–253
Diffraction 12, 54. *See also* Time of flight diffraction (TOFD)
Directional characteristic 17, 57–64, 68, 78
Discontinuities 1–12, 17
Dispersion curves 9, 39, 170–173, 178, 180, 188, 195–197, 207, 210, 216–217, 267–271
Divergence 48, 54, 58, 60–63, 64, 78, 80, 83, 108
Double spiral pattern 177, 189
Dual probes 77, 81, 104
Dual-duplex probes 101–102

Eddy current testing 1, 3, 6, 177
Elasticity of volume 6
Elasticity of shape 7
Energy distribution 178, 197, 198, 199, 213–215
Exit point 24, 27, 32, 67–71, 73, 82, 88, 91, 92, 94, 108, 115, 118, 129, 132, 133, 145, 183, 194, 195, 204, 213, 215, 241, 242, 244, 250, 251–253

Far field 58, 60, 62–63
Flexural mode 54, 178
Focal point 224
Focal zone 218–233
Forward scattering 54, 112, 113–118
Free field 60, 63, 108, 138, 231
Frequency response 34, 248–249
Frequency tuning 217, 218

Gliding waves 133–134
Group velocity 10, 167–172, 188–191, 196–201, 208, 210–213, 267, 269
  measurement 189–192, 199–204
Guided waves 8, 10, 136–140, 148, 164, 165, 175–180, 182–184, 196–199, 203, 204, 215, 217

Head waves 12
Hollow cylinder 10, 117, 118, 122, 163–218
Horizontally polarized shear wave 7, 8

Imaginary crystal 21–23, 67–68, 78–80, 83
Immersion focused transducer (probe) 250
Immersion technique 48, 245
Interchangeable transducers 173

Lamb-type guided waves 10, 165, 175–177, 180, 195–196, 199, 203, 204, 217
  mode selection 182–184
Lamb waves 8–10, 54, 163–176, 178, 197, 199, 213, 271
Lateral waves 113–116, 122
Longitudinal waves 7–11, 15, 19, 30, 36, 61, 68, 77, 122–126, 139, 165, 171–174, 178, 186
Love waves 12

Main lobe 17, 61, 62–68, 75–78, 136, 164
Magnetic particle testing 1, 3, 6
Matching layer 15, 16, 33, 36–38, 42–43, 248, 254, 255

Mirror system 150, 152
Misorientation angle 240
Mode conversion 9, 17–18, 135–136, 163, 170
Multiple crystal probe 99–110

Near field 23, 24, 52, 58–59, 77, 79, 83, 84, 109–110, 225, 227–230, 258
Neper 45
Non-axisymmetric waves 165, 177, 189, 194, 197, 214
Notch area 157–162
Notch reflectors 31, 157, 158

Oblique incident beam 114, 133

Particle displacement 9, 171, 179–180, 189, 194, 196, 198, 206, 208–209, 268, 271
Peak frequency 248
Penetrant testing 1, 3, 6
Phase velocity 167–174, 178, 180, 181, 187–189, 194–196, 207, 216–217, 267–269
Phased array probe 14, 36, 88, 89, 99
Piezoelectric crystal (element) 33, 249
Piezoelectric materials 14, 15
Pulse-echo method 149, 201, 248, 261

Quasi-bent central ray 76

Radial vibration mode 35–37, 54
Radiographic testing 1, 4, 6
Ray tracing 25, 56, 57, 141–142, 154–155, 238–239, 245
  in wedges 104–105
Reference blocks 71, 72, 251–253
Reflection 4, 9, 17–25, 38–40, 48, 55, 105–107, 136, 140, 143, 145, 149, 153, 165, 168, 192, 195, 202, 203, 208, 214, 221, 222
Refracted angle 7–11, 14–19, 26, 32, 65, 69–76, 77, 78, 87, 88, 91, 93, 94, 96, 97, 100–101, 103–108, 115, 118–120, 124, 128, 129, 130, 134, 147, 152, 167, 220, 223, 240, 242, 245, 250–255, 263, 265
Refraction 17–19, 22, 92, 222
Rod waves 10, 135–140

Sealed probes 16
Search unit (probe)
  Types 13–17
Scanning 3, 4, 14, 15, 55–58, 113, 117, 126–131, 173, 234, 238
Sensitivity 4, 27, 34, 37, 38, 52, 54, 81–85, 153, 173, 180, 182, 248–252
Sensitivity curves 81–82, 85
Shadow technique 149
Shadow zone 134, 150
Shear waves 7–12, 16, 19, 36, 41, 61, 65, 66, 78, 122–124, 134, 139, 167, 170–174, 186, 265, 271
Signal shape 175–176
Skew angle 86–88, 91, 96, 238, 240–242
Snell's law 10–12, 18, 19, 30, 65, 68, 70–74, 104, 106, 124, 138, 171, 223
Spherical aberration 221–223
Stoneley waves 12
Stud inspection 144–157
Surface waves 8, 19, 20, 113, 114, 124, 171, 216
  probe 27–32
Symmetric modes 171, 173, 174, 178, 186, 204

Tandem probe 124–129, 133
Test blocks 69, 72–73, 248, 253–255
Thermal infrared 5
Thickness expansion mode 15
Third critical angle 20, 265–266
Time of flight diffraction (TOFD) 54, 111–134
Torsion mode 178, 197
Triplex probe 16, 100–101, 103–110
Tuning components 33, 35

Ultrasonic testing 1, 4, 6–12, 57

Velocity dispersion 9, 173, 180, 188, 196, 197, 207, 210, 217
Velocity measurement. *See also* Group velocity, measurement
  in metals 38–41
  Raleigh wave 216–218
  in wedge materials 42–43
Vertically polarized shear waves 7, 8
Visual testing 2, 5

Water gap thickness 215–216
Water-loaded test object 173, 186
Wave front 112, 167–168
Wave modes 48, 62, 101, 111, 114, 170, 178
Wave propagation 4, 7–10, 17–20, 164–165, 167, 170, 174, 177, 178, 196–204, 214–216, 218
Wave structure 28, 177
Waveform duration 248, 249
Wedge angle 17, 27, 29–32, 65–73, 80, 86, 87, 100, 104, 116, 115, 124, 127, 129, 145, 147, 170–174, 179–184, 187, 189, 195, 197, 202, 205–207, 240, 265, 268, 269
Wedge noise 24–27, 31, 51, 55, 101, 102, 107, 241